Planet-Disc Interactions in Fully Radiative Discs

Dissertation
der Mathematisch-Naturwissenschaftlichen Fakultät
der Eberhard Karls Universität Tübingen
zur Erlangung des Grades eines
Doktors der Naturwissenschaften
(Dr. rer. nat.)

vorgelegt von

Bertram Bitsch

aus Tübingen

Tübingen

2011

Contents

1 Introduction

1.1 Solar System

1.1.1 Ancient developments

In ancient times, seamen used fixed stars to navigate their ships through the Mediterranean Sea. However, they also noticed moving objects in the night skies, the planets. Planet is Greek and stands for 'moving celestial body'. The planets visible to the naked eye (Mercury, Venus, Mars, Jupiter and Saturn) were also linked to the names of gods in ancient mythology.

During the time of Aristotle the first basic ideas of geocentrism were established, however the system did become standard much later. In the 2nd century AD the astronomer Claudius Ptolemaeus finally accomplished this task. His cosmological model was accepted for over a millennium as correct by European and Islamic astronomers. Because of its influence, the Ptolemaic system is sometimes considered to be identical with the geocentric model. In these models, the Earth is believed to be at the centre of the Solar System and the universe (see Fig. 1.1).

In the Ptolemaic system, each planet moves in a system of two circles. One circle, the deferent, is a circle around Earth, while the other circle, the epicycle, describes a circular motion of the planet on the deferent. A planet then moves along the epicycle while at the same time the epicycle moves along the path marked by the deferent. The combination of these two movements shows an effect that was long missing in the ancient greek cosmological systems. In this epicycle model, a given planet seems to move closer to and farther away from the Earth at different points in its orbit, which even makes the observers believe that the planet slowed down, stopped, and even moved backwards (in a retrograde motion). This was actually one of Ptolemy's main reasons for creating the deferent epicycle model. This model was not accurate by far, but it made observations and predictions much more accurate than in all preceding systems.

1.1.2 Modern Ages

The first steps away from the geocentric model were taken in the 16th century, when Nicolaus Copernicus published his book *De revolutionibus orbium coelestium* (On the Revolutions of the Celestial Spheres) in 1543 just before his death. In his system, the Earth and the other planets are revolving around the sun (heliocentric view). Copernicus was not
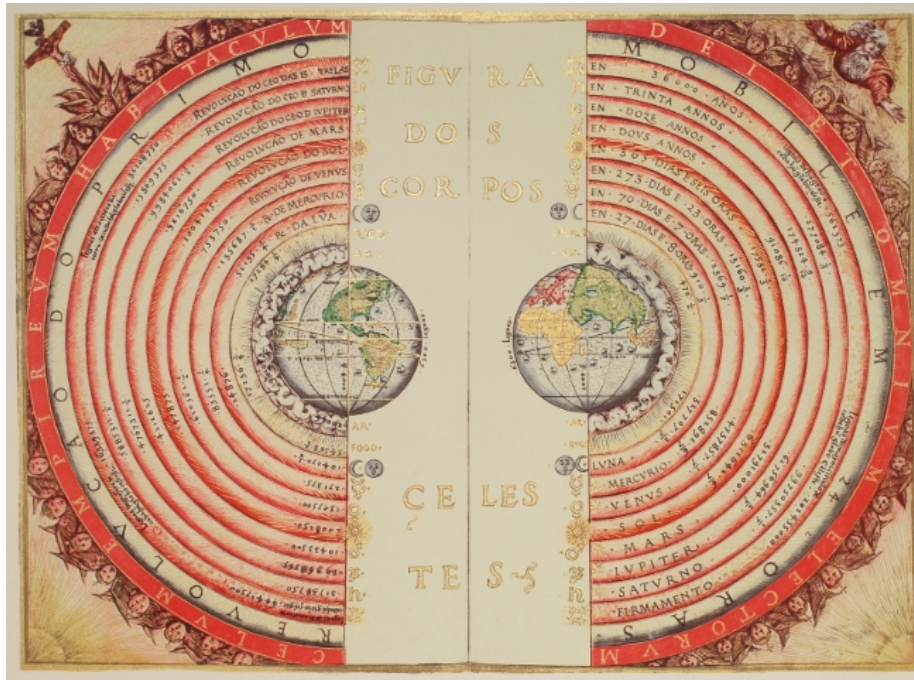
Figure 1.1: An illustration of the Ptolemaic geocentric system by Portuguese cosmographer and cartographer Bartolomeu Velho, 1568 (Bibliothèque Nationale, Paris)

motivated by new observations, he invented his system on a philosophical and theological base. This was not welcomed by the Roman-Catholic Church.

In 1609 Johannes Kepler (Fig. 1.2) published his *Astronomia Nova* where he suggested that the planets move on ellipses around the sun. He obtained his results by analysing the precise astronomical observations of Tycho Brahe and therefore cleared all the remaining doubts about the heliocentric world view, at least in the scientific world. Kepler's laws give a description of the motion of planets around the sun. These laws are (the third one published in 1619):

1. The orbit of every planet is an ellipse with the Sun at one of the two foci.
2. A line joining a planet and the Sun sweeps out equal areas during equal intervals of time.
3. The square of the orbital period of a planet is directly proportional to the cube of the semi-major axis of its orbit.

The Bible and religious dogmas could not stand against scientific facts any more. The theory of heliocentrism therefore contributed to a revolution in philosophy: the age of Enlightenment. Modern science was evolving with the aim of finding universal laws to model the mechanics of the world. One of the most important ones is the gravitational law expressed by Newton in 1687, from which the three Kepler laws can be derived mathematically.
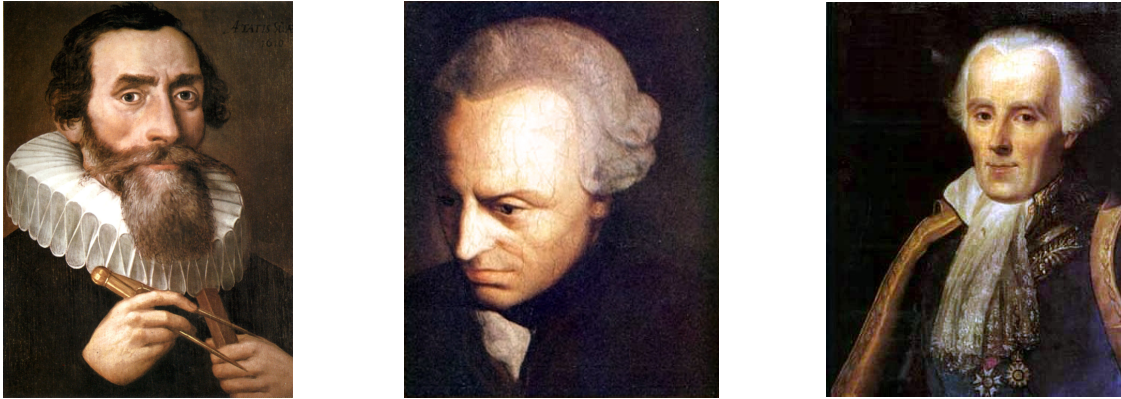
Figure 1.2: Johannes Kepler, 1571-1630 (left), Immanuel Kant, 1724-1804 (middle) and Pierre-Simon Laplace, 1749-1827 (right).

However, a scientific explanation how the solar system was created was still missing. In the second half of the 18th century, Immanuel Kant and Pierre-Simon Laplace (Fig. 1.2) published the idea of a collapsing nebula as the origin of the Solar System independent of each other. In this theory, the Solar System could have formed from a cold disc of dust and gas rotating in an ecliptic plane around the Sun. This would also explain why all the planets in our Solar System have quasi-coplanar, prograde orbits. The discoveries of Uranus (Herschel, 1781) and Neptune (Le Verrier, Adams and Galle, 1846) were consistent with this theory as they also orbit close to the ecliptic in a prograde orbit. In this model, Pluto, with an inclination of 17 degrees, would be a strange planet. However, Pluto is simply one of hundreds of Kuiper Belt Trans Neptunian Objects and now belongs to the category of "dwarf planets" since 2006.

Nevertheless, the model for the formation of the Solar System from a cold gas disc by Kant and Laplace is still the most popular scenario among astronomers. For the last two centuries this model has been observationally confirmed and theoretically refined. In the following Sections, a brief overview over the formation of stars with discs (and planets) around them is given.

1.2 Formation of planets

1.2.1 Star formation

Gas nebulae in the interstellar medium are the birth places of young stars. These clouds mainly consist of Hydrogen and Helium, but also heavy elements (Carbon, Nitrogen, Oxygen, Magnesium, Iron, ...), which represent about one percent of the total mass. A massive gas cloud, heavier than the critical value of the Jeans mass (a few solar masses ($M_\odot$)), collapses because of its self-gravitation into isolated systems. The gas clouds carry a certain amount of angular momentum that is conserved through the whole process. The gas in the

Figure 1.3: Protoplanetary discs in the Orion Nebula (M42). The young star is shining at the centre surrounded by the disc. Credit: NASA/ESA and L. Ricci (ESO)

central part in the clouds undergoes fast compression and forms a core that will become a star later on. Temperature and pressure in this core rise, until the first nuclear fusion sets in and the protostar is born.

As the collapse of the core continues, the gas in the surrounding cloud is prevented from infall by the angular momentum it is carrying. The angular momentum conservation limits the contraction to a plane perpendicular to the rotation axis of the gas cloud, while the gas can freely 'fall' in the vertical direction. Therefore a torus around the protostar is formed that later on becomes a thin disc with height H. The so called *aspect ratio H/r*, normally a few percent, gives the ratio between the height of the disc and the distance to the central star. As this disc is in time accreted onto the central star, it is named *accretion disc*.

The accretion disc is heated by the central star and emits an infrared flux. These discs can be observed by space telescopes (see Fig. 1.3). As the dust and gas particles can only be accreted onto the central star if they lose angular momentum, the angular momentum must be carried away by other parts of the gas drifting outwards. As a result the protostar and the discs radius are growing. The motion of the gas in these discs is determined by

the gravity of the central star and is approximately Keplerian, so that the angular velocity is given by Kepler's third law:

$$\Omega = \sqrt{\frac{GM_*}{r^3}} \ , \tag{1.1}$$

where G is the Gravitational constant, M_* the mass of the central star and r the distance from the star. Using the total mass of the disc and the rotation law, the total angular momentum of the disc can be calculated:

$$J = \int_0^{R_{disc}} \Sigma r^2 \Omega 2\pi r dr = \frac{1}{2} M_{disc} R_{disc}^2 \sqrt{GM_*} \ , \tag{1.2}$$

with $\Sigma = \Sigma_0 r^{-1/2}$ being assumed the surface density profile. The radius of these discs can be up to 1.000 Astronomical Units (AU) if the initial angular momentum of the nebula is large enough. The Astronomical Unit represents the semi-major axis of the Earth's orbit around the sun: 1 AU = 150.000.000 km.

As the accretion disc dissipates within ten million years, it imposes a strong constraint for the formation of planets. These planets have to be formed within this period of time. As planet formation is supposed to occur in these discs, they are also called *protoplanetary discs*.

1.2.2 Planet formation

The formation of a planetary system out of a molecular cloud is illustrated in Fig. 1.4, where the formation is illustrated in 6 phases. The interstellar cloud collapses under its gravity (a) and forms a protostar with an accretion disc (b). In this accretion disc, small dust particles stick to each other and begin to form bigger objects (c). In time these dust particles form planetesimals of several kilometres in size. Through collisions and gas accretion these planetesimals become protoplanets (c-e). In time these protoplanets become bigger objects, planets, and the gas is finally cleared from the disc, so that a solar system is visible (f). This whole process takes several million years until completion.

The process by which molecular grains merge into planetesimals is not yet fully understood and is still under research. The discussion of this process is therefore omitted. After embryos are formed from planetesimals by runaway growth, they collide and merge into bigger objects (planetary cores). During this formation process, these planetary cores can scatter each other out of the system until a stable configuration in the system is achieved.

If the planetary core is massive enough, typically a few Earth masses, to accrete a gaseous atmosphere from the disc gas, they can become giant gaseous planets like Jupiter and Saturn (or even bigger). The main time consumption for this scenario is the slow accretion of gas, after the formation of the core and before the runaway accretion of gas. The whole process takes several million years to finish.

As the formation of massive planetary cores requires a lot of solids, it is favoured if water, which is an abundant molecule, is in the form of ice instead of vapour. The temperature
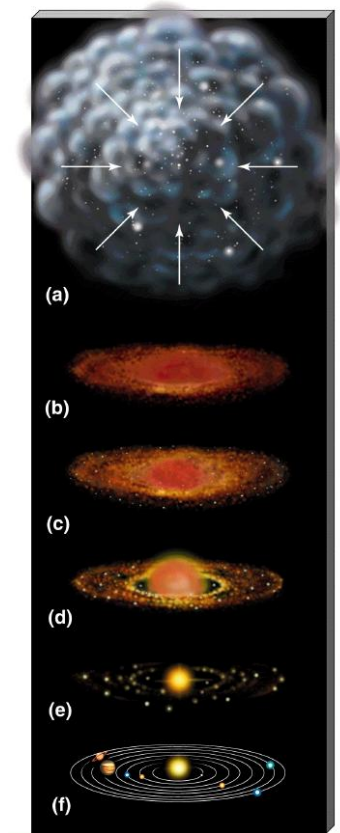
Figure 1.4: Illustration of the creation of a solar system. A detailed description is given in the text.

in the accretion disc reduces with increasing distance from the central star, so beyond a specific point in the disc, water condensates and within it water sublimates. This border in the disc is called *snow line*. Around a star like our Sun, the snow line is located at about 3 to 5 AU. This also implies that the formation of massive planetary cores is easier just outside the snow line, which is consistent with the planetary configuration in our Solar System.

Giant gaseous planets can also be formed by gravitational instability processes in the accretion discs (Boss, 1997, 2000). The formation time of giant gaseous planets in this model is much shorter than in the core accretion model, but this model does not explain the observed masses, obliquity and composition of the giant planets in our Solar System. The presence of solid cores of a few Earth masses in Saturn, Uranus and Neptune are actually in favour of the core accretion model. However, gravitational instability can easily produce big planets far out in the disc. It seems that both theories are applicable to different scenarios in planet formation.
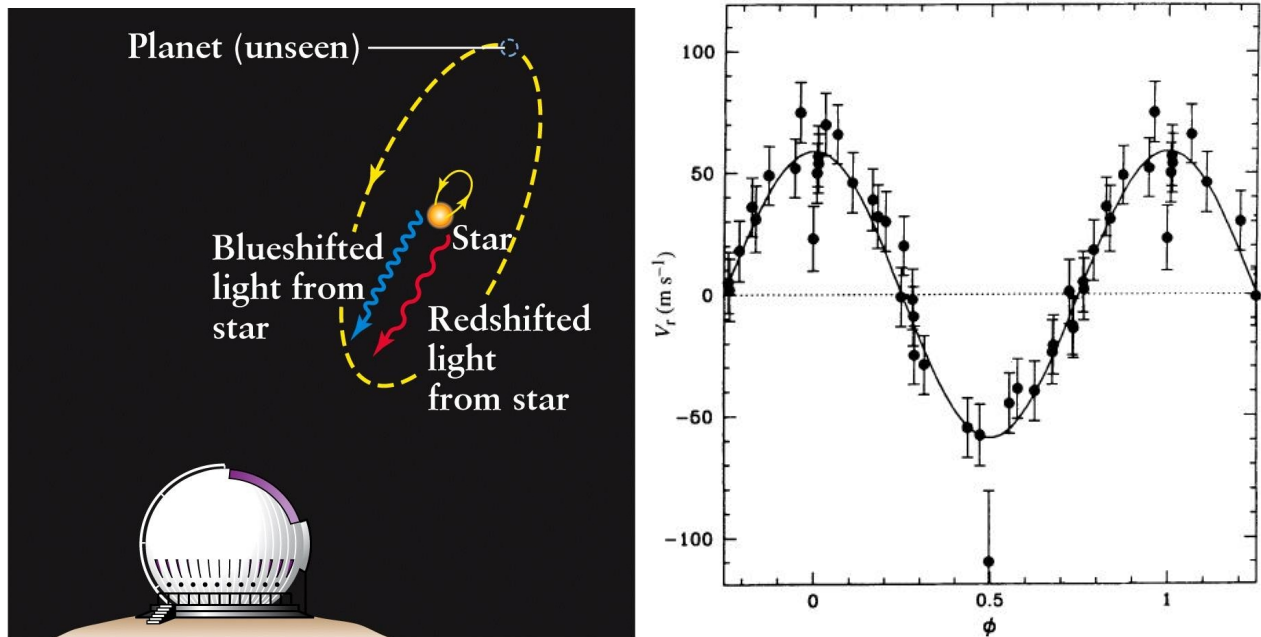
Figure 1.5: Schematics of the radial velocity detection method for planets (left) and radial velocity variations of the star 51 Pegasi in meters per second, as a function of planetary orbits (right). Right picture taken from Mayor and Queloz (1995).

1.2.3 Observation of Exoplanets

Exoplanets are planets observed outside our own Solar System, orbiting other sun-like stars. Up until today there are several methods to observe planets orbiting around other stars. The most successful method (in terms of detected Exoplanets) up to date, is the measuring of the radial velocity. Observers measure the velocity of the star in respect to the line of sight. If the star has a companion, both, star and companion, rotate around their centre of mass. As the companion is rotating around the star, the star is moving either away or towards the observer. This movement has a direct influence on the observed light spectrum because of the Doppler effect. When the star is moving towards the observer, a blue shift is measured, while a red shift is measured when the star is moving away from the observer. An illustration of this process is given in the left panel of Fig. 1.5.

This method obviously works best, when the system of star and planet is viewed 'edge-on', while it does not work when the system is 'face-on'. From the amplitude of the star's motion, the mass of the planet can be determined, or more exactly $M\sin(i)$, as the observed system mostly has an inclination i towards the observer. With the mass of the star (determinable through luminosity and colour of the star), the orbital period gives a direct relation towards the semi-major axis of the orbit of the planet (Kepler's third law).

In 1995 the first Exoplanet was discovered around the star 51 Pegasi by Mayor and Queloz (1995). The variations of the radial velocity as a function of time in normalised units is
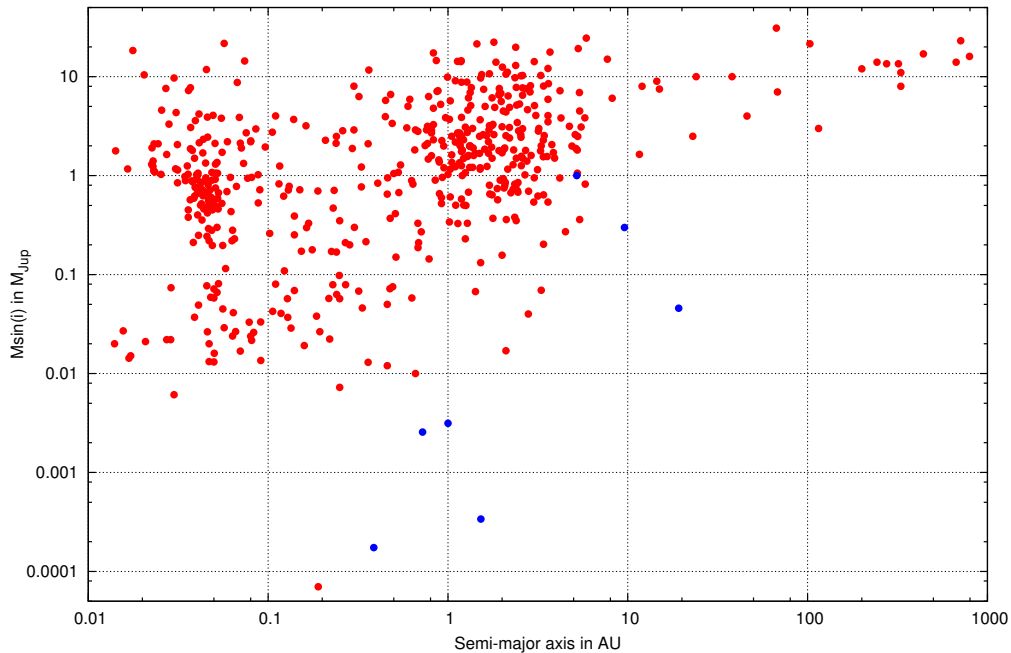
Figure 1.6: Semi-major axis against planetary mass for discovered Exoplanets (red). The planets of the Solar System are highlighted in blue. Plot created with data from exoplanets.eu.

shown in the right panel of Fig. 1.5, which is taken directly from Mayor and Queloz (1995). The discovered planet has a mass of about one half of Jupiter and and orbital period of 4.23 days, which corresponds to about 0.056 AU, which is much smaller than Mercury's semi-major axis. The existence of a massive planet so close to the star is extremely surprising, as the planet could not have formed at this position and must have somehow moved there.

Up until today, many more Exoplanets have been discovered (see Fig. 1.6). Most of the observed Exoplanets are so called *hot Jupiters*, giant planets orbiting very close to their parent star. Not all of these planets have been detected using the radial velocity method. One other mechanism (among others), is the measurement of planetary transits. The planet transits in front of its host star and a resulting diminution of luminosity of the star can be detected and measured. This method additionally provides the radius of the observed Exoplanet.

Considering the observations up to date, the Solar System seems to be an exception, which is also illustrated in Fig. 1.6. Since the hot Jupiters are the easiest planets to detect, it is no surprise that these planets are observed much more often. In fact, the present detection methods are limited to massive close-in planets and are not able to detect terrestrial planets or long-period giants because of resolution problems. Scientist hope to detect planets in the habitable zone (a zone around the star where water is in its liquid form and therefore life, as we know it, can exist) with the new Kepler telescope, which is able to find earth like

planets in this zone. The Kepler telescope observes over 150.000 stars for planets at once, using the transit detection method. So far, over 1.000 planet candidates (not confirmed planets) detected by Kepler have been published.

According to the theories mentioned, the formation of planetary cores is much more likely beyond the snow line. The cores then acquire their final mass while they are still embedded in the disc. Because the hot Jupiters were not formed where they are observed now, there has to be a process to get the planets from their birth place to the location we now observe them. During the process of its creation the planet interacts with the disc it is embedded in and moves in it. This movement is called *migration* and an overview over the different types of migration will be given in the next Section. The theory of migration is therefore a key element to explain the existence of hot Jupiters.

1.3 Planet-disc interactions

This Section gives an overview of the nature of planet-disc interactions. The theory and different kinds of planetary migration are briefly discussed. A more detailed presentation of type-I-migration is given in Chapter 2.

The *heliocentric frame* is centred on the central star and the planets and the disc fluid elements rotate around it with an angular velocity Ω, which is defined by Keplers's law (Eq. 1.1). Consider a right-hand-side orthogonal coordinate system centred on the central star, but with the x axis always pointing at the planet and the z-axis always in the direction of the angular momentum vector of the planet. If this coordinate system rotates with the same speed as the planet in the heliocentric frame, then the planet is motionless in this coordinate system. This system is called *corotating frame*. The angular velocity of fluid elements then is $\Omega - \Omega_P$, where P refers to the planet. A *synodic period* is the period that corresponds to the time between two conjunctions with the planet. The synodic period is equal to $2\pi/|\Omega - \Omega_P|$. Fluid elements on orbits larger than the planetary orbit have a smaller angular velocity in the heliocentric frame than Ω_P. Therefore, these fluid elements have a negative angular velocity in the corotating frame, meaning that these elements seem to move backwards in the corotating frame. This is the reason for the absolute value symbol in the expression of the synodic period.

1.3.1 Angular momentum

Consider an initially axisymmetric disc with an embedded planet. This planet, with mass M_P, disturbs the gas particles and fluid elements in the disc because of its gravitational potential. The fluid elements in the disc begin to oscillate around their initially unperturbed circular orbit. The interferences of these oscillations lead to the formation of a one-armed spiral wave, which is called *wake*. The wake is a pressure supported density wave (visible in the left panel in Fig. 1.7). The wake is directed forwards in the inner disc and backwards in the outer disc (from the planets location in the direction of rotation).

This structure results in a gravitational attraction between the planet and the wake's over-density (compared to the normal density of the disc). Therefore the planet experiences a force from the inner part of the disc, which is directed in the direction of motion, thus leading to an increase of the planet's angular momentum. This angular momentum accelerates the planet and pushes the planet radially outwards. The planet also experiences a force from the outer part of the disc, which is directed in the opposite direction. The planet is slowed down and pushed radially inwards from the outer disc.

On the other hand, the planet exerts a force on the disc as well. The planet exerts a torque on the inner disc, slowing it down and pushing it towards the central star. The planet also exerts a torque on the outer disc, accelerating it and pushing it away from the star. Angular momentum is therefore transported in both directions. As a result, the planet stays in between the inner and outer disc. Planet and disc are transferring angular momentum to and from each other, as symbolised below:

$$\text{inner disc} \quad \overset{\text{a.m. transfer}}{\Leftrightarrow} \quad \text{planet} \quad \overset{\text{a. m. transfer}}{\Leftrightarrow} \quad \text{outer disc} \tag{1.3}$$

The torques acting on planet and disc are proportional to the mass of the planet and to the amplitude of the wake, as planet and wake are gravitationally attracting each other. As the wake is created due to the gravitation of the planet, the amplitude of the wake is proportional to the mass of the planet. Therefore the torques are proportional to the planet mass squared, $\Gamma \propto M_P^2$.

The torque exerted from the outer disc on the planet is always bigger than the torque exerted from the inner disc on the planet. Therefore the planet experiences a total negative torque, which is proportional to M_P^2. The reason for this phenomenon will be discussed in Section 2.1. Thus, the planet loses angular momentum at a rate proportional to the planet's mass. The angular momentum and it's change in time is:

$$j = r^2 \Omega = \sqrt{GMr} \quad \Rightarrow \quad \frac{dj}{dt} = \frac{1}{2}\sqrt{\frac{GM}{r}}\frac{dr}{dt} = \frac{1}{2}r\Omega\frac{dr}{dt} \ . \tag{1.4}$$

As the angular momentum decreases at a rate proportional to the distance from planet to star, r_p, so does the radius itself. This process is called *type-I-migration*. A planet corresponding to the linear type-I-migration regime is shown in the left panel in Fig. 1.7. The planet is clearly embedded in the disc.

The torques exerted by the planet push the outer disc farther away from the star and the inner disc inwards, resulting in a splitting of the disc in an inner and an outer disc. However, the gas of the disc tends to spread into the void regions, cleared by the planet before. These two effects are competing. As the torques exerted by the planet are proportional to the planet's mass squared, a more massive planet is much more effective in pushing the gas away from its orbit. If the planet is massive enough, it opens up a gap in the disc around its orbit. In protoplanetary discs, gas giants are able to do so. In the right panel in Fig. 1.7, a Jupiter mass planet in a protoplanetary disc is shown. The planet clearly opens a gap inside the disc.
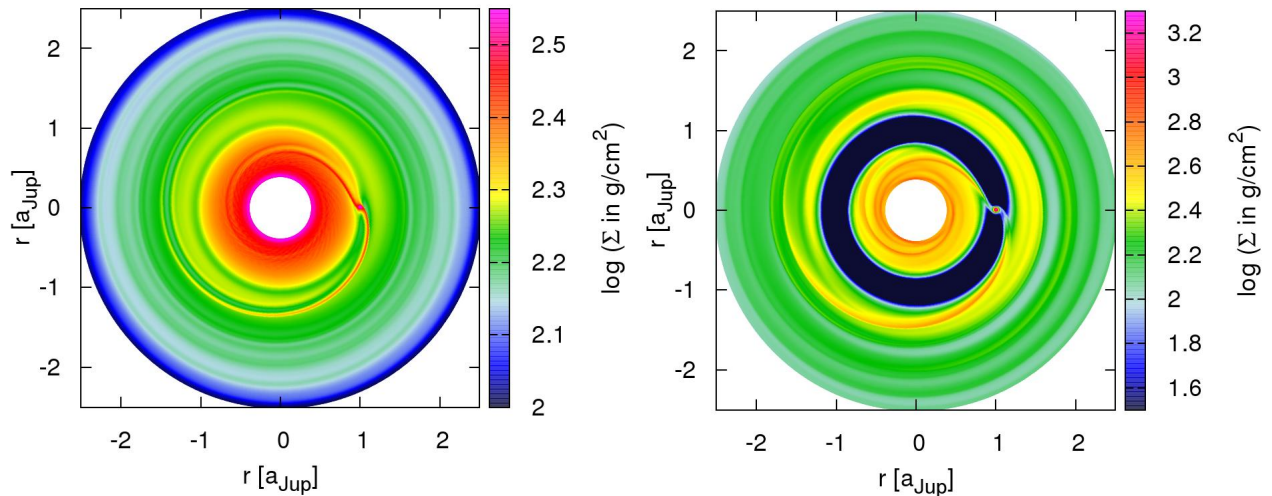
Figure 1.7: Surface density of $20M_{Earth}$ planet (left) and a Jupiter mass planet (right) embedded in a protoplanetary disc. The disc is rotating in both pictures counterclockwise. The planet is located at $(1,0)$ in the (x,y) coordinate system. Please note the different colour scaling for the surface density. Plots taken from simulations from Kley *et al.* (2009).

If a massive planet obrits around a star in a gap in the accretion disc, it is locked in the gap (Fig. 1.7). If the planet moves towards the outer part of the disc, it feels a larger negative torque, which repels the planet inwards. If the planet approaches the inner part of the disc, it gets a larger positive torque, which pushes the planet outwards again. The planet can not move in the gap and the disc, which was still possible in the type-I-migration regime. The disc is still evolving because of its own viscosity. As the inner part of the disc is accreted onto to the central star, the outer parts of the disc are moving outwards because of the conservation of angular momentum. The planet has to follow the evolution of the disc, as it is locked in it. The migration is therefore only dependent on the viscosity of the disc, so that the migration rate is proportional to the viscosity of the disc (Ward, 1997). This process is called *Type-II-migration*.

If the planet only opens up a partial gap in the disc, the outer and inner disc are not fully separated, so that the planet is still able to move inside the disc. If the planet now moves inwards in the disc, it will first enter a region of the disc that has still some gas left. To sustain the dip in the gas (caused by the planetary potential), the planet moves gas from the inside outwards. The planet is transferring angular momentum to the gas that moves outwards. But a loss of angular momentum accelerates the inward migration of the planet. Under certain conditions this can lead to an exponentially growth of the migration rate. This runaway migration is called *type-III-migration*. However, in this migration regime, the planet can migrate inwards or outwards, depending on the initial conditions. The effect is so strong that it can completely modify the orbital radius of the planet in a few orbits.

1.3.2 Problems of planetary migration

As pointed out above, the process of creating a massive Jupiter size planet takes several million years by the core accretion model. In this model, first a core of several earth masses is created. However, a core of several earth masses is prone to type-I-migration and the migration time scale for a planet in this regime is much shorter than the lifetime of the disc. This means that the planet drifts towards the central star in about a hundred thousand years, which is much shorter than the time needed to accrete an gaseous atmosphere (which takes several million years). With this high migration rates, the core accretion model is unable to account for giant gaseous planets. The planetary core has to be stopped at some point in the disc, in order for the model to work.

Population synthesis models try to explain the distributions of Exoplanets (see Fig. 1.6). These models use theoretical migration rates for the evolution of planets. In order to match the observed distributions, the migration rate in these models has to be a factor of 10 to 1000 smaller than in the type-I-migration regime (Alibert *et al.*, 2004; Ida and Lin, 2008; Mordasini *et al.*, 2009). With this adjusted migration rate, population synthesis models show indeed a quite good match for the distribution of Exoplanets.

That indeed migration is present in accretion discs can be seen in the observed Kepler-9 System (Holman *et al.*, 2010). In this three planet system, two Saturn size objects are orbiting the central star on close-in orbits. The gravitational interactions of these two planets are near the 2 : 1 mean motion resonance (MMR). This means, while the outer planet makes one orbit around the star, the inner planet makes exactly two orbits around the star. The planets migrated into this configuration, as the creation of these planets in such a resonance seems highly unlikely.

In order to slow down the migration time scale of planetary cores, several ideas were suggested and discussed in the community. One idea might be the introduction of surface gradients in discs, so that the planetary core is trapped in the disc (Morbidelli *et al.*, 2008). Another, more promising idea, is the inclusion of radiation transport in the disc, which allows to slow down the migration rate (Paardekooper and Mellema, 2006). This process and how the torque acting on an embedded planet is created and influenced will be discussed in Chapter 2.

2 Interactions

When a planet is embedded in a disc, several mechanisms can influence its motion. In order to explain how orbital elements of planets can be changed, a brief overview over these mechanisms is given here.

- *Planet-gas interactions.* As mentioned before, a planet embedded in a gaseous disc experiences a torque. The variation of the planet's semi-major axis is referred to as *planetary migration.* The rate of migration depends on the planetary mass. For low-mass planets, which do not open gaps in the disc, this migration is inwards and proportional to the planet's mass squared (type-I-migration) as described in Ward (1997). If the planet is massive enough and opens up a gap in the disc, the planet is locked in this gap. As the disc is accreted onto the star on a viscous time scale, the planet is moving with the disc (type-II-migration). The migration speed for type-II is much slower than for the type-I-migration.

- *Planet-planetesimal interactions.* As planets form by the collision of planetesimals, it is logical to assume that even as the first planets are formed in a disc, planetesimals are still present in the disc. The planetesimals also interact with the planet, so that they may significantly alter the planets motion in the disc. The change of the planet's semi-major axis is referred to as *planetesimal driven migration.* This mechanisms has been investigated in great detail for the Solar System, where Jupiter might have drifted slightly inwards, whereas Saturn, Uranus and Neptune might have significantly moved outwards. This could also explain the location of the Kuiper Belt (Levison and Morbidelli, 2003). It also can give a nice explanation of the Late Heavy Bombardment of terrestrial planets (Tsiganis *et al.*, 2005; Gomes *et al.*, 2005).

- *Planet-planet interactions.* As planets migrate, caused by interactions with the gas or with planetesimals, they can become locked in a mean motion resonance (MMR). Jupiter and Saturn in the Solar System are close to the 5:2 MMR and also some exoplanetary systems are locked in MMR (for example the Kepler-9 System (Holman *et al.*, 2010)). Planets locked in the MMR can significantly increase their eccentricity or inclination. Also, planets locked in MMR can, under certain conditions, migrate outwards in discs (Crida *et al.*, 2009).

In this Chapter, and in this thesis, the focus is on planet-gas interactions and the interactions of planets with planetesimals and other planets are discarded. In Section 2.1 the linear Lindblad torque and its influence on planetary migration is discussed. In Section 2.2 the corotation torque and its influence on planetary migration is described. Additionally non linear effects on the torque are discussed in Section 2.3. In Section 2.4 the isothermal assumption is dropped and planetary migration in fully radiative discs is discussed.

2.1 Linear Lindblad torque

In this Section, the influence of the gas disc on an embedded low-mass planet is described. Low-mass planet means in this Section that the disc's response to the planetary potential is linear and can be studied in a linear analysis up to a few Earth masses. For the analysis presented here, the disc is assumed to be two dimensional (2D), non-selfgravitating and locally isothermal (fixed temperature profile on cylinders around the central star). The planet is therefore assumed to be in midplane of the disc and on a fixed circular orbit. As the planet is not able to move in the disc (fixed orbit), the torque acting on the planet is used to estimate its change in orbital elements. A positive torque implies outward migration, while a negative torque indicates inward migration.

2.1.1 Lindblad resonances

When a planet is embedded in a gaseous disc, the planetary potential acts as a disturbance. The gravitational potential of the planet is given by

$$\Phi = -\frac{GM_P}{d} \ , \tag{2.1}$$

where d denotes the distance from the planet. In polar coordinates centred on the star, $\Phi(r, \phi)$ is a 2π periodic function in ϕ, where ϕ is the azimuthal angle. The planetary potential is a disturbance in the disc and it can be decomposed into a Fourier series of the variable $(\phi - \phi_P)$, where ϕ_P is the azimuth of the planet. As the planet is on a circular orbit, $\phi_P = \Omega_P t$, and the Fourier series reads:

$$\Phi(r, \phi, t) = \sum_m \Phi^m(r) \exp(im(\phi - \phi_P)) = \sum_m \Phi^m(r) \exp(im(\Omega - \Omega_P)t) \ , \tag{2.2}$$

where Φ_m represents the mth component of the planetary potential. The imaginary part of the expansion does not play a role, as the interest lies in the real part. Therefore the series simplifies to:

$$\Phi(r, \phi, t) = \sum_m \Phi^m(r) \cos[m(\Omega - \Omega_P)t] \ . \tag{2.3}$$

The perturbing frequency can be denoted as $\omega = m(\Omega - \Omega_P)$, which means that the resonances correspond to

$$m(\Omega - \Omega_P) = \pm\Omega \quad \Leftrightarrow \quad \Omega = \frac{m}{m \pm 1}\Omega_P \ . \tag{2.4}$$

These resonances are called *Lindblad resonances*. The resonance with $\frac{m}{m-1}$ is the inner Lindblad resonance (ILR), while the resonance with $\frac{m}{m+1}$ is the outer Lindblad resonance (OLR). Kepler's third law can be used to get the location of the Lindblad resonances:

$$r_{ILR} = r_p \left(\frac{m}{m - 1}\right)^{-2/3} \quad , \quad r_{OLR} = r_p \left(\frac{m}{m + 1}\right)^{-2/3} \tag{2.5}$$

Please note that for $m = 1$ no inner Lindblad resonance exists, but for higher m two Lindblad resonances exist. For $m \to \infty$, the resonances move closer to the planet and converge at r_p. The fluid elements at a Lindblad resonance are in mean motion resonance with the planet, while they take m orbits around the central star, the planet describes $m \pm 1$ orbits.

The torque exerted by the planet on the disc corresponds to the exchange of angular momentum. This is also equal to the torque of the disc on the planet (Newton's third law). For the remainder of the thesis, the term 'torque' describes the torque of the disc acting on the planet. The torque determines the migration rate $\dot{a}$. The time variation of the planet's angular momentum $\dot{J}$ matches the torque Γ exerted on the planet. As the planet is on a circular orbit, $J = M_p a^2 \Omega$ and $\dot{J} = 0.5 a \dot{a} \Omega M_P = \Gamma$.

In a gaseous disc, pressure waves (the spiral waves as seen in Fig. 1.7), transport the angular momentum away from Lindblad resonances. These waves obey the dispersion relation

$$\tilde{\omega}^2 = \Omega^2 + c_s^2 k^2 \ , \tag{2.6}$$

where c_s is the sound speed and k the wave number. Pressure ($p = R_{Gas} \Sigma T / \mu$) can therefore shift the Lindblad resonances, so that the Lindblad torque is changed (Artymowicz, 1993). The effective location of the Lindblad resonances (where r satisfy the dispersion relation) is given by:

$$r_L \approx r_P \left(1 + \epsilon \sqrt{1 + m^2 h_P^2} / m \right)^{2/3} \ , \tag{2.7}$$

with $\epsilon = -1$ for the ILR and $\epsilon = +1$ for the OLR. When m tends to infinity ($m \to \infty$), the Lindblad resonances are located at:

$$r_L = r_P \pm 2/3 H_P \ , \tag{2.8}$$

where H_P is the discs thickness at the planets location and $h_p = H_P / r_P$. This finite distance causes the potential to decrease with increasing m.

The total torque acting on the planet is the sum of the torques exerted at each Lindblad resonance. The total torque reads:

$$\Gamma = \sum_m \Gamma_{LR}^m \ , \tag{2.9}$$

where Γ_{LR}^m is the mth torque component of the Lindblad resonance. The individual components of the torque Γ_{LR}^m can be derived with some mathematical knowledge. This has been done by Goldreich and Tremaine (1979) and Meyer-Vernet and Sicardy (1987). Their result is:

$$\Gamma_{LR}^m = \pm \frac{\pi^2 \Sigma_0 A(r_m)^2}{3 \Omega_m \Omega_P} \ , \tag{2.10}$$

where Σ_0 is the surface density, Ω_m the angular velocity at the mth resonance and $A(r_m) = \mp r_m d\Phi_m / dr + 2\Omega / (\Omega - \Omega_P) \Phi_m$. This results in a negative torque exerted at outer Lindblad
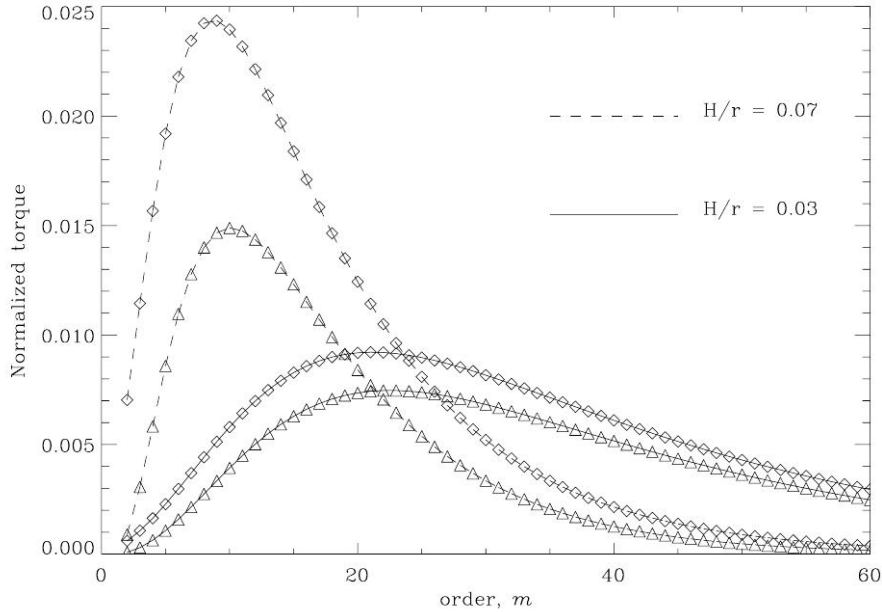
Figure 2.1: Inner (triangles) and outer (diamonds) torques $|\Gamma_{LR}^m|$, normalised to $\Gamma_0 = \pi q^2 \Sigma r_p^4 \Omega_P^2 h^{-3}$, for two different aspect ratios ($h = H/r$). Figure taken from Masset (2008a).

resonances and a positive torque exerted at inner Lindblad resonances. The components of Γ_{LR}^m for different m are shown in Fig. 2.1. For small m, Γ_{LR}^m increases, but then declines. This drop off is referred to as *torque cut-off*. This is because of the fact that for large m, r_m does not tend to r_p (for $m \to \infty$), but to $r_P + 2/3H_P$, while $\Phi_P^m(r)$ peaks at r_P.

The sum over the components of the outer Lindblad resonances is referred to as *outer Lindblad torque* and the sum over the components of the inner Lindblad resonances is referred to as *inner Lindblad torque*. Each of these components is also referred to as *one-sided Lindblad torque*.

2.1.2 Differential Lindblad torque

The outer and inner Lindblad torques are not exactly equal, as has been shown by Ward (1986). The torque exerted by the outer mth Lindblad resonance is larger in absolute value than the inner one, for three reasons (Ward, 1997):

1. The outer resonances are located closer to the planetary orbit as the inner resonances (see Eq. 2.7). But as the potential Φ_P^m declines symmetrically away from the planet, the coefficient $A(r_m)$ in Eq. 2.10 is enhanced.

2. The $\pm$ sign in $A(r)$ makes $A(r)$ larger for the outer resonances, even if the inner and outer resonances of the same order were symmetric with respect to the planet.

16

3. In the expression of Γ_{LR}^m (Eq. 2.10) the angular velocity at the location of the resonance (Ω_m) appears in the denominator. As Ω_m is larger for the inner resonances than for the outer resonances, this favours the latter.

If the slope of the surface density in the disc would be increased, the surface density Σ would be larger in the inner disc compared to the outer disc. This would also increase the pressure gradient in the disc, as the pressure is proportional to the surface density. The angular velocity in the disc would decrease, as this effect partially counterbalances the gravity of the central star. As a result, the resonances are shifted inwards, which increases the strength of the outer resonances with respect to the inner resonances. This effect is referred to as *pressure buffer*.

In Fig. 2.1 the difference between $|\Gamma_{LR}^m|$ at the inner (triangles) and outer resonances (diamonds) for different m and two different aspect ratios is displayed. It seems that the difference between inner and outer resonances increases with increasing aspect ratio H/r. Clearly visible is the afore mentioned torque-cut-off, which appears as a decrease of $|\Gamma_{LR}^m|$ as m increases for larger m. The torque-cut-off appears for smaller m for higher aspect ratios.

The total torque exerted by the disc on the planet, is the sum of each torque component Γ_{LR}^m at both resonances (ILR and OLR). This is the *differential Lindblad torque*, which is denoted as $\Delta\Gamma_{LR}$. The differential Lindblad torque scales with the aspect ratio H/r. As the one-sided Lindblad torque scales with $(H/r)^{-3}$, the differential Lindblad torque is proportional to $(H/r)^{-2}$.

A linear estimate for the torque acting on an embedded low-mass planet in the linear regime in isothermal discs is given by Tanaka *et al.* (2002). Their formula reads:

$$\Delta\Gamma_{LR} = -C_{LR}q^2\Sigma_P\Omega_P^2 r_P^4 h_P^{-2} , \qquad (2.11)$$

with $q = M_P/M_*$ and

$$C_{LR} = 2.340 - 0.099\alpha \quad \text{in 3D} \quad , \quad C_{LR} = 3.200 + 1.468\alpha \quad \text{in 2D} , \qquad (2.12)$$

where α is the slope of the density profile $\Sigma \propto r^{-\alpha}$ (approximated by a power law). Both, the 2D and 3D estimate have the same dependence in surface density and planet mass. The negative torque exerted on the planet leads to inward migration. The migration rate is proportional to the planet mass, as the torque is proportional to the square of the planet mass.

Even as the total torque features other components (see Section 2.2), it is useful to determine the migration rate only for the differential Lindblad torque. The migration rate is defined as $\tau_{migI} = a/\dot{a}$. Using the definition of the angular momentum and of its derivative, it yields:

$$\tau_{migI} = \frac{a}{\dot{a}} = \frac{J}{\Delta\Gamma_{LR}} = \frac{a_P^2\Omega_P M_P}{\Delta\Gamma_{LR}} = \frac{(H/r)^2}{4Cq\mu(r_P)}\frac{2\pi}{\Omega_P} , \qquad (2.13)$$

with $\mu(r) = \Sigma\pi r^2/M_*$ being the reduced disc mass and C from above. For a planet with 10 Earth masses, $10M_{Earth}$, embedded at 5.0 AU in a Minimum Mass Solar Nebular with
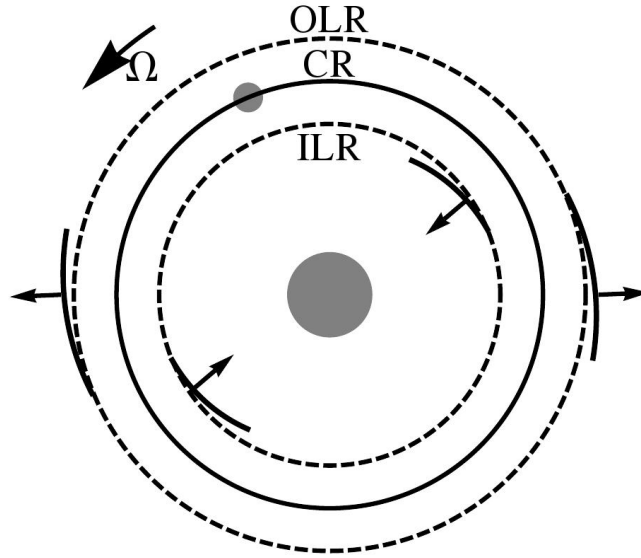
Figure 2.2: Schematic of acoustic (pressure) wave propagation in a gas disc involving an inner Lindblad resonance, outer Lindblad resonance and corotation resonance. Figure taken from Lubow and Ida (2010).

$H/r = 0.07$ and $\mu = 1.4\ 10^{-3}$ the migration is a few thousand orbits, which corresponds to a few ten thousand years. This is at least one order of magnitude smaller than the lifetime of the accretion disc! As planets migrate inwards, this may account for the Hot Jupiters, but for big planets embedded farther out in the disc (like Jupiter in our Solar System), this mechanism is too fast. In the next Sections processes to slow down this rapid inward migration are explained.

2.2 Linear corotation torque

2.2.1 Corotation resonances

In the previous Section, the torques at the Lindblad resonances have been derived. However, as the Lindblad resonances do not reach all the way to the planet (Eq. 2.8), there is an area in between the inner and outer Lindblad resonances, which corresponds to the corotation resonance, see Fig. 2.2, taken from Lubow and Ida (2010). At the Lindblad resonances, spiral waves are launched and propagate away from the orbit of the planet. The corotation region is evanescent (no pressure waves are launched).

In linear analysis of the planetary potential of an embedded planet (Eq. 2.3), the corotation resonances occur when $\Omega = \Omega_P$, which means that they are located directly at the planets radius. The corotation torque in the linear regime does not excite a pressure wave to transport the angular momentum away, it rather accumulates at corotation. The cor-

responding torque appears as a discontinuity in the angular momentum flux at corotation (Goldreich and Tremaine, 1979).

Under the linear analysis, the components of the corotation torque can be derived. Tanaka *et al.* (2002) showed that the mth component of the corotation torque exerted on a perturber in an *isothermal* disc is:

$$\Gamma_{C,m} = -\frac{m\pi^2}{2} \left[\frac{|\Phi_m + \Psi_m|^2}{d\Omega/dr} \frac{d}{dr} \left(\frac{\Sigma}{B} \right) \right]_{r_c} , \qquad (2.14)$$

where Ψ_m is the mth component of the perturbed gas enthalpy. The perturbed gas enthalpy is equal to the perturbed pressure divided by the unperturbed surface density. The torque expression in (Goldreich and Tremaine, 1979) is obtained for $|\Psi_m| \ll |\Phi_m|$. This holds, when the thermal energy is a small fraction of the total energy, depending on the gas temperature and on the strength of the perturbing potential. However, this approximation is incorrect for typical discs and planet parameters (Tanaka *et al.*, 2002).

In Eq. 2.14 the radius r_c is the corotation radius with $\Omega(r) = \Omega_P$. For a disc with power law approximations for surface density $\Sigma(r) \propto r^{-\alpha}$ and temperature $T(r) \propto r^{-\beta}$, the corotation radius can be evaluated:

$$r_C \approx r_P \left[1 - (\alpha - \beta)h^2/3 \right] . \qquad (2.15)$$

If the pressure decreases with r, which is satisfied for $\alpha - \beta > 0$ as $p \propto \Sigma T$, r_C is slightly smaller than the planetary radius r_P. The sign of Eq. 2.14 is determined by B/Σ with B the second Oort's constant ($\Omega/4$ in Keplerian discs), which scales as $r^{-3/2}$ in Keplerian discs. The total linear corotation torque, which is the sum over all m elements of $\Gamma_{C,m}$, is therefore proportional to $3/2 - \alpha$ for an isothermal disc. Interestingly, this means that for large negative surface density gradients, the corotation torque would be positive, which is not possible for the Lindblad torque, which is always negative. However, for the typical MMSN models with $\alpha = 3/2$, the corotation torque cancels out.

As B is also half the vertical component ω of the flow vorticity, the corotation torque scales with the gradient of (the inverse of) the flow *vortensity* ω/Σ, which describes the ratio of vorticity to density of a rotating fluid. From the Navier-Stokes equations, the governing equation of the vortensity can be obtained:

$$\frac{D}{Dt} \left(\frac{\omega}{\Sigma} \right) = -\frac{\nabla p \times \nabla \Sigma}{\Sigma^3} \cdot \mathbf{e_z} + \nu\Delta \left(\frac{\omega}{\Sigma} \right) . \qquad (2.16)$$

In a locally isothermal disc without viscosity (an inviscid disc), the right-hand side of this equation is proportional to dT/dr. For uniform temperatures, $D(\omega/\Sigma)/Dt = 0$ and the vortensity is conserved along fluid element paths. This is also true for barotropic discs, as $p = p(\Sigma)$ and is independent of the temperature.

2.2.2 Inviscid discs

Gas close to the embedded planet is in the coorbital region. It does not pass the planet, it is trapped in so called *librating* orbits in the corotating frame of the planet as can be
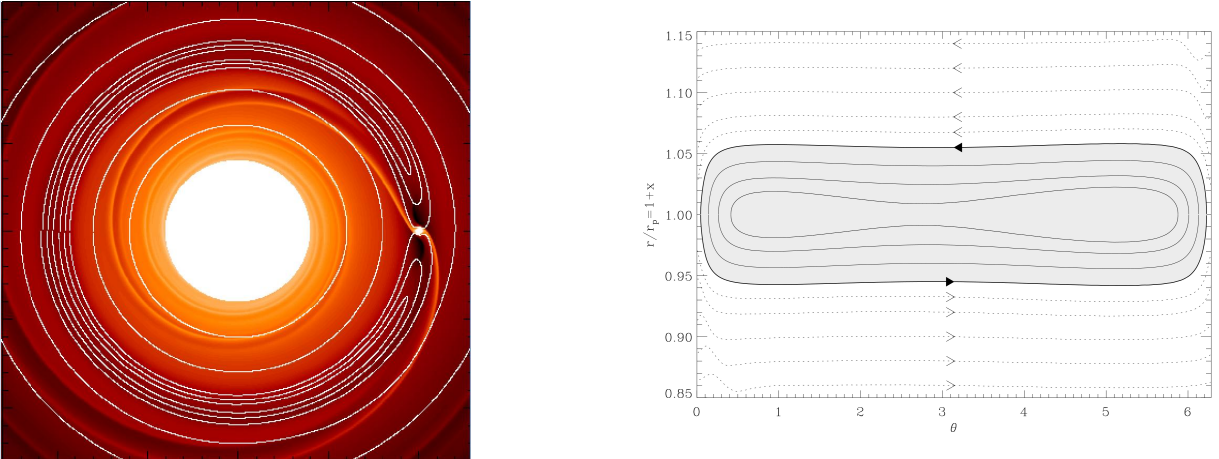
Figure 2.3: Trajectories of fluid elements perturbed by a large mass planet held on a fixed orbit in the corotating frame. The left plot displays the trajectories as white lines over a density map in Cartesian (x, y) coordinates, while in the right plot, polar coordinates (ϕ, r) are used. The shaded area in the right hand plot marks the coorbital region. Picture taken from Masset (2008b).

seen in Fig. 2.3. The gas trapped in librating orbits moves in horseshoe shaped orbits in the coorbital region (left in Fig. 2.3), the orbits are therefore named *horseshoe orbits*. The librating fluid elements in the horseshoe region are separated from the circulating fluid elements outside the coorbital region by the *seperatrix*.

Let us follow the motion of a particle in a librating orbit in the horseshoe region in an inviscid disc (left in Fig. 2.3). When the particle is on an orbit smaller than the planet's orbit, its angular velocity Ω is larger. The particle therefore moves faster in the disc and gains on the planet, until it finally approaches the planet from behind. When the particle is close to the planet, the planet pulls the particle outside by transferring angular momentum to it. During this transfer of angular momentum, the particle describes a U-turn motion in the disc. As the particle is now on a wider orbit than the planet, it moves more slowly. The planet then gains on the particle again until it is approached. The particle then transfers angular momentum to the planet and is moved by another U-turn type of motion into an inner orbit again. As the particle follows a periodic orbit in the frame of the planet, the angular momentum over a complete period of motion does not change.

The corotation torque acting on an embedded planet has its origin in the horseshoe type motion of the gas (Ward, 1991). As the horseshoe region is a closed system in this case, the particles can only give a finite amount of angular momentum to the planet. Even if the particles on different radii were initially lined up to encounter the planet at the same time and give a large amount of angular momentum to the planet, they drift apart in azimuth (phase) and encounter the planet at different times in the next orbits. After a while, when one particle gives an amount of angular momentum to the planet, another particle takes exactly this amount of angular momentum from the planet. This so called *phase mixing*

leads to a flattening of the vortensity profile, which results in a vanishing torque acting on the planet after the gas has made several horseshoe orbits. This process is also called *saturation* of the corotation torque.

The horseshoe region in the disc is characterised by its width and by the libration time scale.

- The half-width of the horseshoe region x_s can be approximated for an isothermal disc by (Masset *et al.*, 2006):

$$x_s = 1.16\, a_P \sqrt{\frac{q}{(H/r)}} \ , \tag{2.17}$$

  where q is the planet-star mass ratio, M_P/M_{Star}, and a_P the planetary distance to the star. For a $20 M_{Earth}$ planet in $H/r = 0.037$ disc, the half width of the horseshoe region is $x_s = 4,67 \cdot 10^{-2} a_P$. As the half-width of the horseshoe region is quite small, one needs very fine grids to resolve the corotation region for small mass planets.

- The libration time scale τ_{lib} gives the period between particle-planet encounters. It depends on the separation from the corotation radius:

$$\tau_{lib} = \frac{8\pi r_P}{3\Omega_P x_s} \ , \tag{2.18}$$

  which is ≈ 180 planetary orbits for the above case of a $20 M_{Earth}$ planet.

One should be aware that only global simulations (if possible with high resolution) can correctly determine the corotation torque. A local description, either a box or a wedge, will prevent saturation for inflow/outflow boundary conditions in azimuth as the 'new' material will be injected with an unperturbed density and velocity profile. Periodic boundary conditions will artificially shorten the libration time scale.

A linear estimate for the corotation torque acting on an embedded low-mass planet in the linear regime in isothermal, inviscid discs is given by Tanaka *et al.* (2002). Their formula reads:

$$\Delta\Gamma_{CR} = -C_{CR} q^2 \Sigma_P \Omega_P^2 r_P^4 h_P^{-2} \ , \tag{2.19}$$

with $q = M_P/M_*$ and

$$C_{CR} = 0.976 - 0.640\alpha \quad \text{in 3D} \quad , \quad C_{CR} = 2.040 + 1.360\alpha \quad \text{in 2D} \ , \tag{2.20}$$

where α is the slope of the density profile $\Sigma \propto r^{-\alpha}$ (approximated by a power law). The combination of the Lindblad torque, eq. 2.11, and the corotation torque, eq. 2.19, gives the total torque acting on the planet in the linear regime. Even with the consideration of the corotation torque, the total torque acting on an embedded small mass planet is negative, indicating inward migration at a too fast rate.

2.2.3 Viscous discs

However, in a real accretion disc, viscosity is present. In Fig. 2.4 the streamlines in a viscous disc are plotted. In the left hand plot a toy model to illustrate the movement of
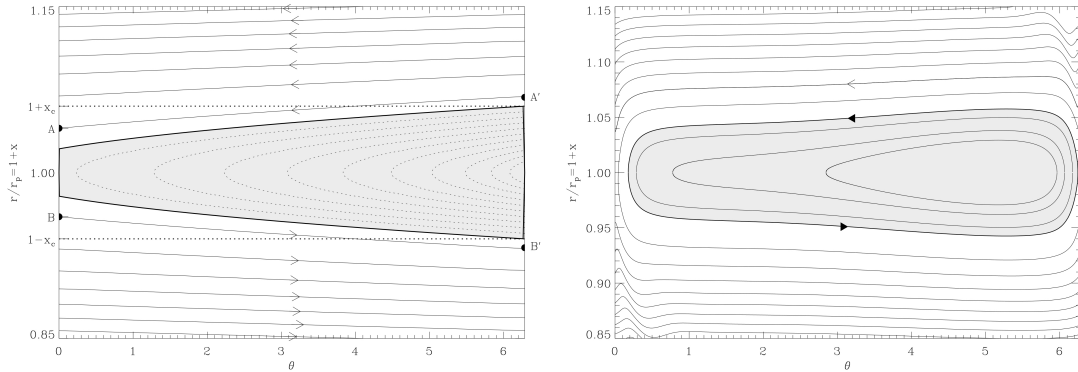
Figure 2.4: Horseshoe streamlines in the corotating frame for a viscous disc. The left-hand plot describes a toy model presented in the text, while the right-hand shows streamlines from a numerical simulation of a planet in the disc. The grey shaded area marks fluid elements trapped in the coorbital region of the disc, while the white region represents the path of fluid elements that are initially circulating in the outer disc, make a horseshoe U-turn and then circulate in the inner disc. Figures taken from Masset (2001)

particles is displayed, while the right hand plot shows the result of numerical simulation with an embedded planet. The description of the toy model follows Masset (2001).

In a viscous disc with uniform viscosity ν and surface density Σ, the velocity of the fluid elements in the corotating frame is given by

$$\dot{x} = -\frac{3}{2}\frac{\nu}{r_p} , \quad \dot{\phi} = -\frac{3}{2}\frac{\Omega_P}{r_P}x , \tag{2.21}$$

which integrates to

$$\phi = \frac{1}{2}\frac{\Omega_P}{\nu}x^2 + \phi_0 . \tag{2.22}$$

The streamlines are therefore parabolic arcs, as can be seen in the left hand plot in Fig. 2.4. Following a fluid element starting form the outer disc, it first follows a circular trajectory and approaches progressively the coorbital zone of the planet. Finally the fluid element reaches the point A', which is slightly beyond the coorbital region (its distance is greater than x_s). The fluid element at this point is not sent to the other side through a horseshoe U-turn. However, as the fluid element progresses on its orbit towards A, it crosses the horseshoe boundary and is now inside the coorbital region of the disc. When the fluid element reaches A, it is sent through a horseshoe U-turn to B, giving a positive amount of angular momentum to the planet. The fluid element loses that amount of angular momentum. It then flows towards B', which is outside the horseshoe region. Therefore the fluid element keeps circulating inwards in the inner disc and eventually gets accreted onto the primary.

This schematic picture gives a first clue about what is going on in a real accretion disc. The streamlines for that case are displayed in the right hand plot in Fig. 2.4. In this case, again, a set of closed streamlines in the coorbital region is visible. This region is quite similar to that obtained in the toy model (left in Fig. 2.4). Material is also able to flow from the outer disc to the inner disc as in the toy model.

In the viscous accretion disc, still a set of closed librating streamlines is present in the coorbital region, enclosed by the seperatrix. This material will not accrete onto the primary star, but as the outer and inner disc can now communicate, material can flow from the outer disc to the inner disc, which exerts a positive torque on the planet. However, for decreasing viscosities, the librating region becomes more rectangular shaped, as in the inviscid case (see right in Fig. 2.3). If the viscosity is too low, the effect of transporting angular momentum from the outer disc onto the planet ceases to exist.

Maintaining a non zero-coorbital torque over long time scales requires a process that permits exchanges between inner and outer disc. This process is, as described above, viscosity. In sufficiently viscous discs (with a viscosity probably too high for real accretion discs), the viscous diffusion and radial transport of material across the horseshoe region prevent the saturation of the corotation torque and keep the gradient in vorticity alive. If the viscous diffusion time scale, $\tau_{visc} = x_s^2/\nu$ across the coorbital region is larger than the horseshoe libration time (eq. 2.18), then no corotation torque is acting on the planet. On the other hand, if the viscous diffusion time scale is shorter than the libration time scale, the corotation torque reaches its maximum value (Masset, 2001).

The linear analysis of perturbed circular orbits around corotation resonances is called *linear corotation torque*. However, non-linear effects have an influence on the torque acting on embedded planets as well.

2.3 Non linear effects

The linear analysis shown above (in Section 2.1 and 2.2) was based on the assumption that a low-mass planet only induces linear perturbations. In fact, introducing a planet in a disc results in a singular perturbation at the corotation radius, which suggests that the corotation torque can differ from its linear value.

Basically, there are two ways to look at the corotation torque. In the first way (see Section 2.2), a linear analysis of perturbed circular orbits around the corotation resonance is performed. Alternatively, one can look at the expected pattern of the streamlines close to the planet (see Fig. 2.3) and analyse the torque exerted from material executing horseshoe turns (Ward, 1991). The torque obtained from linear analysis is called *linear corotoation torque*, while the torque resulting from streamline analysis is called *horseshoe drag*. The horseshoe drag is sometimes also referred to as *non-linear coorbital torque*. Please keep in mind that in linear theory *no* horseshoe drag exists. This torque is a strictly non-linear phenomenon, as will be shown below.

In an isothermal disc with conserved specific vorticity along streamlines, the density
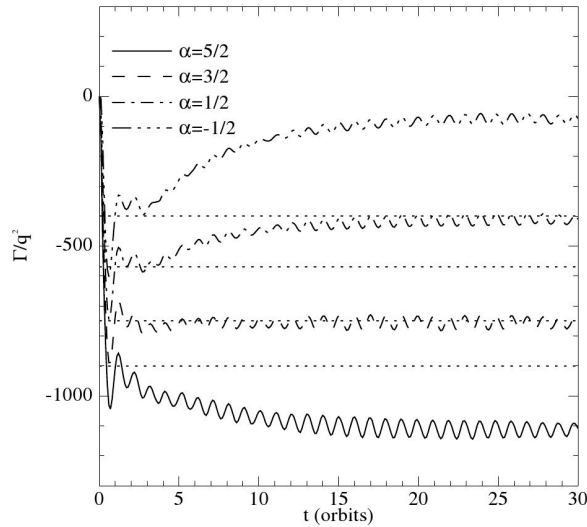
Figure 2.5: Total torque acting on the planet in an isothermal, inviscid disc with $h_P = 0.05$ and $q = 1.26 \ 10^{-5}$ for different surface density profiles. The horizontal lines indicate the linear torque for increasing α from top to bottom. Picture taken from Paardekooper and Papaloizou (2009b).

changes in the corotation region, when the material is executing the U-turns. As the material is undergoing the U-turn and moves to a different orbit, it changes vorticity. But a change in vorticity is followed by a change in density. On the two sides of the planets, the direction of the U-turn is opposite, resulting in an change of density that is directly opposite for the two U-turns. As a result, the planet feels a torque. This torque is dependent on the width of the horseshoe region (Ward, 1991) and is:

$$\Gamma_{C,HS} = \frac{3}{4} \left(\frac{3}{2} - \alpha \right) x_s^4 \Sigma_P r_P^4 \Omega_P^2 \ , \tag{2.23}$$

with x_s being the half-width of the horseshoe region. Please note that $x_s \propto \sqrt{q/h}$, so that the horseshoe drag scales exactly the same way as the linear corotation torque (Paardekooper and Papaloizou, 2009b). This also indicates, that the differences between these two torques may only lie in the magnitude of them.

In Fig. 2.5 (taken from Paardekooper and Papaloizou (2009b)) the total torque acting on planets with $q = 1.26 \ 10^{-5}$ in an isothermal, inviscid disc with $h_P = 0.05$ with different surface density profiles (α) is displayed. The horizontal lines indicate the linear torque estimate for the embedded planet. As the linear torque estimate depends on the surface density gradient, the linear results differ from each other.

Taking a look at eq. 2.23, it is not surprising that the torque for the $\alpha = 3/2$ disc is identical with the linear estimate, as the horseshoe torque vanishes. However, for planets in discs with $\alpha \neq 3/2$ the horseshoe torque does not vanish, and the corresponding torque in the simulations differs from the linear estimate. The sign of the difference from linear

theory is dictated by the vortensity gradient. This indicates that the corotation torque is enhanced with respect to the linear value (Paardekooper and Papaloizou, 2009b).

The evolution of the total torque in the simulations is another interesting feature. In the beginning of the simulations, after about 2 orbits, the torques are nearly identical to the linear estimate, but as time evolves the torques depart from the linear estimate. This indicates that the linear theory is only valid at early times in the evolution. The linear torque is then replaced by the non-linear torque, the horseshoe drag, which takes about 20 orbits to develop in this case.

The replacement of the linear torque with the horseshoe drag also implies that both torques do not exist at the same time. The material can either follow a perturbed circular orbit or execute a horseshoe turn. At early times after inserting the planet in the disc, linear theory is valid, as the material did not have time to make horseshoe U-turns. When the material starts to execute horseshoe turns, the linear corotation torque is replaced by the non-linear horseshoe drag. The development for the linear corotation torque follows no definite time scale (it is developed after about one planetary orbit). However, the horseshoe drag needs a fraction of the libration time scale (see eq. 2.18) to develop, which is about $2h_P\tau_{lib}$ (Paardekooper and Papaloizou, 2009b). The development of the horseshoe drag is also faster for higher planetary masses, as $x_s \propto \sqrt{q}$.

This result also confirms that non-linear effects in the corotation region play a role, even for a small planet mass, contrary to the original assumption for the linear analysis. The horseshoe drag is also in general much stronger than the linear torque (as can be seen in Fig. 2.5). One also notices that the total torque approaches zero for slightly positive surface density gradients (remember $\Sigma \propto r^{-\alpha}$). For surfaces density gradients with $\alpha \approx -1$, the total torque can become positive, indicating outward migration.

In inviscid discs, the corotation torque becomes non-linear, but saturates after a few libration cycles, so that only the Lindblad torque remains. For the linear corotation torque, a sufficiently large enough viscosity can act to prevent the corotation torque from saturation. In that case the horseshoe drag is decreased to the linear estimate of the corotation torque. This also depends on the planetary mass, which is show in Fig. 2.6.

In this figure, a schematic overview over the possibilities (in $\log q$ and $\log \nu$) of the corotation torque is given (following Paardekooper and Papaloizou (2009b)). The boundaries between the three regimes is given by two lines. The boundary between the non-linear torque maintained by viscosity (non-linear, sustained in the picture) and the non-linear saturated regime is given approximately by the condition that viscous diffusion across the coorbital region occurs in one libration cycle. The line separating the sustained horseshoe drag regime from the linear regime is expected to occur where viscous effects become large enough to disrupt horseshoe turns.

Interestingly, the linear regime is only present in a small fraction of the plotted parameter space. Also, the boundaries between the different regimes are not razor sharp, but may contain slight wiggles as the non-linear torque can be partially saturated or reduced by viscosity. Nevertheless, the corotation torque is almost always a non-linear phenomenon.
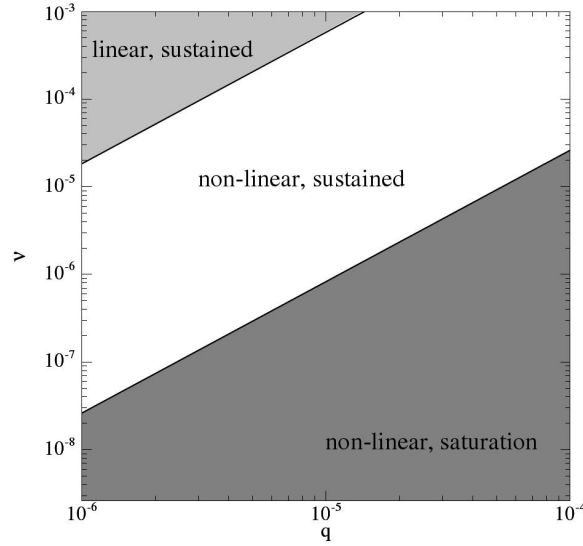
Figure 2.6: Overview over the different migration regimes. Depending on the viscosity in the disc, a low-mass planet will either experience a linear, unsaturated torque, a non-linear, unsaturated torque or a non-linear, saturated torque. Picture taken from Paardekooper and Papaloizou (2009b).

2.4 Non isothermal discs

In the above Sections, the torque acting on low-mass planets in isothermal discs has been described. The isothermal assumption is only valid, when the disc is able to radiate away all excess energy efficiently. But, as density is increasing and therefore opacity as well, less energy can be radiated away, and the cooling time scale becomes then much longer than the dynamical time scale in the dense inner regions of the disc, so that the isothermal assumption might not be valid any more. This is especially the case for high-mass discs. In this Section, the influence of a proper treatment of thermodynamics on planetary migration is discussed.

2.4.1 First results

First pointed out by Paardekooper and Mellema (2006), the inclusion of radiative transfer can cause a reduction of the migration speed and even reverse migration from inwards to outwards. In their letter, they treated radiative transfer in the flux-limited diffusion approach (Levermore and Pomraning, 1981) with a flux limiter of Kley (1989). In 3D hydrodynamical simulations in inviscid (to filter out effects of viscous heating) discs, they showed that for high density discs, the torque acting on an embedded $5M_{Earth}$ planet can be positive (Fig. 2.7).

In Fig. 2.7 the influence of density on the torque acting on an embedded $5M_{Earth}$ planet is shown. When varying the density in midplane of the disc, the initial temperature profile is
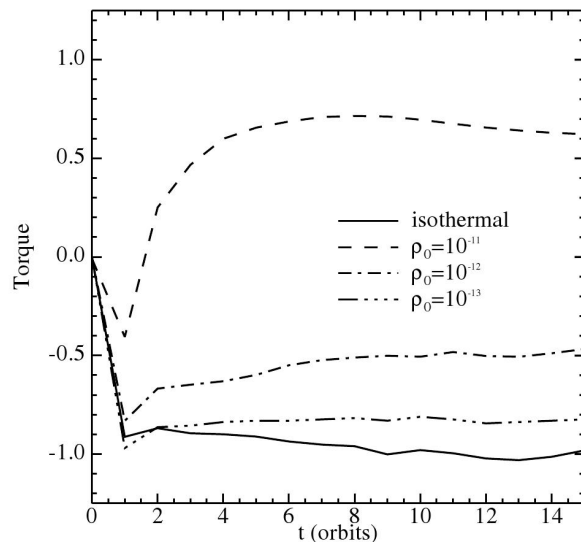
Figure 2.7: Total torque acting on a $5M_{Earth}$ planet as function of time for different mid-plane densities in radiative discs and for an isothermal disc. The torques are normalised to the analytical value found by Tanaka *et al.* (2002). The picture is taken from Paardekooper and Mellema (2006).

fixed in order to study different cooling regimes (Paardekooper and Mellema, 2006). For low opacities (and low densities), the planet still migrates inwards. For very low densities the isothermal limit can be reached. For large opacities (and densities), the planet experiences a positive torque and is thus migrating outwards. The magnitude of this outward migration is about a factor of 2 smaller than the magnitude of migration in the isothermal case.

The difference in the torque acting on the planet in these discs with different thermodynamic systems is originated in a region close to the planet, mainly $0.95 \leq r_P \leq 1.05$. Including radiative diffusion resulted in a change, more correct, in an asymmetry, in the temperature profile near the planet, that in return induced a density asymmetry in the region near the planet. This density asymmetry leads to a positive contribution to the torque, resulting in outward migration. But this is only valid, if the disc can not radiate away heat efficiently. This is possible as long as the libration time scale is larger than the radiative diffusion time scale in the disc. In this case the asymmetry in temperature and density can be maintained.

On one hand, the torque in the coorbital region is enhanced and generates a large positive contribution to the total torque. On the other hand, the Lindblad torque is reduced in strength (but still negative). The compression of material at the turn-over point of the horseshoe orbits generates a warm region behind the planet, but as the disc tries to maintain the pressure equilibrium, the density behind the planet is reduced ($p \propto \Sigma T$), leading to a positive contribution to the corotation torque. It has been shown, that this effect is supported by a gradient in entropy (Baruteau and Masset, 2008).

27

2.4.2 Energy equation

In numerical hydrodynamic simulations, the inclusion of radiation transport has direct influences on the energy equation compared to isothermal simulations. The energy equation for a 2D disc (as in Kley and Crida (2008)) is:

$$\frac{\partial \Sigma c_V T}{\partial t} + \nabla \cdot (\Sigma c_V T \mathbf{u}) = -p \nabla \cdot \mathbf{u} + D - Q - 2H \nabla \cdot \mathbf{F} , \tag{2.24}$$

where $\mathbf{u} = (u_r, u_\phi)$ is the 2D velocity, Σ the density, p the pressure, T the mid-plane temperature of the disc and c_V is the specific heat at constant volume. The first term on the right hand side describes compressional heating, D the (vertically averaged) dissipation function, Q the local radiative cooling from the two surfaces of the disc and $\mathbf{F}$ denotes the 2D radiative flux in the (r, ϕ)-plane. The discs thickness H is calculated from the sound speed $H(r) = c_s / \Omega_K(r)$ with $c_s = \sqrt{\gamma p / \Sigma}$ and $\gamma = 1.43$ being the adiabatic index. The 2D pressure is given by $p = R_{gas} \Sigma T / \mu$ with the mean molecular weight $\mu = 2.35$.

The radiative transport in the plane is treated by the flux-limited diffusion approximation, where the flux is given by:

$$\mathbf{F} = -\frac{\lambda c \, 4 a_R T^3}{\rho \kappa} \nabla T , \tag{2.25}$$

with c the speed of light, a_R the radiation constant, $\rho = \Sigma / (2H)$ the mid-plane density and λ the flux-limiter (Kley, 1989) and κ the opacity.

When only the first term on the right hand side of Eq. 2.24 is used, the disc is *adiabatic*. When only the last term is omitted, it is a disc with *local heating and cooling*. If the full energy equation is used, the disc is *fully radiative*. For *isothermal* discs, the radial temperature distribution is maintained constant and no energy equation is solved at all. For the isothermal simulations the result is well known, an embedded low-mass planet migrates inwards.

2.4.3 Adiabatic and fully radiative discs

The time evolution of torques acting on embedded $20 M_{Earth}$ planets in 2D discs with different treatments of the energy equation are displayed in Fig. 2.8. In the isothermal case, the torque acting on the planet is negative, indicating inward migration. Let us now focus on the adiabatic simulation first.

In the initial phase of the torque evolution, right after the insertion of the planet, the torque is positive, indicating outward migration in the adiabatic case. But as time progresses, the torque becomes negative and settles at a value of about 40% of the isothermal case. It seems that the torque in the adiabatic case is first unsaturated, but then, as time evolves, it begins to saturate, so that the total torque becomes negative (Baruteau and Masset, 2008; Paardekooper and Papaloizou, 2008).

In order to bring more detail into the evolution and origin of the torques acting on embedded planets, it is useful to define the torque density $\Gamma(r)$ in such a way, that the total
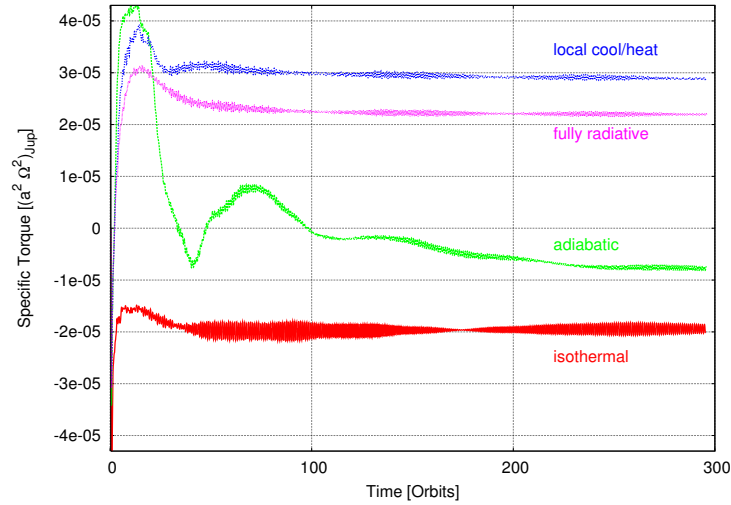
Figure 2.8: Time evolution of the specific total torque exerted by the disc on an embedded protoplanet of $20 M_{Earth}$ for various approximations to the energy equation (picture taken from Kley and Crida (2008)).

torque is given by:

$$\Gamma_{tot} = \int_{r_{min}}^{r_{max}} \Gamma(r) \, dr \; , \qquad (2.26)$$

where r_{min} and r_{max} define the inner and outer edge of the simulated disc. In Fig. 2.9 the torque density acting on planets in 3D discs with different thermodynamics is displayed. These results have been adopted from Kley *et al.* (2009). The individual parameters of the disc's properties differ a little bit from Kley and Crida (2008), but only the general picture is of interest here.

Comparing the torque density of the isothermal with adiabatic simulations (Fig. 2.9), two main differences are clearly visible. First, the Lindblad torques are reduced for the adiabatic case compared to the isothermal case and, second, the torque density reduces in time for the adiabatic simulations because of satuartion of the torque, which is not the case for isothermal simulations. Please note here that the total torque is constant in time (Fig. 2.8). This reduction in the torque density can also be seen in the evolution of the total torque in time (Fig. 2.8), as the torque in the adiabatic disc is first positive and then becomes negative in time.

Even without the effects of saturation, the torque density is smaller in the adiabatic disc compared to the isothermal disc because of a different sound speed. The Lindblad torque is therefore reduced by a factor of γ in the adiabatic disc compared to the isothermal disc (Paardekooper and Papaloizou, 2008).

In contrast to the adiabatic models, both radiative models show a constant positive torque acting on the embedded planet (see Fig. 2.8). In the fully radiative case, the torque is about 25% smaller than for the local heating and cooling model. It seems that the torque
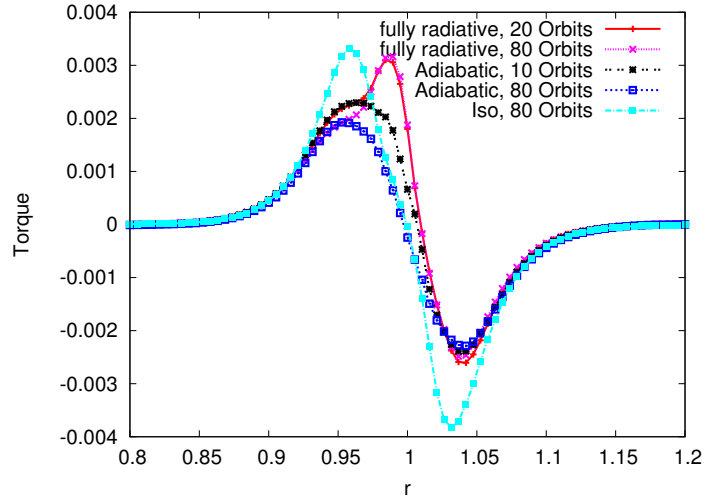
Figure 2.9: Torque density acting on $20 M_{Earth}$ planets embedded in 3D discs with different variations of the energy equation. The picture is derived from Kley *et al.* (2009).

remains unsaturated in a fully radiative disc, resulting in a long term outward migration.

This behaviour is also seen in the torque density distribution (Fig. 2.9) as the torque density in the fully radiative case does not change over time. There is another interesting feature in the torque density distribution for the fully radiative disc. In contrast to the isothermal and adiabatic simulations, a small spike overlaying the Lindblad torque density is visible. This spike in the torque density has its origin in a change in the density structure near the planet (Kley *et al.*, 2009). A change in the density structure has also be observed in Paardekooper and Mellema (2006); Kley and Crida (2008); Paardekooper and Papaloizou (2008).

The density structure of embedded planets in isothermal and fully radiative discs is shown in Fig. 2.10. In the isothermal model, a higher mass concentration in the Roche lobe of the planet can be observed. In the fully radiative model the spiral arms have a slightly larger opening angle and a reduced density because of the higher temperature in the disc. Less density in the spiral waves results in a reduction of the Lindblad torque.

The density in the inner half of the horseshoe region ahead of the planet (below the planet in Fig. 2.10) is denser in the radiative case compared to the isothermal case. This has also been observed in Baruteau and Masset (2008); Paardekooper and Papaloizou (2008). Symmetrically, the outer half of the horseshoe region is depleted slightly behind the planet.

In order to explain the change of density ahead and behind the planet, let us consider the movement of a particle on a horseshoe orbit, see right in Fig. 2.10. The particle makes a horseshoe turn from the outer disc ($r > 1$ and $\phi > 180°$) to the inner disc ($r < 1$). The radial temperature and density gradients imply a gradient in entropy, $S \propto p/\rho^{\gamma}$. Caused by this gradient in entropy, a parcel coming from outside has a lower density than
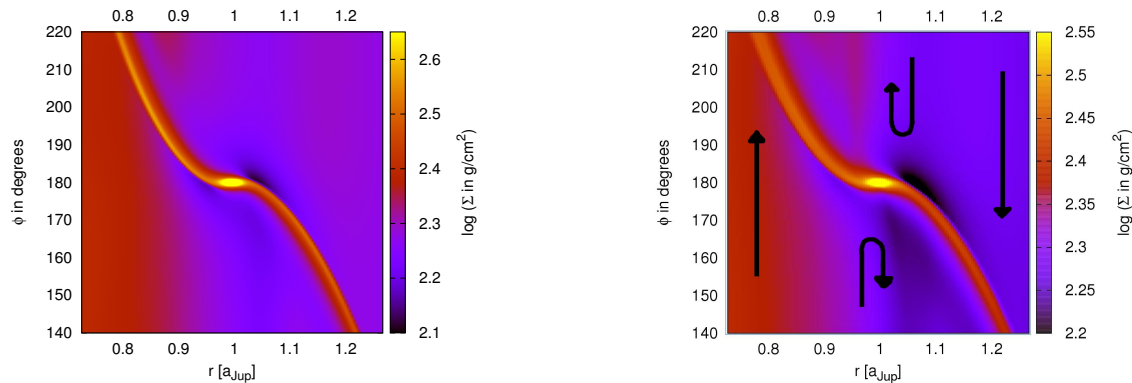
Figure 2.10: Surface density in the vicinity of a $20M_{Earth}$ planet in an isothermal (left) fully radiative (right) disc with indicated directions of flow for the fully radiative disc. Plots taken from Kley *et al.* (2009).

the inner disc which it is entering. Assuming that the entropy does not change in this short distance and that the pressure is nearly constant as well, the entropy law implies an increase in density. At the same time, the density is decreased behind the planet ($r > 1$ and $\phi < 180°$) by the same reasoning.

Resulting from these changes in the density structure is a reduction of the Lindblad torque and an enhancement of the entropy related corotation torque. In total these changes give a positive total torque acting on the planet, indicating outward migration. To maintain this density structure or, more exactly, the unsaturated torque, the libration time scale must be comparable to the cooling times (Baruteau and Masset, 2008; Paardekooper and Papaloizou, 2008). In an adiabatic disc, this effect disappears in time, as the material in the horseshoe region begins to interact with itself and density and entropy will be smeared out because of the mixing, and saturation of the torque sets in. Radiative diffusion (with viscosity) prevents torque saturation and keeps the entropy related corotation torque unsaturated, thus sustaining the outward migration of low-mass planets.

The positive torque acting on the embedded planet is a result of the cooling properties of the disc. When the disc is not able to radiate away energy efficiently, the isothermal approximation is not valid any more. The inclusion of radiative transport then results in a positive torque acting on the embedded planet. When the planetary mass increases, planets start to open gaps in the disc and the density around the planet therefore decreases. But, as the density decreases, the disc is able to radiate energy away more efficiently, thus preventing outward migration. This can clearly be seen in Fig. 2.11.

In Fig. 2.11 the specific torque acting on embedded planets is displayed. In the fully radiative case, planets up to about $50M_{Earth}$ are prone to outward migration. Bigger planetary cores migrate inwards. In the isothermal case, planets migrate inwards at a rate predicted by Tanaka *et al.* (2002).

Outward migration of protoplanets will not continue forever. In Paardekooper and Mellema (2006), the influence of the opacity on low-mass planets in radiative discs is investigated
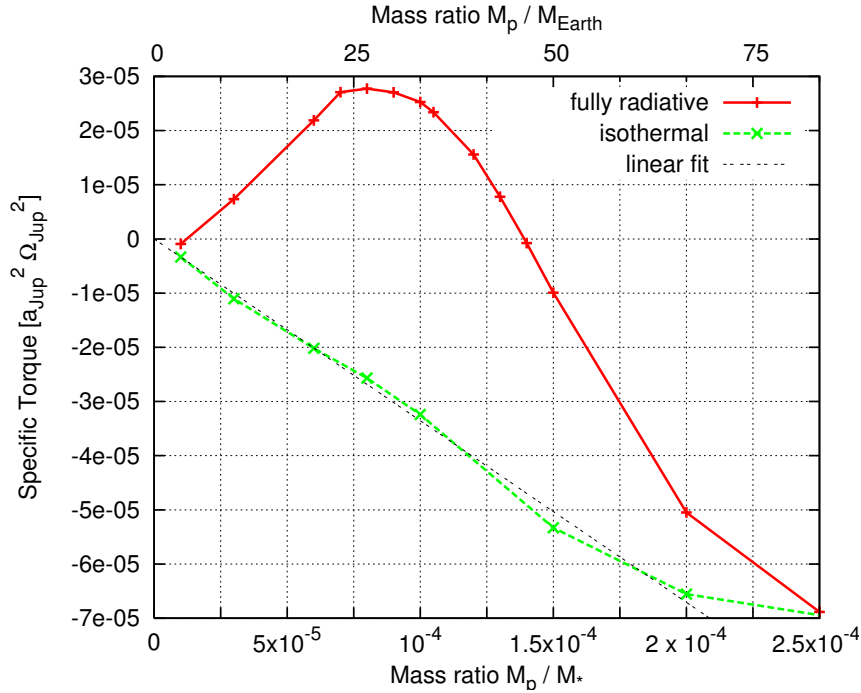
Figure 2.11: Specific torque exerted on an embedded protoplanet for isothermal and fully radiative models. An analytic curve is superimposed. Plot taken from Kley and Crida (2008).

(see Fig. 2.7). For lower densities, the planets migrate inwards, even in the radiative case. As the density is reduced with increasing distance to the central star for accretion discs, outward migration will stop at some point in the disc. This so called *zero-torque radius* defines a region in the disc, where planets migrating from inside out and planets migrating from outside in stop. As the disc is slowly accreted onto the star, this zero-torque radius moves inwards as well, but on the much longer viscous time scale (like type-II-migration). This way, low-mass planets can be saved from the too fast inward migration (Paardekooper and Mellema, 2006). This is also investigated in much more detail in Bitsch and Kley (2011).

3 Work in context

In this Chapter, I will put the work and publications done in my Ph.D.-Thesis in context with ongoing and future research. The publications written during my research are then presented in Chapter 4.

Fully radiative discs

In isothermal discs, low-mass planets migrate inwards at a rate proportional to the planets mass (linear type-I-migration). In this migration regime, the planets migrate inwards at a rate way too fast to account for Hot-Jupiter type planets. The planetary core migrates so fast that it might be lost in the central star, before it has time to accrete gas from the disc to form such a planet. This has been discussed in Chapter 2.

In recent years, the linear estimate of the Lindblad and corotation torque was proven to be incomplete for low-mass planets, and non-linear effects have been taken into account. These effects resulted in a reduction of inward migration. Planets could even migrate outwards, if the radial surface density gradient in the disc is positive by a factor of $\alpha < -1$, with $\Sigma \propto r^{-\alpha}$. However, in realistic discs, low-mass planets are still prone to inward migration at a rate that is too fast to form giant gaseous planets near the host star, let alone farther out in the disc.

As pointed out first by Paardekooper and Mellema (2006), the inclusion of radiative transfer can cause a strong reduction in the migration speed. The process has been subsequently investigated by several groups (Baruteau and Masset, 2008; Paardekooper and Mellema, 2008; Paardekooper and Papaloizou, 2008; Kley and Crida, 2008), who show that the migration process can indeed be slowed down or even reversed for sufficiently low-mass planets. This new effect occurs in non-isothermal discs and scales with the gradient of the entropy (Baruteau and Masset, 2008), hence entropy-related torque. However, in a strictly adiabatic situation after a few libration time scales, the entropy gradient will flatten within the corotation region caused by phase mixing. This will lead to saturation (and subsequent disappearance) of the part of the corotation torque that is caused by the entropy gradient in the horseshoe region (Baruteau and Masset, 2008; Paardekooper and Papaloizou, 2009a). To prevent saturation of this entropy-related torque, some radiative diffusion (or local radiative cooling) is required (Kley and Crida, 2008).

Since for genuinely inviscid flows, the streamlines in the horseshoe region will be closed and symmetric with respect to the planet's location, some level of viscosity is always necessary to avoid torque saturation (Masset, 2001; Ogilvie and Lubow, 2003; Paardekooper and Papaloizou, 2008, 2009a). This applies to both the vortensity- and entropy-related

corotation torques. The maximum planet mass for which a change of migration may occur because of this effect lies for typical disc masses in the range of about 40 earth masses, beyond which the migration rate follows the standard (isothermal) case, as gap formation sets in, which reduces the corotation effects (Kley and Crida, 2008). Most of the above simulations have studied only the two-dimensional case, while three-dimensional models including radiative effects have been presented only for very low masses (Paardekooper and Mellema, 2006), or for Jupiter type planets (Klahr and Kley, 2006).

In (Kley *et al.*, 2009), we investigate planet-disc interactions in fully radiative discs, using 3D radiation hydrodynamic simulations of protoplanetary accretion discs with embedded planets for a variety of planetary masses, which has not been investigated in that detail in 3D to that date. In Kley and Crida (2008) planets with up to $\approx 45 M_{Earth}$ could migrate outwards in fully radiative discs in 2D. In 3D, only planets up to $\approx 33 M_{Earth}$ are prone to outward migration (Kley *et al.*, 2009). The differences between 2D and 3D simulations have several reasons beside the inclusion of another dimension.

In isothermal discs, a different aspect ratio leads to a different migration speed (Tanaka *et al.*, 2002). There seems to be no reason, why this should change in fully radiative discs. In Kley and Crida (2008), the aspect ratio of the disc was slightly higher compared to (Kley *et al.*, 2009) ($[H/r]_{2D} = 0.045 > 0.037 = [H/r]_{3D}$). Also the smoothing of the planetary potential is treated differently. In 2D simulations the ϵ potential is used, while in Kley *et al.* (2009) the cubic potential is used (Klahr and Kley, 2006). Using the cubic potential results in a deeper planetary potential, which results in a higher density around the embedded planet, as the planet is able to accumulate more mass.

When a planet is inserted in a viscous fully radiative disc, the material near the planet starts its horseshoe type of motion. This process leads to an increase of density in front of the planet and to a decrease behind the planet (Paardekooper and Mellema, 2006; Kley and Crida, 2008; Paardekooper and Papaloizou, 2008), resulting in a positive torque acting on the embedded planet. This density structure is very sensitive, and even very small disruptions might destroy the effect of outward migration.

Eccentric orbits

Even in the Solar System none of the planets is on a perfect circular orbit. All planets feature a small, but non-zero eccentricity ($e_{Earth} = 0.0167$). Exoplanets, on the other hand, have a high mean eccentricity ≈ 0.29 (Udry and Santos, 2007). There are several explanations to account for the discrepancy in eccentricity between the Solar System and exoplanet systems.

The interactions between planet and discs are typically considered in explaining the migration process, but it may be possible that this process influences the planetary eccentricity as well (Goldreich and Tremaine, 1980). Under certain conditions, in linear analysis, the planets eccentricity can be increased through planet-disc interactions (Goldreich and Sari, 2003; Sari and Goldreich, 2004; Moorhead and Adams, 2008). They estimate that eccentric Lindblad resonances can cause eccentricity growth for gap-forming planets. Also, a Kozai-

type interaction between the embedded planet and an inclined planet has been considered to increase eccentricity (Terquem and Ajmia, 2010).

However, numerical simulations tend to show eccentricity damping by the disc for various planetary masses (Cresswell *et al.*, 2007; Moorhead and Ford, 2009). On the other hand, very massive planets can induce an eccentric instability in the disc (Kley and Dirksen, 2006). Then, in turn, the disc can possibly increase the planetary eccentricity (Papaloizou *et al.*, 2001; D'Angelo *et al.*, 2006). However, this process only applies for very massive planets ($\approx 5 - 10 M_{Jup}$). Through mutual gravitational interactions between two or more planets in the system, eccentricity of the planets can rise through this scattering process. The resulting eccentricity distribution matches the observed one reasonably well (Adams and Laughlin, 2003; Jurić and Tremaine, 2008; Ford and Rasio, 2008). Similar results can be found by the fly-by of a nearby star (Malmberg and Davies, 2009).

Theoretical analysis of planets on eccentric orbits mainly focus on low eccentric planets and predict exponential decay on short time scales $\tau_{ecc} \approx (H/r)^2 \tau_{mig}$, where H/r is the aspect ratio of the disc and τ_{mig} and τ_{ecc} the migration and eccentricity damping time scale, respectively (Tanaka and Ward, 2004). For larger values of e, Papaloizou and Larwood (2000) found an extended eccentricity damping time scale such that $de/dt \propto e^{-2}$ if $e > 1.1 H/r$. Cresswell and Nelson (2006) have performed hydrodynamical simulations of embedded small mass planets and find good agreement with the work by Papaloizou and Larwood (2000). These 2D results have been confirmed by Cresswell *et al.* (2007) using fully 3D isothermal simulations.

All these simulations and theories so far have only considered an isothermal disc. In Kley *et al.* (2009) it is stated that the inclusion of radiative transport changes the direction of migration from inwards to outwards. Therefore, in Bitsch and Kley (2010), we investigate the effects of a fully radiative disc on planets on eccentric orbits. In fully radiative discs, eccentricity is damped at a similar rate as in isothermal discs. However, even very small eccentricities destroy the very sensitive density structure near the planet, so that it migrates inwards again. This density structure is only maintained for very small eccentricities. Only planets on very small eccentric orbits are therefore still prone to outward migration (Bitsch and Kley, 2010).

Inclined orbits

The planets in our Solar System do not all move in the same plane, they are inclined to the ecliptic. The inclination for most planets is small (Mercury with the highest inclination of $i = 7.01°$), but some dwarf planets feature high inclinations (e.g. Pluto at $i = 17°$, or Eris at $i = 44.2°$). The low inclination of planets is taken as a an indication that planets form within the flattend protoplanetary disc. The high inclination of the dwarf planets is then a result of scattering processes in the early evolution of the Solar System. However, discoveries have shown that close-in Exoplanets can feature a high inclination (see e.g. Triaud *et al.*, 2010). This means that inclination has to be taken into account, when investigating planet-disc interactions in numerical simulations and theoretical considerations.

However, 3D simulations of inclined planets require a lot of computation time, so that not many studies have been done up to date covering this topic. Linear analysis has shown that inclination is damped. The inclination of low inclined planets is damped at an exponential rate, but the results are formally only valid for $i \ll H/r$ (Tanaka and Ward, 2004). Numerical simulations of low-mass planets in isothermal discs have shown that the exponential damping is in fact supported up to $i \approx 2H/r$ (i in radians). For higher inclined orbits, inclination is still damped, but at a much slower rate of $di/dt \propto i^{-2}$ (Cresswell *et al.*, 2007). In these studies only planets with a mass of $20 - 30 M_{Earth}$ were considered. Higher mass planets, e.g. Jovian mass planets, lose their inclination and eccentricity at a much faster rate (Marzari and Nelson, 2009). However, when the high-massive planet enters the disc again, it starts to open up a gap in it. When the gap is complete, eccentricity and inclination damping occurs at a much slower rate.

These simulations so far have only considered the isothermal assumption. In a typical accretion disc the density falls off above and below the midplane such that the migration of an inclined planet might be substantially different compared to a planet embedded directly in the midplane of the disc. In Bitsch and Kley (2011) we investigate the evolution of inclined planets on circular and eccentric orbits in isothermal and fully radiative discs. Damping of inclination occurs on roughly the same time scale in isothermal and fully radiative discs, but only in a fully radiative disc planets are prone to outward migration. The inclination also has an effect on the magnitude of migration. A higher inclination leads to slower inward migration, until the migration is about zero for $i \geq 4.5°$ (Bitsch and Kley, 2011). For lower inclinations, low-mass planets on circular orbits can still migrate outwards. For isothermal discs, the linear results of Tanaka and Ward (2004) and the simulations of Cresswell *et al.* (2007) could be confirmed.

Migration time scales

On of the main problems to form Jovian mass planets is the long time scale. In the isothermal regime, the planets migrate inwards, so that the planetary core would be lost in the star before it could accrete gas to form such a planet. In a fully radiative disc, the planetary cores can migrate outwards. However, it is not clear how far planets migrate outwards in discs. Paardekooper and Mellema (2006) stated that outward migration should stop at a point in the disc, where the disc does not support outward migration any more. In this region in the disc, planetary cores would accumulate and eventually merge to bigger cores. Radiation transport could therefore serve as a mechanism to form planetary traps in the disc at a so called zero-torque radius. This can also be achieved through surface density gradients in the disc (Morbidelli *et al.*, 2008), but it is not clear how realistic these jumps in the surface density gradients are.

The inclusion of radiative transport, and therefore taking into account unsaturated torques, can solve the problem of forming big cores in discs. The concept of an equilibrium radius (zero torque radius) for planetary embryos in fully unsaturated discs has been stated in Lyra *et al.* (2010) as well and it could easily act as a feeding or collection zone for planetary

embryos. In Sándor *et al.* (2011) it is shown in N-body simulations that caused by the inclusion of unsaturated type-I-migration (Paardekooper *et al.*, 2010) big planetary cores (up to $10 M_{Earth}$) can form in protoplanetary discs well before the disc is accreted onto the star.

Up until now, several theoretical formulae to capture the effects of unsaturated torques have been derived (Paardekooper *et al.*, 2010, 2011; Masset and Casoli, 2010). These formulae have only been tested against 2D simulations to check their validity. In 3D simulations the torque acting on the embedded planet differs from 2D simulations (Kley *et al.*, 2009). In Bitsch and Kley (2011), we numerically determine the zero-torque distance to the central star and check the validity of the torque formulae. Overall agreement of the torques acting on embedded low-mass planets is reasonable with Paardekooper *et al.* (2011).

Disc physics

This is extremely important for population synthesis models, where it is tried to explain the distribution of exoplanets (Alibert *et al.*, 2004; Ida and Lin, 2008; Mordasini *et al.*, 2009). These models also required a much shorter time scale for type-I-migration compared to the isothermal migration regime. The inclusion of outward migration in these models with a so called zero-torque radius is implemented in (Mordasini *et al.*, 2010), which shows very promising results.

The influence of the disc mass is also discussed in Bitsch and Kley (2011). The mass of the disc changes not only the structure of it, but it is also needed to form bigger planets, as the planets in the disc can not become more massive than the disc to begin with. This is also a key point in population synthesis models, as planets with different masses have to be formed. On the other hand, in a more massive disc, convection can arise because of the increased heating in the midplane. Convection then disturbs the motion of a planet embedded in the disc in such a way that the movement of the planet becomes very hard to predict. On the other hand, the zero-torque radius is farther out from the central star compared to less massive discs (Bitsch and Kley, 2011).

The structure of a fully radiative disc is determined through viscous heating and radiative transport/cooling. If the viscosity in the disc changes, the structure of the disc changes as well. But not only the structure changes, but the torque acting on a planet as well. A certain viscosity is needed to sustain the unsaturated torques (Chapter 2.3) and therefore outward migration (Chapter 2.4). In isothermal discs, the torque acting on an embedded planet becomes smaller with decreasing viscosity (Bitsch and Kley, 2010). If the viscosity is too low in fully radiative discs, outward migration can no longer be supported. This is discussed in Bitsch *et al.* (2011). A change in the disc structure also changes the temperature and density profiles and the aspect ratio of the disc. These properties of the disc influence the torque acting on an embedded planet as well, which is also the case for isothermal discs (Tanaka *et al.*, 2002).

The disc structure is also determined by the adiabatic index of gas, as it changes the pressure of the gas. Boley *et al.* (2007) stated that the adiabatic index of the gas is

dependent on the temperature of the disc. This dependence has its origins in the behaviour of the gas for different temperatures. It also changes when a different gas mixture is assumed (e.g. ortho-para mixed gas or an equilibrium gas with equal ortho and para hydrogen). As the adiabatic index can vary between $\gamma = 1.3$ and $\gamma = 1.67$, there can be huge differences in the structure of the disc, which influences the migration of an embedded planet as well. This is also discussed in Bitsch *et al.* (2011).

4 Publications

In the following, the five publications written during my thesis are presented. The first three papers (Kley *et al.*, 2009; Bitsch and Kley, 2010; Bitsch and Kley, 2011) are all accepted by Astronomy and Astrophysics and published there. The fourth paper (Bitsch and Kley, 2011) is currently in review in Astronomy and Astrophysics. The last paper (Bitsch *et al.*, 2011) is in preparation and will therefore most probably change in the following weeks. Nevertheless, all five publications are included in the following.

Astronomy
&
Astrophysics

Planet migration in three-dimensional radiative discs

W. Kley[1], B. Bitsch[1], and H. Klahr[2]

[1] Institut für Astronomie & Astrophysik, Universität Tübingen, Auf der Morgenstelle 10, 72076 Tübingen, Germany
e-mail: wilhelm.kley@uni-tuebingen.de
[2] Max-Planck-Institut für Astronomie, Heidelberg, Germany

ABSTRACT

Context. The migration of growing protoplanets depends on the thermodynamics of the ambient disc. Standard modelling, using locally isothermal discs, indicate an inward (type-I) migration in the low planet mass regime. Taking non-isothermal effects into account, recent studies have shown that the direction of the type-I migration can change from inward to outward.
Aims. In this paper we extend previous two-dimensional studies and investigate the planet-disc interaction in viscous, radiative discs using fully three-dimensional radiation hydrodynamical simulations of protoplanetary accretion discs with embedded planets, for a range of planetary masses.
Methods. We use an explicit three-dimensional (3D) hydrodynamical code `NIRVANA` that includes full tensor viscosity. We have added implicit radiation transport in the flux-limited diffusion approximation, and to speed up the simulations significantly we have newly adapted and implemented the `FARGO`-algorithm in a 3D context.
Results. First, we present results of test simulations that demonstrate the accuracy of the newly implemented `FARGO`-method in 3D. For a planet mass of 20 M_{earth}, we then show that including radiative effects also yields a torque reversal in full 3D. For the same opacity law, the effect is even stronger in 3D than in the corresponding 2D simulations, due to a slightly thinner disc. Finally, we demonstrate the extent of the torque reversal by calculating a sequence of planet masses.
Conclusions. Through full 3D simulations of embedded planets in viscous, radiative discs, we confirm that the migration can be directed outwards up to planet masses of about 33 M_{earth}. As a result, the effect may help to resolve the problem of inward migration of planets that is too rapid during their type-I phase.

Key words. accretion, accretion disks – hydrodynamics – radiative transfer – planets and satellites: formation

1. Introduction

The process of migration in protoplanetary discs allows forming planets to move away from the location of creation and finally end up at a different position. The cause of this change in distance from the star are the tidal torques acting from the disturbed disc back on the protoplanet. These can be separated into two parts: i) the so-called Lindblad torques that are created by the two spiral arms in the disc and ii) the corotation torques that are caused by the co-orbital material as it periodically exchanges angular momentum with the planet on its horseshoe orbit. For comprehensive introductions to the field, see for example Papaloizou et al. (2007) or Masset (2008), and references therein. The Lindblad torques, caused by density waves launched at Lindblad resonances, quite generally lead to an inward motion of the planet explaining the observed hot planets very nicely (Ward 1997). The corotation torques are mainly caused by two effects, first by a gradient in the vortensity (Tanaka et al. 2002) and second by a gradient in the entropy (Baruteau & Masset 2008). For typical protoplanetary discs, both contributions can be positive, possibly counterbalancing the negative Lindblad torques (Paardekooper & Mellema 2006; Baruteau & Masset 2008). For the typically considered locally isothermal discs where the temperature only depends on the radial distance from the star, the net torque is negative, and migration is directed inwards for typical disc parameters (Tanaka et al. 2002). Through planetary synthesis models, the inferred rapid inward migration of planetary cores has been found to be inconsistent with the observed mass-distance distribution of exoplanets

(Alibert et al. 2004; Ida & Lin 2008). Possible remedies are the retention of icy cores at the snow line or a strong reduction in the speed of type-I migration (of embedded low-mass planets). Here we focus on the latter process.

Different mechanisms for slowing down the too rapid inward migration have been discussed (Masset et al. 2006; Li et al. 2009), but including more realistic physics seems to be particularly appealing. As pointed out first by Paardekooper & Mellema (2006), the inclusion of radiative transfer can cause a strong reduction in the migration speed. The process has been subsequently investigated by several groups (Baruteau & Masset 2008; Paardekooper & Mellema 2008; Paardekooper & Papaloizou 2008; Kley & Crida 2008), who show that the migration process can indeed be slowed down or even reversed for sufficiently low-mass planets. This new effect occurs in non-isothermal discs and scales with the gradient of the entropy (Baruteau & Masset 2008), hence entropy-related torque. However, in a strictly adiabatic situation after a few libration time scales, the entropy gradient will flatten within the corotation region due to phase mixing. This will lead to saturation (and subsequent disappearance) of the part of the corotation torque that is caused by the entropy gradient in the horseshoe region (Baruteau & Masset 2008; Paardekooper & Papaloizou 2009). To prevent saturation of this entropy-related torque, some radiative diffusion (or local radiative cooling) is required (Kley & Crida 2008). Since for genuinely inviscid flows, the streamlines in the horseshoe region will be closed and symmetric with respect to the planet's location, some level of viscosity is always necessary to avoid torque saturation (Masset 2001; Ogilvie & Lubow 2003;

Paardekooper & Papaloizou 2008, 2009). This applies to both the vortensity- and entropy-related corotation torques. The maximum planet mass for which a change of migration may occur due to this effect lies for typical disc masses in the range of about 40 earth masses, beyond which the migration rate follows the standard (isothermal) case, as gap formation sets in which reduces the corotation effects (Kley & Crida 2008). Most of the above simulations have studied only the two-dimensional case, while three-dimensional models including radiative effects have been presented only for very low masses (Paardekooper & Mellema 2006), or for Jupiter type planets (Klahr & Kley 2006). A range of planet masses has not yet been studied systematically in full 3D.

In this paper we investigate the planet-disc interaction in radiative discs using fully three-dimensional radiation hydrodynamical simulations of protoplanetary accretion discs with embedded planets for a variety of planetary masses. For that purpose we modified and substantially extended an existing multi-dimensional hydrodynamical code `Nirvana` (Ziegler & Yorke 1997a; Kley et al. 2001) by incorporating the `FARGO`-algorithm (Masset 2000a) and radiative transport in the flux-limited diffusion approximation (Levermore & Pomraning 1981; Kley 1989). The code `Nirvana` can in principle handle nested grids which allows us to zoom-in on the detailed structure in the vicinity of the planet (D'Angelo et al. 2002, 2003), however in the present context we limit ourselves to single grid simulations. We present several test cases to demonstrate first the accuracy of the `FARGO`-method in 3D. We then proceed to analyse the effects of radiative transport on the disc structure and torque balance. For our standard planet of 20 M_{earth}, we find that the effect of torque reversal appears to be even stronger in 3D than in 2D for an otherwise identical physical setup. We have a more detailed look at the implementation of the planet potential and show that it has definitely an influence on the strength of the effect. Finally, we perform simulations for a sequence of different planet masses to evaluate the mass range over which the migration may be reversed. The consequence for the migration process and the overall evolution of planets in discs is discussed.

2. Physical modelling

The protoplanetary disc is treated as a three-dimensional (3D), non-self-gravitating gas whose motion is described by the Navier-Stokes equations. The turbulence in discs is thought to be driven by magneto-hydrodynamical instabilities (Balbus & Hawley 1998). Since we are interested in this study primarily on the average effect the disc has on the planet, we prefer in this work to simplify and treat the disc as a viscous medium. The dissipative effects can then be described via the standard viscous stress-tensor approach (e.g. Mihalas & Weibel Mihalas 1984). We assume that the heating of the disc occurs solely through internal viscous dissipation and ignore in the present study the influence of additional energy sources such as irradiation from the central star or other external sources. The internally produced energy is then radiatively diffused through the disc and eventually emitted from its surfaces. To describe this process we utilise the flux-limited diffusion approximation (FLD, Levermore & Pomraning 1981) which allows to treat approximately the transition from optically thick to thin regions near the disc's surface.

2.1. Basic equations

Discs with embedded planets have mostly been modelled through 2D simulations in which the disc is assumed to be

infinitesimal thin, and vertical integrated quantities are used to describe the time evolution of the disc with the embedded planet. This procedure saves considerable computational effort but is naturally not as accurate as truly 3D simulations, in particular the radiation transport is difficult to model in a 2D context.

In this work we present an efficient method for 3D disc simulations based on the `FARGO` algorithm (Masset 2000a). For accretion discs where material is orbiting a central object the best suited coordinates are spherical polar coordinates (r, θ, φ) where r denotes the radial distance from the origin, θ the polar angle measured from the z-axis, and φ denotes the azimuthal coordinate starting from the x-axis.

In this coordinate system, the mid-plane of the disc coincides with the equator ($\theta = \pi/2$), and the origin of the coordinate system is centred on the star. Sometimes we will need the radial distance from the polar axis which we denote by a lower case s, which is the radial coordinate in cylindrical coordinates.

For a better resolution of the flow in the vicinity of the planet, we work in a rotating coordinate system which rotates with the orbital angular velocity Ω, which is identical to the orbital angular velocity of the planet

$$\Omega_P = \left[\frac{G(M_* + m_p)}{a^3} \right]^{1/2} \tag{1}$$

where M_* is the mass of the star, m_p the mass of the planet, and a the semi-major axis of the planet. Only for testing purposes for our implementation of the `FARGO`-method we let the planet move under the action of the disc.

The Navier-Stokes equations in a rotating coordinate system in spherical coordinates read explicitly:

a) Continuity equation

$$\frac{\partial \rho}{\partial t} + \nabla \cdot (\rho \, \boldsymbol{u}) = 0. \tag{2}$$

Here ρ denotes the density of the gas and $\boldsymbol{u} = (u_r, u_\theta, u_\varphi)$ its velocity.

b) Radial momentum

$$\frac{\partial \rho u_r}{\partial t} + \nabla \cdot (\rho \, u_r \boldsymbol{u}) = \rho \frac{u_\theta^2}{r} + \rho r \sin^2 \theta (\omega + \Omega)^2$$
$$+ \rho a_r - \frac{\partial p}{\partial r} - \rho \frac{\partial \Phi}{\partial r} + f_r. \tag{3}$$

Here ω is the azimuthal angular velocity as measured in the rotating frame, p is the gas pressure, and Φ denotes the gravitational potential due to the star and the planet. The vector $\boldsymbol{a} = (a_r, a_\theta, a_\varphi)$ represents inertial forces generated by the accelerated origin of the coordinate system. Specifically, $\boldsymbol{a}$ equals the negative acceleration acting on the star due to the planet(s).

c) Meridional momentum

$$\frac{\partial \rho r u_\theta}{\partial t} + \nabla \cdot (\rho r u_\theta \boldsymbol{u}) = \rho r^2 \sin \theta \cos \theta (\omega + \Omega)^2$$
$$+ \rho r \, a_\theta - \frac{\partial p}{\partial \theta} - \rho \frac{\partial \Phi}{\partial \theta} + r \, f_\theta. \tag{4}$$

d) Angular momentum

$$\frac{\partial \rho h_t}{\partial t} + \nabla \cdot (\rho \, h_t \boldsymbol{u}) = \rho r \sin \theta \, a_\varphi - \frac{\partial p}{\partial \varphi} - \rho \frac{\partial \Phi}{\partial \varphi} + r \sin \theta \, f_\varphi, \tag{5}$$

where we defined the *total* specific angular momentum (in the inertial frame)

$$h_t = r^2 \sin^2 \theta (\omega + \Omega); \tag{6}$$

i.e. the azimuthal velocity in the rotating frame is given by $u_\varphi = \omega r \sin\theta$.

The Coriolis force in Eq. (5) for u_φ (or h_t) has been incorporated into the left hand side. Thus, it is written in such a way as to conserve total angular momentum best. This conservative treatment is necessary to obtain an accurate solution of the embedded planet problem (Kley 1998).

The function $\boldsymbol{f} = (f_r, f_\theta, f_\varphi)$ in the momentum equations denotes the viscous forces which are stated explicitly for the three-dimensional case in spherical polar coordinates in Tassoul (1978). For the description of the viscosity we use a constant kinematic viscosity coefficient ν.

e) Energy equation (internal energy)

$$\frac{\partial \rho c_v T}{\partial t} + \nabla \cdot (\rho \, c_v T \boldsymbol{u}) = -p \nabla \cdot \boldsymbol{u} + Q^+ - \nabla \cdot \boldsymbol{F}. \tag{7}$$

Here T denotes the gas temperature in the disc and c_v is the specific heat at constant volume. On the right hand side, the first term describes compressional heating, Q^+ the viscous dissipation function, and $\boldsymbol{F}$ denotes the radiative flux. In writing Eq. (7) we have assumed that the radiation energy density $E = a_R T^4$ is always lower than the thermal energy density $e = \rho c_v T$. Here, a_R denotes the radiation constant. Furthermore, we utilise the one-temperature approach and write for the radiative flux, using flux-limited diffusion (FLD)

$$\boldsymbol{F} = -\frac{\lambda c \, 4 a_R T^3}{\rho (\kappa + \sigma)} \nabla T \,, \tag{8}$$

where c is the speed of light, κ the Rosseland mean opacity, σ the scattering coefficient, and λ the flux-limiter. Using FLD allows us to perform stable accretion disc models that cover several vertical scale heights. We use here the FLD approach described in Levermore & Pomraning (1981) with the flux-limiter of Kley (1989). Its suitability for protostellar discs has been shown in Kley & Lin (1996, 1999), and for embedded planets in Klahr & Kley (2006). In this work we use for the Rosseland mean opacity $\kappa(\rho, T)$ the analytical formulae by Lin & Papaloizou (1985) and set the scattering coefficient σ to zero. To close the basic system of equations we use an ideal gas equation of state where the gas pressure is given by $p = R_{gas}\rho T/\mu$, with the mean molecular weight μ and gas constant R_{gas}. For a standard solar mixture we assume here $\mu = 2.35$. The speed of sound is calculated from $c_s = \sqrt{\gamma p/\rho}$ with the adiabatic index $\gamma = 1.43$.

2.2. Planetary potential

The total potential Φ acting on the disc consists of two contributions, one from the star Φ_*, the other from the planet Φ_p

$$\Phi = \Phi_* + \Phi_p = -\frac{GM_*}{r} - \frac{Gm_p}{\sqrt{(\boldsymbol{r} - \boldsymbol{r}_p)^2}},$$

where $\boldsymbol{r}_p$ denotes the radius vector of the planet location. The embedded planet is modelled as a point mass that orbits the central star on a fixed circular orbit. In numerical simulations the planetary potential has to be smoothed over a few gridcells to avoid divergences.

Typically in 2D simulations the planetary potential is modelled by an ϵ-potential

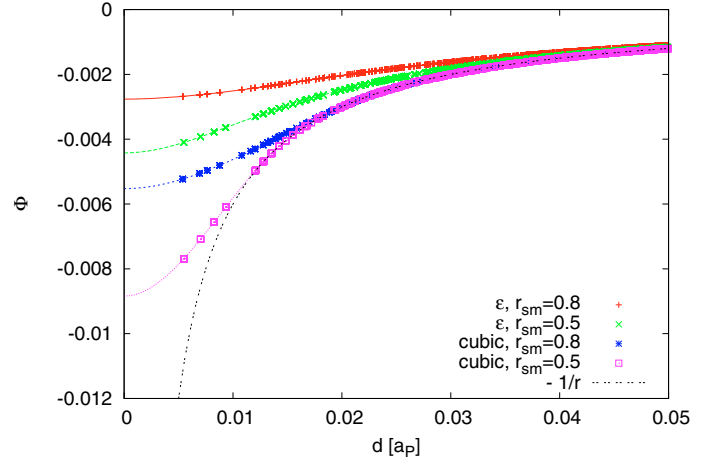$$\Phi_p^\epsilon = -\frac{Gm_p}{\sqrt{d^2 + \epsilon^2}}, \tag{9}$$

Fig. 1. The gravitational potential of a 20 M_{earth} planet with different smoothings applied, see Eqs. (9) and (10). The distance d from the planet is given in units of a_p (here a_{Jup}), and the smoothing length r_{sm} in units of the Hill radius of the planet which refers here to $R_H = 0.0271 a_p$. Note that the data points are drawn directly from the used 3D computational grid and indicate our standard numerical resolution (see Sect. 2.4).

where we denote the distance of the disc element to the planet with $d = |\boldsymbol{r} - \boldsymbol{r}_p|$ and ϵ is the smoothing length. In a 2D configuration a potential of this form is indeed very convenient, as the smoothing takes effects of the otherwise neglected vertical extent of the disc into account. To account for the finite disc thickness H which depends on the temperature in the disc, an often used value for the smoothing length in 2D-simulations is $\epsilon = r_{sm} = 0.6H$. The obtained 2D torques are then found to be in reasonable agreement with three-dimensional analytical estimates of the torques, that do not include a softening length for the planet potential.

However in a 3D configuration the same approach is not necessary and would lead to an unphysical "spreading" of the potential over a large region. Hence, we apply a different type of smoothing, follow Klahr & Kley (2006) and use a *cubic*-potential of the form

$$\Phi_p^{cub} = \begin{cases} -\frac{m_p G}{d} \left[\left(\frac{d}{r_{sm}}\right)^4 - 2\left(\frac{d}{r_{sm}}\right)^3 + 2\frac{d}{r_{sm}} \right] & \text{for} \quad d \leq r_{sm} \\ -\frac{m_p G}{d} & \text{for} \quad d > r_{sm}. \end{cases} \tag{10}$$

This potential is constructed in such a way as to yield for distances d greater than r_{sm} the correct $1/r$ potential of the planet, and inside that radius ($d < r_{sm}$) the potential is smoothed with a cubic polynomial such that at the transition radius r_{sm} the potential and its first and second derivative agree with the analytic outside $1/r$-potential. To illustrate the various types of smoothing, we display in Fig. 1 the behaviour of the different forms of the planetary potential. Clearly the ϵ-potential leads for the same values of r_{sm} to a much wider and shallower potential than our *cubic*-approach. For the often used value $\epsilon = 0.6H$ the ϵ-potential is felt way outside the Hill radius

$$R_H = a_p \left(\frac{m_p}{3 \, M_*}\right)^{1/3},$$

and leads to a significant underestimate of the potential depth already at r_{sm}. The *cubic*-potential (Eq. (10)) will always be accurate down to $d = r_{sm}$ and is inside much deeper than the ϵ-potential, and hence more accurate. In the simulations

presented below we study in detail the influence that the potential description has on the value of the torques acting on the planet.

We calculate the gravitational torques acting on the planet by integrating over the whole disc, where we apply a tapering function to exclude the inner parts of the Hill sphere of the planet. Specifically, we use the smooth (Fermi-type) function

$$f_b(d) = \left[\exp\left(-\frac{d/R_H - b}{b/10}\right) + 1\right]^{-1} \tag{11}$$

which increases from 0 at the planet location ($d = 0$) to 1 outside $d \geq R_H$ with a midpoint $f_b = 1/2$ at $d = bR_H$, i.e. the quantity b denotes the torque-cutoff radius in units of the Hill radius. This torque cutoff is necessary to avoid first a large, possibly very noisy contribution from the inner parts of the Roche lobe, and second to disregard material that is gravitationally bound to the planet. The question of torque cutoff and exclusion of Roche lobe material becomes very important when i) the disc self-gravity is neglected, and ii) there exists material bound to the planet (e.g. a circumplanetary disc). This issue should definitely be addressed in the future. Here, we assume a transition radius of $b = 0.8$ Hill radii (see Crida et al. 2008, Fig. 2). For reference we quote the width of the horseshoe region which is given for an isothermal disc approximately by (Masset et al. 2006)

$$x_s = 1.16\, a_p \sqrt{\frac{q}{(H/r)}} \tag{12}$$

with the mass ratio $q = m_p/M_*$ and the local relative disc thickness H/r. For an adiabatic disc H has to be replaced by γH (Baruteau & Masset 2008).

2.3. Setup

The three-dimensional (r, θ, φ) computational domain consists of a complete annulus of the protoplanetary disc centred on the star, extending from $r_{\min} = 0.4$ to $r_{\max} = 2.5$ in units of $r_0 = a_{\text{Jup}} = 5.2$ AU. In the vertical direction the annulus extends from the disc's midplane (at $\theta = 90°$) to about $7°$ (or $\theta = 83°$) above the midplane. In case of an inclined planet the domain has to be extended and cover the upper and lower half of the disc. The mass of the central star is one solar mass $M_* = M_\odot$, and the total disc mass inside $[r_{\min}, r_{\max}]$ is $M_{\text{disc}} = 0.01\, M_\odot$. For the present study, we use a constant kinematic viscosity coefficient with a value of $\nu = 10^{15}$ cm^2/s, a value that relates to an equivalent $\alpha = 0.004$ at r_0 for a disc aspect ratio of $H/r = 0.05$, where $\nu = \alpha H^2 \Omega_K$. In standard dimensionless units we have $\nu = 10^{-5}$.

The models are initialised with a locally isothermal configuration where the temperature is constant on cylinders and has the profile $T(s) \propto s^{-1}$, where s is related to r through $s = r \sin \theta$. This yields a constant ratio of the disc's vertical height H to the radius s. The initial vertical density stratification is approximately given by a Gaussian:

$$\rho(r, \theta) = \rho_0(r) \exp\left[-\frac{(\pi/2 - \theta)^2 r^2}{2H^2}\right]. \tag{13}$$

Here, the density in the midplane is $\rho_0(r) \propto r^{-1.5}$ which leads to a $\Sigma(r) \propto r^{-1/2}$ profile of the vertically integrated surface density. The vertical and radial velocities, u_θ and u_r, are initialised to zero. The initial azimuthal velocity u_φ is given by the equilibrium of gravity, centrifugal acceleration and the radial pressure gradient. In case of purely isothermal calculations this setup is equal to the equilibrium configuration (in the case

of closed radial boundaries). For fully radiative simulations the model is first run in a 2D axisymmetric mode to obtain a new self-consistent equilibrium where viscous heating balances radiative transport/cooling from the surfaces (see Sect. 4.1 below). This initialisation through an axisymmetric 2D phase (in the $r-\theta$ plane) reduces the required computational effort substantially, as the evolution from the initial isothermal state towards the radiative equilibrium takes about 100 orbits, if the disc is started with an isothermal equilibrium having constant H/r. After reaching the equilibrium between viscous heating and radiative transport/cooling, we extend this model to a full 3D simulation, by expanding the grid into the ϕ-direction, and the planet is embedded.

2.4. Numerics

We adopt a coordinate system, which rotates at the orbital frequency of the planet. For our standard cases, we use an equidistant grid in r, θ, φ with a resolution of $(N_r, N_\theta, N_\varphi) = (266, 32, 768)$. To minimise disturbances (wave reflections) from the radial boundaries, we impose, at $r_{\min}$ and $r_{\max}$, damping boundary conditions where all three velocity components are relaxed towards their initial state on a timescale of approximately the local orbital period. The radial velocities at the inner and outer radius vanish. The angular velocity is relaxed towards the Keplerian values. For the density and temperature, we apply reflective radial boundary conditions. In the azimuthal direction, periodic boundary conditions are imposed for all variables. In the vertical direction we apply outflow boundary conditions. The boundary conditions do not allow for mass accretion through the disc, such that the total disc mass remains nearly constant during the time evolution, despite a possible small change due to little outflow through the vertical boundaries and the used density floor (see below).

The numerical details of the used finite volume code (NIRVANA) relevant for these planet disc simulations were described in Kley et al. (2001) and D'Angelo et al. (2003). In the latter paper the usage of the nested grid-technique is described in more detail as well. The original version of the NIRVANA code, on which our programme is based upon, has been developed by Ziegler & Yorke (1997b). The empowerment with FARGO is based on the original work by Masset (2000a). Our implementation appears to be the first inclusion of the FARGO-algorithm in a 3D spherical coordinate system. More details about the implementation are given in the appendix. The basic algorithm of the newly implemented radiation part in the energy Eq. (7) is presented in the appendix as well. To avoid possible time step limitations this part is always solved implicitly.

3. Test calculations

3.1. The FARGO-algorithm

To test the 3D implementation of the FARGO-algorithm in our NIRVANA-code we have run several models with planets on circular, elliptic and inclined orbits with and without the FARGO-method applied. Here, we follow closely the models presented in Cresswell et al. (2007) and consider moving planets in 3D discs. As the tests are dynamically already complicated we use here only the isothermal setup. The different setups gave very similar results in all cases, and we present results for one combined case of a 20 M_{earth} planet embedded in a locally isothermal disc with an initial non-zero eccentricity ($e = 0.2$) and non-zero inclination ($i = 5°$). All physical parameters of this
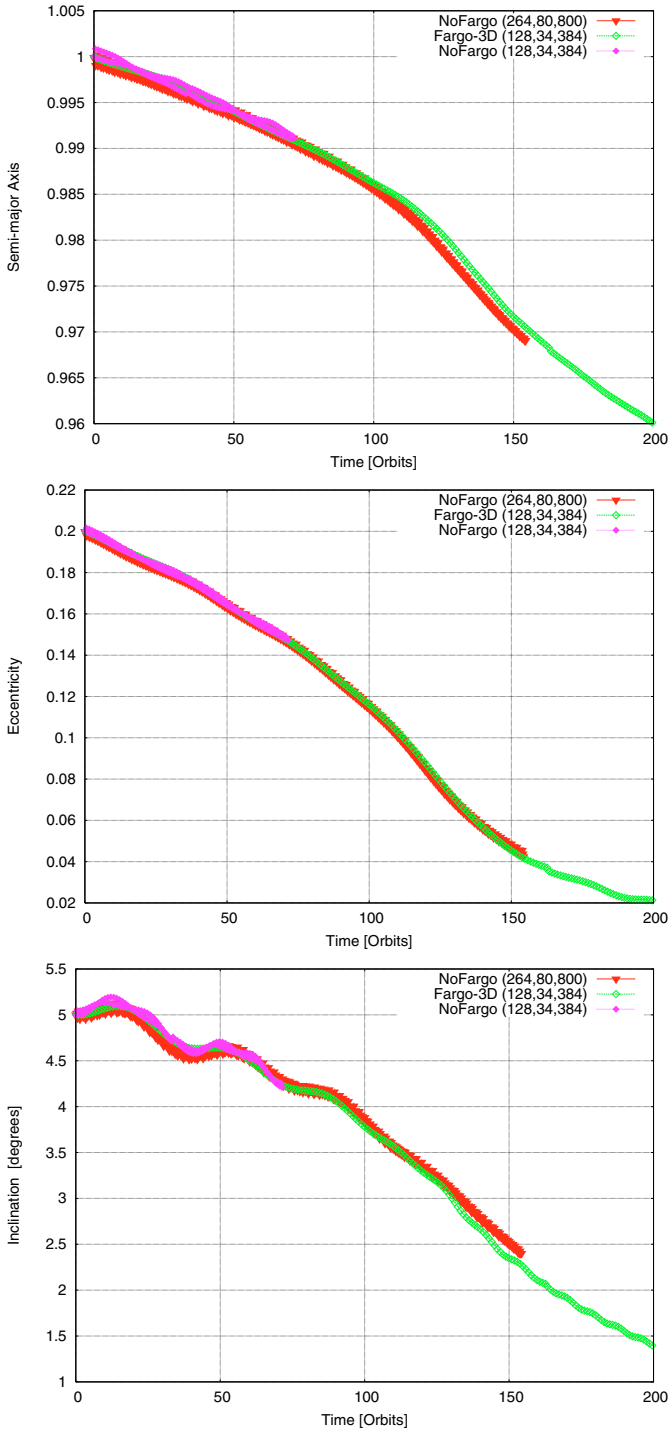
Fig. 2. Evolution of semi-major axis, eccentricity and inclination as a function of time for a 20 M_{earth} planet in a three-dimensional disc. Results are displayed for different numerical resolutions (N_r, N_θ, N_φ), and using Fargo and Non-Fargo runs.
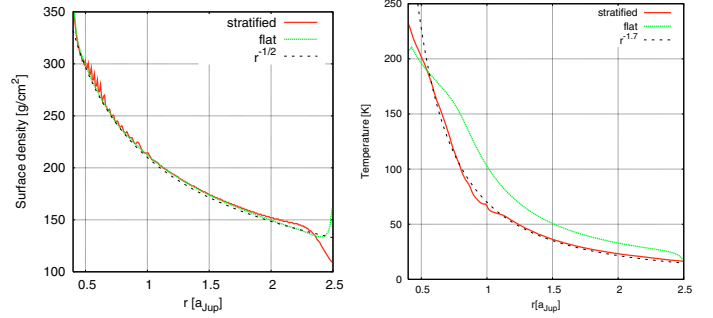

Fig. 3. Radial stratification of surface density (*left*) and the midplane temperature (*right*) in the disc. This dashed lines represent simple approximations to the 3D stratified results. The solid (green) curves labelled "flat" refer to corresponding results for a vertically integrated flat 2D disc using the same input physics.
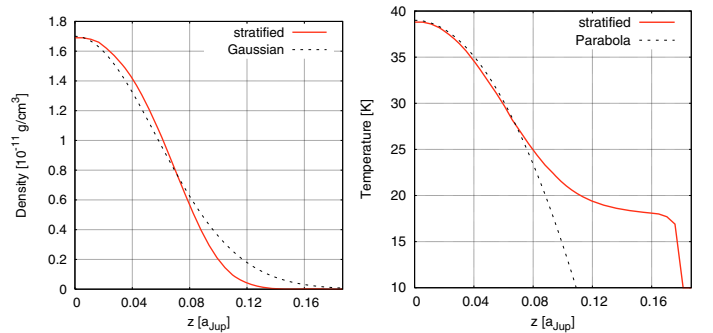
Fig. 4. Vertical stratification of density (*left*) and temperature (*right*) at a radius of $r = 1.44$. Thin dashed lines just represent simple functional relations.

different codes, methods and resolutions) yield very similar results. The scatter of the data points is slightly reduced in the FARGO-run.

3.2. The radiation algorithm

To obtain an independent test of the newly implemented radiation transport module in our NIRVANA-code we performed a run with the standard setup as described above but with no embedded planet. Hence, this setup refers to an axisymmetric disc with internal heating and radiative cooling. For a fixed, closed computational domain it is only the total mass enclosed that determines the final equilibrium state of the system, once the physics (viscosity, opacity, and equation of state) have been prescribed. The radial dependence of the vertically integrated surface density and the midplane temperature are displayed in Fig. 3, and the corresponding vertical profiles at a radius of $r = 1.44$ in Fig. 4. First of all, these new results obtained with NIRVANA agree very well with those obtained with the completely independent 2D-code RH2D used in the $r - \theta$ mode, such as presented for example in Kley et al. (1993), which are not shown in the figures, however. As the final configuration of the system is given by the equilibrium of internal (viscous) dissipation and radiative transport, this test demonstrates the consistency of our implementations.

To relate our 3D results to previous radiative 2D runs which use vertically integrated quantities, and hence can only use an approximative energy transport and cooling (Kley & Crida 2008), we compare in Fig. 3 the results obtained with the two methods. Both models are constructed for the same disc mass and identical physics. The label "flat" in the figure refers to the flat 2D case (obtained with RH2D, see Kley & Crida 2008) and

run are identical to those described in Cresswell et al. (2007), and we compare our results to the last models presented in that paper (their Fig. 16). The outcome of this comparison is shown in Fig. 2, where we display the results of a standard non-Fargo run with the resolution (N_r, N_θ, N_ϕ) = (264, 80, 800) with the data taken from Cresswell et al. (2007) (where a different code has been used) to two runs having a lower resolution of (N_r, N_θ, N_φ) = (128, 34, 384), one with FARGO and the other one without. We can see that all 3 models (obtained with two

the "stratified" label to our new 3D implementation presented here. The left graph displays the vertically integrated surface density distribution, here $\Sigma(r) = f_\Sigma \int_{\theta_{max}}^{\theta_{min}} \rho r \sin(\theta) d\theta$, with $f_\Sigma = 1$ for two-sided and 2 for one-sided discs. Our result is well represented by a $\Sigma \propto r^{-1/2}$ profile as expected for a closed domain and constant viscosity. Interesting is the irregular structure at radii smaller than $r \approx 1.0$ in the full 3D stratified case, and we point out that these refer to the onset of convection inside that radius. To model convection is of course not possible in a flat 2D approach. The temperature distribution for the full 3D case follows approximately a $T \propto r^{-1.7}$ profile. Here, the approximate flat-disc model leads to midplane temperatures that are about 40% higher for the bulk part of the domain than in the true 3D case. Possibly a refined modelling of the vertical averaging procedure and the radiative losses in the flat 2D case could improve the agreement here, but in the presence of convection we may expect differences in any case.

In Fig. 4 we display the vertical stratification of the disc at a specific radius in the middle of the computational domain at $r = 1.44$. Two simple approximations are over-plotted as dashed lines. Note, that in these plots the stratification is plotted along the $r = $ const. lines which deviates for thin discs only slightly from $z = r \cos \theta$. Taking $z_0 = 0.08$, the Gaussian curve for the density refers to $\rho_0 \exp\left[-(z/z_0)^2\right]$ and the temperature fit to $T(z) = T_0[1 - 0.4 (z/z_0)^2]$. These simple formulae are intended to guide the eye rather than meant to model exactly the structure at this radius which depends on the used opacities. Given the simplicity of these, it is interesting that they approximate the true solution reasonably well within one scale height.

3.3. Density floor

By expanding the computed area in the θ-direction beyond the 90° to 83° region of our standard model, the code would have to cover several orders of magnitude in the density. Thus, many more grid cells would be required to resolve the physical quantities. In order to avoid this and save computation time, we apply a minimum density function (floor) for the low-density regions high above the equatorial plane of the disc. It reads

$$\rho = \begin{cases} \rho & \text{for} \quad \rho > \rho_{min} \\ \rho_{min} & \text{for} \quad \rho \le \rho_{min}. \end{cases} \quad (14)$$

Of course, applying a density floor like this will create mass inside the computed domain. The density floor ρ_{min} has now to be chosen such that: firstly the computation is not handicapped by too low values and secondly the inner (optically thick) parts of the disc are not influenced. To test the sensitivity of the disc structure against the density floor we performed a series of test calculations, and show the results of simulations with different ρ_{min} in Fig. 5. These runs cover $\theta = 90°$ to 70°, a range about 3 times as large as before. The density and temperature profiles in these simulations do not differ for the regions near the equatorial plane, because the density is too high for the minimum density to take effect. Indeed, all curves are nearly indistinguishable in the region for optical depths greater than $\tau = 1.0$, with

$$\tau(z) = \int_z^\infty \rho \kappa dz. \quad (15)$$

Please note, that in the plot we do display the results along lines of constant (spherical) radius. Moving further away from the equatorial plane, one can see in the density profile the different minimum densities, but in the temperature profile there is hardly
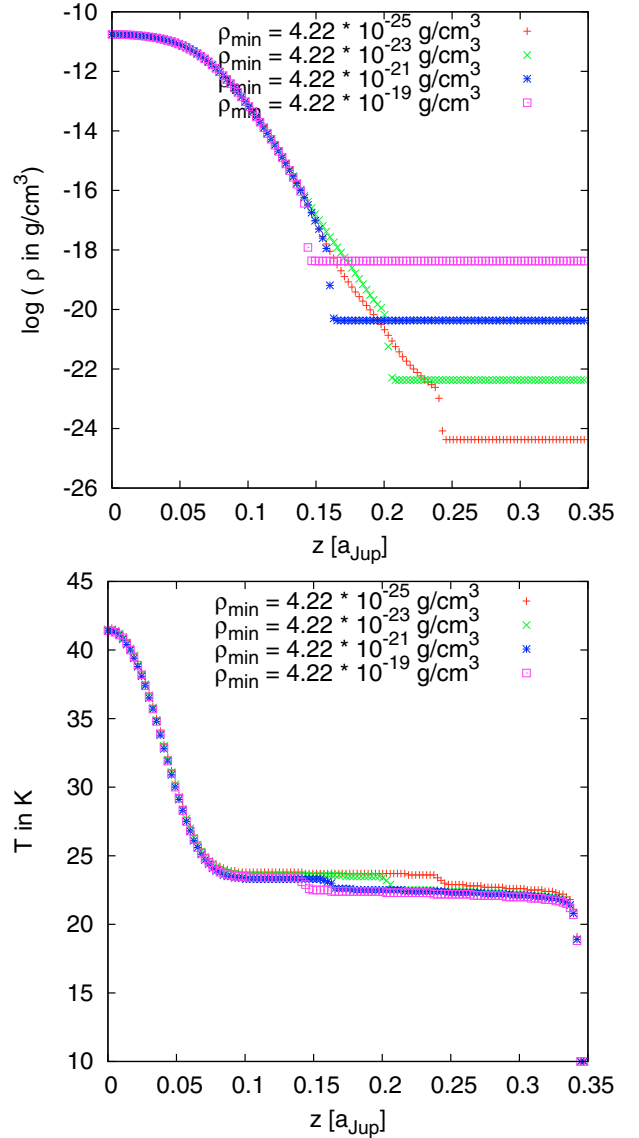

Fig. 5. Vertical stratification of density in logarithmic scale (*top*) and temperature (*bottom*) at a radius of $r = 1.00$ for a simulation covering the $\theta = 90°$ to 70° region. The optical depth $\tau = 1.0$ is reached at about $z = 0.055$.

any difference at all. Above a certain distance from the equatorial plane the temperature remains constant. The little fluctuations visible in the profile are due to oscillations in the temperature for the low mass regions.

By applying a minimum density the code is capable of resolving large distances above the equatorial plane with a reasonable number of grid cells. Also note that it is not necessary to use a minimum density for calculations covering only the $\theta = 90°$ to 83° regions, as the density is always high enough.

4. Models with an embedded planet

For all the models with embedded planets we use our standard disc setup as described in Sect. 2.3 with the corresponding boundary conditions in Sect. 2.4. Here, we briefly summarise some important parameter of the setup. The three-dimensional (r, θ, φ) structure of the disc extends form $r_{min} = 0.4$ to $r_{max} = 2.5$ in units of $r_0 = a_{Jup} = 5.2$ AU. In the vertical direction the annulus extends from the disc's midplane (at $\theta = 90°$) to about
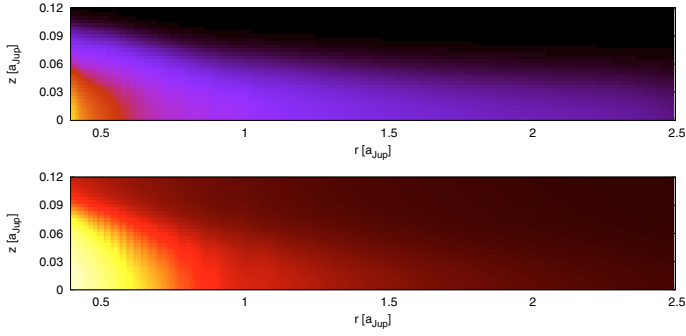
Fig. 6. Density (*top*) and Temperature (*bottom*) for a fully radiative model in a 2D axisymmetric simulation.

Fig. 7. Vertical density distribution at $r = 1.4$ for a fully radiative model in a 2D axisymmetric simulation. "+": isothermal starting configuration, "×": relaxed radiation equilibrium configuration.

7° (or $\theta = 83°$) above the midplane. For our chosen grid size of $(N_r, N_\varphi, N_\theta) = (266, 32, 768)$ this refers to linear grid resolution of $\Delta \approx 0.008$ at the location of the planet, which corresponds to 3.3 gridcells per Hill radius, and to about 5 gridcells per horseshoe half-width for a 20 M_{earth} planet in a disc with $H/r = 0.05$. In this configuration the planet is located exactly at the corner of a gridcell. In the fully radiative disc, the temperature at the disc surface is kept at the fixed ambient temperature of 10 K. This simple "low-temperature" boundary condition ensures that all the internally generated energy is liberated freely at the disc's surface. It is only suitable for optically thin boundaries and does not influence the inner parts of the optically thick disc (see Fig. 5). The disc has a mass of 0.01 $M_\odot$, and an aspect ratio $H/r = 0.05$ in the beginning.

4.1. Initial setup

Before placing the planet into the 3D disc we have to bring it first into a radiative equilibrium state such that our results are not corrupted by initial transients. As described above this initial equilibration is performed in an axisymmetric 2D setup that is then expanded to full 3D. Tests with our code have shown that we reach the 3D equilibrium state (a constant torque) in a calculation with embedded planets about 50% faster when starting first with the 2D radiative equilibrium disc.

In Fig. 6 the 2D density and temperature distributions for such an equilibrated disc are displayed. In the equilibrium state of the fully radiative model the disc is much thinner than the isothermal starting case, see Fig. 7. Consequently, the density is increased in the equatorial plane, leaving the areas high above and below the disc with less material. Apparently, for this disc mass and the chosen values of viscosity and opacity, the balance of viscous heating and radiative cooling reduces the aspect ratio of the disc from initially 0.05 to about 0.037 in the radiative case. Had we started with an initially thinner disc, the difference would of course not be that pronounced.

After successfully completing the equilibration we now embed a 20 M_{earth} planet into the disc. The planet is held on a fixed orbit and we calculate the torques acting on it through integrating over the whole disc taking into account the above tapering function with a cutoff $r_{torq} = 0.8R_H$, which refers to $b = 0.8$ in Eq. (11). In addition to this value of the torque cutoff we have tested how the obtained total torque changes when using $b = 0.6$. For our standard 20 M_{earth} planet presented in the following we found that for the isothermal cases the results change by about 10% and in the radiative case by about 30%, which can be considered as a rough estimate of the numerical uncertainties of the results. The deviation is greater in the radiative
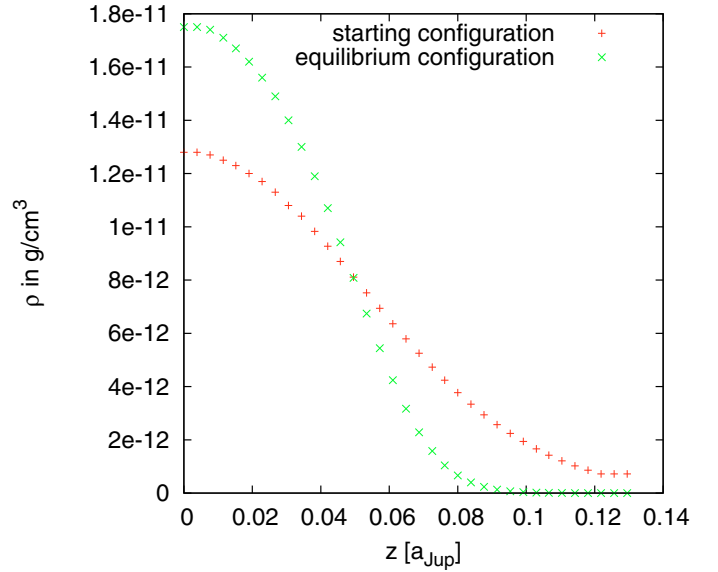
situation because in this case important (corotation) contributions to the total torque originate from a region very close to the planet, which is influenced stronger by the applied torque cutoff. Here, cancellation effects caused by adding the negative Lindblad and the positive corotation torque may explain part of the larger relative uncertainty in the radiative case. We note, that our applied torque cutoff is not hard but refers to the smooth function (11). Keeping in mind that there are only 3.3 gridcells per Hill radius, lower values for b are not useful.

4.2. Isothermal discs

Due to the applied smoothing, we expect the planetary potential to modify the density structure of the disc near the planet and subsequently change the torques acting on the planet. First, we investigate the influence of the planetary potentials (see Fig. 1) on the disc and torques in the isothermal regime. The 2D surface density distribution in the disc's midplane at 100 planetary orbits corresponding to our two extreme planetary potentials (the shallowest and the deepest) is displayed in Fig. 8, where we used a cutoff for the maximum displayed density to make both cases comparable. As expected, a deeper planetary potential results in a higher density concentration inside the planetary Roche lobe and to a slightly reduced density in the immediate surroundings. This accumulation of mass near the planet for deeper potentials is illustrated in more detail in Fig. 9. For our deepest $r_{sm} = 0.5$ cubic potential the maximum density inside the planet's Roche-lobe is over an order of magnitude greater than in the shallowest $r_{sm} = 0.8$ ϵ-potential.

In Fig. 10 we show the specific torques acting onto the planet using different potentials for the case of $H/r = 0.05$. The total torque is continuously monitored and plotted versus time in the upper panel. The radial torque density $\Gamma(r)$ for the same models is displayed in the lower panel. Here, $\Gamma(r)$ is defined such that the total torque T^{tot} acting on the planet is given by

$$T^{tot} = \int_{r_{min}}^{r_{max}} \Gamma(r) \, dr. \qquad (16)$$

Fig. 9. Radial density distribution in the equator along $(\rho(r, \varphi = \pi, \theta = \pi/2))$, i.e. along a ray through the location of the planet for all 4 planetary potentials used.
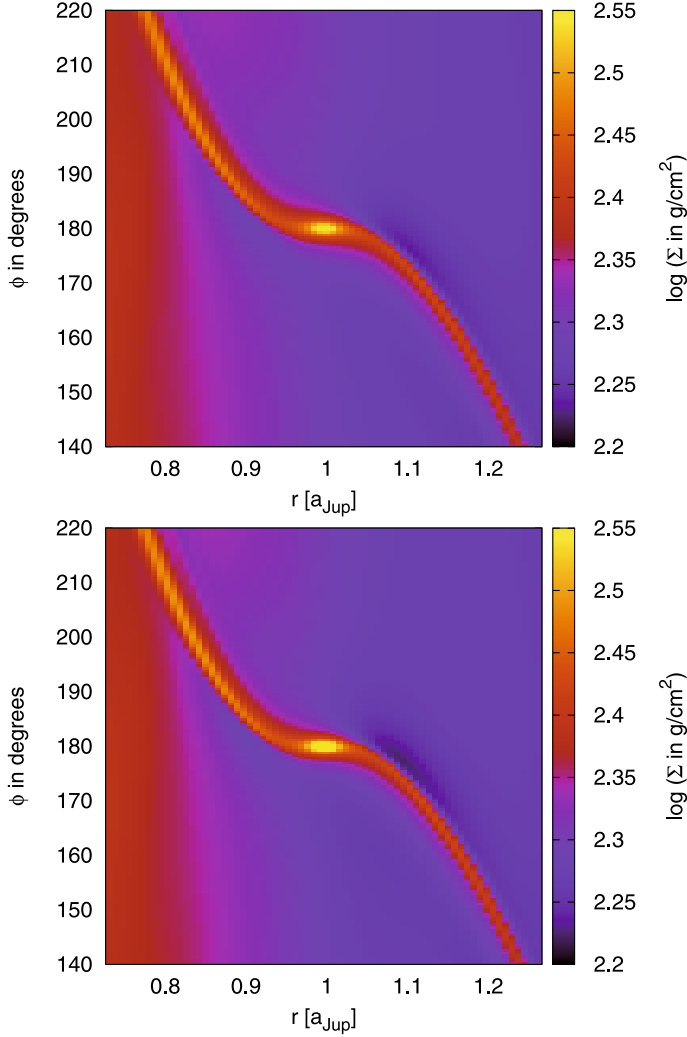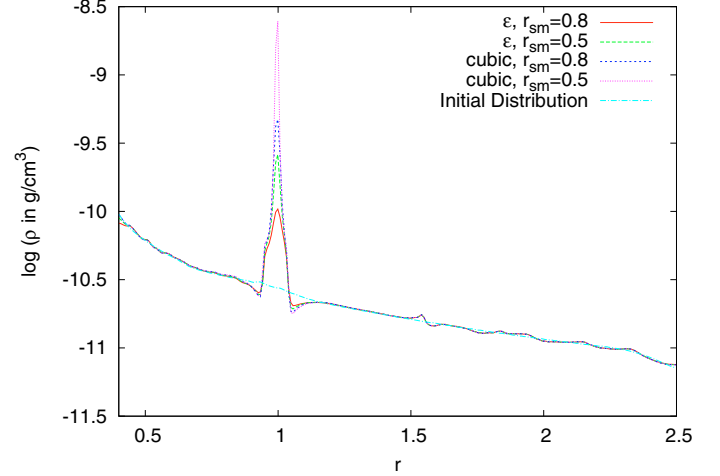
Fig. 8. Surface density distribution for isothermal simulations with $H/r = 0.05$ at 100 planetary orbits. Displayed are results for the shallowest and deepest potential. *Top*: ϵ-potential with $r_{sm} = 0.8$, *bottom*: cubic with $r_{sm} = 0.5$.

The time evolution of the total torque displays a characteristic behaviour. Starting from the axisymmetric case, a first intermediate plateau is reached at early times between $t \approx 5$–10, after which the torques settle on longer timescales towards their final equilibria. The initial plateaus correspond to the values of the torques shortly after the disc material has started its horseshoe-type motion in the co-orbital region. The level of this so-called unsaturated torque depends on the local disc properties and on the applied smoothing of the potential, as indicated clearly in the top panel of Fig. 10. In the following evolution, the material in this horseshoe region will be mixed thoroughly, the torques decline and settle eventually to their final equilibria, here reached after about 40 orbits. This process of phase mixing inside the horseshoe region is called torque saturation, and it occurs on timescales of the order of the libration time, which is given by

$$\tau_{lib} = \frac{4\,a_p}{3\,x_s} P_p \qquad (17)$$

where P_p is the orbital period of the planet, and x_s the half-width of the horseshoe region (see Eq. (12)). In our case (for $q = 6 \times 10^{-5}$ and $H/r = 0.05$) the libration time is about $30P$. The different initial values of the unsaturated torques depend on the form of the potential (e.g. smoothing length), but note

that the timescale to reach equilibrium is similar in all cases. This particular time behaviour of the torques and the process of saturation has been described recently for isothermal discs by Paardekooper & Papaloizou (2009), see also Masset et al. (2006).

The two runs with the ϵ-potential result in the most negative torque values, i.e. the fastest inward migration (lower two curves in the upper panel). While the total torques of the two ϵ-potentials are nearly identical, in the corresponding radial torque distribution the cases are clearly separated, a fact which is due to cancellation effects when adding the inner (positive) and outer (negative) contribution. The slightly deeper cubic $r_{sm} = 0.8$ potential leads to a marginally decreased (in magnitude) torque compared to the simulations with ϵ-potential. For the cubic $r_{sm} = 0.5$ potential we obtain an even less negative equilibrium torque compared to all the other isothermal simulations. As most of the corotation torque is generated in the vicinity of the planet, a change in the density structure there (by deepening the potential) may have a significant impact on the torque values. We can compare our values of the torque with the well known formulae for the specific torque in a 3D strictly *isothermal disc* as presented by Tanaka et al. (2002)

$$T_0^{tot} = -f_\Gamma \, q \left(\frac{H}{r}\right)^{-2} \left(\frac{\Sigma a_p^2}{M_*}\right) a_p^2 \Omega_p^2 \qquad (18)$$

with

$$f_\Gamma = (1.364 + 0.541\,\alpha_\Sigma) \qquad (19)$$

where α_Σ denotes the radial gradient of the surface density through $\Sigma \propto r^{-\alpha_\Sigma}$. For our standard parameter this formula gives about $T_0^{tot} = -2.5\,10^{-5}a_p^2\Omega_p^2$, which is, in absolute value, about a factor 1.4–2.2 times greater than our results. We note however, that Eq. (18) has been derived for constant temperature, inviscid disc. The influence of viscosity on the torque has been studied by Masset (2002), who found that a reduction of the viscosity from our used value of 10^{-5} to zero will fully saturate the (vortensity-related) corotation torque, leading easily to a reduction of the total torque by a factor of two. Additional simulations with much lower viscosity (not shown here) indicate indeed that then the equilibrium torque is in good agreement with Eq. (18).

It seems at first surprising and unpleasing that the torques depend so much on the treatment of the planetary potential.
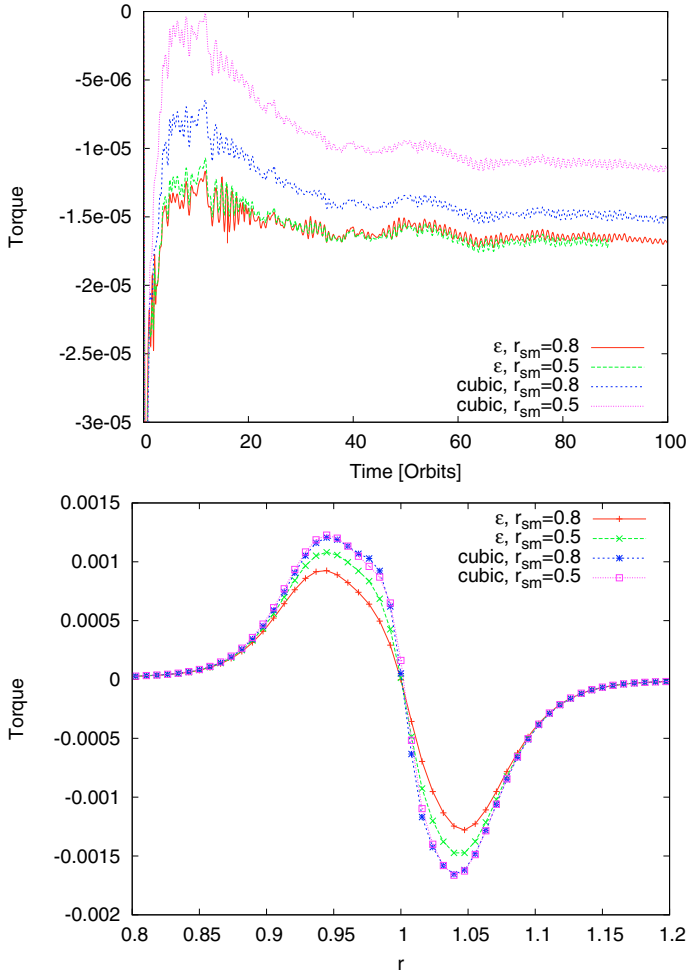
Fig. 10. Specific torque (in units of $a_p^2 \Omega_p^2$) acting on the planet using 4 different smoothings for the planetary potential in the isothermal case with $H/r = 0.05$. *Top*: evolution of total torque with time. *Bottom*: radial variation of the specific torque density $\Gamma(r)$ at $t = 80$ orbits.

Fig. 11. Specific torque acting on the planet using different grid resolutions for the isothermal case with $H/r = 0.037$. In all cases the cubic potential with $r_{sm} = 0.5$ has been used. *Top*: evolution of total torque with time. *Bottom*: radial variation of the specific torque density, at $t = 80$ orbits for the standard and medium resolution, and at 60 orbits for the high resolution.

However, an ϵ-potential has an influence far beyond the Roche-radius of the planet and certainly will change the torques acting on the planet. Here the corotation torques are affected most prominently and become more and more positive as the smoothing length is lowered (see also Paardekooper & Papaloizou 2009). Nevertheless, in two-dimensional simulations it has become customary to rely on ϵ-potentials for the purpose to take into account the finite thickness of the disc. In a three-dimensional context, the more localised cubic-potential with its finite region of influence may be more realistic. But for the isothermal case the increased potential depth leads to a very large accumulation of mass, as seen in Fig. 9. In such a case it will be very difficult to achieve convergence. In the more realistic radiative case the situation is eased somewhat through a temperature increase near the planet, as outlined below.

To check numerical convergence we performed additional runs using a larger number of gridcells. In Fig. 11 we display the total torque versus time and the radial torque density $\Gamma(r)$ for different grid resolutions, again for the isothermal disc case. In contrast to the previous plot we use here a slightly cooler disc with $H/r = 0.037$, as this matches more closely the results from the fully radiative calculations presented below. In this case the initial unsaturated torques reach even positive values due to the smaller thickness of the disc. The grid resolution seems to be sufficient for resolving the structures near the Roche-lobe. For
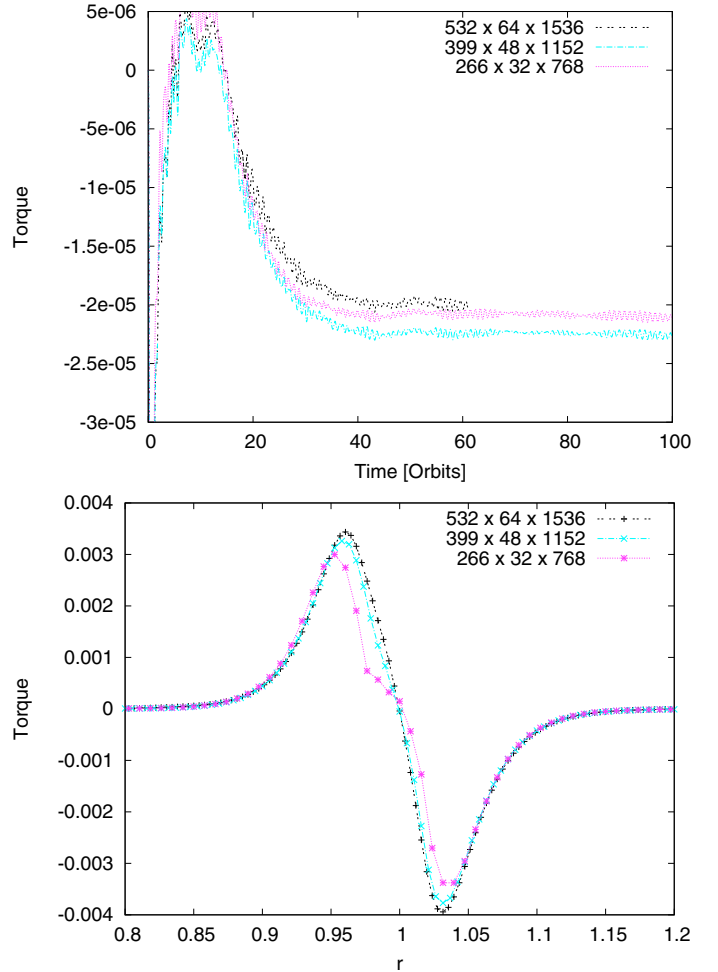
the displayed $\Gamma(r)$ distribution in the lower panel both cases are very similar and the higher resolution case is a bit smoother.

4.3. Fully radiative discs

The simulations are started from the radiative disc in equilibrium as described above, and are continued with an embedded planet of 20 M_{earth}. The obtained equilibrium configuration for the surface density and midplane-temperature is displayed in Fig. 12 after an evolutionary time of 100 orbits. As in the isothermal case the density within the Roche lobe of the planet is strongly enhanced for the deeper potentials, displayed are the two extreme cases of our different potentials. Comparing with the corresponding density maps of the isothermal case in Fig. 8, one can also observe slightly smaller opening angles of the spiral arms in the radiative case. For identical H/r the sound speed would be $\sqrt{\gamma}$ times larger in the radiative case leading to a bigger opening angle. Here, the effect is overcompensated by the reduced temperature (lower thickness) in the radiative case. A different opening angle of the spiral arms will affect the corresponding Lindblad torques acting on the planet.

At the same time, a slight density enhancement is visible "ahead" of the planet ($\varphi > 180°$) at a slightly smaller radius
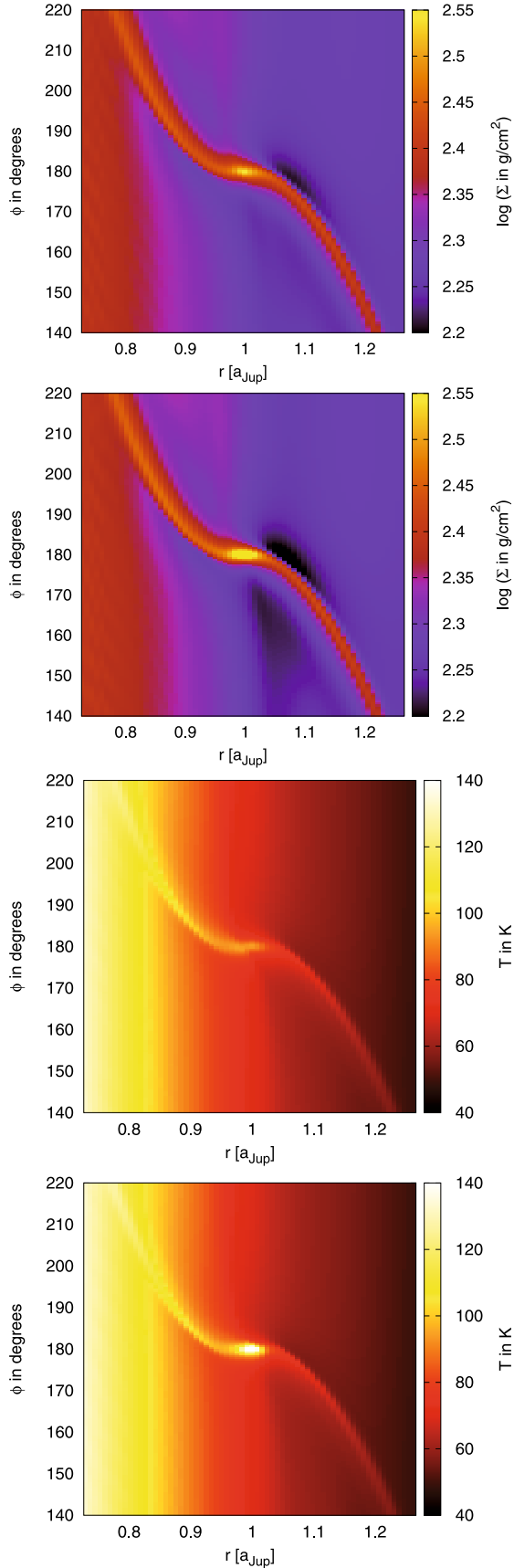
Fig. 12. Surface density (*upper two panels*) and temperature in the equatorial plane (*lower two*) for fully radiative simulations at 100 planetary orbits. Displayed are results for the shallowest and deepest potential. Upper panels refer to the ϵ-potential with $r_{sm} = 0.8$, and lower to the cubic-potential with $r_{sm} = 0.5$, respectively.

($r \lesssim 1$). This feature that is not visible in the isothermal case is caused by including the thermodynamics of the disc. Let us consider an *adiabatic situation* just after the planet has been inserted into the disc, and follow material on its horseshoe orbit (in the co-rotating frame) as it makes a turn from the outer disc ($r > 1, \varphi > 180°$) to the inner ($r < 1$). The radial temperature and density gradient imply for our ideal gas law a gradient in the entropy function S in the disc through

$$S \propto \frac{p}{\rho^\gamma}.$$

As shown above, in our simulations we find for the surface density $\Sigma \propto r^{-1/2}$ as due to the assumption of a constant viscosity, and the midplane temperature follows $T \propto r^{-1.7}$. Due to this gradient in S a parcel (coming from outside) has in our case a lower entropy than the inner disc which it is entering. Now the entropy remains constant on its path, due to the adiabatic assumption. Additionally, dynamical equilibrium requires that the pressure of the parcel does not change significantly upon its turn, and entropy conservation then implies that the density has to increase. At the same time the density "behind" the planet ($\varphi < 180°$ and $r \gtrsim 1$) will be lowered by similar reasoning. Both components produce a positive contribution to this entropy-related corotation torque that acts on the planet, and which adds to the negative Lindblad torque and the positive vortensity-related corotation torque. In truly adiabatic discs this effect will disappear after a few libration times (Baruteau & Masset 2008; Kley & Crida 2008) because the material, being within the horseshoe region, will start interacting with itself, and the density and entropy will be smeared out due to the mixing, leading to the described torque saturation process. Adding radiative diffusion will prevent this and keep the entropy-related torques unsaturated, and a non-zero viscosity is also required.

In this fully radiative case the temperature within the Roche radius of the planet has also increased substantially due to compressional heating of the gas (lower two panels in Fig. 12). In addition, the temperature in the spiral arms is increased as well due to shock heating.

The density and temperature runs in the disc midplane along a radial line at $\varphi = 180°$ cutting through the planet are displayed in Fig. 13. As in the isothermal case, deeper potentials lead to higher densities within the Roche lobe. The increase is somewhat lower because now the temperature is higher as well due to the compression of the material. The higher pressure lowers the density in comparison to the isothermal case. Interesting is that the maximum temperature is substantially higher than in the ambient disc even for this very low mass planet of 20 M_{earth}. Considering accretion onto the planet the increase in temperature might be even stronger due to the expected accretion luminosity.

4.4. Torque analysis for the radiative case

In the upper panel of Fig. 14 we display the time evolution of the total specific torque acting on a 20 M_{earth} planet for the full radiative case. In contrast to the isothermal situation, all four potentials result now in a positive total torque acting on the planet. As in the previous isothermal runs, the torques reach their maximum shortly after the onset of the simulations (between $t \approx 10-20$) and then settle toward their final value. In the corresponding isothermal case with $H/r = 0.037$ the difference between the initial positive unsaturated torque and the final saturated value has been very pronounced (see Fig. 11). In contrast, in this fully radiative case the inclusion of energy diffusion and the subsequent radiative cooling of the disc will prevent saturation of the
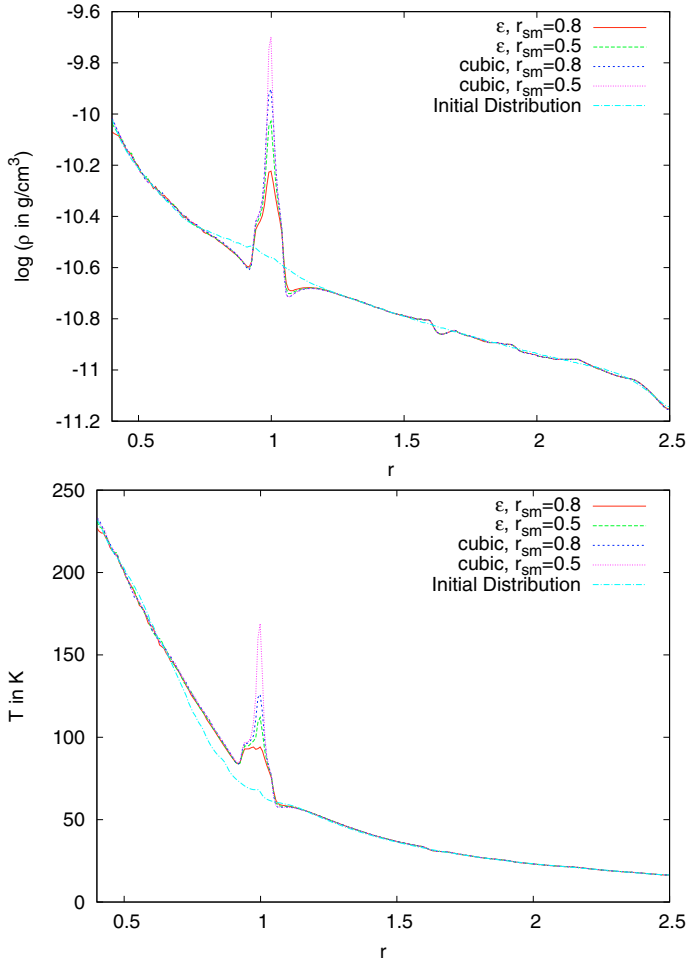
Fig. 13. Radial density (*top*) and temperature (*bottom*) distribution in the equator along a ray through the location of the planet for all 4 planetary potentials used, for the fully radiative case.

Fig. 14. Specific torques acting on a 20 M_{earth} planet for different numerical potentials in the fully radiative case. *Top*: evolution of total torque with time. *Bottom*: radial variation of the specific torque for $t = 80$ orbits.

entropy-related corotation torque, resulting in a positive equilibrium torque. Very similar results have been found previously in the fully radiative regime in 2D simulations (Kley & Crida 2008). It is important to notice, that the two cubic-potentials (which are more realistic in the 3D case) yield very similar results. The more unrealistic ϵ-potentials show rather strong deviations because, due to their extended smoothing of the potential, they tend to weaken in particular the corotation torques which originate in the close vicinity of the planet. In the lower panel of Fig. 14 the radial torque distribution is displayed for the same 4 potentials. In comparison to the corresponding plot for the isothermal $H/r = 0.037$ case (see Fig. 11) we notice that the regular Lindblad part is slightly reduced in the radiative case due to the higher sound speed.

Additionally, clearly seen is the additional positive contribution just inside $r = 1$ which appears to be responsible for the torque reversal. This feature is caused by an asymmetric distribution of the density in the very vicinity of the planet, see also Fig. 17 below. It pulls the planet gravitationally ahead, increasing its angular momentum, leading to a positive torque. Above we argued that this effect may be due to the entropy-related corotation torque of material moving on horseshoe orbits (see also Baruteau & Masset 2008). Due to the symmetry of the problem one might expect a similar feature caused by the material moving from inside out. However, there is no sign of this present in the lower panel of Fig. 14. To analyse this asymmetry, we
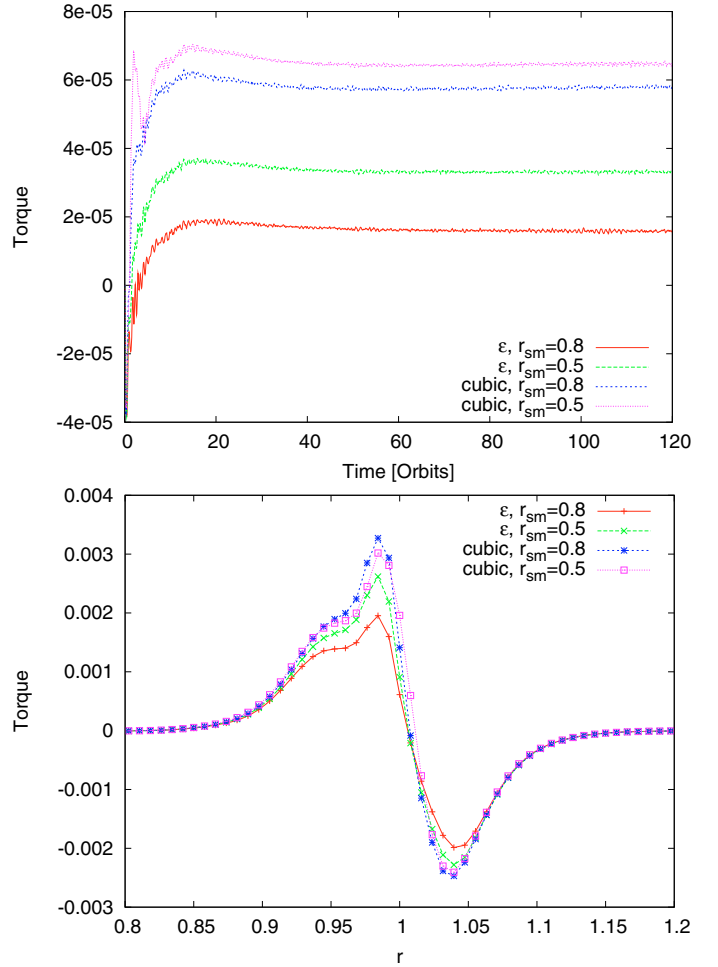
performed additional simulations varying the grid resolution and disc thermodynamics. That the feature is not caused by lack of numerical resolution is demonstrated in Fig. 15, where results obtained with two different grids are displayed. Both models show the same characteristic torque enhancement just inside the planet. In Fig. 16 we compare the radial torque density of the isothermal and a new adiabatic model for $H/r = 0.037$ with the fully radiative model, all for the cubic potential with $r_{sm} = 0.5$ at intermediate resolution. For the adiabatic case we show $\Gamma(r)$ at two different times. The first at $t = 10$ when the torques are unsaturated, and the second at $t = 80$ after saturation has occurred. Please note, that the isothermal and adiabatic models start from the same initial conditions (locally isothermal), while the radiative model starts from the radiative equilibrium without the planet. While the adiabatic model at $t = 10$ shows signs of the enhanced torque just inside the planet, there is no sign of a similar feature at a radius just outside of the planet. Hence, this asymmetry of the entropy-related corotation torque is visible in both the adiabatic and radiative case. Outside of the planet the adiabatic model and the radiative agree very well as H/r is similar, while the isothermal model deviates due to the different sound speed. Whether the location of the maximum in the torque density is identical in the radiative and adiabatic case is hard to say from these simulations because in 3D adiabatic runs the peak appears to be substantially broader with respect to corresponding
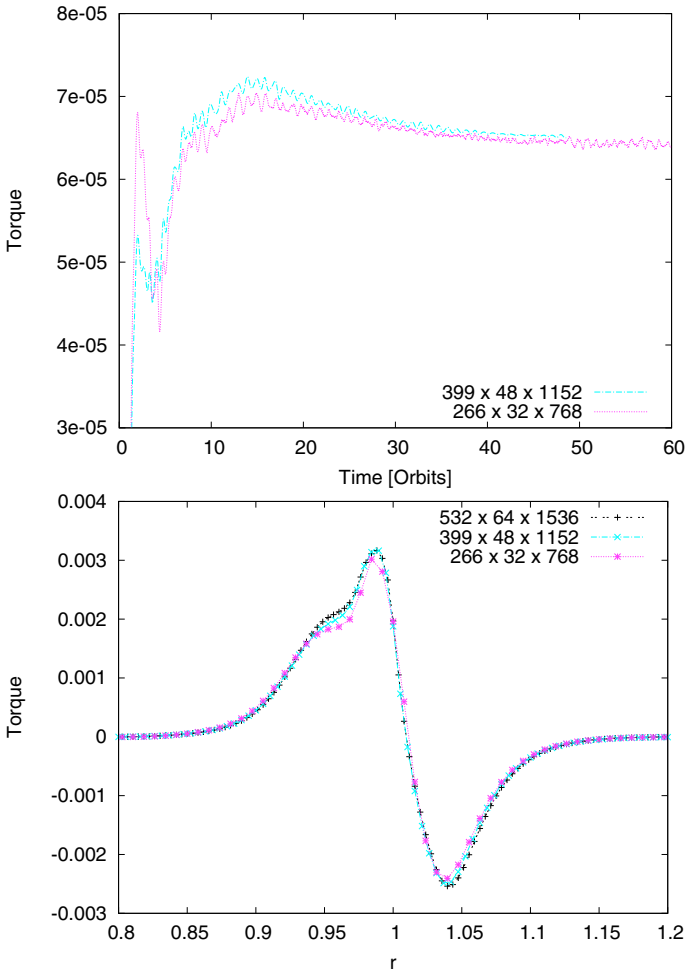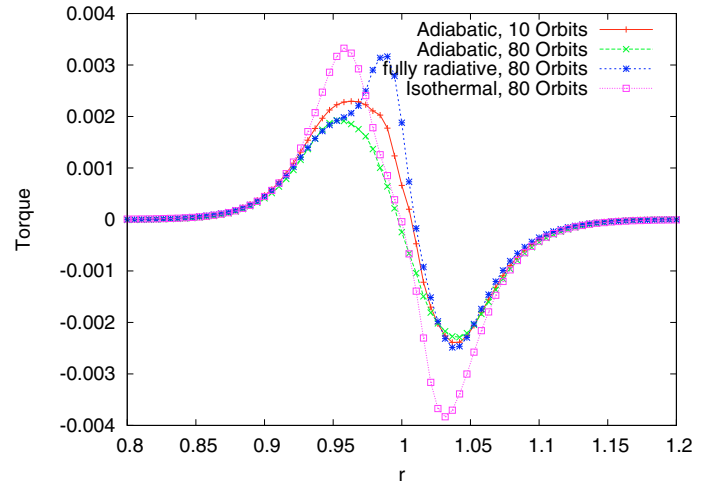
Fig. 16. Radial variation of the specific torque acting on the planet using different thermodynamical disc models. In all cases the cubic potential with $r_{sm} = 0.5$ and standard resolution have been used. The adiabatic model at $t = 10$ corresponds to the time where the corresponding total torque has its maximum. The models at $t = 80$ have all reached their equilibria.

Fig. 15. Specific torque acting on the planet using different grid resolutions for the fully radiative case. In all cases the cubic potential with $r_{sm} = 0.5$ has been used. *Top*: evolution of total torque with time. *Bottom*: radial variation of the specific torque density at $t = 50$ orbits.

2D cases. It has been argued by Baruteau & Masset (2008) that it should occur exactly at the corotation radius, which is shifted (very slightly) from the planet's location due to the pressure gradient in the disc. In our radiative simulations it seems that the maximum is slightly shifted inwards, an effect which may be caused by adding radiative diffusion to the models and consider discs in equilibrium. An issue that certainly needs further investigation.

In Fig. 17 we present additional results of supporting 2D simulations for the fully radiative case, as shown for lower resolution in Kley & Crida (2008). All physical parameter are identical to our 3D fully radiative case. The top panel shows the surface density distribution next to the planet. Seen is the density enhancement just inside and ahead of the planet, and some indication for a lowering outside and behind. Please note, that the planet moves counter-clockwise into the positive ϕ-direction. i.e. upward in Fig. 17. In the lower panel we display for each grid-cell the net torque ($\tilde{\Gamma}^\pm$) acting on the planet. It is constructed by adding each cell's individual contribution to the torque and that of the symmetric cell with respect to the planet location, i.e.

$$\tilde{\Gamma}^\pm_{i,j} = \pm \left[\Gamma(r_i, \phi_{planet} + \phi_j) + \Gamma(r_i, \phi_{planet} - \phi_j) \right]. \quad (20)$$

Hence, in absolute values the bottom half of the plot (with $\phi < \phi_{planet}$) resembles exactly the top half ($\phi > \phi_{planet}$). The

colours are chosen such that blue refers to negative $\tilde{\Gamma}^\pm_{i,j}$ and yellow/red to positive values. The signs of $\tilde{\Gamma}^\pm_{i,j}$ are chosen such that the top left and lower right quadrant have the correct sign (+) and the other two are just reversed. Due to this redundancy in the plot, only the upper left and lower right quadrant should be taken into account to estimate global effects. The mirroring process at the $\phi = \pi$-line (with the mirroring of the colour scale) allows an easy evaluation and comparison of the individual contributions. One can notice that the net torque will be positive due to excess material just ahead and inside of the planet. From the plot it is also clear that there exists indeed an asymmetry of the torques induced by horseshoe material coming from outside-in versus material turning inside-out. In the figure, there is only a weak indication of a marginal positive contribution just below the planet. In additional simulations for purely adiabatic discs with different (positive and negative) entropy gradients which have either constant density or temperature it has become apparent that the asymmetry is caused by the entropy gradient. In the case of a negative entropy gradient (as in our fully radiative model) the positive excess torque comes from inside/ahead the planet, while for a positive gradient the negative excess torque comes from outside/behind the planet. Whether the maximum of $\Gamma(r)$ lies at corotation (Baruteau & Masset 2008) or is slightly shifted when radiative effects are considered may deserve further studies.

In Fig. 18 we show the perturbed entropy and density in the 2D fully radiative model in equilibrium, for a larger domain. Caused by the flow in the horseshoe region, there is an entropy minimum for larger ϕ inside of the planet, and a maximum for lower ϕ outside, for $r + r_p$. Both lie inside the horseshoe region and close to the separatrix. The overall entropy distribution is very similar to that found by Baruteau & Masset (2008) for adiabatic discs shortly after the insertion of the planet. Due to the included radiative diffusion this effect does not saturate in our case, and we clearly support their findings even for the long term evolution. The disturbed entropy shows in fact a slight asymmetry (in amplitude) with respect to the planet, that reflects back on to to the density distribution (bottom panel).
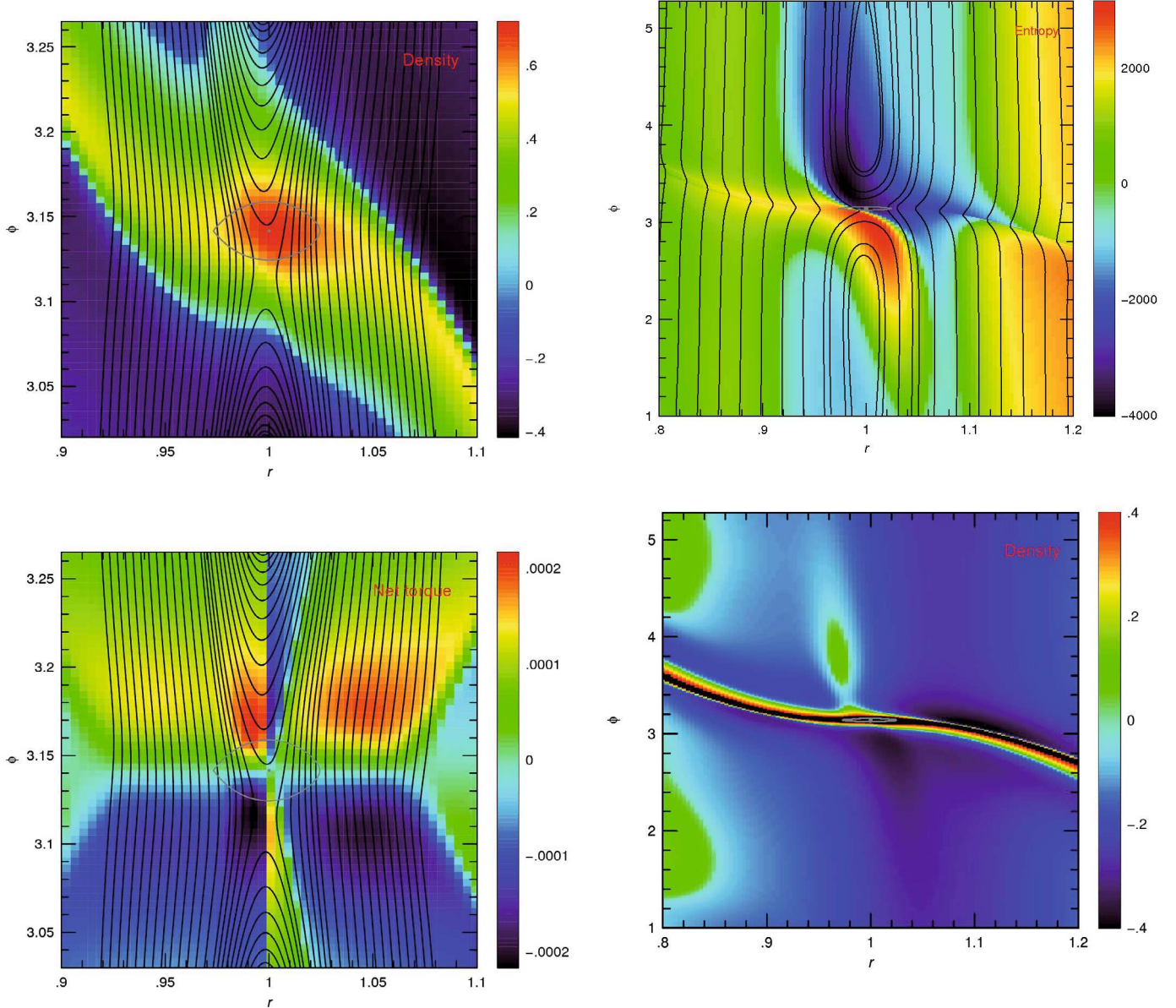
Fig. 17. Results of a 2D fully radiative model using a resolution of 512×1536 gridcells. The gray dot indicates the location of the planet, and the curve its Roche lobe. The solid black lines show the streamlines. *Top*: perturbed surface density with respect to the case without an embedded planet. The values are scaled as $\Sigma^{1/2}$. *Bottom*: the net torque acting on the planet caused by the mass in each individual gridcell using the prescribed smoothed torque cutoff function with $b = 0.8$, see explanation in text. The values are scaled as $(\tilde{\Gamma}^{\pm})^{1/2}$.

4.5. Planets with different planetary masses

Following the results obtained in the previous sections we adopt now the cubic $r_{\text{sm}} = 0.5$ planetary potential assuming that it is closest to reality, and study the effects of planets with various masses in fully radiative discs. Starting from the 2D radiative equilibrium state (see Sect. 4.1) we now place planets with masses ranging from 5 up to 100 M_{earth} in the initially axisymmetric 3D disc. The numerical parameters for these simulations are identical to those discussed above.

In recent 2D simulations of radiative discs with embedded low mass planets the torque acting on the planet depends on the

Fig. 18. Perturbed entropy (*top*) and perturbed density (*bottom*) for the 2D fully radiative equilibrium model using a resolution of 512×1536 gridcells. The values are scaled as $\Sigma^{1/2}$ and $S^{1/2}$, respectively.

planetary mass in such a way that for planets with a size lower than about 40 earth masses the total torque is positive implying outward migration (Kley & Crida 2008). For large masses the forming gap reduces the contribution of the corotation torques, and the results of the radiative simulations approach those of the fixed temperature (locally isothermal) runs. Our 3D simulations show indeed very similar results for planets in this mass regime, see Fig. 19. Planets in the isothermal regime migrate inward with a torque proportional to the planet mass squared, as predicted for low mass planets undergoing Type-I-Migration. Note, that we use in these models the temperature distribution for a fixed $H/r = 0.037$. The values for the three lowest mass planets (with 5, 10, 15 M_{earth}) are not as accurate due to the insufficient grid resolution, remember the "kink" in Fig. 11 which refers to 20 M_{earth} at standard resolution. For the fully radiative disc the planets up to about 33 M_{earth} experience a positive torque, while
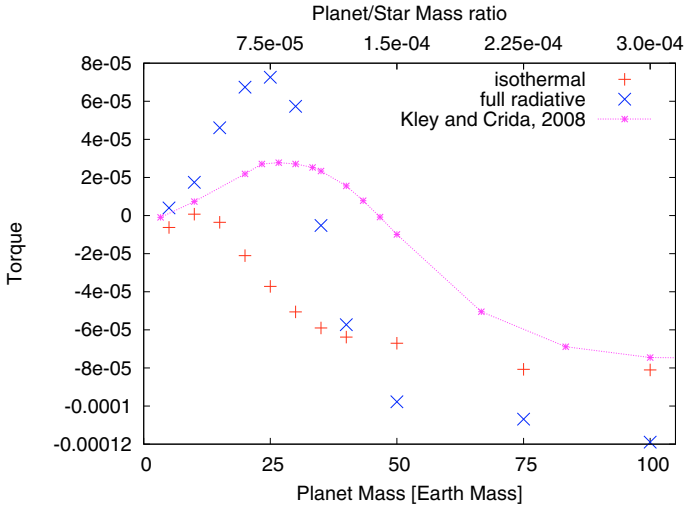
Fig. 19. Specific torques acting on planets of different masses in the fully radiative (blue crosses) and isothermal (red plus signs) regime. Note, that the isothermal models are run for a fixed $H/r = 0.037$. All torque values are displayed at a time when the equilibrium has been reached.
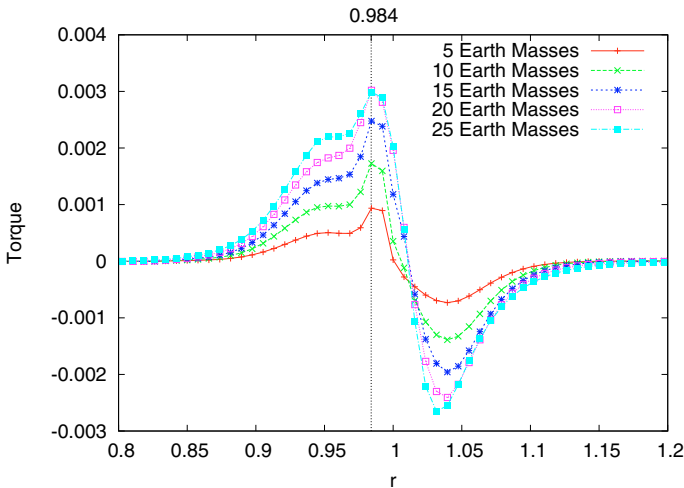

Fig. 20. Radial torque distribution in equilibrium for various planet masses. The vertical dotted line indicates the location of the maximum.

larger mass planets migrate inward, due to the negative torque acting on them.

When comparing the 3D torques to the corresponding 2D values as obtained by Kley & Crida (2008) for the same disc mass and opacity law, we note two differences: i) the absolute magnitudes of the torques in the radiative case are enhanced in the 3D simulations with respect to the corresponding 2D results, resulting in even faster outward migration of the planets. This result can be explained by the reduced temperature (i.e. vertical thickness) of the 3D disc with respect to the 2D counterpart (cf. Fig. 3), as a reduction in H typically increases the torques (Tanaka et al. 2002); ii) the turnover mass from positive to negative torques is reduced in the 3D simulations. This effect is caused again by the reduced disc thickness, as now the onset of gap formation ($R_H \approx H$) occurs for lower planetary masses. The different form of the potential and the softening length may also play a role in explaining some of the differences observed between the 3D and 2D results.

Finally, in Fig. 20 we show that the position of the maximum of the radial torque density is independent of the planet mass, and is therefore a result of the underlying disc physics.

5. Summary

We have investigated the migration of planets in discs using fully three-dimensional numerical simulations including radiative transport using the code NIRVANA. For this purpose we have presented and described our implementation of implicit radiative transport in the flux-limited diffusion approximation, and secondly our new FARGO-implementation in full 3D.

Before embedding the planets we studied the evolution of axisymmetric, radiative accretion discs in 2D. Starting with an isothermal disc model having a fixed $H/r = 0.05$, we find that for our physical disc parameter the inclusion of radiative transport yields discs that are thinner ($H/r = 0.037$ at $r = 1$). We note that in the isothermal case the disc thickness is a chosen input parameter, while in the fully radiative situation it depends on the local surface density and the chosen viscosity and opacity. Interesting is here the direct comparison to the equivalent 2D models using the same viscosity, opacity and disc mass (Kley & Crida 2008), as displayed in Fig. 3. Here, our new 3D disc yields lower temperatures (by a factor of 0.6–0.7) than the 2D runs. Since the 2D simulations have to work with vertically averaged quantities, it will be interesting whether it might be possible to adjust those as to yield results in better agreement to our 3D results.

Concerning planetary migration we have confirmed the occurrence of outward migration for planetary cores in radiative discs. As noticed in previous research, the effect is driven by a radial entropy gradient across the horseshoe region in the disc, that is maintained by radiative diffusion. Our results show that planets below the turnover mass of about $m \approx 33\ M_{earth}$ migrate outward while larger masses drift inward. The reduced temperature in the 3D versus 2D runs has direct influence on the magnitude of the resulting torques acting on the planet. As the disc is thinner in 3D the resulting torques, corotation as well as Lindblad, are also stronger. The turnover mass from outward to inward migration is slightly reduced as well for the 3D disc since the smaller vertical thickness allows for gap opening at lower planet masses. Due to the reduced temperature in the 3D case, the spiral waves have a slightly smaller opening angle compared to the isothermal case.

Another interesting, partly numerical, issue that we have addressed concerns the influence that the smoothing of the planetary potential has on the density structure in the vicinity of the planet and the speed of migration. We have compared the standard ϵ-potentials in contrast with so-called cubic-potentials. The results indicate, that a deeper (cubic) potential results in a higher density inside the planet's Roche lobe for isothermal, as well as radiative discs. Since the potential depth influences the density in the immediate vicinity of the planet the resulting torques show some dependence on the chosen smoothing length. We note that for the more realistic cubic-potential, changing the smoothing from 0.8 to 0.5 does not alter the results for the fully radiative simulations considerably, and runs at different numerical resolutions have indicated numerical convergence. Hence, we believe that this value is suitable for performing planet disc simulations in 3D. The usage of an ϵ-potential cannot be recommended in 3D. Outside of the planet's Roche lobe one can hardly notice a difference in the density structure. Since the cubic-potential agrees with the true planetary potential outside of the smoothing-length r_{sm}, it is of course desirable to choose this transition

radius as small as possible, but the achievable numerical resolution always will set a lower limit. We found $r_{sm} = 0.5$ a suitable value for our grid resolution and used that in our parameter studies for different planet masses. We note, that independent of the chosen form of the potential the outward migration of planetary cores seems to be a robust result for radiative discs. As the magnitude (and direction) of the effect depends on the viscosity and opacity, further studies, investigating different radial locations in the disc, will be very interesting.

The outward migration of planet embryos with several earth masses certainly represents a solution to the too rapid inward migration found in this mass regime of classical type-I migration. Growing planets can spend more time in the outer disc regions and move then later via type-II migration towards the star. On the other hand it may be difficult to reconcile this finding with the presence of the discovered Neptune-mass planets that reside closer to the central star ($a \approx 0.1$ AU), but still too far away to be ablated by stellar irradiation.

As seen in our simulations, parts of the disc can display convection due to the form of the opacity law used. It will be certainly interesting in the future to analyse what influence the convective motions have on the migration properties of the embedded protoplanets. Additionally, fully radiative 3D-MHD simulations are definitely required to judge the efficiency of this process in turbulent discs.

Appendix A: Fargo algorithm

Multi-dimensional simulations of accretion discs that include the φ-direction typically suffer from severe timestep limitations. This is due to the fact that the azimuthal velocity u_φ is Keplerian and falls off with radius. Hence, the innermost rings determine the maximum timestep allowed even though the region of interest lies much further out. One suggestion to resolve this issue is given by the FARGO algorithm which stands for "Fast Advection in Rotating Gaseous Objects" (Masset 2000a). It has originally been developed for 2D disc simulations in a cylindrical coordinate system, for details of the implementation see Masset (2000a,b). Here, we briefly describe our extension to three spatial dimensions in spherical polar coordinates.

The basic method relies on a directional splitting of the advection part, where first the radial and meridional (in θ direction) advection are performed in the standard way. To calculate the azimuthal part we follow Masset (2000a) and split the angular velocity into three parts: From the angular velocity of each grid cell $\omega_{i,j,k} = (u_\varphi)_{i,j,k}/r_i$ first an average angular velocity $\bar{\omega}_i$ is calculated for each radial ring i, which is obtained here by averaging over the azimuthal (index k) and vertical (index j) direction

$$\bar{\omega}_i = \frac{1}{N_\varphi N_\theta} \sum_{j,k} \omega_{i,j,k} \tag{A.1}$$

where the summation runs of all azimuthal and meridional gridcells, and N_φ, N_θ denote the number of these gridcells, respectively. We note, that the summation over the vertical direction

with index j is not required at this point. In our case, for a thin disc where the angular velocity does not vary much with height, the vertical averaging simplifies matters somewhat. From this, one calculates an integer-valued shift quantity

$$n_i = \mathtt{Nint}\,(\bar{\omega}_i \Delta t/\Delta\varphi)\,, \tag{A.2}$$

where Nint denotes the nearest integer function. This corresponds to a transport by the angular "shift velocity"

$$\omega_i^{\mathrm{SH}} = n_i \frac{\Delta\varphi}{\Delta t}\,. \tag{A.3}$$

Then we calculate the constant residual velocity of each ring

$$\omega_i^{\mathrm{cr}} = \bar{\omega}_i - \omega_i^{\mathrm{SH}}, \tag{A.4}$$

and finally the residual velocity for each individual gridcell

$$\omega_{i,j,k}^{\mathrm{res}} = \omega_{i,j,k} - \bar{\omega}_i. \tag{A.5}$$

Rewritten, we find for the angular velocity the following expression

$$\omega_{i,j,k} = \omega_{i,j,k}^{\mathrm{res}} + \omega_i^{\mathrm{cr}} + \omega_i^{\mathrm{SH}}. \tag{A.6}$$

The advection algorithm in the φ-direction proceeds now in three steps. In the first two steps all quantities are advected using the standard advection routine with the transport velocities ω_i^{cr} and $\omega_{i,j,k}^{\mathrm{res}}$ and then all quantities are shifted by the integer values n_i in each ring i which corresponds to a transport velocity ω_i^{SH}. Using this splitting, the transport velocities in the advection part are given by the two residual velocities ω_i^{cr} and $\omega_{i,j,k}^{\mathrm{res}}$, which are typically much lower than $\omega_{i,j,k}$. Hence, the time step limitation for the azimuthal direction is determined by the local variation from the mean azimuthal flow in the disc which is typically much lower than the Keplerian value. In our case of a 3D disc the time step criterion is first given by the normal CFL-criterion as presented for example in Stone & Norman (1992) where the angular velocity $\omega_{i,j,k}$ is just replaced by the residual cell values $\omega_{i,j,k}^{\mathrm{res}}$ and ω_i^{cr}. This change provides the major reduction in the transport velocity and a substantial increase in the time step size. An additional time step limitation is given by the requirement that the shift should not disconnect two neighbouring grid cells in the radial and in the meridional direction (Masset 2000a). Here, this additional limit on the time step reads

$$\Delta t_{\mathrm{shear}} = 0.5 \min_{i,j,k} \left\{ \frac{\Delta\varphi}{|\omega_{i,j,k} - \omega_{i-1,j,k}|}, \frac{\Delta\varphi}{|\omega_{i,j,k} - \omega_{i,j-1,k}|} \right\}. \tag{A.7}$$

The second restriction is only necessary in the case, where the above vertical averaging in Eq. (A.1) has not been performed. The sequencing of the advection sweeps in the FARGO algorithm has to be such that the azimuthal sweep comes at the end, hence in our simulations we use always: radial, meridional, and finally azimuthal.

In a staggered mesh code such as our NIRVANA code, that is essentially based on the ZEUS method, an additional complication arises in the straightforward application of the FARGO method, due to the fact that the velocity variables are located at the cell interfaces and not at the centres. Hence, the corresponding "momentum cells" for the radial and meridional momenta (ρu_r and $\rho r u_\theta$) are shifted with respect to the standard density cells by half a gridcell in the radial or meridional direction, respectively. To apply the FARGO method one has first to split all the momentum cells in two halves, use the algorithm outlined

above on each of the halves, and then combine them afterwards to calculate from the updated momenta the new velocities on the interfaces. This leads of course to an overhead in the simulation cost which is counterbalanced however by the much larger time step.

Appendix B: Radiative transport

Here, we outline briefly the method to solve the flux-limited diffusion equation in 3D. Radiative transport is treated as a sub-step of the integration procedure. In equilibrium viscous heating is balancing radiative diffusion and to ensure this also numerically we incorporate the dissipation into this sub-step. Using the appropriate parts of the energy Eq. (7) and the flux (8) we obtain a diffusion equation for the gas temperature.

$$\frac{\partial T}{\partial t} = \frac{1}{c_v \rho} \left[\nabla \cdot D \nabla T + Q^+ \right] \tag{B.1}$$

where the diffusion coefficient is given by

$$D = \frac{\lambda c 4 a_R T^3}{\rho(\kappa + \sigma)}, \tag{B.2}$$

and Q^+ denotes the viscous dissipation that is added to the system. The flux-limiter λ depends on the local physical state of the gas and approaches $\lambda = 1/3$ in the optically thick parts and reduces the flux to $F = c a_R T^4$ in the optically thin parts. Here we use an expression for λ as given in Kley (1989).

A straight forward finite difference form of Eq. (B.1) in Cartesian Coordinates is given by

$$\frac{T_{i,j,k}^{n+1} - T_{i,j,k}^n}{\Delta t} = \frac{1}{(cv\rho)_{i,j,k}} \tag{B.3}$$

$$\times \left[\frac{1}{\Delta x} \left(\bar{D}_{i+1,j,k}^x \frac{T_{i+1,j,k} - T_{i,j,k}}{\Delta x} - \bar{D}_{i,j,k}^x \frac{T_{i,j,k} - T_{i-1,j,k}}{\Delta x} \right) \right.$$

$$+ \frac{1}{\Delta y} \left(\bar{D}_{i,j+1,k}^y \frac{T_{i,j+1,k} - T_{i,j,k}}{\Delta y} - \bar{D}_{i,j,k}^y \frac{T_{i,j,k} - T_{i,j-1,k}}{\Delta y} \right)$$

$$\left. + \frac{1}{\Delta z} \left(\bar{D}_{i,j,k+1}^z \frac{T_{i,j,k+1} - T_{i,j,k}}{\Delta z} - \bar{D}_{i,j,k}^z \frac{T_{i,j,k} - T_{i,j,k-1}}{\Delta z} \right) \right].$$

In orthogonal curvilinear coordinates additional geometry terms have to be added in the above equation. Here $\bar{D}_{i,j,k}^x$ denotes

$$\bar{D}_{i,j,k}^x = \frac{1}{2} \left(D_{i,j,k} + D_{i-1,j,k} \right) \tag{B.4}$$

and so forth.

The grid structure from which Eq. (B.3) follows is outlined in the two-dimensional case in Fig. B.1. One has to keep in mind that the temperature (being a scalar) is defined in the cell centre, while the values of $\bar{D}_{i,j,k}^x$ are defined at the cell interfaces.

In Eq. (B.3) no time levels are specified on the right hand side. For explicit differencing the time level should be t^n such that the new temperature on the left T^{n+1} is entirely given by the old values T^n at time t^n. This might lead to very small timesteps since the timestep limitation is approximately given by

$$\Delta t \leq \min_{i,j,k} \left(\frac{\Delta x^2, \Delta y^2, \Delta z^2}{\tilde{D}_{i,j,k}} \right) \tag{B.5}$$
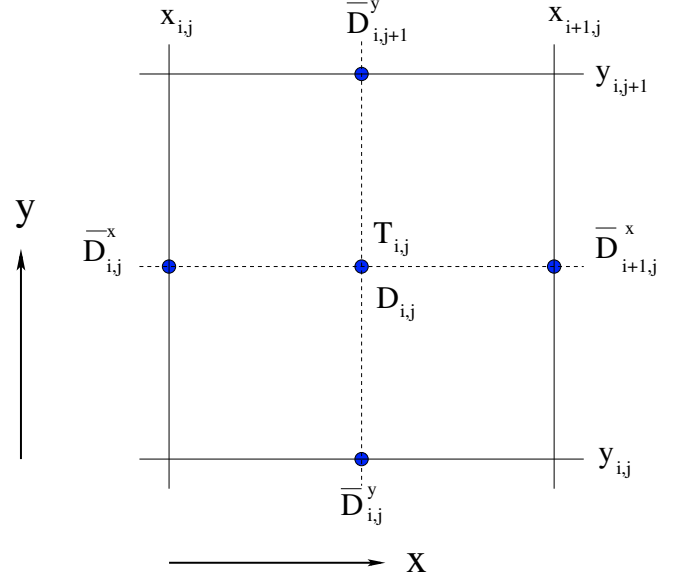
where $\tilde{D}$ is given by $D/(\rho c_v)$.

Fig. B.1. The grid structure used in a staggered grid code for a two-dimensional example. Shown is the cell i, j where the coordinates of the cell centre $[x_i^c, y_j^c]$ is given by $[1/2(x_{i,j} + x_{i+1,j}), 1/2(y_{i,j} + y_{i,j+1})]$. The temperature $T_{i,j}$ is located at the cell centre where also the diffusion coefficient D is defined. The averaged diffusion coefficients $\bar{D}$ are defined at the cell interfaces.

Hence, often an *implicit* version of the equation has to be used, where all the temperature values $T_{i,j,k}$ on the r.h.s. are evaluated at the new time t^{n+1} or an arithmetic mean between new and old times. Even though the diffusion coefficients may depend on temperature, we always evaluate those at the old time t^n. Otherwise this would lead to a non-linear matrix equation.

Collection all the terms in Eq. (B.3) this leads to a linear system of equations with the form

$$A_{i,j,k}^x T_{i-1,j,k} + C_{i,j,k}^x T_{i+1,j,k} + A_{i,j,k}^y T_{i,j-1,k} + C_{i,j,k}^y T_{i,j+1,k}$$

$$A_{i,j,k}^z T_{i,j,k-1} + C_{i,j,k}^z T_{i,j,k+1} + B_{i,j,k} T_{i,j,k} = R_{i,j,k} \tag{B.6}$$

where the superscript $n+1$ has been omitted on the left hand side. The coefficients $A_{i,j,k}^x$ to $C_{i,j,k}^z$ can be obtained straightforwardly from Eq. (B.3). The right hand side is given by

$$R_{i,j,k} = T_{i,j,k}^n + \frac{1}{(c_v \rho)_{i,j,k}} Q_{i,j,k}^+.$$

Written in matrix notation Eq. (B.6) reads

$$M T^{n+1} = R. \tag{B.7}$$

Obviously the matrix M is a sparse matrix with a banded structure. Usually M is diagonally dominant but in situations with extended optically thin regions this property will be lost.

Equation (B.7) can in principle be solved by any linear equation package. For simplicity and testing purposes we work presently with a standard SOR solver. Using an optimised relaxation parameter $\tilde{\omega}$ we need about 130 iterations per timestep in the initial phase which is far from equilibrium and only 80 iterations at later times near equilibrium.

The radiation module of the code has been tested extensively in different coordinate systems in Bitsch (2008), and we have compared our new results on radiative viscous discs obtained with the 3D version of NIRVANA in detail with those of the existing 2D code RH2D.

References

Alibert, Y., Mordasini, C., & Benz, W. 2004, A&A, 417, L25
Balbus, S. A., & Hawley, J. F. 1998, Rev. Mod. Phys., 70, 1
Baruteau, C., & Masset, F. 2008, ApJ, 672, 1054
Bitsch, B. 2008, Diploma Thesis, University of Tübingen
Cresswell, P., Dirksen, G., Kley, W., & Nelson, R. P. 2007, A&A, 473, 329
Crida, A., Sándor, Z., & Kley, W. 2008, A&A, 483, 325
D'Angelo, G., Henning, T., & Kley, W. 2002, A&A, 385, 647
D'Angelo, G., Kley, W., & Henning, T. 2003, ApJ, 586, 540
Ida, S., & Lin, D. N. C. 2008, ApJ, 673, 487
Klahr, H., & Kley, W. 2006, A&A, 445, 747
Kley, W. 1989, A&A, 208, 98
Kley, W. 1998, A&A, 338, L37
Kley, W., & Crida, A. 2008, A&A, 487, L9
Kley, W., & Lin, D. N. C. 1996, ApJ, 461, 933
Kley, W., & Lin, D. N. C. 1999, ApJ, 518, 833
Kley, W., Papaloizou, J. C. B., & Lin, D. N. C. 1993, ApJ, 416, 679
Kley, W., D'Angelo, G., & Henning, T. 2001, ApJ, 547, 457
Levermore, C. D., & Pomraning, G. C. 1981, ApJ, 248, 321
Li, H., Lubow, S. H., Li, S., & Lin, D. N. C. 2009, ApJ, 690, L52
Lin, D. N. C., & Papaloizou, J. C. B. 1985, in Protostars and Planets II, 981
Masset, F. 2000a, A&AS, 141, 165
Masset, F. S. 2000b, in Disks, Planetesimals, and Planets, ed. G. Garzón, C. Eiroa, D. de Winter, & T. J. Mahoney, ASP Conf. Ser., 219, 75
Masset, F. S. 2001, ApJ, 558, 453
Masset, F. S. 2002, A&A, 387, 605
Masset, F. S. 2008, in EAS Publications Series, ed. M.-J. Goupil, & J.-P. Zahn, 29, 165
Masset, F. S., D'Angelo, G., & Kley, W. 2006, ApJ, 652, 730
Mihalas, D., & Weibel Mihalas, B. 1984, Foundations of radiation hydrodynamics (New York: Oxford University Press)
Ogilvie, G. I., & Lubow, S. H. 2003, ApJ, 587, 398
Paardekooper, S.-J., & Mellema, G. 2006, A&A, 459, L17
Paardekooper, S.-J., & Mellema, G. 2008, A&A, 478, 245
Paardekooper, S.-J., & Papaloizou, J. 2009, MNRAS, 394, 2283
Paardekooper, S.-J., & Papaloizou, J. C. B. 2008, A&A, 485, 877
Papaloizou, J. C. B., Nelson, R. P., Kley, W., Masset, F. S., & Artymowicz, P. 2007, in Protostars and Planets V, ed. B. Reipurth, D. Jewitt, & K. Keil, 655
Stone, J. M., & Norman, M. L. 1992, ApJS, 80, 753
Tanaka, H., Takeuchi, T., & Ward, W. R. 2002, ApJ, 565, 1257
Tassoul, J. 1978, Theory of rotating stars, Princeton Series in Astrophysics (Princeton: University Press)
Ward, W. R. 1997, Icarus, 126, 261
Ziegler, U., & Yorke, H. 1997a, Computer Physics Commun., 101, 54
Ziegler, U., & Yorke, H. W. 1997b, Computer Physics Commun., 101, 54

Astronomy & Astrophysics

Orbital evolution of eccentric planets in radiative discs

B. Bitsch and W. Kley

Institut für Astronomie & Astrophysik, Universität Tübingen, Auf der Morgenstelle 10, 72076 Tübingen, Germany
e-mail: bertram.bitsch@uni-tuebingen.de

ABSTRACT

Context. With an average eccentricity of about 0.29, the eccentricity distribution of extrasolar planets is markedly different from the solar system. Among other scenarios considered, it has been proposed that eccentricity may grow through planet-disc interaction. Recently, it has been noticed that the thermodynamical state of the disc can significantly influence the migration properties of growing protoplanets. However, the evolution of planetary eccentricity in radiative discs has not been considered yet.
Aims. In this paper we study the evolution of planets on eccentric orbits that are embedded in a three-dimensional viscous disc and analyse the disc's effect on the orbital evolution of the planet.
Methods. We use the three-dimensional hydrodynamical code NIRVANA that includes full tensor viscosity and implicit radiation transport in the flux-limited diffusion approximation. The code uses the FARGO-algorithm to speed up the simulations. First we measure the torque and power exerted on the planet by the disc for fixed orbits, and then we let the planet start with initial eccentricity and evolve it in the disc.
Results. For locally isothermal discs we confirm previous results and find eccentricity damping and inward migration for planetary cores. For low eccentricity ($e \lesssim 2H/r$) the damping is exponential, while for higher e it follows $\dot{e} \propto e^{-2}$. In the case of radiative discs, the planets experience an inward migration as long as its eccentricity lies above a certain threshold. After the damping of eccentricity cores with masses below 33 $M_{\rm Earth}$ begin to migrate outward in radiative discs, while higher mass cores always migrate inward. For all planetary masses studied (up to 200 $M_{\rm Earth}$) we find eccentricity damping.
Conclusions. In viscous discs the orbital eccentricity of embedded planets is damped during the evolution independent of the mass. Hence, planet-disc interaction does not seem to be a viable mechanism to explain the observed high eccentricity of exoplanets.

Key words. accretion, accretion disks – planets and satellites: formation – hydrodynamics – radiative transfer – planet disk interactions

1. Introduction

One of the surprising orbital characteristics of extrasolar planets is their high mean eccentricity ≈0.29 (Udry & Santos 2007). Several explanations have been put forward to explain this discrepancy in comparison to the solar system. Planet-disc interactions are typically invoked to explain the planetary migration towards the central star that has occurred during the early formation phase. In addition to the change in semi-major axis, it is to be expected that the planet's eccentricity will be influenced through this process as well (Goldreich & Tremaine 1980). It has then been suggested, by performing linear analysis, that the planetary eccentricity can be increased through the planet-disc interaction under some conditions (Goldreich & Sari 2003; Sari & Goldreich 2004; Moorhead & Adams 2008). They estimate that eccentric Lindblad resonances can cause eccentricity growth for gap-forming planets. Recently, a Kozai-type effect between the disc and an inclined planet has been considered (Terquem & Ajmia 2010). Numerical simulations, however, tend to show predominantly eccentricity damping for a variety of masses (Cresswell et al. 2007; Moorhead & Ford 2009). Additionally, the existence of resonant planetary systems with relatively low eccentricities (such as the system GJ 876) seems to indicate a damping action of the disc on planetary eccentricity rather than an enhancement (Lee & Peale 2002; Kley et al. 2005; Crida et al. 2008).

On the other hand, very high-mass planets can induce an eccentric instability in the disc (Kley & Dirksen 2006). In turn, the eccentric disc can possibly increase the planetary eccentricity (Papaloizou et al. 2001; D'Angelo et al. 2006). However,

this process can only explain the eccentricity of very massive (≈5−10 $M_{\rm Jup}$) planets. Alternatively, planet-planet scattering seems to be a viable mechanism for increasing eccentricities through mutual gravitational interactions between the planets. The resulting eccentricity distribution matches the observed one reasonably well (Adams & Laughlin 2003; Jurić & Tremaine 2008; Ford & Rasio 2008). Another option is the fly-by of a nearby star (Malmberg & Davies 2009).

Planet-disc interactions have so far been studied mostly in the locally isothermal approach, where the temperature only depends on the distance from the central star. In this case for typical disc parameters, a negative torque is acting on the planet, and it migrates inward (Tanaka et al. 2002). However, recently it has been shown that the torque acting on an embedded planet depends on the thermodynamics of the disc. Following the pioneering work of Paardekooper & Mellema (2006), various groups have now analysed the effect of the equation of state on the migration properties (Baruteau & Masset 2008; Paardekooper & Papaloizou 2008; Paardekooper & Mellema 2008; Kley & Crida 2008). Through full 3D radiative simulations of embedded planets, we have recently confirmed that including of radiation transport can produce a positive torque acting on low-mass planets embedded in protoplanetary discs (Kley et al. 2009), because through its action the required radial entropy gradient can be maintained in the disc. This results in slowing down the inward migration, and under some conditions it may indeed be possible to reverse the inward migration process.

The linear estimates of the eccentricity evolution of embedded planets (Artymowicz 1993; Ward & Hahn 1994; Tanaka & Ward 2004) concentrate on low eccentricities and predict

exponential decay on short timescales $\tau_{ecc} \approx (H/r)^2 \tau_{mig}$, where H/r is the aspect ratio of the disc and τ_{mig} and τ_{ecc} the migration and eccentricity damping timescale, respectively. Papaloizou & Larwood (2000) have also considered larger values for e and they find an extended eccentricity damping timescale such that $de/dt \propto e^{-2}$ if $e > 1.1 H/r$. Cresswell & Nelson (2006) have performed hydrodynamical simulations of embedded small mass planets and find good agreement with the work by Papaloizou & Larwood (2000). These 2D results have been confirmed by Cresswell et al. (2007) using fully 3D isothermal simulations.

As mentioned above, the thermodynamics of protoplanetary discs is a crucial parameter for the torque acting on the planet (Paardekooper & Mellema 2006). Including radiation transport/cooling in a disc will give rise to positive torques acting on a planet embedded in such a disc, which indicates outward migration. In our previous work (Kley et al. 2009) we have shown that the inclusion of radiation transport/cooling in simulations with embedded low mass planets in three-dimensions (3D) can result in outward migration. So far these simulations have been limited to planets on fixed circular orbits. Now we extend this work and focus on the evolution of planets on eccentric orbits for both, the isothermal and fully radiative regime. We focus first on low-mass planets and study the influence of the thermodynamics of the disc on eccentricity damping as well as on the evolution of the planet inside the disc. First we estimate the theoretical migration and eccentricity damping rate for planets on fixed eccentric orbits. Secondly, we let the planets evolve in the disc and finally we investigate the influence of the planet mass on the change in eccentricity and semi-major axis.

2. Physical modelling

The protoplanetary disc is modelled as a three-dimensional (3D), non-self-gravitating gas whose motion is described by the Navier-Stokes equations. We treat the disc as a viscous medium, where the dissipative effects can then be described via the standard viscous stress-tensor approach (e.g. Mihalas & Weibel Mihalas 1984). We also assume that the heating of the disc occurs solely through internal viscous dissipation and ignore the influence of additional energy sources (e.g. irradiation form the central star). This internally produced energy is then radiatively diffused through the disc and eventually emitted from its surface. For this process we use the flux-limited diffusion approximation (FLD, Levermore & Pomraning 1981), which allows us to treat the transition form optically thick to thin regions approximately. The viscous forces used in our code are stated explicitly for the three-dimensional case in spherical coordinates in Tassoul (1978). We use a constant kinematic viscosity coefficient ν with a dimensionless value of $\nu = 10^{-5}$ (in code units, see below). This relates to the typically used α-parameter through $\nu = \alpha c_s H$, where c_s is the sound speed and H the vertical thickness of the disc. A more detailed prescription of the modelling and the numerical methodology is described in our previous paper (Kley et al. 2009). We now extend the simulations, compared to our previous paper, by including planets on eccentric orbits with different masses.

2.1. General setup

An important issue in modelling planetary dynamics in discs is the gravitational potential of the planet since this has to be artificially smoothed to avoid singularities. We have shown in (Kley et al. 2009) that the physics of embedded planets can be described better by a cubic-potential rather than the often used

ϵ-potential. Hence, we use in this work the following form for the planetary potential throughout

$$\Phi_p^{cub} = \begin{cases} -\frac{m_p G}{d} \left[\left(\frac{d}{r_{sm}}\right)^4 - 2\left(\frac{d}{r_{sm}}\right)^3 + 2\frac{d}{r_{sm}} \right] & \text{for} \quad d \leq r_{sm} \\ -\frac{m_p G}{d} & \text{for} \quad d > r_{sm} \end{cases} \quad (1)$$

here m_p is the planetary mass, $d = |\mathbf{r} - \mathbf{r}_P|$ denotes the distance of the disc element to the planet and r_{sm} is the smoothing length of the potential measured in units of the Hill radius. The construction of the planetary potential is in such a way that for distances larger than r_{sm} the potential matches the correct $1/r$ potential and is smoothed inside that radius ($d < r_{sm}$) by a cubic polynomial. The parameter r_{sm} is equal to 0.5 in all our simulations, unless stated otherwise.

The gravitational torques acting on the planet are calculated by integrating over the whole disc, where we apply a tapering function to exclude the inner parts of the Hill sphere of the planet. Specifically, we use the smooth (Fermi-type) function

$$f_b(d) = \left[\exp\left(-\frac{d/R_H - b}{b/10}\right) + 1 \right]^{-1} \quad (2)$$

which increases from 0 at the planet location ($d = 0$) to 1 outside $d \geq R_H$ with a midpoint $f_b = 1/2$ at $d = bR_H$, i.e. the quantity b denotes the torque-cutoff radius in units of the Hill radius. This torque-cutoff is necessary to avoid large, probably noisy contributions from the inner parts of the Roche lobe and to disregard material that is gravitational bound to the planet (Crida et al. 2009). Here we assume (as in our previous paper) a transition radius of $b = 0.8$ Hill radii.

2.2. Initial setup

The three-dimensional (r, θ, ϕ) computational domain consists of a complete annulus of the protoplanetary disc centred on the star, extending from $r_{min} = 0.4$ to $r_{max} = 2.5$ in units of $r_0 = a_{Jup} = 5.2$ AU. In the vertical direction the annulus extends from the disc's midplane (at $\theta = 90°$) to $7°$ (or $\theta = 83°$) above the midplane for the simulations of planets with eccentric orbits in the midplane of the disc. Here θ denotes the polar angle of our spherical polar coordinate system measured from the polar axis. The central star has one solar mass $M_* = M_\odot$, and the total disc mass inside $[r_{min}, r_{max}]$ is $M_{disc} = 0.01 M_\odot$. For the isothermal simulations we assume an aspect ratio of $H/r = 0.037$ for the disc, in very close agreement with the fully radiative models of our previous studies. For the radiative models H/r is calculated self-consistently from the equilibrium structure given by the viscous internal heating and radiative diffusion. The isothermal models are initialised with constant temperatures on cylinders with a profile $T(s) \propto s^{-1}$ with $s = r \sin\theta$. This yields a constant ratio of the disc's vertical height H to the radius s. The initial vertical density stratification is approximately given by a Gaussian:

$$\rho(r, \theta) = \rho_0(r) \exp\left[-\frac{(\pi/2 - \theta)^2 r^2}{2H^2} \right]. \quad (3)$$

Here, the density in the midplane is $\rho_0(r) \propto r^{-1.5}$ which leads to a $\Sigma(r) \propto r^{-1/2}$ profile of the vertically integrated surface density. In the radial and θ-direction we set the initial velocities to zero, while for the azimuthal component the initial velocity u_ϕ is given by the equilibrium of gravity, centrifugal acceleration and the radial pressure gradient. This corresponds to the equilibrium configuration for a purely isothermal disc.

For our fully radiative model we first run a 2D axisymmetric model (starting from the given isothermal equilibrium) to obtain a new self-consistent equilibrium where viscous heating balances radiative transport/cooling from the surfaces. After reaching that equilibrium, we extend this model to a full 3D simulation, by expanding the grid into ϕ-direction. The resulting disc for this model has $H/r \approx 0.037$ so we choose that value for our isothermal runs.

2.3. Numerical setup

Our coordinate system rotates at the initial orbital frequency of the planet (at $r = r_0$). We use an equidistant grid in r, θ, ϕ with a resolution of $(N_r, N_\theta, N_\phi) = (266, 32, 768)$ active cells for our simulations. At r_{min} and r_{max} we use damping boundary conditions for all three velocity components to minimise disturbances (wave reflections) at these boundaries. The velocities are relaxed towards their initial state on a timescale of approximately the local orbital period. The angular velocity is relaxed towards the Keplerian values, while the radial velocities at the inner and outer boundaries vanish. Reflecting boundary conditions are applied for the density and temperature in the radial directions. We apply periodic boundary conditions for all variables in the azimuthal direction. In the vertical direction we set outflow boundary conditions for θ_{min} (the surface of the disc) and symmetric boundary conditions at the disc's midplane ($\theta_{max} = \pi/2$). We use the finite volume code NIRVANA (Ziegler & Yorke 1997) with implicit radiative transport in the flux-limited diffusion approximation and the FARGO extension as described in Kley et al. (2009).

2.4. Simulation setup

In the first part of our model sequence we consider the orbital evolution of a planet with a fixed mass ($20 \, M_{Earth}$) on eccentric orbits using different initial eccentricities. For comparison we consider isothermal and fully radiative models. Using radiative discs here is a direct extension of a previous study under purely isothermal disc conditions using the same planet mass (Cresswell et al. 2007). We distinguish two different approaches for these $20 \, M_{Earth}$ models: first, a model sequence where the planet stays on a fixed eccentric orbit and secondly where the planet is free to move inside the computational domain under the action of the planet-disc gravitational forces. For the second models we insert the planet in the disc and let it move immediately, but using a time-dependent mass growth of the planet (through the planetary potential) until it reaches its destination mass. For the first set of models the $20 \, M_{Earth}$ planet is inserted as a whole in the disc at the start of the simulation. Initially the planet starts at a distance $r = a_{Jup} = 5.2$ AU from the central star. For the fully radiative simulations we set the ambient temperature to a fixed value of 10 K at the disc surface (at θ_{min}), which ensures that all the internally generated energy is liberated freely at the disc's surface. This low temperature boundary condition works very well at optically thin boundaries and does not effect the inner parts of the optically thick disc (Kley & Lin 1999; Kley et al. 2009). In the second part of the project we consider sequences of models for a variety of planet masses. We note, that a $20 \, M_{Earth}$ planet has in our simulations using our standard resolution a Roche radius of about 3.3 grid cells. As we will see later in the results section, there is indication that for small mass planets and isothermal runs (using the cubic-potential) a higher resolution is required.

3. Models with an embedded planet on fixed eccentric orbits

In this section we consider planets remaining on fixed eccentric orbits embedded in either isothermal or fully radiative discs. From the disc forces acting on the planet we calculate its theoretical migration rate and eccentricity change. Below we will compare this directly to moving planets in the isothermal and fully radiative regime.

3.1. Torque and power

From the gravitational forces acting on the planet we can calculate the torque and energy loss (power) of the planet. These can be used to estimate the theoretical change of the eccentricity and the semi-major axis of the planet. Here we follow Cresswell et al. (2007).

The angular momentum L_p of a planet on an eccentric orbit is given by

$$L_p = m_p \sqrt{GM_* a} \sqrt{1 - e^2}. \tag{4}$$

In our particular case, for non-inclined planets $L_p = L_z$. We can then obtain the rate of change of the semi-major axis and the eccentricity by

$$\frac{\dot{L}_p}{L_p} = \frac{1}{2}\frac{\dot{a}}{a} - \frac{e^2}{1-e^2}\frac{\dot{e}}{e} = \frac{T_{disc}}{L_p}, \tag{5}$$

where T_{disc} is the total torque exerted by the disc onto the planet

$$T_{disc} = \int_{disc} (r_p \times F)\,|_z \, dV. \tag{6}$$

Here r_p denotes the radius vector from the star to the planet, F the (gravitational) force per unit volume between the planet and a disc element (at location r from the star), and dV the volume element. Equation (5) implies that a positive torque may also result in eccentricity damping rather than outward migration. This is actually the observed result for our moving planets.

The energy change per time (power) of the planet due to the work done by the gravitational forces of the disc is given by

$$P_{disc} = \int_{disc} r_p \cdot F \, dV. \tag{7}$$

The energy of the planet depends only on the semi-major axis a of the planet and is given by

$$E_p = -\frac{1}{2}\frac{GM_* m_p}{a}. \tag{8}$$

We can now obtain for the energy loss and semi-major axis change

$$\frac{\dot{E}_p}{|E_p|} = \frac{\dot{a}}{a} = \frac{P_{disc}}{|E_p|}. \tag{9}$$

From Eqs. (9) and (5) we can calculate the theoretical change of the semi-major axis and the eccentricity for planets on a fixed eccentric orbit for the isothermal and fully radiative cases. We find for the theoretical change of the semi-major axis

$$\frac{\dot{a}}{a} = \frac{P_{disc}}{|E_P|} = \frac{2a}{GM_* m_p} P_{disc} \tag{10}$$

and for the change of eccentricity

$$\frac{\dot{e}}{e} = \frac{1-e^2}{e^2}\left(\frac{1}{2}\frac{\dot{a}}{a} - \frac{T_{disc}}{L_P}\right) \tag{11}$$
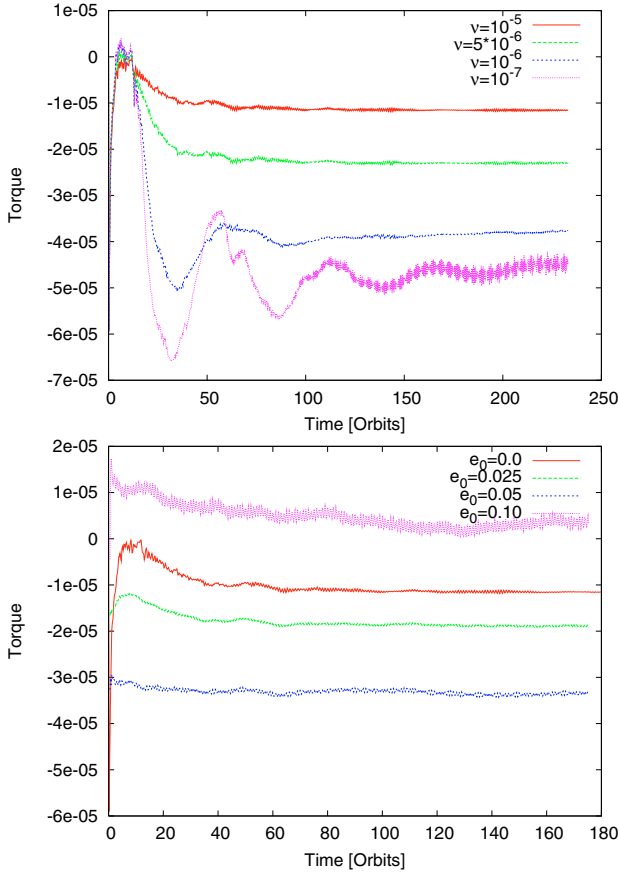
with our calculated $\dot{a}$.

Fig. 1. Time dependence of the torque for different isothermal models with planets on fixed orbits. *Top*: circular planets for different values of the viscosity. The curves are ordered from high to small viscosity. For smaller viscosities the settling towards equilibrium takes longer. *Bottom*: evolution for our standard viscosity ($\nu = 10^{-5}$) for different eccentricities. Due to the large time variability of the torque for eccentric orbits these curves use sliding time averaged values with a window width of 1 period.

Fig. 2. Torque (*top*) and power (*bottom*) acting on a planet on a fixed eccentric orbit in dependency of the eccentricity and thermodynamics of the planet. The torque and the power have been averaged over 20 orbits, taken from $t = 140$ to $t = 160$ orbits for the isothermal (solid red line) and from $t = 120$ to $t = 140$ for the fully radiative simulation (dashed blue line).

Our simulations with planets on a fixed eccentric orbit feature eccentricities ranging from $e_0 = 0.0125$ to $e_0 = 0.4$. To investigate a possible change in the orbital elements of a planet we first analyse the torques and power acting on the planet for fixed eccentric orbits. The time evolution of the torques for different models is displayed in Fig. 1. The top panel refers to planets on circular orbits for different viscosities, as quoted in the caption. For the smallest viscosity ($\nu = 10^{-7}$) the torque is unsaturated and evolves through long period oscillations towards the equilibrium value. The timescale of the oscillation is comparable to the libration time of a particle near the edge of the horseshoe region (see Appendix A). For larger viscosity the equilibration time becomes shorter as the the viscous diffusion time shortens. The results are in very good agreement with existing 2D simulations (Paardekooper & Papaloizou 2009; Paardekooper et al. 2010), and confirm clearly that viscosity is a necessary ingredient for torque saturation. Additionally, this result indicates that the intrinsic (numerical) diffusivity is much smaller than that given by our standard physical viscosity. In the lower panel of Fig. 1 we display similar curves for eccentric planets and the standard viscosity $\nu = 10^{-5}$. Due to the strong variability of the torque on the orbital timescale for eccentric orbits (see Cresswell et al. 2007, and below) we display time averaged torques.

In Fig. 2 we display the torque and power acting on such a planet for isothermal and fully radiative runs in dependency
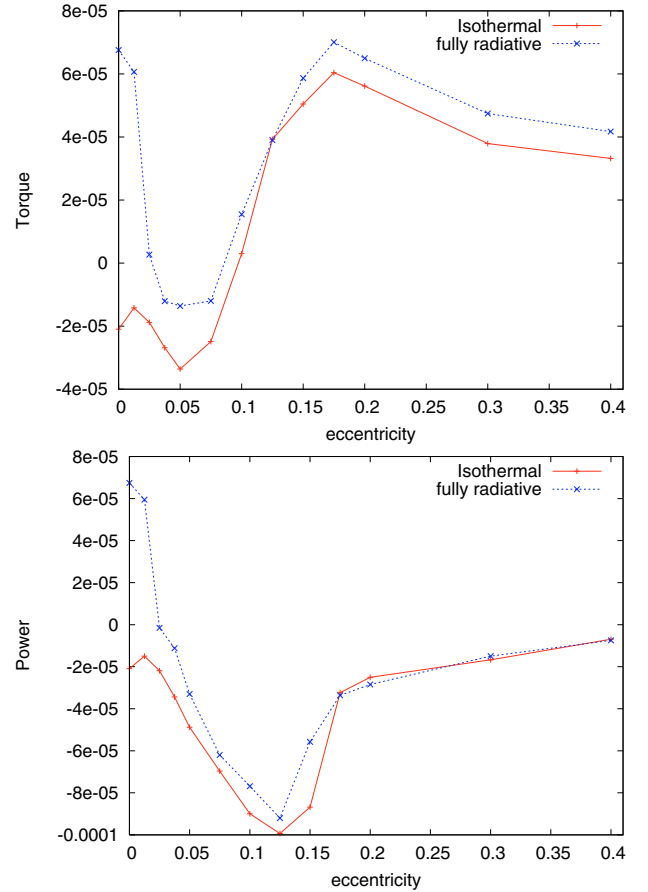
of the eccentricity of the planet. As only every 10th time step was plotted in our output file we averaged the torque over 20 orbits to minimise the numerical fluctuations due to this procedure. For eccentricities smaller than 0.1 the planet experiences a negative torque in the isothermal simulations, while for higher eccentricities the planet feels a positive torque. The torque reaches a maximum at $e = 0.175$ and settles down to a nearly constant value for larger eccentricities, which is in good agreement with Cresswell et al. (2007). The differences in the absolute values of their torque compared to ours have their origin in the aspect ratio H/r of the disc. Our torque is generally higher, as a result of our lower $H/r = 0.037$ compared to their $H/r = 0.05$ disc.

The torque acting on the planet is in general higher for the fully radiative simulations than for the isothermal ones. This phenomenon was observed in various simulations in the past for planets staying on fixed circular orbits, so it is no surprise that the torque for the fully radiative simulation is higher for planets on eccentric orbits as well. For low eccentric planets the fully radiative simulation yield positive torques (and power) in agreement with our previous results for planets on purely circular orbits. On circular orbits, inclusion of radiation transport/cooling, gives rise to a positive torque, which implies outward migration in contrast to the isothermal simulations. The effect is caused by corotation region that gives rise to a positive contribution to the torque in the case of a positive entropy gradient. Interesting is the narrow range in eccentricity of this outward migration. Already for
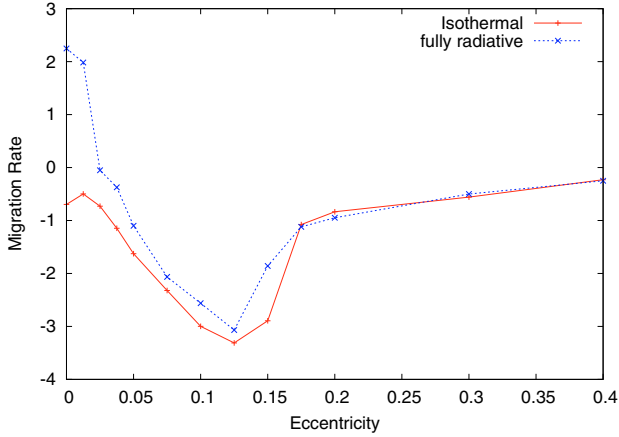
Fig. 3. Theoretical rate of change of the semi-major axis ($\dot{a}/a$) for eccentric planets on fixed orbits. For eccentricities smaller than about 0.025 we find a positive migration rate for the fully radiative disc, which indicates outward migration. This can actually been observed for moving planets later in the text.

Fig. 4. Theoretical rate of change of the eccentricity ($\dot{e}/e$) for eccentric planets on fixed orbits.

$e \approx 0.03$ the direction of migration is directed inward again. This effect is caused by the spatially narrow region that contributes to the positive torque on the planet (Kley et al. 2009). For larger eccentricities the isothermal and radiative results match reasonably well, but the radiative results are always slightly larger than the isothermal ones. Different effects can contribute to this offset: the difference in sound speed, the spatially varying H/r for the radiative runs in contrast to the constant value for the isothermal runs, or a difference in the corotation torques.

In the bottom diagram of Fig. 2 the displayed power of the planet follows the trend of the diagram of the torque acting on the planet with one big difference: the power of the planet is always negative for the isothermal simulations (implying inward migration), while it is positive for low eccentric planets in the fully radiative scheme. For small e the torque and power are very similar for both cases, since they must be identical for $e = 0$.

The consequences for the inferred change in semi-major axis and eccentricity are displayed in Figs. 3 and 4. The theoretical migration rate (Eq. (10)) for planets on fixed eccentric orbits (Fig. 3) reflects our assumptions. When a planet has a high initial eccentricity ($e > 0.2$) the migration rate is nearly constant and inward for the isothermal and fully radiative case, but as soon as the eccentricity gets damped to a value smaller than $e = 0.2$ the inward migration increases by a factor of 2 to 3. The fastest inward migration is seen for planets with an eccentricity of $e \approx 0.125$ for both thermodynamic cases. If the eccentricity evolves to lower values this rapid inward migration is slowed down in the isothermal case. In the fully radiative case this process is even stronger, so that planets with a very low eccentricity ($e \leq 0.025$) have a positive migration rate, indicating outward migration. The positive migration rate is a consequence of the positive torque and power acting on the planet. This confirms very well our previous work of low-mass planets on circular orbits in fully radiative discs migrating outward (Kley et al. 2009). The causes for this outward migration are the same as for circular orbits, as we will see later on. The migration rate in the isothermal case is faster for low eccentric planets (with $e \approx 0.125$) and a little bit slower for high eccentric planets compared to the zero eccentricity case.

The theoretical damping of eccentricity in the isothermal case (Fig. 4) indicates eccentricity damping for all values of e, in agreement with our results for moving planets (see Fig. 13 below). For low eccentric planets ($e \leq 0.10$) the damping of
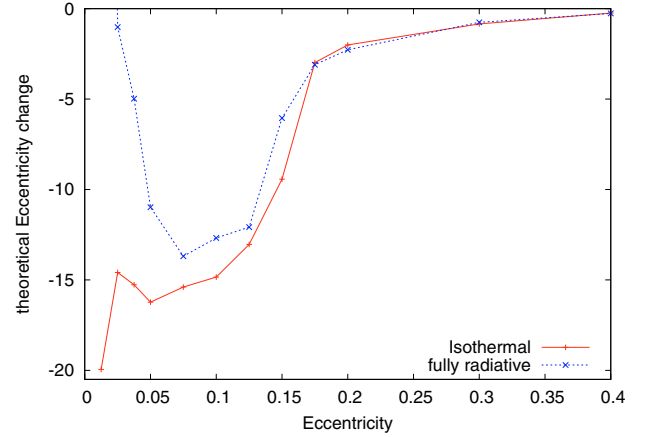
eccentricity is much faster than for high eccentric planets. As soon as the eccentricity of high eccentric planets is damped to a low eccentricity, the damping of eccentricity becomes faster, but will then come to a constant value. In the fully radiative case, the damping of eccentricity is slower for low eccentric planets ($e \leq 0.10$) compared to the isothermal simulations but is nearly the same for high eccentric planets. This means the damping rate for eccentric planets is somewhat bigger in the fully radiative case compared to the isothermal case. For very small eccentricities we even get a positive value for the change of eccentricity (cut off in the figure) in the fully radiative case. In the isothermal case we note the opposite effect: for very small eccentricities the change of eccentricity is somewhat larger than for slightly higher eccentricities. This phenomenon might have its origin in a numeric feature: for small eccentricities the calculations of the migration rate and the change of eccentricity become very sensitive. Interestingly the slower change in eccentricity for the fully radiative simulations results in a lower final eccentricity. For eccentricities smaller than about 0.025 we find a positive eccentricity change in the fully radiative case, which is actually not seen in our simulations of moving planets, and is a result of small numerical inaccuracy combined with the division by e in Eq. (11).

3.2. Torque analysis

To understand the behaviour of the total torque in more detail we analyse now the space-time variation of the torque and power of the planet. For that purpose we introduce the radial torque density $\Gamma(r)$, which is defined in such a way that the total torque T^{tot} acting on the planet is given by

$$T^{\text{tot}} = \int_{r_{\min}}^{r_{\max}} \Gamma(r) \, dr. \tag{12}$$

The radial torque density has been a very useful tool to investigate the origin of the torques in our previous work on planets on fixed circular orbits. In Fig. 5 we display $\Gamma(r)$ for a selection of our planets. All the snapshots were taken when the planet was located at apoastron. Note, that $\Gamma(r)$ changes during the orbit, as the planet moves on an eccentric orbit.

On can clearly see, that the major contribution to the torque originates at larger radii for larger eccentricities by construction, as the planets location is at apoastron and its distance from the central star is $r = a + e$, with $a = 1.0$. For eccentricities smaller than $e = 0.1$ Fig. 5 suggests a negative total torque, while for larger eccentricities a positive torque is assumed, which can be
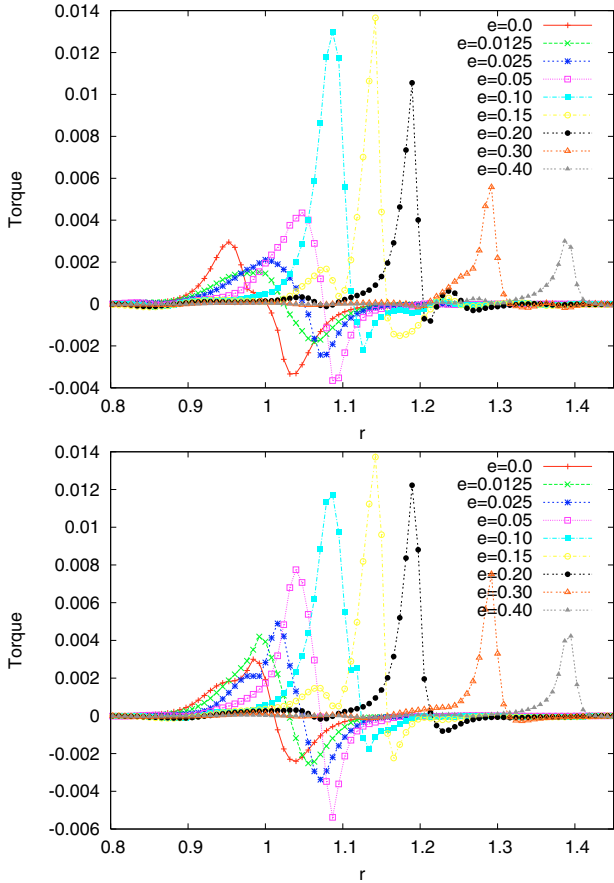
Fig. 5. Torque density acting on a planet on a fixed eccentric orbit in dependency of the eccentricity of the planet embedded in an isothermal disc (*top*) and a fully radiative disc (*bottom*). The snapshots are taken at $t = 150$ orbits for the isothermal simulations and at $t = 100$ orbits for the fully radiative simulations. The planet is located at apoastron in all cases.

Fig. 6. Torque density acting on a planet on a fixed eccentric orbit ($e = 0.10$) during the time of one planetary orbit in an isothermal disc (*top*) and in a fully radiative disc (*bottom*). One can clearly see that the torque changes according to the position of the planet to the central star, making it clear why the torques have to be averaged.

clearly seen in Fig. 2. One might also argue, that the torque acting on the planet for eccentricities larger than $e = 0.1$ should be much higher than shown in Fig. 2. But keep in mind that the torque acting on the planet changes during one orbit as the planet moves on eccentric orbits, see Fig. 6.

In Fig. 6 the planet has initially a distance of $r = 1.1$ to the central star (the planet is located at apoastron) and after half an orbit it is nearest to the central star (at $r = 0.9$, the planet is located at periastron) and moves then further away from the central star to $r = 1.1$ again. The motion of the planet in respect to the central star is the reason for the change in the $\Gamma(r)$-function with respect to time.

In Fig. 7 we display the surface density of planets moving on fixed eccentric orbits with $e = 0.025$, $e = 0.05$, $e = 0.10$ and $e = 0.20$ in isothermal discs. These plots are taken at $t = 150$ orbits. For all surface densities displayed the planet is at apoastron, meaning the x value of the planet is $-(a + e)$, with $a = 1.0$, while the y value of the planet is 0 for all cases.

Despite the fact that for eccentric orbits the density structure and flow patterns appear and disappear periodically in phase with the orbit, one can see for the $e = 0.025$ case clearly two spiral waves exerted from the planet (one in the outer disc ($r > r_p$) and one in the inner disc ($r < r_p$)). The spiral wave structure is comparable to the zero eccentric case.

For higher eccentricities ($e = 0.05$ and $e = 0.10$) the outer spiral wave is more pronounced. At the time the snapshot was
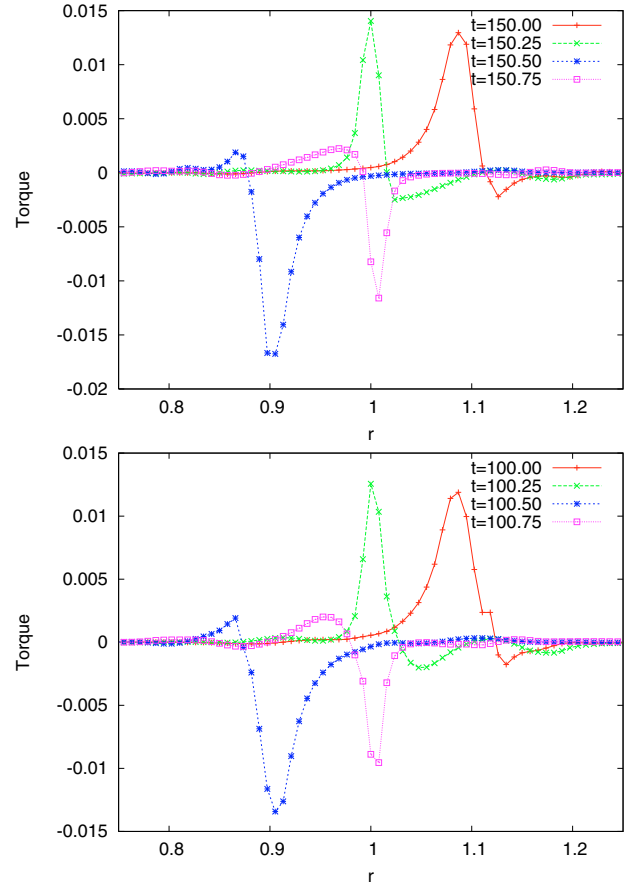
taken, the planet lies in apoastron where it moves more slowly through the gas, meaning that it is overtaken by disc matter on orbits that lie both inside and outside the planetary location. We also note a significant density enhancement close to the vicinity of the planet, which lies in front of the planet and will drag the planet forward, exerting a positive torque, see Fig. 5. The reason for this phenomenon lies in the flow lines, which are distorted by the planet's gravitational potential, and come to a focus in front of the planet. The corresponding azimuthally averaged density is displayed in Fig. 8. Interestingly, for higher eccentricities there is no gap visible anymore in the averaged Σ-profile due to the complex structure of the spiral arms. These are actually the reason for the high torque density displayed in Fig. 6 (for $t = 150$ orbits). At periastron this effect is reversed, leading to a negative torque acting on the planet. For $e = 0.20$ we even see a stronger distortion in the density structure at apoastron. A more eccentric orbit of the planet will reduce the speed of it at apoastron more and leads thus to a more distorted density structure, compared to the zero eccentricity case.

Comparing the torque density of the fully radiative simulation (see Fig. 5) with the isothermal torque density one notices only small differences for the different eccentricities. The torque acting on the planet is slightly larger for the fully radiative simulation compared for the isothermal simulation. For smaller eccentricities the reason for this phenomena lies in the spiral waves exerted from the planet. For very low eccentric planets, the arguments for a positive torque acting on the planet are the same as
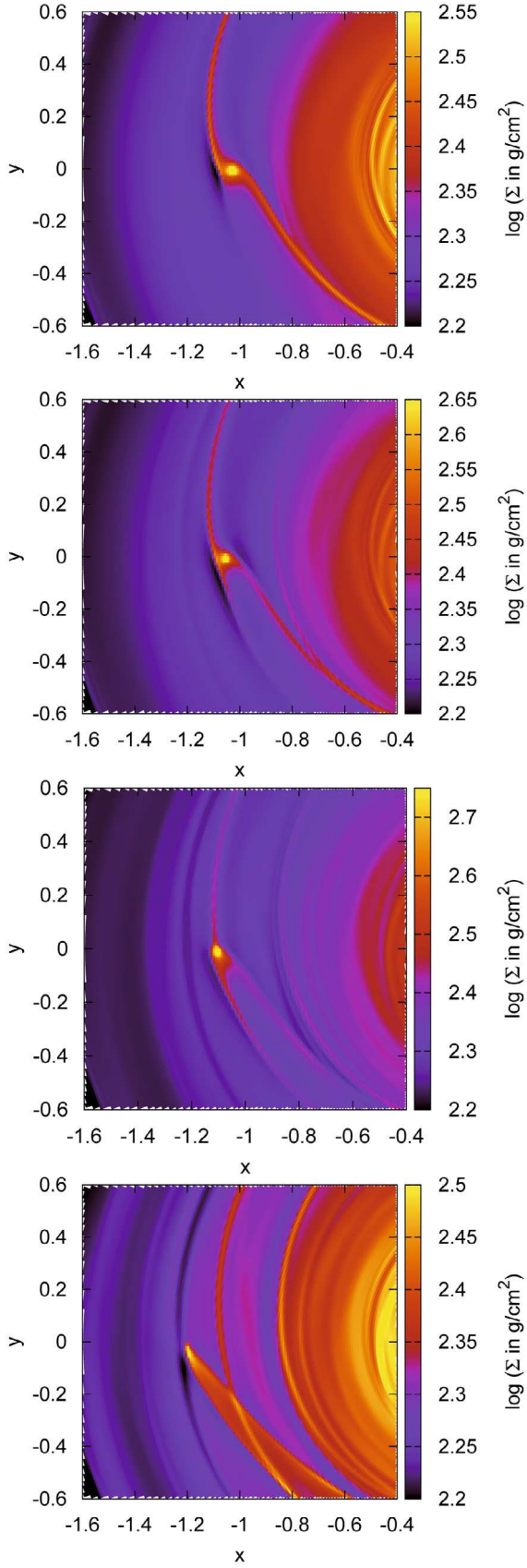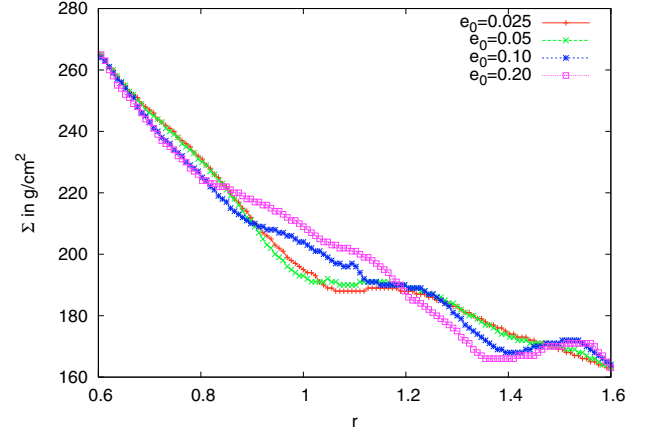
Fig. 8. Azimuthally averaged surface density for planets on fixed eccentric orbits in the isothermal case. The displayed densities correspond to the surface maps displayed in the previous Fig. 7.
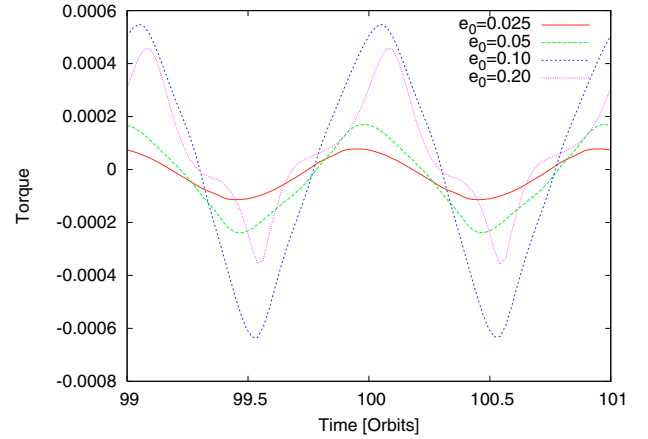

Fig. 9. Torque acting on the planet during the time of 2 planetary orbits for planets on fixed eccentric orbits in the isothermal case. The displayed torques correspond to the surface density maps displayed in Fig. 7.

for planets moving on fixed circular orbits, which are explained in much detail in Kley et al. (2009).

In Fig. 6 we plot the change of torque density during one orbit for the fully radiative case for a planet on a fixed eccentric orbit with $e = 0.1$. The orbital evolution of the torque density $\Gamma(r)$ for the fully radiative simulation does not differ much from the isothermal one. One exception is the absolute value of the torque density at the location of the planet during the time of evolution in one orbit, which is higher for the isothermal case. The change of the torque density during one planetary orbit has the same reasons as for the isothermal case. In Fig. 9 we display the torque acting on planets on stationary eccentric orbits in the isothermal case. The eccentricities of the planet correspond to those shown in Fig. 7 for the surface density. One can clearly see that planets with a higher eccentricity (to about $e \approx 0.10$) show a higher amplitude in the torque acting on the planet, but for even higher eccentricities the amplitude is being reduced. One should also keep in mind that the averaged torque acting on the planet is negative for small eccentricities while it is positive for larger ($e \geq 0.10$) eccentricities. During periapses ($t = 99.5$ and 100.5) the planet also experiences a large energy loss (not displayed here), which follows in trend the same structure as the torque profile (e.g. the energy loss is greatest for $e \approx 0.10$). This leads to an enhanced inward migration for planets with an eccentricity

Fig. 7. Displayed are the surface density maps for planets on fixed eccentric orbits at $t = 150$ orbits for isothermal simulations with $H/r = 0.037$. The plots feature eccentricities of $e = 0.025$, $e = 0.05$, $e = 0.10$ and $e = 0.20$ from top to bottom. The planet is located at apoastron, meaning $(x_p, y_p) = (-(a + e), 0)$, for each displayed eccentricity.

around $e \approx 0.10$, as can be seen in Fig. 3 for the calculated migration rate.

The top figure in Fig. 10 displays the surface density for an $e = 0.025$ planet on a fixed eccentric orbit in a fully radiative disc. The surface density distribution shown in this figure is very similar to those found for fixed circular orbits (see Kley et al. 2009). For higher eccentricities the spiral wave structure can no longer be observed as clearly as for the low eccentricity case, no matter whether we are in the isothermal or fully radiative regime. The overall surface density structure for high eccentric planets for the fully radiative case matches nearly the corresponding structure in the isothermal case. As we calculate the torque acting on the planet due to the interaction with the disc material it is not surprising that the torques acting on the planet for high eccentric planets are very similar for the isothermal and fully radiative simulations. The corresponding azimuthally averaged density is displayed in Fig. 11. The profiles look very similar to those of the isothermal case, where for larger eccentricities the gap becomes invisible in the Σ-profile.

In Fig. 12 we display the torque acting on planets on stationary eccentric orbits in the fully radiative case. The eccentricities of the planet correspond to those shown in Fig. 10 for the surface density. One can clearly see that planets with a higher initial eccentricity (to about $e \approx 0.10$) show a higher amplitude in the torque acting on the planet, but for even higher eccentricities the amplitude is being reduced. One should also keep in mind that the averaged torque acting on the planet is positive for very small eccentricities ($e \leq 0.025$) and negative for $0.025 < e < 0.10$ while it is positive for larger ($e \geq 0.10$) eccentricities. During periapses ($t = 99.5$ and 100.5) the planet also experiences a large energy loss (not displayed here), which follows in trend the same structure as the torque profile (e.g. the energy loss is greatest for $e \approx 0.10$). This leads to an enhanced inward migration for planets with an eccentricity around $e \approx 0.12$, as can be seen in Fig. 3 for the calculated migration rate.

4. Moving planets on initial eccentric orbits

To study eccentricity damping of a planet embedded in a protoplanetary disc dynamically we now change our configuration in such a way, that the planet is able to evolve its orbit in time. In the beginning of the simulation we put the planet in the disc, and let the mass of the planet grow in such a way that the planet reaches its final mass of $m_p = 20\ M_{Earth}$ at $t = 10$ orbits. This way we do not disturb the density distribution of the disc as much as by putting the planet with its full mass immediately into the unperturbed disc.

4.1. Isothermal discs

The eccentricity evolution of various planets with individual starting eccentricity can be seen in Fig. 13. Planets with an initial eccentricity lower than about $e \approx 0.10$ experience an exponential damping of eccentricity (as soon as the planet has reached its destined mass), while planets with larger initial eccentricity adopt initially a slower damping. As soon as planets with a higher initial eccentricity reach an eccentricity of about $e \approx 0.10$ they undergo an exponential damping of eccentricity as well. For eccentricities $0.10 < e < 0.15$ the damping of eccentricity is accelerated compared to the damping for higher eccentricities. This was expected as a result of our calculations of the change of eccentricities for planets on fixed eccentric orbits (see Fig. 4). In the end all planets have settled to about the same value of eccentricity ($e \approx 0.02$), independent of their starting eccentricity.
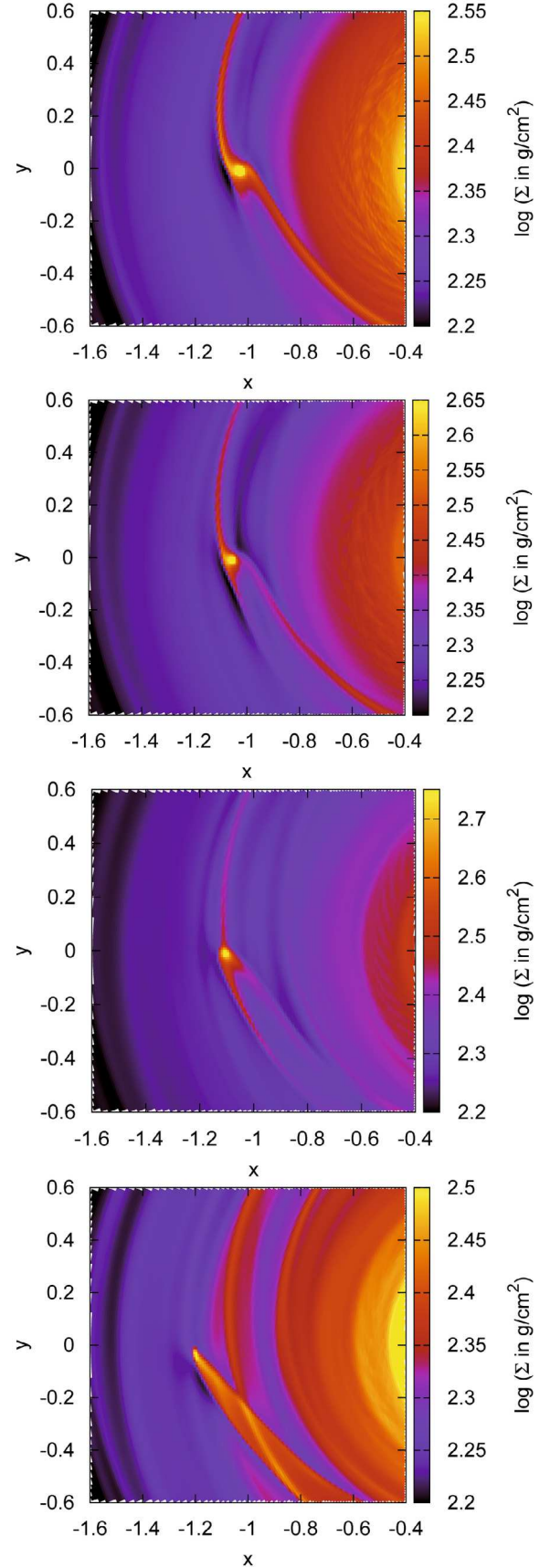
Fig. 10. Displayed are the surface density maps for planets on eccentric orbits on fixed orbits at $t = 100$ orbits for fully radiative simulations. The plots feature eccentricities of $e = 0.025$, $e = 0.05$, $e = 0.10$ and $e = 0.20$ from top to bottom. The planet is located at apoastron, meaning $(x_P, y_P) = (-(a + e), 0)$, for each displayed eccentricity.
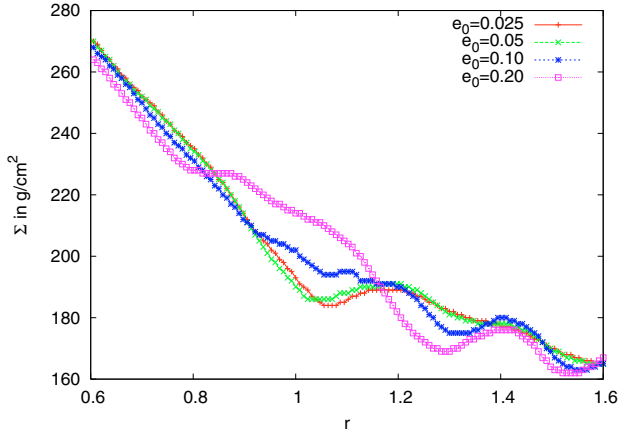
Fig. 11. Azimuthally averaged surface density for planets on fixed eccentric orbits in the fully radiative case. The displayed densities correspond to the surface maps displayed in the previous Fig. 10.
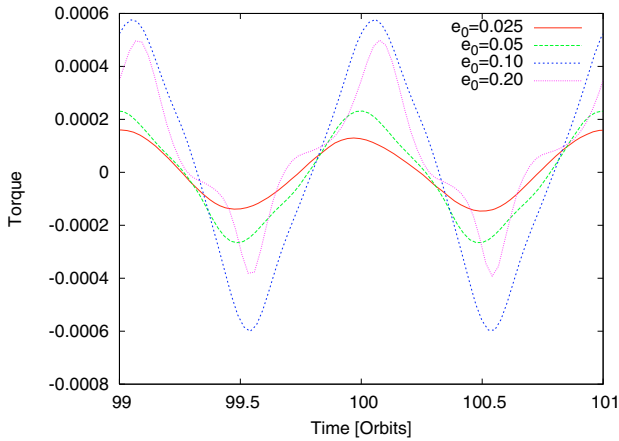

Fig. 12. Torque acting on the planet during the time of 2 planetary orbits for planets on fixed eccentric orbits in the fully radiative case. The displayed torques correspond to the surface density maps displayed in Fig. 10.

Fig. 13. Time evolution of eccentricity of planets embedded in isothermal discs with $H/r = 0.037$ and individual starting eccentricity. The vertical dotted line at $t = 10$ indicates the time at which the planets have grown to their full mass. The black dashed lines indicate an exponential decay with a fitted $\tau_{ecc} = 29$ shifted to obtain a match for $e_0 = 0.1, 0.2, 0.3$ and 0.4.

Fig. 14. Time evolution of the semi-major axis of planets embedded in isothermal discs with $H/r = 0.037$ and individual starting eccentricity.

Using linear analysis for small eccentricities Tanaka & Ward (2004) find that the mean eccentricity change (averaged over one planetary orbit) is given by

$$\frac{\overline{de/dt}}{e} = -\frac{0.780}{t_{wave}} \tag{13}$$

with the characteristic time

$$t_{wave} = q^{-1} \left(\frac{\Sigma_P a^2}{M_*}\right)^{-1} \left(\frac{c_s}{a\Omega_P}\right)^4 \Omega_P^{-1}, \tag{14}$$

where q denotes the mass ration between the planet and the star and Σ_P the local surface density at the planetary orbit. For our 20 M_{Earth} planet at 5.2 AU in the isothermal $H/r = 0.037$ disc we find the characteristic time to be $t_{wave} = 7.70$ orbits, which gives an eccentricity damping time scale of about $\tau_{ecc} = t_{wave}/0.78 = 9.88$ orbits. Apparently, this theoretically estimated decay time scale does not match the fitted value of $\tau_{ecc} = 29$ as obtained from our numerical results. This exponential decay time is indicated by the black dashed lines in Fig. 13. As will be seen below, this strong difference occurs only for the isothermal case and is much reduced in the fully radiative models. In previous simulations on the evolution of eccentric planets *in isothermal discs* the agreement between theory and numerics has been much better (Cresswell et al. 2007). We attribute
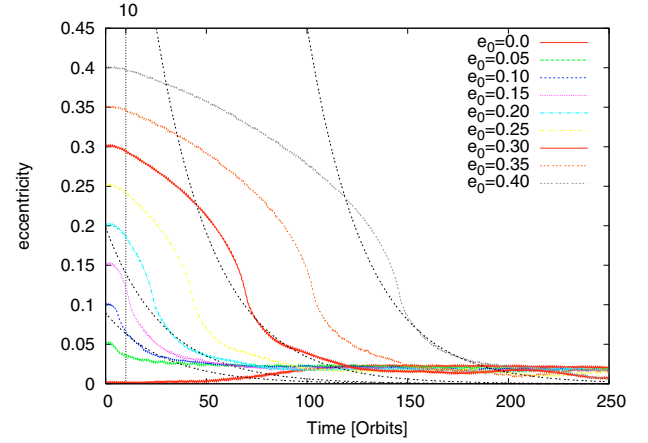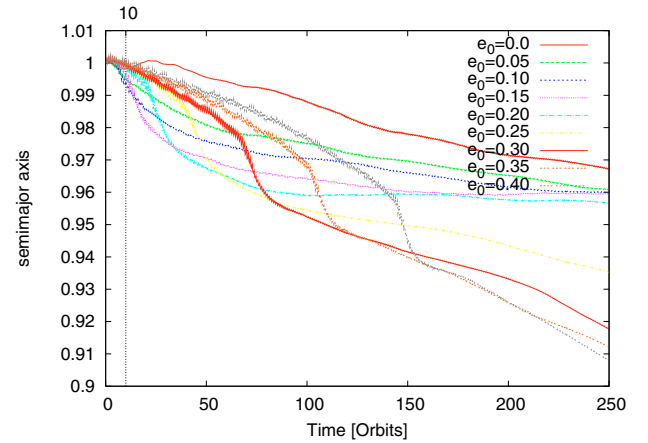
the difference to two effects, a smaller H/r and the usage of the steeper more realistic cubic-potential instead of the more shallow ϵ-potential that was used in Cresswell et al. (2007). Indeed, an additional run for the $e_0 = 0.20$ case with the ϵ potential using $r_{sm} = 0.8$ yields a fitting parameter of $\tau_{ecc} = 17$. This is much closer to the theoretical computed value.

But not only the eccentricity evolves in time on a moving planet, but also the semi-major axis of the planet as can be seen in Fig. 14. The reduction of the semi-major axis is in direct correlation with the damping of eccentricity. For planets with initially low eccentricity (lower than $e = 0.12$), we see a immediately reduction of the semi-major axis on a fast rate. This rapid inward migration is then reduced to a very slow migration rate when the planets reach their final value of eccentricity ($e \approx 0.02$). Planets with higher initial eccentricity first migrate inward at a slower rate as their low eccentric counterparts, but at the time their eccentricity reaches the above mentioned point of $e \approx 0.10$ their migration rate changes and they undergo a rapid inward migration, as their eccentricity damps exponentially. This rise in the migration rate was actually expected from the calculations of the theoretical migration rate for planets on fixed eccentric orbits (see Fig. 3). When the eccentricity damping then changes to a slower decay the migration rate becomes nearly linear and
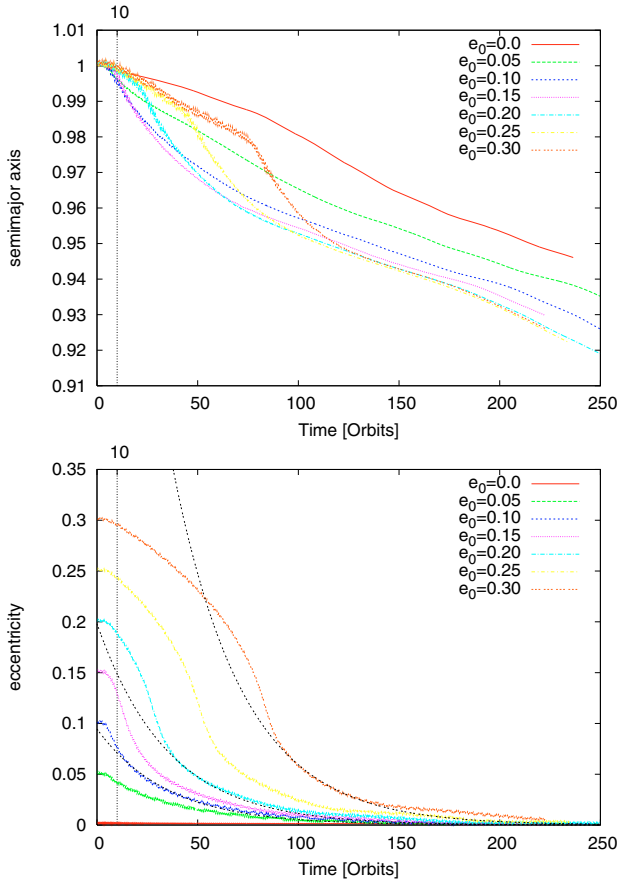
Fig. 16. Time evolution of eccentricity for planets with individual starting eccentricity for the fully radiative case. The black dashed lines indicate an exponential decay with $\tau_{ecc} = 25$ for $e_0 = 0.1, 0.2, 0.3$ and 0.4.

From our disc-data we estimate a theoretical exponential decay time for eccentricity damping timescale as $\tau_{ecc} = 32.95$ orbits. This value is larger than the previous one for the lower $H/r = 0.037$ case by a factor of $(0.05/0.037)^4$. Numerically we obtain $\tau_{ecc} = 35$, see the black dashed curves in Fig. 15. Hence, the numerical exponential decay in the simulations matches quite well to the theoretical damping rate. We attribute this better match to the smoothing effect of the higher pressure in the disc.

4.2. Fully radiative discs

If we now let the planet evolve its orbit with time for the fully radiative case, we obtain a very similar behaviour to the isothermal case for the evolution of eccentricity (see Fig. 16), but a quite different behaviour concerning the semi-major axis evolution (see Fig. 17). The damping of eccentricity for the fully radiative discs proceeds on a comparable timescale to the two previous results, and we find for the exponential behaviour $\tau_{ecc} = 25$.

The inclusion of radiation transport/cooling seems to have only a little effect on the damping of eccentricity. The damping of eccentricity is somewhat slower in the fully radiative case compared to the isothermal simulations. For planets with eccentricities lower than about $e = 0.10$ the damping of eccentricity follows approximately an exponential law. The eccentricity damping for high eccentric planets is first slower, until the eccentricity reaches a value of about $e = 0.10$ and is then increased to an exponential value (see the fit in Fig. 16). This rise in the speed of eccentricity damping is expected from the calculation of the theoretical change of the migration rate for planets on fixed eccentric orbits (see Fig. 4). The reduction rate of eccentricity slows down when it reaches $e \approx 0.05$. In the end, as for the isothermal case, the eccentricity reaches the same value for all starting eccentricities, but the absolute value of eccentricity for the isothermal case ($e \approx 0.02$) is about a factor of five higher as for the fully radiative case ($e \approx 0.004$). The characteristic time for eccentricity damping in our fully radiative disc for the embedded 20 M_{Earth} planet is $t_{wave} = 15.1$ orbits, leading to a eccentricity damping time scale of $\tau_{ecc} = 19.37$ orbits, if we use $H/r = 0.037$ and an adiabatic sound speed. The black dashed lines in Fig. 16 indicate the exponential decay for our fitting, $\tau_{ecc} = 25$. This is not exactly matching our theoretical results but the agreement is satisfactory. Note that as soon as the eccentricity of our simulations reaches $e \approx 0.05$ we observe a difference between our numerical results and the theoretical

Fig. 15. Time evolution of the semi-major axis (*top*) and eccentricity (*bottom*) of a 20 M_{Earth} planet in an isothermal $H/r = 0.05$ disc. The black dashed lines indicate an exponential decay of eccentricity with $\tau_{ecc} = 35$ for $e_0 = 0.1, 0.2$ and 0.3.

the planets move inward with a constant rate again. The planet starting with a zero eccentricity attains a low eccentricity during time and is also the planet migrating inward with the slowest speed. These results lead to the conclusion that planets on eccentric orbits do migrate inward at a slightly faster speed compared to their circular counterparts and that planets starting from initial higher eccentricity migrate inward faster than those with a lower initial eccentricity.

But not only the initial eccentricity of the planet changes the evolution of the planet, but also the disc parameters. Our above shown simulations used a $H/r = 0.037$ in the isothermal case. We now compare these results with isothermal simulations featuring $H/r = 0.05$. In Fig. 15 we display the change of the semi-major axis and the eccentricity of 20 M_{Earth} planets in an isothermal $H/r = 0.05$ disc. The other disc parameters are the same as for the $H/r = 0.037$ planets. On the one hand the overall trend that the planet starting from a zero eccentricity orbit has the slowest inward migration is also true for the simulations with $H/r = 0.05$. On the other hand the inward migration in a $H/r = 0.05$ disc is faster for all initial eccentricities. In a $H/r = 0.037$ disc the planets with an initial eccentricity lower than $e_0 = 0.20$ end up with a very slow inward migration, while in the $H/r = 0.05$ case all planets end up with nearly the same migration rate, even the planets with an initial high eccentricity. These findings are in very good agreement with the results of Cresswell et al. (2007).
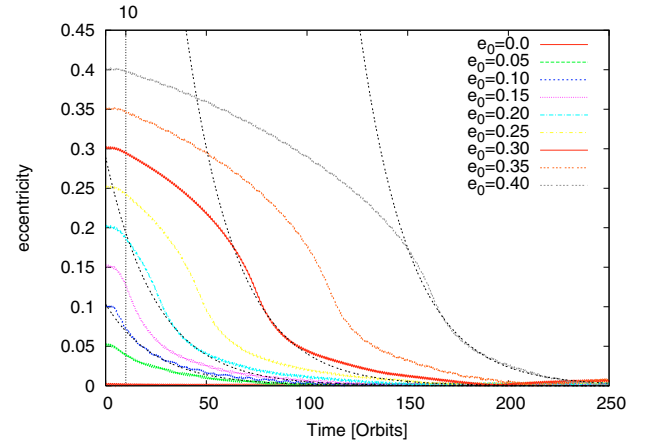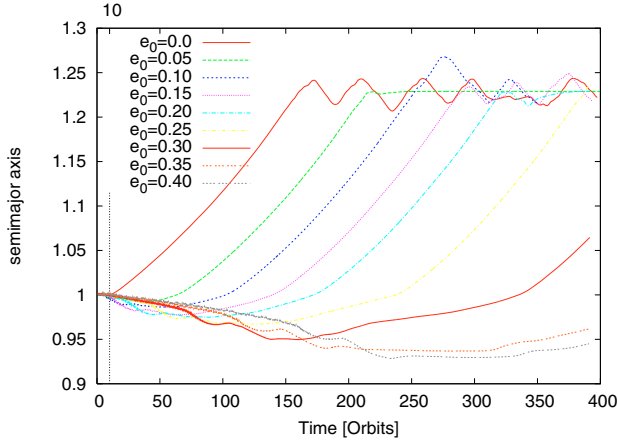
Fig. 17. Time evolution of the semi-major axis of planets with individual starting eccentricity for the fully radiative case for 20 M_{Earth} planets.

insufficient numerical resolution. For more information about this, see Appendix A.

5. Higher mass planets on eccentric orbits

As was shown in many previous works the migration rate of a planet embedded in a protoplanetary disc does not only depend on the disc's structure and thermodynamics, but also on the planetary mass (e.g. Kley et al. 2009). In our previous work we found that planets up to about 33 M_{Earth} experience a positive torque (which indicates outward migration), while higher mass planets experience a negative torque (indicating inward migration). It is now very interesting to investigate the evolution of planets with higher masses on eccentric orbits. In this chapter we focus on the eccentricity change and migration of planets ranging for 30 to 200 earth masses in the isothermal and fully radiative regime. We focus here directly on migrating planets, and we do not provide a torque analysis as we did for the 20 M_{Earth} planet.

5.1. Isothermal discs

In the isothermal regime using the cubic $r_{sm} = 0.5$ potential may cause numerical problems (as described above) which become even more severe when the moving planets have a higher mass. The potential becomes just too deep for higher mass planets to consider our results as correct for the grid resolution we use for moving planets. A deeper planetary potential will give rise to a much higher density distribution near the planet which will become unrealistic in the isothermal case as the disc is not able to heat up upon compression. So we use in this section the common ϵ-Potential with $r_{sm} = 0.8$ for planets with higher mass (as described in Kley et al. 2009), which will give us smoother and more realistic results in this case. Again, we let the planet reach its final mass during a time of 10 orbits. By this way the disturbances in the disc are not as big as by inserting the planet with its full mass at once. As the mass of the inserted planets becomes higher this feature becomes more and more important.

In Fig. 18 we display the evolution of the semi-major axis for planets with 30, 50, 80, 100 and 200 M_{Earth} in the isothermal case for $e_0 = 0.10$ and $e_0 = 0.40$. The high mass planets ($M \geq$ 50 M_{Earth}) migrate inward at the same rate, in contrast to the 30 M_{Earth} planet, when starting with $e_0 = 0.10$. The planets seem all to migrate inward on a linear scale. However when the planets start with $e_0 = 0.40$ we observe a different picture; now only the 80, 100 and 200 M_{Earth} planets migrate inward at the same speed and faster than the planets with lower mass. The migration speed is faster in the beginning for the planets starting with $e_0 = 0.10$ compared to those starting with $e_0 = 0.40$, meaning that a high initial eccentricity tends to slow down the initial inward migration for planets with a higher mass ($M \geq 30$ M_{Earth}) which is in contrast to the results found for the 20 M_{Earth} planet. As the eccentricity is damped during time the migration speed for the planets starting with $e_0 = 0.4$ becomes faster than for the $e_0 = 0.1$ planets. The observed bumps in the evolution of the semi-major axis occur for all planetary masses at the same time when we observe a change in the damping of eccentricity (displayed in the bottom figure of Fig. 19).

In Fig. 19 we display the time evolution of eccentricity for planets starting with $e_0 = 0.10$ and $e_0 = 0.40$. The eccentricity drops immediately at the start of the simulation for the $e_0 = 0.10$ case for all planetary masses, but the damping seems slowest for planets with higher mass, and in the end all high mass planets ($M > 50$) end up with an eccentricity below $e = 0.02$. In the $e_0 = 0.4$ case the eccentricity damping sets in as soon as
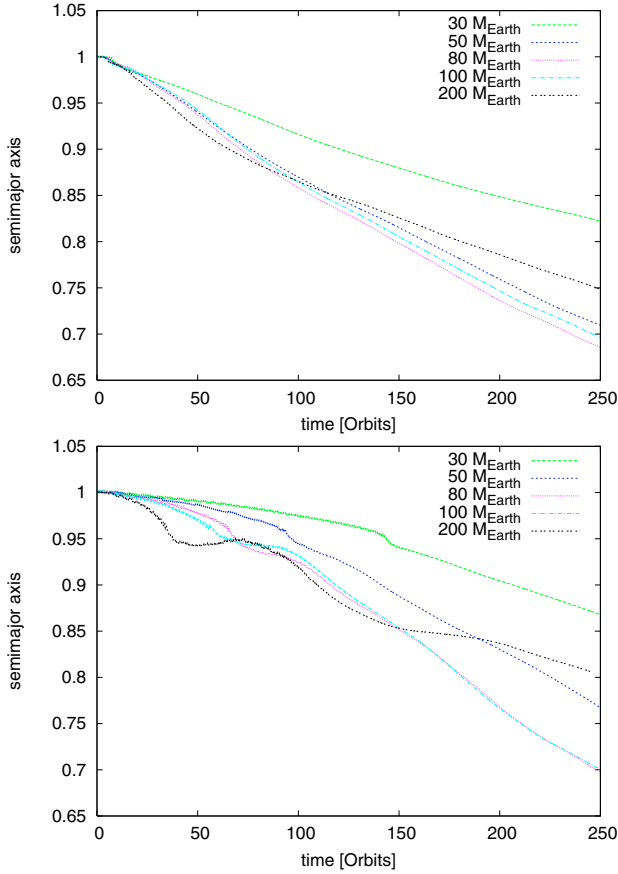
eccentricity damping. The damping in the simulations is much slower than the theoretical damping, as the planet stops inward migration at this point and stays on an orbit with nearly constant semi-major axis, which might slow down eccentricity damping.

The density structure near the planet is smoothed for the fully radiative case. As the mass in the disc and near the planet is able to cool, it will give a smoother density profile. If the eccentricity is damped to a small enough value, the effects of radiation transport/cooling can set in, and will give rise to a positive torque, which results in outward migration (see plot of the semi-major axis Fig. 17). As long as the eccentricity of the planet is higher than ≈ 0.03 the planet will migrate inward, even for the fully radiative simulations, but with a rate smaller than the corresponding isothermal simulations. When the eccentricity reaches the critical value of $e \approx 0.10$ we observe a bump in the semi major axis of the planet. We expected this as the migration rate determined by planets on fixed eccentric orbits (see Fig. 3) has its minimum there.

Starting from a zero eccentricity planet, which will not gain much eccentricity during its evolution, one can see direct outward migration, as predicted in our paper (Kley et al. 2009) for planets moving on circular orbits. Planets starting from a higher initial eccentricity will have to damp their eccentricity to a very low value to feel a positive torque acting on them and thus leading them to outward migration. The eccentricity needed for outward migration is the same for all planets in our simulations (independent of the starting eccentricity) with a average value $e \approx 0.03$ for reversal. As soon as the e-damping is complete the planet experiences a positive torque and will migrate outward, even for the highest initial eccentricity in our simulations.

The inclusion of radiation transfer/cooling in disc for embedded low mass planets on eccentric orbits will result in outward migration as soon as the eccentricity of the planet is damped to a value near the circular eccentricity. If the planet reaches low eccentric orbits which are nearly circular, the density structure will also become nearly like the one of a planet on a circular orbit. The planet will then migrate outward as if it was on a circular orbit. This outward migration will then be stopped as soon as the planet reaches regions in the disc where the density and temperature are too low to support outward migration.

Looking at Fig. 17 it seems, that the outward migration is stopped for all planets at a certain critical radius in the disc. Even though at some point one might expect a termination of the outward migration depending on the local disc conditions, we note that in our case this feature appears to be a result of

Fig. 18. Time evolution of the semi-major axis for planets in an isothermal disc ($H/r = 0.037$) with 30, 50, 80, 100 and 200 Earth masses. In *the top graph* the planets have an initial eccentricity of $e_0 = 0.10$ and in *the bottom plot* the initial eccentricity is $e_0 = 0.40$.
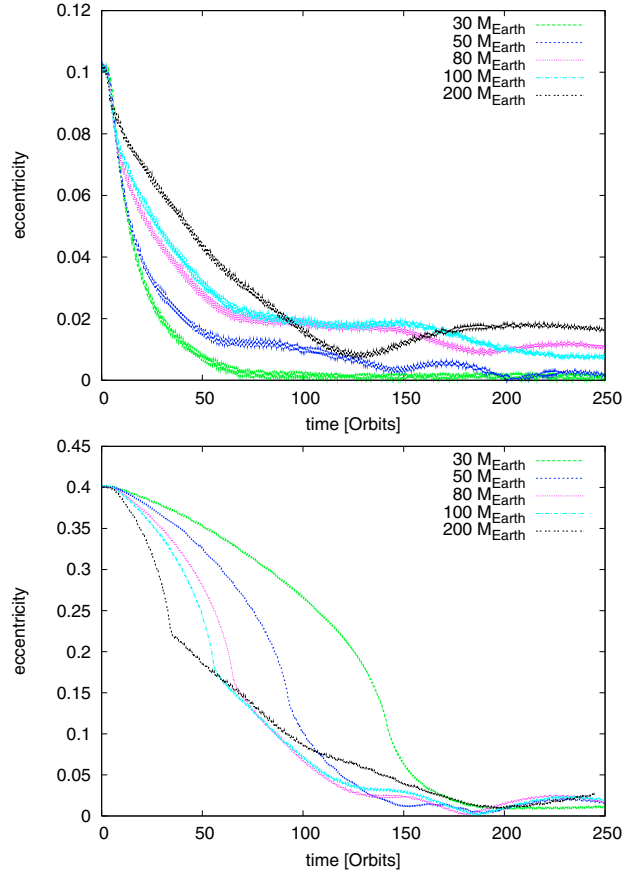
Fig. 19. Time evolution of the eccentricity for planets in an isothermal disc ($H/r = 0.037$) with 30, 50, 80, 100 and 200 Earth masses. In *the top figure* the planets have an initial eccentricity of $e_0 = 0.10$ and in *the bottom figure* the initial eccentricity is $e_0 = 0.40$.

the planets have reached their final mass (after 10 orbits). The 200 M_{Earth} planet experiences initially the fastest eccentricity damping until $e \approx 0.22$ and then the damping is slowed down to a nearly linear damping. The smaller planets follow in principal the same trend in eccentricity damping, only that the initial damping is slower compared to the 200 M_{Earth} planet and terminates at a lower eccentricity. After the eccentricity reaches $e \leq 0.17$ the 100 and 200 M_{Earth} planet have a very similar subsequent eccentricity and semi-major evolution; at $e \leq 0.15$ the 80 M_{Earth} planet joins this evolution.

The initial damping of eccentricity for planets with a high initial eccentricity ($e_0 = 0.40$) depends on the planetary mass, meaning the eccentricity for planets with higher mass is damped faster. This faster eccentricity damping is accompanied by a faster inward migration for higher mass planets. This trends seems to stop as soon as the planets have cleared their gap and the eccentricity damping and evolution of the semi-major axis is nearly the same for all the different high mass planets. Figure 20 shows the azimuthally averaged surface density at the time of 200 planetary orbits for the two different initial starting eccentricities. The profiles after 200 orbits look very similar, the largest difference occurs for the 200 M_{Earth} model which displays clearly a wider gap and slower migration in the long run. For the models with 80 and 100 Earth masses it appears that the migration is slightly faster for the high eccentric case. However, the averaged profile does not give a clear hint toward the cause.

5.2. Fully radiative discs

In the fully radiative regime we can use our suggested cubic potential without problems for higher mass planets as the inclusion of radiation transport/cooling in a disc prevents a large density build-up near the planet, as the temperature near the planet rises and stops further mass accumulation.

In Fig. 21 we display the change of the semi-major axis and eccentricity over time of a 30 M_{Earth} planet for different initial eccentricities. One can clearly see that the outward migration starts when the eccentricity is damped to a small value as we already expected from our results of the 20 M_{Earth} planet. The damping of eccentricity is about 50% faster than for the 20 M_{Earth} planet. This speed up in the damping of eccentricity is due to the increase of the planet's mass. We also observe a change in the damping rate of the eccentricity as soon as the planet reaches $e \approx 0.10$, as for our previous simulations. For an initial low eccentricity ($e_0 = 0.05$) we observe an earlier outward migration until the planets semi-major axis reaches the aforementioned barrier of outward migration in our discs. This barrier is dependent on the planets mass, as the final semi-major axis is slightly smaller for the 30 M_{Earth} planet compared to the 20 M_{Earth} planet (see Appendix A).

In our previous work we obtained a limiting planet mass of about 33 M_{Earth} for the occurrence of outward migration (see Kley et al. 2009). This implies that planets with a higher mass will not migrate outward but inward in a fully radiative disc. In Fig. 22 we display the evolution of the semi-major axis of planets
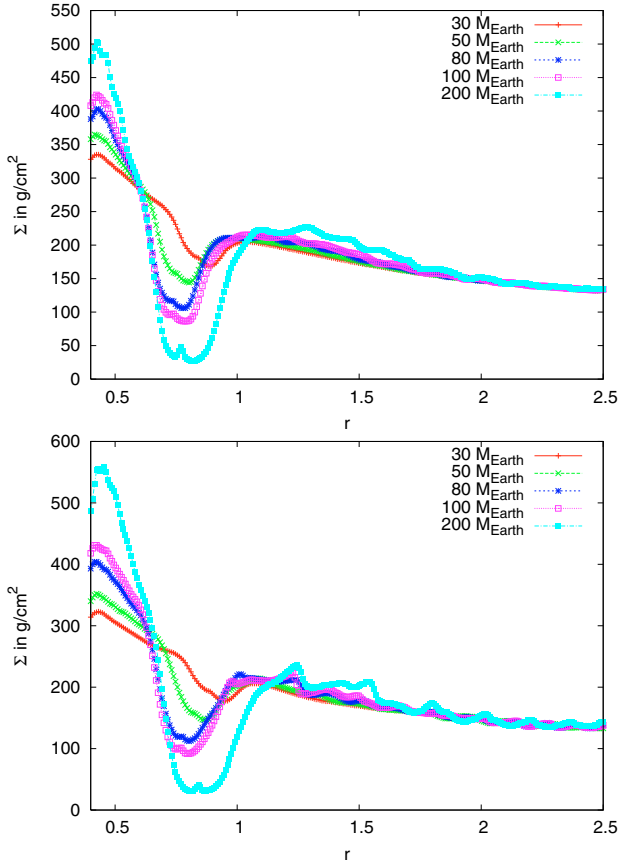
Fig. 20. Azimuthally averaged surface density after 200 orbits for isothermal models with different planet masses. *Top*: initial $e_0 = 0.1$, and *bottom*: initial $e_0 = 0.4$.
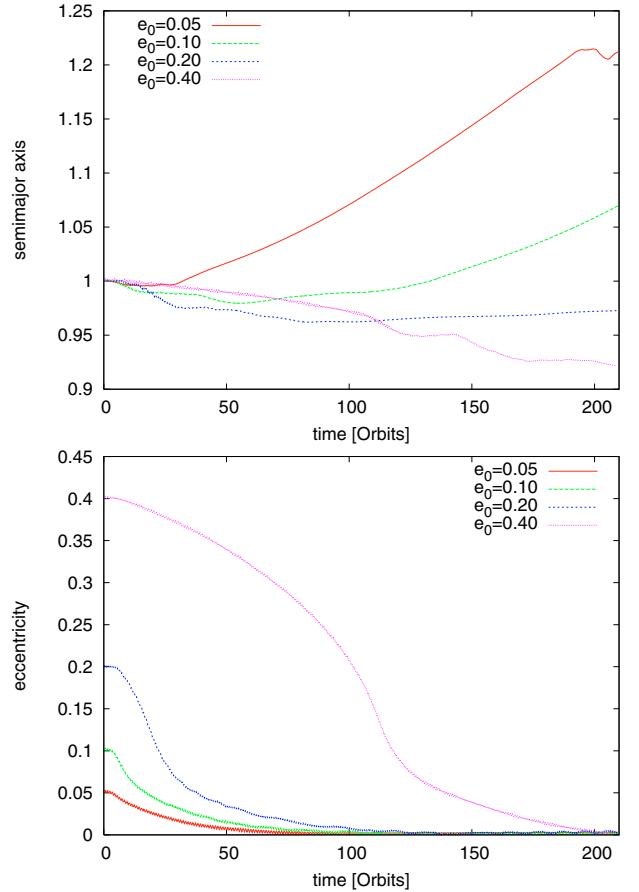

Fig. 21. Time evolution of the semi-major axis (*top*) and eccentricity (*bottom*) of a 30 M_{Earth} planet in a fully radiative disc. The eccentricity shrinks in the same fashion as for a 20 M_{Earth} planet, but about 50% faster. The semi-major axis increases also in the same trend, but the outward migration starts about 50% later than in the 20 M_{Earth} case. The outward migration is then stopped at a radius slightly smaller than for a 20 M_{Earth} planet.

with 20, 30, 50, 80, 100 and 200 Earth masses for planets with an initial eccentricity of $e_0 = 0.10$ and $e_0 = 0.40$. In Fig. 23 we display the eccentricity for the same set of parameters.

For the planets with 20 and 30 Earth masses we observe outward migration as soon as the eccentricity is damped to a small value ($e \leq 0.02$). As this damping is only achieved for the $e_0 = 0.1$ simulations during the run-time of our simulations, we can not see outward migration in the $e_0 = 0.40$ figure, but we have seen it for the 20 M_{Earth} planet in Fig. 17.

The planets with 50, 80, 100 and 200 Earth masses migrate always inward, independent of the initial eccentricity value. However the inward migration is much slower for the 50 M_{Earth} planet compared to the high mass counterparts. The 80, 100 and 200 M_{Earth} planets migrate inward with the fastest rate, but the relative speed of inward migration for these three planets does not differ that much as it does for the 50 and 80 M_{Earth}. If high mass planets ($M > 50 \ M_{\text{Earth}}$) have an initial higher eccentricity they migrate inward a little bit slower than their low eccentric counterparts. As an eccentric orbit disrupts the typical spiral wave structure of a circular orbit the migration rate of a planet on an eccentric orbit is altered compared to the migration rate of a planet on a nearly circular orbit. Having reached a nearly circular orbit the effects of radiation transport/cooling set in and the planet can (if its mass is low enough) migrate outward.

In Fig. 23 we display the eccentricity evolution for planets starting with $e_0 = 0.1$ and $e_0 = 0.4$. The eccentricity damping for planets starting with $e_0 = 0.10$ seems to be independent of the planet's mass, if $M_P \geq 25 \ M_{\text{Earth}}$. The damping sets in immediately after the planets reach their final mass and the eccentricity

is damped to nearly the same value for all simulations. The planet's mass seems to have little effect on eccentricity damping for planets with a low initial eccentricity. The 100 and 200 M_{Earth} planet show little fluctuations in the eccentricity when the eccentricity reaches zero. These fluctuations have their origin in the fact that this planet lies very close to the inner boundary of our simulation (we use reflective boundary conditions at the inner boundary) and thus interacts with it which give rise to the fluctuations in the eccentricity. These fluctuations are also enhanced by the planet's mass.

On the other hand, if the planets have an initial high eccentricity (e.g. $e_0 = 0.40$), we observe a quite different damping rate of the eccentricity. The damping is faster for planets with higher mass, but the final eccentricity reached is the same for all planetary masses in our simulations. As soon as the 100 and 200 M_{Earth} planet reach an eccentricity of $e \approx 0.3$ they loose half their eccentricity in a time of a few orbits, which also affects the migration rate of the planet, as we can observe a little bump at the same time. As in the isothermal case the initial damping rate of eccentricity is reduced for smaller mass planets. Interestingly, all planets experience a similar $\dot{e}$-rate once the eccentricity has dropped below about 0.1–0.15.

As for planets with 20 M_{Earth} an initial eccentricity influences the migration of planets with higher masses. In case the planet is small enough to undergo outward migration the effect of an
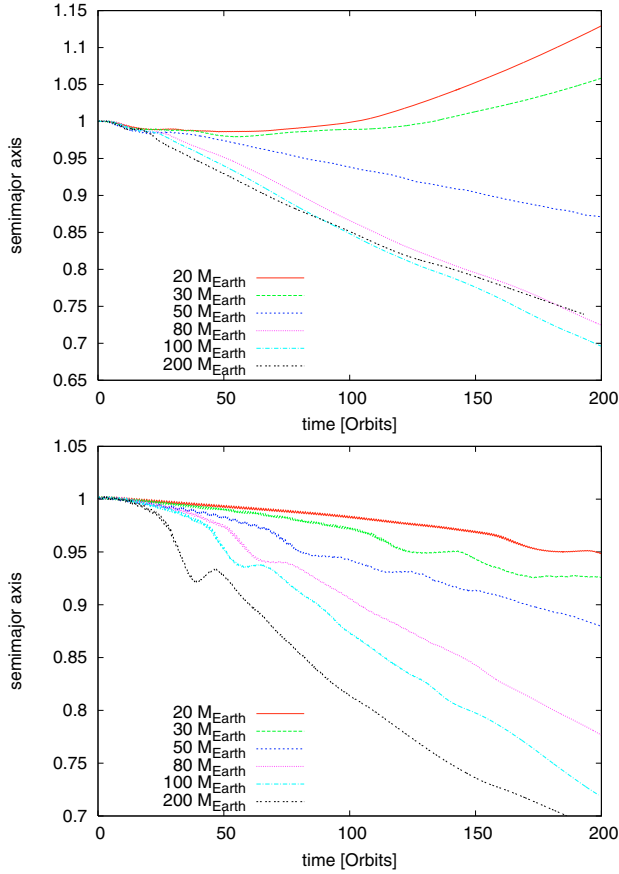
Fig. 22. Time evolution of the semi-major axis for planets in a fully radiative disc with 20, 30, 50, 80, 100 and 200 Earth masses. In *the top figure* the planets have an initial eccentricity of $e_0 = 0.10$ and in *the bottom figure* the initial eccentricity is $e_0 = 0.40$.

Fig. 23. Time evolution of the eccentricity for planets in a fully radiative with 20, 30, 50, 80, 100 and 200 Earth masses. In the *top figure* the planets have an initial eccentricity of $e_0 = 0.10$ and in the *bottom figure* the initial eccentricity is $e_0 = 0.40$.

initial eccentricity is a halting of outward migration to the point the eccentricity is damped to a very small value so that the effects of radiation transport/cooling can take effect as if the planet was moving on a circular orbit. For planets with a mass so high that they will not undergo outward migration an initial eccentricity can slow down the inward migration process by only a very small amount.

5.3. The criterion for outward migration

In the previous simulations we have seen that planets can migrate outward only for sufficiently small orbital eccentricities. The occurrence of outward migration is linked to the detailed structure of the horse-shoe region since the torques originate from a region with a very small radial extent (Kley et al. 2009). It is to be expected that eccentric orbits will destroy the detailed balance, and this is what we see in our simulations. Nevertheless, it is interesting to estimate the value of eccentricity at which this reversal of migration can occur. For that purpose we have run additional series of test simulations in only two spatial dimensions but with identical physical disc parameter for various planetary masses. We measured the limiting value of the eccentricity with two alternative methods. In the first set we performed simulations with planets on fixed orbits for different eccentricities and masses. The point of migration reversal (equivalent to a sign-reversal of the power) has then been determined from the time averaged torque and power measured after 100 orbits. The time averaging has been done over 5 orbits. In the second alternative
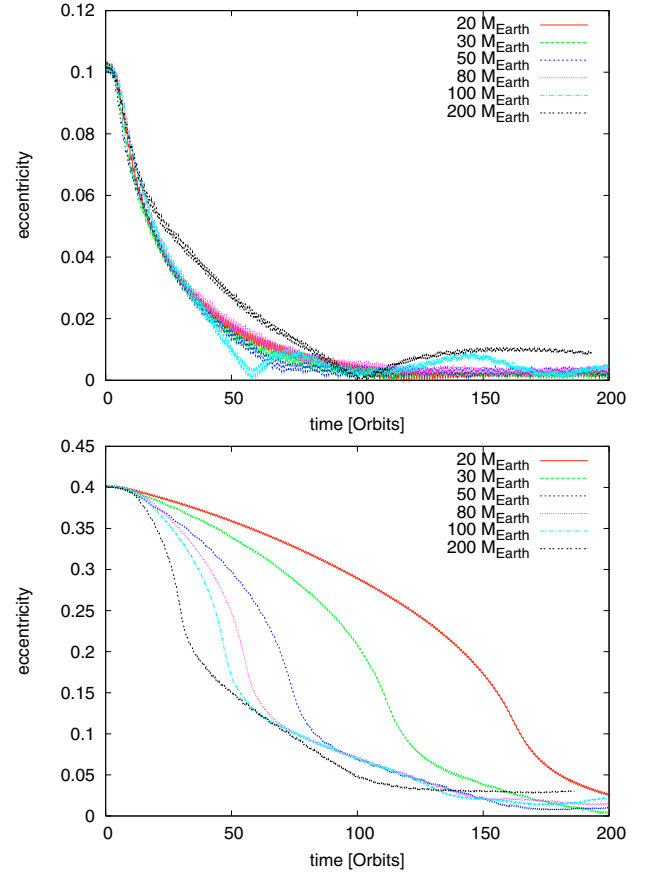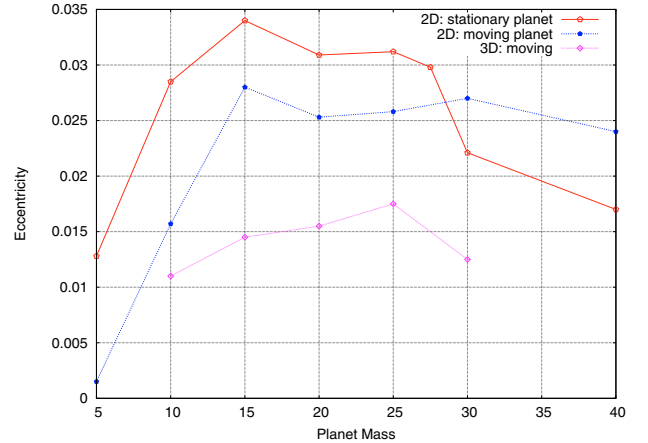

Fig. 24. The critical eccentricity for reversal of migration obtained using 2D and 3D simulations for fully radiative discs. Only planets having eccentricities below this curve are prone to outward migration.

we followed the orbital evolution of the planet in the disc starting with an initial eccentricity of $e_0 = 0.10$. As demonstrated above all planets reduce this initial eccentricity and will migrate outward in a radiative disc after the eccentricity has dropped below a certain value. From the time evolution we determine this critical eccentricity. This second method is used for our full 3D disc as well.

The results obtained using these procedures are displayed in Fig. 24 for the three sets of simulations. While the general

trend is similar in all three series there are nevertheless differences. The 2D results have an average value of $e_{crit} = 0.027$ with a drop for smaller mass planets. The values are systematically larger than those of the 3D runs with $e_{crit} = 0.015$. This effect may be caused by the slightly higher temperature in the disc ($[H/r]_{2D} \approx 0.045$) compared to the 3D runs or due to genuine flow differences in 2D and 3D geometry. Due to this larger H/r planets may experience outward migration for higher masses as well in a 2D geometry (Kley & Crida 2008). Within the 2D runs the results obtained for fixed stationary orbits yield slightly larger values for smaller masses and drop below the results for evolving planets for masses above 25 M_{Earth}. In Kley et al. (2009) we have observed that the location of the torque maximum responsible for the outward migration lies slightly offset of the planet location at $r \approx 0.984$. Interestingly, for an eccentricity of $e = 0.015$ the apoastron lies close to this position, and we expect a destruction of this effect. So the planet can only migrate outward if its eccentricity is smaller than the distance to the offset in the torque distribution, which explains why the fully radiative effects do not turn the planet to outward migration if it has a high eccentricity. This eccentricity has to be damped below this value before the planet can undergo outward migration. The offset distance appears to be relatively insensitive to the mass of the planet (Kley et al. 2009) and does not scale directly with the planet's Hill radius. Baruteau & Masset (2008) even suggest a torque maximum directly at the location of the planet. Our simulations seem to indicate a dependence on the thermodynamic structure of the disc, such as radiative diffusion and temperature (entropy) gradients. This issue still requires resolution.

6. Summary and conclusions

We have performed full 3D radiation hydrodynamical simulations of accretions discs with embedded planets of different masses on eccentric orbits. In a first sequence of simulations we have analysed in detail the dynamics of a planet with a given mass of 20 M_{Earth} for the isothermal as well as fully radiative case. In the isothermal situation we studied the cases $H/r = 0.05$ (a value often used in planet-disc simulations) and $H/r = 0.037$ (the value that matches the fully radiative case). In both cases we find similar behaviour for the eccentricity and semi-major axis evolution, and results that match those of Cresswell et al. (2007) very well. Small eccentricities (with $e \lesssim 2H/r$) are damped exponentially with a time scale given approximately by the linear results (Ward & Hahn 1994). Larger eccentricities are damped initially according to $\dot{e} \propto e^{-2}$ in agreement with Papaloizou & Larwood (2000) and Cresswell et al. (2007). The final value of the eccentricity does not depend on the initial eccentricity of the planet.

The planet migrates inward in the isothermal regime. Low mass planets (e.g. 20 M_{Earth}) on eccentric orbits with large eccentricity ($e > 0.20$) have a slower migration rate as their low eccentric counterparts in the isothermal regime. As soon as the damping of eccentricity proceeds to smaller values the migration rate is pumped up as if the planet had started with a low eccentricity. The maximum inward migration rate occurs at $e \approx 2H/r$. In the fully radiative regime high eccentric planets ($e > 0.20$) with 20 M_{Earth} migrate inward on a rate comparable with the isothermal regime. The corresponding eccentricity damping rate for the fully radiative scheme is about the same as for the isothermal simulations, taking into account the different sound speeds.

But as soon as the eccentricity becomes small enough the planets undergo a change in the direction of migration. The inclusion of radiation transport/cooling in discs with embedded

low mass planets will give rise to a change in the direction of migration for planets whose initial eccentricity has been damped to a nearly circular orbit. The maximum eccentricity a planet can have to still undergo outward migration seems to be determined by the torque maximum in our $\Gamma(r)$ function. This torque maximum has a slight offset compared to the planets location as demonstrated in Kley et al. (2009), corresponding to a limiting eccentricity of about 0.015–0.025. If the eccentricity of the planet is larger than this value it will migrate inward, while it will migrate outward if its eccentricity is smaller (see Fig. 24). For very small planet masses the maximum eccentricity is reduced. For planets on nearly circular orbits the effects of radiation keep the positive torques acting on the planet unsaturated, which implies continuous outward migration. Moving planets experience this result directly, and do indeed migrate outward in the disc in contrast to planets in the isothermal regime.

Eccentric planets with higher mass are slowed down in their migration at the beginning if they have a high initial eccentricity ($e_0 \geq 0.20$) in the isothermal as well as in the fully radiative scheme. If $e \geq 0.02$ all planets move inward independent of their mass, even those embedded in a fully radiative disc. When the eccentricity is damped further the high mass planets ($M \geq 50 M_{Earth}$) still move inward for both regimes, as they open a gap in the disc and migrate as Type II. The eccentricity damped 30 M_{Earth} planet moves outward in the fully radiative scheme as we expected from our previous results (Kley et al. 2009).

Independent of the discs thermodynamics and planet mass, we find that an embedded planet with a given initial eccentricity will lose this eccentricity in time. The rate of the eccentricity loss depends on the value of the initial eccentricity but is much faster than the migration time. Hence, according to our results planet-disc interaction cannot be the cause of the observed high mean eccentricity of extrasolar planets. This finding is supported by the fact that the existence of planetary systems in mean-motion resonance with small libration angles require damping of eccentricity (Lee & Peale 2002; Kley et al. 2005). A solution to this problem might be planet-planet interaction, which we have not considered here.

While performing our studies we noticed that numerical resolution is a serious issue in these type of simulations. As shown in the appendix, only for very high numerical resolution or in an adapted rotating coordinate system which rotates with the present location of the planet, can we observe the outward migration. Finally, as the origin of this outward migration for planets below $M_p \approx 33 M_{Earth}$ is created by a delicate balance of torques which is destroyed by even a very small eccentricity of the planet, the question arises how this effect can persist under realistic conditions. It remains to be studied what effect the turbulent motions within the disc have on the corotation torque of the planet.

Appendix A: Numerical features for moving planets

In Fig. 17 we have noticed that the outward migration of the moving 20 M_{Earth} planet terminates at a well defined radius independent of its initial eccentricity. To determine theoretically the extent of outward migration from our disc properties it seems
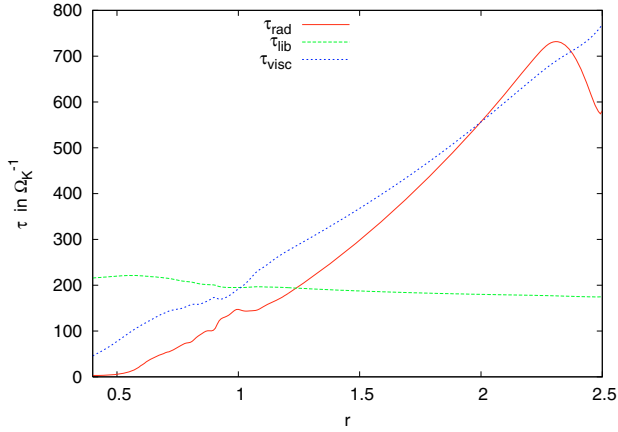
Fig. A.1. Timescales in dependence of the distance from the central star. To compute the timescales we used the density and temperature of the midplane at the beginning of the fully radiative simulations.

useful to compare different timescales: the libration time and the radiation time scale of the disc. The necessary unsaturated torques needed for sustained outward migration require approximately equal libration and cooling time (see Baruteau & Masset 2008; Paardekooper & Papaloizou 2008). For the latter we use in our case the radiative diffusion time scale. We define

$$\tau_{\rm rad} = \frac{s^2}{D_{\rm rad}} \tag{A.1}$$

with $s = H$ and

$$D_{\rm rad} = \frac{4caT^3}{3c_v\rho^2\kappa}. \tag{A.2}$$

The libration time is (as in Baruteau & Masset (2008)) $\tau_{\rm lib} = 8\pi r_{\rm P}/(3\Omega_K x_{\rm s})$ with the half-width of the horseshoe-orbit $x_{\rm s} = 1.16 r_{\rm P} \sqrt{q/(H/r)}$. To compute the timescales we use the density and temperature at the midplane of the disc at the beginning of the simulations. The timescales are displayed in Fig. A.1. The timescales seem to be comparable to about $r = 1.4$, so the planet should be able to migrate outward at least to this point and should not stop at $r = 1.23$ as observed in Fig. 17. In the plot we also show additionally the viscous timescale $\tau_{\rm visc} = s^2/\nu$ which should be comparable to the radiative time for accretion discs in equilibrium. Apparently, this relation is well fulfilled.

The migration of the planet inside the disc is calculated via the torque acting on the planet. In our previous work (Kley et al. 2009) we found that the calculated torque acting on the planet appears to be converged already for our standard resolution if the simulation is performed in a rotating coordinate system where the planet is fixed for circular orbits. If the planet is allowed to move freely inside the disc, for example due to the disc's gravitational force, this is no longer possible, as the planet changes its semi-major axis during time. If the planet moves to an orbit with larger radius the rotating frame will not be able to keep the planet at the same point in the grid, as the rotation frequency of the frame is not linked to the planet anymore.

To investigate this, we performed a series of simulations with a 20 $M_{\rm Earth}$ planet on a fixed circular orbits placed at various distances from the star. In each of the runs the coordinate system rotated with the orbital period of the planet such that the planet did not move through the grid. In Fig. A.2 we display the torques acting on this planet in the fully radiative scheme. The planets are placed in a disc, corresponding to our standard model, at different planetary radii ranging from $r_{\rm p} = 0.8\ r_{\rm Jup}$ to $r_{\rm p} = 2.0\ r_{\rm Jup}$.
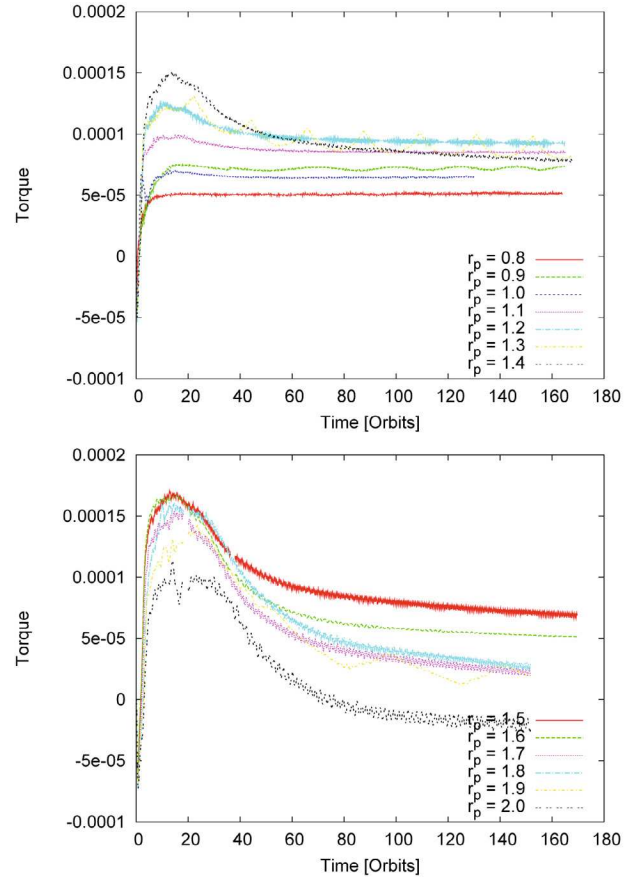
Fig. A.2. Torque for planets on fixed circular orbits with distances $r_{\rm p} = 0.8\ r_{\rm Jup}$ to $r_{\rm p} = 2.0\ r_{\rm Jup}$. In each simulation the coordinate system is rotated with the planet.

As the rotation frequency of the planet matches the rotation frequency of the coordinate system, the planet remains at a fixed location in the grid during the whole simulations. Clearly, the torque acting on these planets is positive for planets with $r_{\rm p}$ up to $r_{\rm p} = 1.9\ r_{\rm Jup}$, indicating that a planet at these radii should still migrate outward. The positive torques are contrary to the results of the moving planets in Fig. 17, where the planets stop their outward migration already at about $r = 1.23$.

The torques acting on theses planets indicate, that a planet in the disc should migrate outward until at least $r = 1.9$. Or possibly even further, if not stopped by our finite computational domain where numerical effects from the outer boundary may disturb its way. To test this hypothesis we calculated the evolution of a 20 $M_{\rm Earth}$ planet starting at $r = 1.5$ with a rotation frequency of the grid matching the rotation frequency of the planet at this distance ($r = 1.5$). Indeed, as Fig. A.3 shows, the planet now migrates outward as the torques presented in Fig. A.2 suggested. Note that the mass of the planet has been increased gradually within the first 10 orbits. Again, this result is in contradiction to the stopped outward migration in Fig. 17.

May this effect be caused by the difference in the rotation frequency of the planet and the numerical grid? To answer this, we first place a 20 $M_{\rm Earth}$ planet at $r_{\rm p} = 1.5$ with a rotation frequency corresponding to a $r = 1.0$ and let it evolve in the disc. The evolution of the semi-major axis is displayed in Fig. A.4. Secondly, we started an identical planet at $r_{\rm p} = 1.0$ with the same rotation frequency of the numerical grid. In the end of the evolution both planets comes to a halt at the same radius. Obviously, the chosen rotation frequency of the numerical grid has an influence
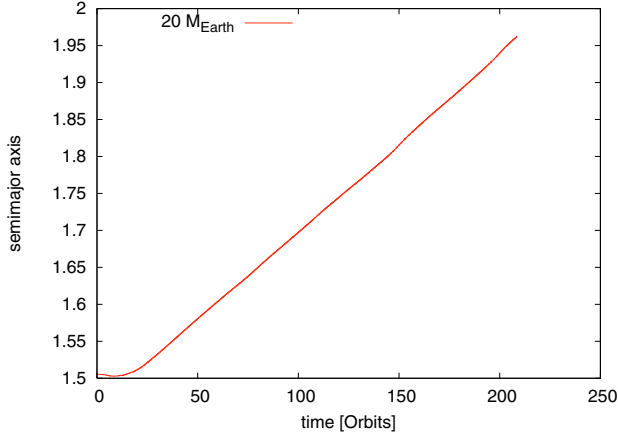
Fig. A.3. Semi-major axis of a 20 M_{Earth} planet starting at $r_p = 1.5$ with a grid rotating with the initial angular speed of the planet.
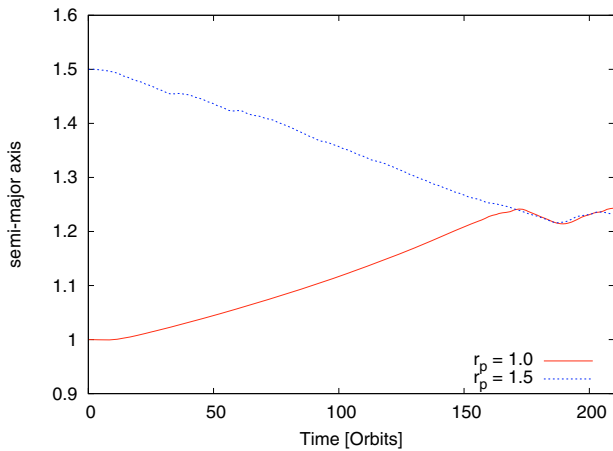

Fig. A.4. Semi-major axis of planets starting at $r = 1.0$ and $r = 1.5$ with a rotation frequency of the numerical grid matching the Keplerian rotation at $r = 1.0$ for both cases.

of the migration of the planet inside the disc. The reason lies in the increased numerical diffusion that occurs if matter moves with a fast speed through the disc. The implemented `FARGO` algorithm helps to solve this problem but cannot fully eliminate it. The problem is enhanced in our situation because it is the detailed fine structure in the flow near the planet that determines the outcome of migration.

Being caused by numerical diffusion, the effect may be (partially) cured by increasing the resolution of the grid. We now double the grid size to $532 \times 64 \times 1532$ active cells in r, θ, ϕ direction and let a planet fixed at $r_p = 1.5$ evolve with a rotation frequency corresponding to $r = 1.0$. The torque acting on the planet is displayed in Fig. A.5 and is clearly positive, indicating outward migration. Over-plotted is the torque of a planet at $r_p = 1.5$ with matching rotation frequency and our standard resolution (the same as in Fig. A.2).

Hence, it seems that the rotation frequency of the numerical grid influences the migration of the planet in the disc, if the numerical resolution of the grid is too small and the planet moved to a radius where its rotation frequency differs by more than 25% from rotation frequency of the grid. In that way, our results determined in the main article are correct, as the planets have migrated inside the disc only by a little bit before their eccentricity is damped and they start their outward migration. The obtained limit of $r = 1.23$ for the outward migration seems to be a
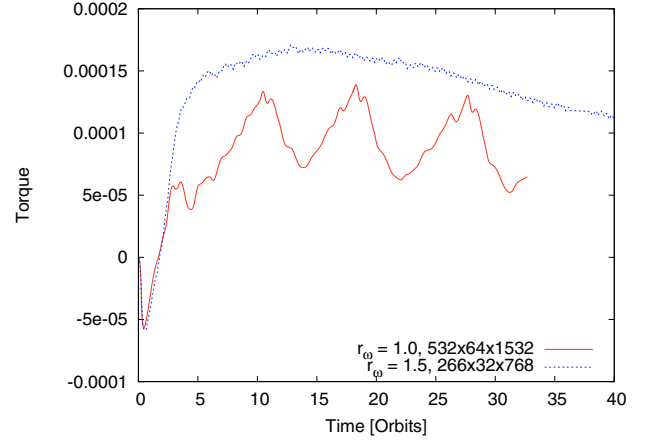

Fig. A.5. Torque acting on a 20 M_{Earth} planet at $r_p = 1.5$. Red solid line: The rotation frequency of the grid matching the Keplerian rotation frequency at $r = 1.0$, and the grid resolution has been doubled compared to our standard simulations. Blue dotted line: Standard resolution with grid velocity equal to the planet.

numerical artefact, however. To obtain an accurate migration for planets under these conditions it seems best to perform the simulations in a coordinate system that rotates always with the speed of the planet. For multiple planetary systems this is not possible and a higher resolution is required.

References

Adams, F. C., & Laughlin, G. 2003, Icarus, 163, 290
Artymowicz, P. 1993, ApJ, 419, 166
Baruteau, C., & Masset, F. 2008, ApJ, 672, 1054
Cresswell, P., & Nelson, R. P. 2006, A&A, 450, 833
Cresswell, P., Dirksen, G., Kley, W., & Nelson, R. P. 2007, A&A, 473, 329
Crida, A., Sándor, Z., & Kley, W. 2008, A&A, 483, 325
Crida, A., Baruteau, C., Kley, W., & Masset, F. 2009, A&A, 502, 679
D'Angelo, G., Lubow, S. H., & Bate, M. R. 2006, ApJ, 652, 1698
Ford, E. B., & Rasio, F. A. 2008, ApJ, 686, 621
Goldreich, P., & Sari, R. 2003, ApJ, 585, 1024
Goldreich, P., & Tremaine, S. 1980, ApJ, 241, 425
Jurić, M., & Tremaine, S. 2008, ApJ, 686, 603
Kley, W., & Crida, A. 2008, A&A, 487, L9
Kley, W., & Dirksen, G. 2006, A&A, 447, 369
Kley, W., & Lin, D. N. C. 1999, ApJ, 518, 833
Kley, W., Lee, M. H., Murray, N., & Peale, S. J. 2005, A&A, 437, 727
Kley, W., Bitsch, B., & Klahr, H. 2009, A&A, 506, 971
Lee, M. H., & Peale, S. J. 2002, ApJ, 567, 596
Levermore, C. D., & Pomraning, G. C. 1981, ApJ, 248, 321
Malmberg, D., & Davies, M. B. 2009, MNRAS, 394, L26
Mihalas, D., & Weibel Mihalas, B. 1984, Foundations of radiation hydrodynamics (New York: Oxford University Press)
Moorhead, A. V., & Adams, F. C. 2008, Icarus, 193, 475
Moorhead, A. V., & Ford, E. B. 2009, ApJ, submitted [arXiv:0904.3336]
Paardekooper, S.-J., & Mellema, G. 2006, A&A, 459, L17
Paardekooper, S.-J., & Mellema, G. 2008, A&A, 478, 245
Paardekooper, S.-J., & Papaloizou, J. 2009, MNRAS, 394, 2283
Paardekooper, S.-J., & Papaloizou, J. C. B. 2008, A&A, 485, 877
Paardekooper, S., Baruteau, C., Crida, A., & Kley, W. 2010, MNRAS, 401, 1950
Papaloizou, J. C. B., & Larwood, J. D. 2000, MNRAS, 315, 823
Papaloizou, J. C. B., Nelson, R. P., & Masset, F. 2001, A&A, 366, 263
Sari, R., & Goldreich, P. 2004, ApJ, 606, L77
Tanaka, H., & Ward, W. R. 2004, ApJ, 602, 388
Tanaka, H., Takeuchi, T., & Ward, W. R. 2002, ApJ, 565, 1257
Tassoul, J. 1978, Theory of rotating stars, Princeton Series in Astrophysics (Princeton: University Press)
Terquem, C., & Ajmia, A. 2010, MNRAS, 404, 409
Udry, S., & Santos, N. C. 2007, ARA&A, 45, 397
Ward, W. R., & Hahn, J. M. 1994, Icarus, 110, 95
Ziegler, U., & Yorke, H. 1997, Comp. Phys. Commun., 101, 54

Evolution of inclined planets in three-dimensional radiative discs

B. Bitsch and W. Kley

Institut für Astronomie & Astrophysik, Universität Tübingen, Auf der Morgenstelle 10, 72076 Tübingen, Germany
e-mail: bertram.bitsch@uni-tuebingen.de

ABSTRACT

Context. While planets in the solar system only have a low inclination with respect to the ecliptic there is mounting evidence that in extrasolar systems the inclination can be very high, at least for close-in planets. One process to alter the inclination of a planet is through planet-disc interactions. Recent simulations considering radiative transport have shown that the evolution of migration and eccentricity can strongly depend on the thermodynamic state of the disc. So far, this process has only been studied for a few selected planet masses using isothermal discs.

Aims. We extend previous studies to investigate the planet-disc interactions of fixed and moving planets on inclined and eccentric orbits. We also analyse the effect of the disc's thermodynamic properties on the orbital evolution of embedded planets in detail.

Methods. The protoplanetary disc is modelled as a viscous gas where the internally produced dissipation is transported by radiation. To solve the equations we use an explicit three-dimensional (3D) hydrodynamical code `NIRVANA` that includes full tensor viscosity, as well as implicit radiation transport in the flux-limited diffusion approximation. To speed up the simulations we apply the `FARGO`-algorithm in a 3D context.

Results. For locally isothermal discs, we confirm previous results and find inclination damping and inward migration for planetary cores. For low inclinations ($i \lesssim 2H/r$), the damping is exponential, while it follows $di/dt \propto i^{-2}$ for larger i. For radiative discs, the planetary migration is very limited, as long as their inclination exceeds a certain threshold. If the inclination is damped below this threshold, planetary cores with a mass up to $\approx 33\ M_{\rm Earth}$ start to migrate outwards, while larger cores migrate inwards right from the start. The inclination is damped for all analysed planet masses.

Conclusions. In a viscous disc an initial inclination of embedded planets will be damped for all planet masses. This damping occurs on timescales that are shorter than the migration time. If the inclination lies beneath a certain threshold, the outward migration in radiative discs is not handicapped. However, only planets with a mass up to $\approx 33\ M_{\rm Earth}$ are prone to this outward migration. Outward migration is strongest for circular and non-inclined orbits.

Key words. accretion, accretion disks – planets and satellites: formation – hydrodynamics – planet-disk interactions – radiative transfer

1. Introduction

Planets in our solar system do not all move in the same plane, but are inclined with respect to the ecliptic. The inclinations are in general small. The highest inclined planet is Mercury ($i = 7.01°$), and only some of the dwarf planets are inclined much higher (e.g. Pluto at $i = 17°$, or Eris at $i = 44.2°$). This low inclination with respect to the ecliptic is typically taken as an indication that planets form within a flattened protoplanetary disc. The observed high i for smaller objects are then a result of gravitational scattering processes in the early solar system evolution. Recently, it has been discovered that a relatively large number of transiting close-in planets in extrasolar systems can be inclined significantly with respect to the stellar rotation axis (see e.g. Triaud et al. 2010). This discovery makes it necessary to take inclination into consideration in both numerical simulations and theoretical considerations of planet-disc interaction.

Starting from early work (Goldreich & Tremaine 1980; Papaloizou & Lin 1984; Ward 1986), the effect a protoplanetary disc has on the migration of the planets has been analysed intensively after the discovery of hot Jupiters close to the star (for a review see Papaloizou et al. 2007). Numerical simulations of planet-disc interactions are a valuable tool for a

better understanding. Two-dimensional (2D) studies have been performed for example by Bryden et al. (1999); D'Angelo et al. (2002) and later fully three-dimensional (3D) simulations (D'Angelo et al. 2003; Bate et al. 2003) followed. All these simulations only considered isothermal discs. However, recent studies (starting with the work of Paardekooper & Mellema 2006) have shown that including radiation transport in planet-disc interaction studies resulted in a slowed down or even reversed migration (Baruteau & Masset 2008; Paardekooper & Papaloizou 2008; Paardekooper & Mellema 2008; Kley & Crida 2008; Ayliffe & Bate 2010). All authors agree that the inclusion of radiative transfer is important and that it strongly affects the migration properties of low mass planets (type-I-migration) in discs, even though there are differences in the magnitude of the effect. It also affects whether it actually leads to reversal of migration or only to a slow down.

Recently, we have analysed the disc's influence on the orbital eccentricity (Bitsch & Kley 2010) for planets of different masses in fully radiative discs. We showed that planet-disc interaction leads quite generally (for all planet masses) to a damping of planetary eccentricity on shorter timescales than the migration timescale. Additionally, planets on eccentric orbits embedded in fully radiative discs only migrate outwards, when

the eccentricity is damped to a nearly circular orbit. Clearly, eccentricity destroys the very sensitive corotation torques near the planet, which results in inward migration until the orbit is circularised again.

The effect of disc-planet interaction on inclination has not yet been studied in any wide extent, owing to the heavy computational requirements. Tanaka & Ward (2004) analysed the influence of the disc on the inclination of low mass planets in linear studies. They find an exponential damping for any non-vanishing inclination, but their results are only formally valid for $i \ll H/r$. Numerical simulations of inclined planets with higher inclinations than H/r (inclination in radians) have shown that exponential damping may be valid up to $i \approx 2H/r$. For planets on higher initial inclined orbits, the damping rate deviates from being exponential, and it can be fitted best with a $\mathrm{d}i/\mathrm{d}t \propto i^{-2}$ function (Cresswell et al. 2007). Only low mass planets with a mass of about $20-30$ earth masses were considered in these studies. The influence on an inclined Jupiter type planet has been considered by Marzari & Nelson (2009). They find that highly inclined and eccentric planets with Jovian masses lose their inclination and eccentricity very fast (on a timescale of order of 10^3 years), when entering the disc again. Since a highly inclined planet is only disturbed in a small way by the accretion disc (and vice versa), such a planet is only able to open a gap in the disc, when the inclination drops to $i < 10.0°$. Terquem & Ajmia (2010) considered inclination evolution utilising a Kozai-type of effect for planets on high inclined and eccentric orbits in the presence of the disc.

In the present work we will extend the work on inclined planets and analyse the effect of planet-disc interaction on embedded planets of all masses. In fully three-dimensional hydrodynamical simulations we will consider isothermal as well as fully radiative discs and study the change in inclination of an embedded planet.

In Sect. 2 we give a short overview of our code and numerical methods. In Sect. 3 we measure the change of inclination and semi-major axis for 20 M_{Earth} planets on fixed circular inclined orbits and then let these planets evolve their orbits in the disc due to the torque acting on the planet form the disc in Sect. 4. In Sect. 5 we study the influence of the planetary mass on the evolution of planets on inclined orbits. In Sect. 6 we follow the evolution of 20 M_{Earth} planets on eccentric and inclined orbits. In Sects. 3 to 6 we also point out the differences between the isothermal and fully radiative simulations. Finally we summarise and conclude in Sect. 7.

2. Physical modelling

The protoplanetary disc is modelled as a 3D, non-self-gravitating gas whose motion is described by the Navier-Stokes equations. We treat the disc as a viscous medium, where the dissipative effects can then be described via the standard viscous stress-tensor approach (e.g. Mihalas & Weibel Mihalas 1984). We also assume that the heating of the disc occurs solely through internal viscous dissipation and ignore the influence of additional energy sources (e.g. irradiation form the central star). This internally produced energy is then radiatively diffused through the disc and eventually emitted from its surface. For this process we use the flux-limited diffusion approximation (FLD, Levermore & Pomraning 1981), which allows us to treat the transition from optically thick to thin regions as an approximation. A more detailed description of the modelling and the numerical methodology is provided in our previous papers (Kley et al. 2009) and (Bitsch & Kley 2010). Compared to our previous papers, we now extend the simulations by including planets with different masses on inclined orbits.

2.1. General setup

An important issue in modelling planetary dynamics in discs is the gravitational potential of the planet since this has to be artificially smoothed to avoid singularities.

While in two dimensions a potential smoothing takes care of the otherwise neglected vertical extension of the disc, in three dimensional simulations the most accurate potential should be used. As the planetary radius is much smaller than a typical grid cell, and the planet is treated as a point mass, a smoothing of the potential is required to ensure numerical stability. In Kley et al. (2009) we have discussed two alternative prescriptions for the planetary potential. The first is the classic ϵ-potential

$$\Phi_{\mathrm{P}}^{\epsilon} = -\frac{Gm_{\mathrm{P}}}{\sqrt{d^2 + \epsilon^2}}. \tag{1}$$

Here m_{P} is the planetary mass, and $d = |\boldsymbol{r} - \boldsymbol{r}_{\mathrm{P}}|$ denotes the distance of the disc element to the planet. This potential has the advantage that it leads to very stable evolutions when the parameter ϵ (stated in units of the Hill radius) is not too small, i.e. is a significant fraction of the Roche-lobe size. The disadvantage is that for smaller ϵ, which would yield a higher accuracy at larger d, the potential becomes very deep at the planetary position. Additionally, due to the long range nature, the potential differs from the exact one even for medium to larger distances d from the planet.

To resolve these problems at small and large d simultaneously, we have suggested the following *cubic*-potential (Klahr & Kley 2006; Kley et al. 2009)

$$\Phi_{\mathrm{P}}^{\mathrm{cub}} = \begin{cases} -\frac{m_{\mathrm{P}}G}{d} \left[\left(\frac{d}{r_{\mathrm{sm}}}\right)^4 - 2\left(\frac{d}{r_{\mathrm{sm}}}\right)^3 + 2\frac{d}{r_{\mathrm{sm}}} \right] & \text{for} \quad d \leq r_{\mathrm{sm}} \\ -\frac{m_{\mathrm{P}}G}{d} & \text{for} \quad d > r_{\mathrm{sm}}. \end{cases} \tag{2}$$

Here, r_{sm} is the smoothing length of the potential in units of the Hill radius. The construction of the planetary potential is in such a way that for distances larger than r_{sm} the potential matches the correct $1/r$ potential. Inside this radius ($d < r_{\mathrm{sm}}$) it is smoothed by a cubic polynomial. This potential has the advantage of exactness outside the specified distance r_{sm}, while being finite inside. The parameter r_{sm} is equal to 0.5 in all our simulations, unless stated otherwise. The value of the smoothing length of the planetary potential r_{sm} was discussed in great detail in Kley et al. (2009), where we compared different smoothing lengths and potential types, resulting in our choice of $r_{\mathrm{sm}} = 0.5$. In this work we use the cubic-form for the planetary potential for all fully radiative simulations and for the isothermal simulations with planets on fixed orbits. We note that for $\epsilon = 0.25$ the depth of the ϵ-potential at the position of the planet, $d = 0$, is identical to the cubic-potential with $r_{\mathrm{sm}} = 0.5$. However, the difference reaches a maximum of about 20% at $d = 0.25$, is 10% at $d = 0.5$, and slowly diminishes for larger d.

Our simulations for moving planets in isothermal discs have shown that in this case the $r_{\mathrm{sm}} = 0.5$ cubic potential yields unstable evolutions. This is due to the relatively steep centre which leads to a significant density enhancement for isothermal discs. Hence, we used in this case directly the much smoother ϵ-potential with $\epsilon = 0.8$ instead, which has been used before in a similar context (Cresswell et al. 2007), without having explored other choices here.

The gravitational torques and forces acting on the planet are calculated by integrating over the whole disc, where we apply a tapering function to exclude the inner parts of the

Hill sphere of the planet. Specifically, we use the smooth (Fermi-type) function

$$f_b(d) = \left[\exp\left(-\frac{d/R_H - b}{b/10}\right) + 1\right]^{-1} \tag{3}$$

which increases from 0 at the planet location ($d = 0$) to 1 outside $d \geq R_H$ with a midpoint $f_b = 1/2$ at $d = bR_H$, i.e. the quantity b denotes the torque-cutoff radius in units of the Hill radius. This torque-cutoff is necessary to avoid large, probably noisy contributions from the inner parts of the Roche lobe and to disregard material that is possibly gravitationally bound to the planet (Crida et al. 2009). Here we assume (as in our previous paper) a transition radius of $b = 0.8$ Hill radii, as a change in b did not influence the results significantly (Kley et al. 2009).

2.2. Initial setup

The three-dimensional (r, θ, ϕ) computational domain consists of a complete annulus of the protoplanetary disc centred on the star, extending from $r_{min} = 0.4$ to $r_{max} = 2.5$ in units of $r_0 = a_{Jup} = 5.2$ AU. In the vertical direction the annulus extends $7°$ below and above the disc's midplane, meaning $83° < \theta < 97°$. Here θ denotes the polar angle of our spherical polar coordinate system measured from the polar axis. The central star has one solar mass $M_* = M_\odot$, and the total disc mass inside $[r_{min}, r_{max}]$ is $M_{disc} = 0.01 \, M_\odot$. For the isothermal simulations we assume an aspect ratio of $H/r = 0.037$ for the disc, in very close agreement with the fully radiative models of our previous studies. For the radiative models H/r is calculated self-consistently from the equilibrium structure given by the viscous internal heating and radiative diffusion. The isothermal models are initialised with constant temperatures on cylinders with a profile $T(s) \propto s^{-1}$ with $s = r \sin\theta$. This yields a constant ratio of the disc's vertical height H to the radius s. The initial vertical density stratification is approximately given by a Gaussian:

$$\rho(r, \theta) = \rho_0(r) \exp\left[-\frac{(\pi/2 - \theta)^2 \, r^2}{2H^2}\right]. \tag{4}$$

Here, the density in the midplane is $\rho_0(r) \propto r^{-1.5}$ which leads to a $\Sigma(r) \propto r^{-1/2}$ profile of the vertically integrated surface density. In the radial and θ-direction we set the initial velocities to zero, while for the azimuthal component the initial velocity u_ϕ is given by the equilibrium of gravity, centrifugal acceleration and the radial pressure gradient. This corresponds to the equilibrium configuration for a purely isothermal disc.

For our fully radiative model we first run a 2D axisymmetric model (starting from the given isothermal equilibrium) to obtain a new self-consistent equilibrium where viscous heating balances radiative transport/cooling from the surfaces. After reaching that equilibrium, we extend this model to a full 3D simulation, by expanding the grid into ϕ-direction. The resulting disc for this model has $H/r \approx 0.037$ so we choose that value for our isothermal runs.

2.3. Numerical setup

Our coordinate system rotates at the initial orbital frequency of the planet (at $r = r_0$). We use an equidistant grid in r, θ, ϕ with a resolution of $(N_r, N_\theta, N_\phi) = (266, 64, 768)$ active cells for our simulations. At r_{min} and r_{max} we use damping boundary conditions for all three velocity components to minimise disturbances (wave reflections) at these boundaries. The velocities are relaxed

towards their initial state on a timescale of approximately the local orbital period. The angular velocity is relaxed towards the Keplerian values, while the radial velocities at the inner and outer boundaries vanish. Reflecting boundary conditions are applied for the density and temperature in the radial directions. We apply periodic boundary conditions for all variables in the azimuthal direction. In the vertical direction we set outflow boundary conditions for $\theta_{min} = 83°$ and $\theta_{max} = 97°$ (the surfaces of the disc). We use the finite volume code NIRVANA (Ziegler & Yorke 1997) with implicit radiative transport in the flux-limited diffusion approximation and the FARGO (Masset 2000) extension as described in Kley et al. (2009).

2.4. Simulation setup

In the first part of our model sequence we consider the orbital evolution of a planet with a fixed mass ($20 \, M_{Earth}$) on inclined orbits using different initial inclinations. For comparison we consider isothermal and fully radiative models. Using radiative discs here is a direct extension of a previous study under purely isothermal disc conditions using the same planet mass (Cresswell et al. 2007). We distinguish two different approaches for these $20 \, M_{Earth}$ models: first, a model sequence where the planet stays on a fixed inclined orbit and secondly where the planet is free to move inside the computational domain under the action of the planet-disc gravitational forces. For the second models we insert the planet in the disc and let it move immediately, but using a time-dependent mass growth of the planet (through the planetary potential) with a typical switch on time of 10 planetary orbits. For the first set of models the $20 \, M_{Earth}$ planet is inserted at the nominal mass in the disc at the start of the simulation. Initially the planet starts at a distance $r = a_{Jup} = 5.2$ AU from the central star. For the fully radiative simulations we set the ambient temperature to a fixed value of 10 K at the disc surface (at θ_{min} and θ_{max}), which ensures that all the internally generated energy is liberated freely at the disc's surface. This low temperature boundary condition works very well at optically thin boundaries and does not effect the inner parts of the optically thick disc (Kley & Lin 1999; Kley et al. 2009). In the second part of the project we consider sequences of models for a variety of planet masses. We note that a $20 \, M_{Earth}$ planet has in our simulations, using our standard resolution, a Roche radius of about 3.3 grid cells. In the last part we limit ourselves to a $20 \, M_{Earth}$ planet and simulate the evolution of planets with an initial eccentricity and inclination. For all isothermal simulations, which allow the planet to move freely inside the disc, we use the ϵ-potential. Only for isothermal simulations of planets on fixed inclined orbits, the cubic potential is used. Additionally, the cubic potential is used for all fully radiative simulations as well.

3. Models with an embedded planet on fixed circular inclined orbits

In this section we consider planets on fixed circular and inclined orbits embedded in either isothermal or fully radiative discs. From the disc forces acting on the planet on the fixed orbit we calculate its change of inclination and its migration rate. In this section all simulations use the cubic potential, featuring $M_{Planet} = 20 \, M_{Earth}$, and a semi-major axis of $a = 1.0$. Our simulations only cover up to $7°$ above and below the equatorial plane, as the disc gets very thin for these regions. However, we investigate the motion of planets for higher inclinations (for fixed

planets up to 15°). The results are not influenced by our limited vertical extent of our computational grid, as the density is very low in the upper layers of the disc.

3.1. Change of inclination

To determine the change of orbital elements for planets on fixed inclined orbits, we follow Burns (1976). If a small disturbing force dF (given per unit mass) due to the disc is acting on the planet, the planet changes its orbit. This small disturbing force dF may change the planetary orbit in size (semi-major axis a), eccentricity e and inclination i. The inclination i gives the angle between the orbital plane and some arbitrary fixed plane, which is in our case the equatorial ($\theta = 90°$) plane, which corresponds to the midplane of the disc. Only forces lying in the orbit plane can change the orbits size and shape, while these forces can not change the orientation of the orbital plane. In Burns (1976) the specific disturbing force is written as

$$\mathrm{d}F = R + T + N = R e_R + T e_T + N e_N, \quad (5)$$

where the e's represent an orthogonal unit vector triad. The perturbing force can be split in these components: R is radially outwards along r, T is transverse to the radial vector in the orbit plane (positive in the direction of motion of the planet), and N is normal to the orbit planet in the direction $R \times T$.

Burns (1976) finds for the change of inclination

$$\frac{\mathrm{d}i}{\mathrm{d}t} = \frac{aN \cos \xi}{H}, \quad (6)$$

where the numerator is the component of the torque which rotates the specific angular momentum $H = r \times \dot{r}$ about the line of nodes (and which thereby moves the orbit plane). The specific angular momentum H is defined as

$$H = \sqrt{GMa(1 - e^2)}. \quad (7)$$

The angle ξ is related to the true anomaly f in the following way $f = \xi - \omega$, with ω being the argument of periapsis. ξ describes the angle between the line of nodes and the planet on its orbit around the star. For our case of circular orbits the argument of periapsis ω is zero.

In the simulations the planet's inclination spans from $i = 0.5°$ to $i = 15.0°$, in the isothermal as well as in the fully radiative regime. In Fig. 1 we display the rate of change of inclination for planets on fixed inclined orbits in the isothermal and fully radiative scheme, after we average di/dt over 2 planetary orbits, after 150 orbits. As the angle ξ changes after every time step, one needs to average the quantity of di/dt over the time of a planetary orbit to determine an exact value for the change of inclination of the planetary orbit. For both thermodynamic systems the change in inclination is nearly identical and always negative, meaning that moving planets with a non zero inclination lose their initial inclination at a rate according to the current inclination. At $i = 4.0°$ the loss of inclination is at it's maximum and is reduced for higher and lower inclinations. For high inclined planets ($i > 6.0°$) this loss is di/d$t \propto i^{-2}$, as indicated by the short-dashed fit in black in Fig. 1, and for lower inclined planets ($i < 4.0°$) the inclination is damped with an exponential decay as indicated by the linear fits in light blue and purple in Fig. 1. This is identical to the behaviour found in Cresswell et al. (2007) and is also confirmed by our simulations of moving planets below.

From our measured di/dt for planets on fixed orbits, we can calculate the inclination damping timescale τ_{inc} according to

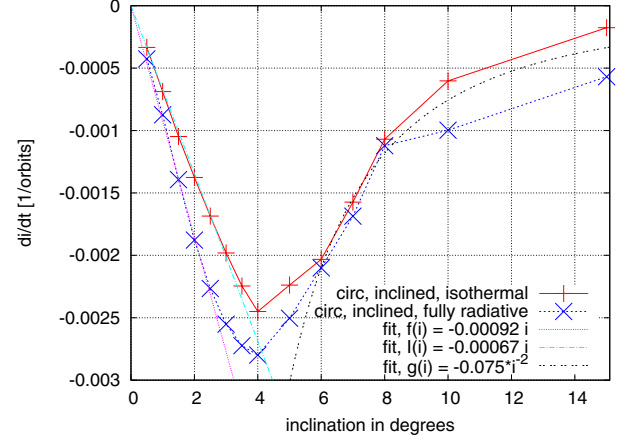$$\frac{\overline{\mathrm{d}i/\mathrm{d}t}}{i} = -\frac{1}{\tau_{\mathrm{inc}}} \quad (8)$$

Fig. 1. Calculated rate of change of the inclination (di/dt) for inclined 20 M_{Earth} planets on fixed circular orbits. Results for the isothermal (red) and fully radiative simulations (dark blue) are shown. Overlayed are in light blue and purple fits for the exponential decay of inclination for small inclinations and in black for the decay di/d$t \propto i^{-2}$ for larger inclinations.

with i being the inclination of the planet. In the exponential, small i regime we obtain for the isothermal simulations $\tau_{\mathrm{inc}} = 27$ orbits and for the fully radiative simulations $\tau_{\mathrm{inc}} = 20$ orbits. Below we compare this to the linear results of Tanaka & Ward (2004) and moving planets.

3.2. Change of semi-major axis

The power on the planet determines the change in semi-major axis of the planet, while the torque represents a change in both eccentricity and semi-major axis (Bitsch & Kley 2010). For circular orbits torque and power are identical. For that reason we display and refer only to the torque acting on the planet, instead of mentioning the power as well. A positive torque indicates outward migration, while a negative torque represents inward migration.

In Fig. 2 we display the torque acting on the planet for both thermodynamic systems. The torque is positive for the fully radiative disc and negative for the isothermal disc. In the fully radiative scheme the torque has its maximum at $i = 0.0°$ with a massive loss towards higher inclinations until about $i \approx 4.5°$, when the torque is about zero. For even higher inclinations the torque remains at about zero level. In the isothermal case the torque is negative and nearly constant for all inclinations, but with an increase towards higher inclinations.

As for circular orbits the torque determines the change of semi-major axis for our embedded planets, we expect a positive migration rate for planets in a fully radiative disc and a negative migration rate for planets in an isothermal disc. To determine a migration rate for planets on fixed orbits, we follow Burns (1976) again:

$$\frac{\mathrm{d}a}{\mathrm{d}t} = \frac{2}{(GM_*)^{1/2}} a^{3/2}(1 - e^2)^{-1/2} \left[R e \sin f + T(1 + e \sin f) \right], \quad (9)$$

where a is the semi-major axis, e the eccentricity, $f = \xi - \omega$ the true anomaly and R and T are radial and tangential directions of the disturbing force, see Eq. (5). Please note that only forces lying in the orbit plane can change the orbit size, and that for circular orbits the specific total torque on the planet is simply given by $\Gamma_{\mathrm{tot}} = aT$, with $\dot{H} = \Gamma_{\mathrm{tot}}$.
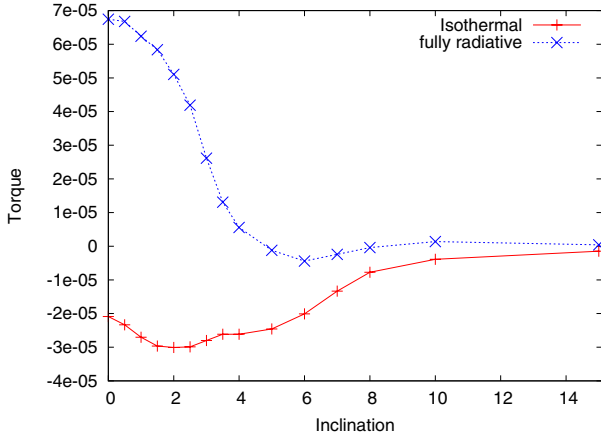
Fig. 2. Torque acting on a 20 $M_{\rm Earth}$ planet on a fixed inclined circular orbit in dependency of the inclination and thermodynamics of the disc. Torque and power are the same for planets on circular orbits. The torque has been averaged over 20 orbits, taken from $t = 180$ to $t = 200$ orbits for the isothermal (solid red line) and from $t = 120$ to $t = 140$ for the fully radiative simulation (dashed blue line).
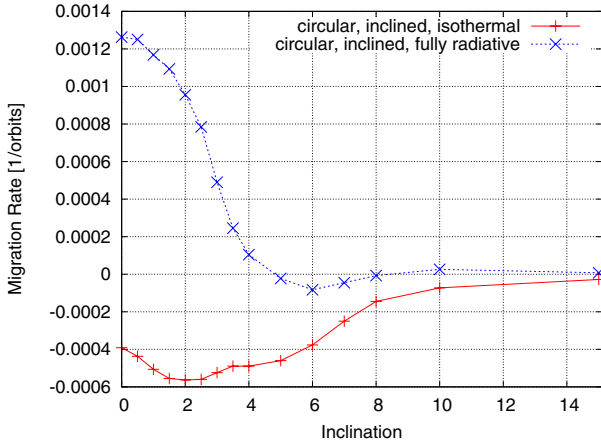

Fig. 3. Calculated rate of change of the semi-major axis ($\dot{a}/a$) for inclined 20 $M_{\rm Earth}$ planets on fixed, circular orbits. For inclinations lower than $i \le 4.5°$ we observe a positive migration rate, which suggest that low inclinations do not stop outward migration, while we observe a negative migration rate for the isothermal case.

The rate of migration is displayed in Fig. 3. In the fully radiative scheme the planet experiences a positive migration rate (outward migration) for all inclinations smaller than $i \le 4.5°$, but with a strong increase towards lower inclinations (about a factor of 10 for the difference between $i = 4.0°$ and $i = 1.5°$). For inclinations lower than $i \approx 1.5°$ the migration rate stays approximately constant. Planets with an inclination of $4.5°$ and higher seem to be stalled and migrate neither inwards nor outwards. The effects responsible for outward migration seem to be only valid in the small inclined case.

In the isothermal case the migration rate is nearly constant and negative with a slight increase towards higher inclinations, suggesting that an inclined planet will move inwards in the isothermal regime for low inclined planets. Higher inclined planets will move inwards only at a very small rate compared to their low inclined counterparts. For large i the change of semimajor axis approaches zero, as the planet's orbit is high above the dense regions of the disc, which are capable of influencing the planet's orbit.
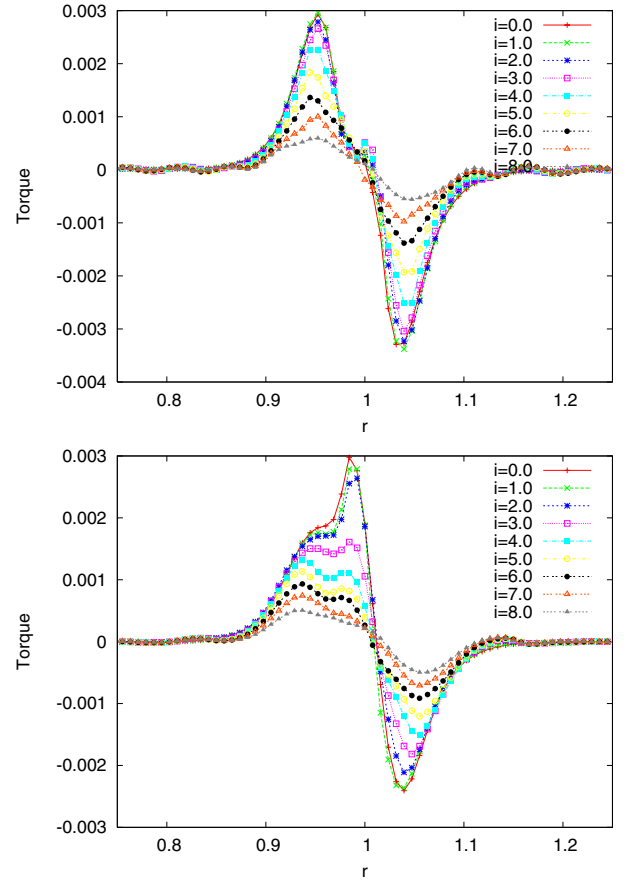

Fig. 4. Torque density acting on a planet on a fixed inclined orbit in dependency of the inclination of the planet embedded in an isothermal $H/r = 0.037$ disc (*top*) and a fully radiative disc (*bottom*). The snapshots are taken at $t = 90$ orbits for the isothermal simulations and at $t = 150$ orbits for the fully radiative simulations. At this time planet-disc interactions are in equilibrium and the planet is at its lowest point in orbit (lower culmination).

From these results we conclude that a planet with a non-zero initial inclination will lose this inclination in time. This inclination loss has in principal no effect on the trend of migration, so a planet in a fully radiative disc will migrate outwards, while a planet in an isothermal disc will migrate inwards. In one of the next chapters we will observe moving planets with a non-zero inclination, which will do exactly that.

3.3. Torque analysis

To understand the behaviour of the total torque in more detail we now analyse the space-time variation of the torque of the planet. For that purpose we introduce the radial torque density $\Gamma(r)$, which is defined in such a way that the total torque $\Gamma_{\rm tot}$ acting on the planet is given by

$$\Gamma_{\rm tot} = \int_{r_{\rm min}}^{r_{\rm max}} \Gamma(r) \, {\rm d}r. \tag{10}$$

The radial torque density has been a very useful tool to investigate the origin of the torques in our previous work on planets on fixed circular orbits. Even though the planet may be on an inclined orbit, this does not alter our definition of the radial torque density $\Gamma(r)$ which is calculated in any case with respect to the orbital plane of the planet. In Fig. 4 we display $\Gamma(r)$ for a selection of our planets in the isothermal and fully radiative regime.
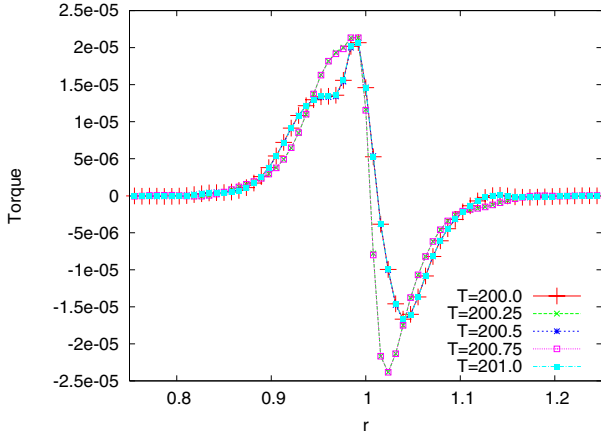
Fig. 5. Torque density acting on a 20 M_{Earth} planet on a fixed inclined orbit with $i = 2.0°$ in a fully radiative disc at different phases within its orbit. Integer (half integer) values of the indicated time refer to the upper (lower) culmination. At the intermediate quarterly orbit times the planet moves through the nodal line.

In the isothermal case the $\Gamma(r)$-function follows the same trend for all displayed inclinations. The only difference is near the planet, around the $r = 1.0$ region. The torque of the low inclined planets declines constantly, while the higher inclined planets ($2.0 \leq i \leq 4.0$) form a little spike in the $\Gamma(r)$ distribution, which disappears for even higher inclinations again. For higher inclinations the Lindblad-Torques become less and less pronounced, as can be seen in Fig. 4 (top panel). Please keep in mind that for the inclined planets the torque density changes during one orbit, as can be seen from the change in the total torque acting on the planet (top panel in Fig. 6). This is also illustrated in Fig. 5 for the planet with $i = 2.0°$. It can been seen that for symmetry reasons $\Gamma(r)$ is identical at upper and lower culmination, and at the crossings of the nodal line, respectively.

In Fig. 6 the torque acting on planets (please note that for circular orbits torque and power are identical) with different inclinations on fixed circular orbits (top) and the normal component of the disturbing force dF (bottom) for fully radiative discs is displayed. The torque acting on the planets oscillates with time, making two oscillations every orbit. The planet starts at the highest point in orbit (upper culmination) and evolves to the lowest point in orbit (lower culmination) in the time of half an orbit. Then the planet moves to the upper culmination again and reaches it at the end of the orbit. The planets with a lower inclination ($i < 4.0°$) have clearly a positive average torque, while for the planets with higher inclinations positive and negative contributions approximately cancel out such that the average total torque is very small (see Fig. 2). Higher inclinations also trigger higher amplitudes in the torque distributions. These amplitudes in the torque distribution suggest oscillations in the evolution of the semi-major axis of the planet (to a small degree), which are visible when the planet is allowed to move freely inside the disc (see Figs. 12, 13 and 15).

In the lower panel in Fig. 6 the normal component of the disturbing force $N \cos \xi$ is displayed. $N \cos \xi$ oscillates also twice in every orbit, as the torque, but it is slightly shifted with respect to the torque. Negative values indicate a reduction of inclination, while a positive force indicates an increase of inclination. The oscillations in $N \cos \xi$ indicate oscillations in the inclination, when the planet is allowed to move freely in the disc. Indeed, in case the planet moves inside the disc, these oscillations in the inclination become visible at the beginning of the simulations
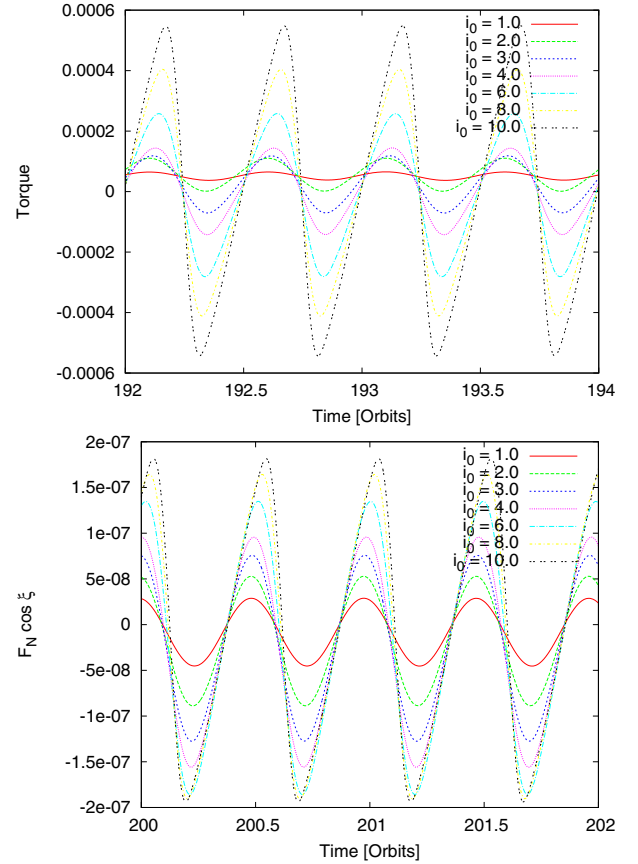

Fig. 6. In *the top panel* we display the evolution of the torque acting on planets in a fully radiative disc on fixed circular, inclined orbits in time. In *the bottom panel* the normal component of the disturbing force dF, $N \cos \xi$ as to be used Eq. (6), is displayed in dependency of time.

(see Figs. 11, 13 and 14 below). On average the normal component of the disturbing force $N \cos \xi$ is negative, which indicates inclination damping for all simulated inclinations, see Fig. 1.

For simulations in the isothermal regime, the results are nearly identical, with only one exception: the overall torque is negative, which results in inward migration. The normal component of the disturbing force, $N \cos \xi$, is also very similar compared to the results in the fully radiative regime. We therefore forgo to discuss the isothermal results in detail at this point.

To illustrate the dynamical impact of the planet on the disc, we display the surface density of planets with $i = 1.0°$ and $i = 4.0°$ in Fig. 7.

The surface density of the $i = 1.0°$ planet is very similar to that of a non inclined planet (not displayed here, but compared to bottom picture of Fig. 8 in Kley et al. 2009), and the torque density $\Gamma(r)$ is nearly identical. The surface density also shows no disturbances for the $i = 1.0°$ planet, so that we only observe the Lindblad Torques in the isothermal case, see Fig. 4. However, the surface density of the higher inclined planet ($i = 4.0°$) shows density disturbances near the planet. For the $i = 1.0°$ we also observe a higher density in the planets surroundings and a stronger pronounced spiral wave compared to higher inclined planets. The less pronounced spiral wave for the higher inclined planets leads to a smaller Lindblad Torque for these planets compared to the low inclined planets, which can be seen clearly in Fig. 4.

In Fig. 8 the density of a $r - \theta$ slice through the planets in the isothermal $H/r = 0.037$ disc is display. The planets are at their lowest point in orbit when the snapshot was taken. On the one
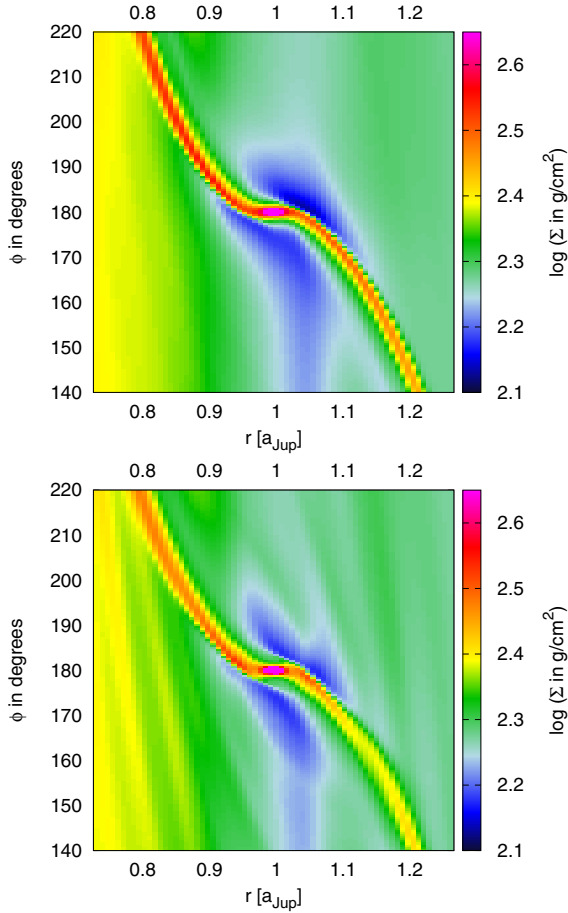
Fig. 8. Density (in g/cm³) of a $r - \theta$-slice through the isothermal $H/r = 0.037$ disc with embedded 20 M_{Earth} planets on fixed circular inclined orbits with $i = 1.0°$ (*top*) and $i = 4.0°$ (*bottom*). The planet is at its lowest point in orbit (lower culmination) at the time of the snapshot.

Fig. 7. Surface density for 20 M_{Earth} planets on fixed circular inclined orbits embedded in an isothermal $H/r = 0.037$ disc with $i = 1.0°$ (*top*) and $i = 4.0°$ (*bottom*). The planet is at its lowest point in orbit (lower culmination) at the time of the snapshot.

hand, the $i = 1.0°$ planet (top) has accumulated more mass in its vicinity as the $i = 4.0°$ planet (bottom), as the density in the middle of the disc is higher and thus it is easier to accumulate mass. On the other hand, the higher inclined planet seems to disturb the density structure of the disc stronger than the lower inclined planet. This distortion in the density distribution in the $r - \theta$ plane reflects in the distorted surface density structure, displayed in the bottom picture of Fig. 7.

In the fully radiative case, the torque density (Fig. 4) shows the well discussed spike in the torque distribution at $r = 0.984$ (see Kley et al. 2009). This spike is more pronounced for lower inclinations ($i \leq 2.0°$) and is reduced for the higher inclinations. This reduction for the torque density at $r = 0.984$ causes the total torque to decrease for higher inclinations, see Fig. 2. For higher inclinations the Lindblad Torques are also reduced compared to the lower inclined planets.

In Fig. 9 the surface density of 20 M_{Earth} planets in a fully radiative disc with $i = 1.0°$ and $i = 4.0°$ are displayed. The overall surface density distribution of the $i = 1.0°$ planet is nearly identical with the surface density distribution of a non inclined planet (see Fig. 12 in Kley et al. 2009), which is also supported by the identical torque density distributions. The surface density for the higher inclined planet ($i = 4.0°$) on the other hand shows some differences. The density ahead of the planet ($r < 1.0$ and $\phi > 180°$) is reduced and the density behind the planet ($r > 1.0$ and $\phi < 180°$) is increased compared to the density distribution of the low inclined ($i = 1.0°$) planet. This loss and gain of
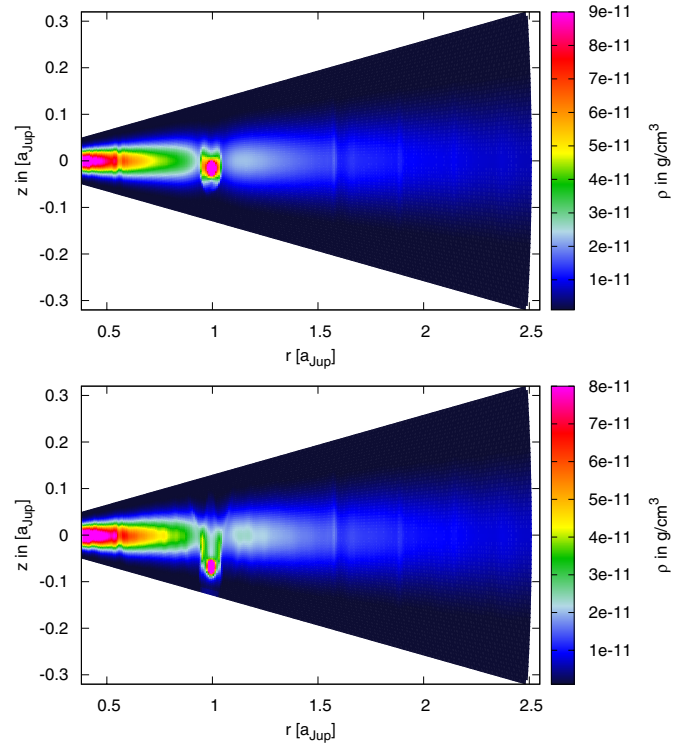
density results directly in a reduced spike (at $r = 0.984$) in the torque density (Fig. 4), which reduces the total torque. The density inside the planet's Roche lobe is also reduced in the high inclined case, as the planet can not accumulate as much mass as a lower inclined planet. This feature was also visible in the isothermal case, but keep in mind that the planet in the isothermal case accumulates more mass than in the fully radiative disc. Also the density in the spiral waves is reduced in the high inclined case, which results in lower Lindblad Torques compared to the low inclined case, see Fig. 4.

In Fig. 10 the density through the fully radiative disc (a $r - \theta$ slice) at the planets location for $i = 1.0°$ and $i = 4.0°$ is displayed. Clearly the higher inclined planet accumulated less mass than the lower inclined planet, as the density in the surroundings of the high inclined planet is reduced compared to the discs midplane. Also the higher inclined planet seems to disturb the disc's density more than the lower inclined planet, which results in small fluctuations in the surface density, see Fig. 9. The little fluctuations in the surface density are less compared to the isothermal case, as the radiative transport/cooling smoothes the density in the disc and the planet does not accumulate as much mass as in the isothermal case, which disturbs the density structure as well.

In the $r - \theta$ slices of the disc, the difference in the mass accumulation of the planet in the isothermal and fully radiative regime is very obvious. This effect is caused by the thermodynamics of the disc, as the isothermal disc is unable to heat and cool, the planet can accumulate more mass as in the fully radiative regime. Nevertheless, only in the fully radiative regime the calculated change of semi-major axis predicts outward migration for planets on fixed orbits with $i_0 \leq 4.5°$.

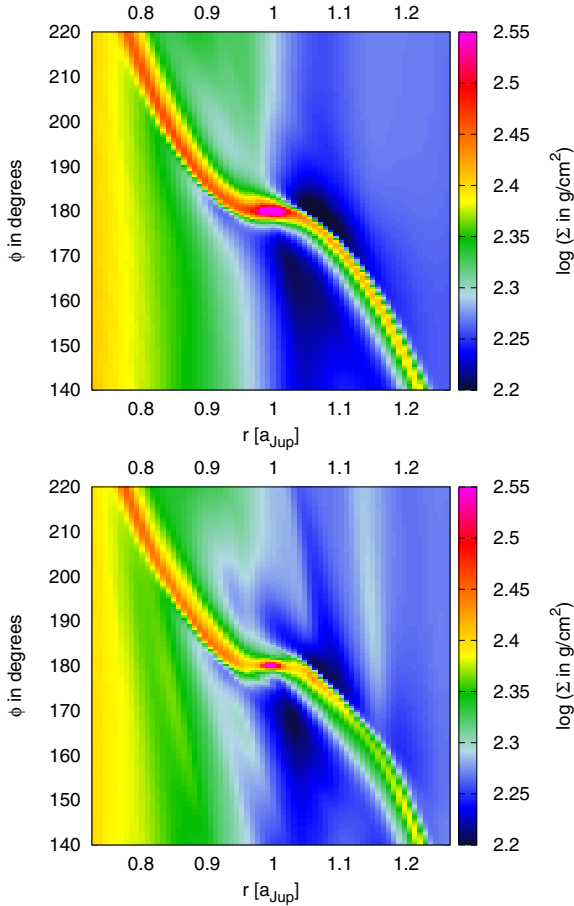**Fig. 9.** Surface density for 20 M_{Earth} planets on fixed circular inclined orbits embedded in a fully radiative disc with $i = 1.0°$ (*top*) and $i = 4.0°$ (*bottom*). The planet is at its lowest point in orbit (lower culmination) at the time of the snapshot.

4. Moving planets on initially inclined orbits

In the previous section we calculated the change of inclination and semi-major axis for 20 M_{Earth} planets on fixed inclined orbits in the isothermal and fully radiative regime. The results stated that the planets will lose their inclination in time and will migrate inwards in the isothermal and outwards in the fully radiative scheme (for $i_0 \leq 4.5°$). We now want to confirm these results by allowing the planets to move freely inside the disc. For the following simulations we use our standard resolution, with a 20 M_{Earth} planet embedded at $r = 1.0$ with different inclinations i. The discs thickness is $H/r = 0.037$. In the first 10 orbits of the planetary evolution the mass of the planet will rise until it reaches its desired mass of 20 M_{Earth} after 10 planetary orbits. This way the disc will not be disturbed as much as by putting a planet with its full mass inside the disc at once. By monitoring inclination and semi-major axis at the same time for a given planet, we can easily observe what influence the inclination has on the migration of the planet. The planets embedded in the isothermal disc are modelled with the ϵ-potential, using $r_{\mathrm{sm}} = 0.8$, while the planets embedded in the fully radiative disc are modelled using the cubic potential with $r_{\mathrm{sm}} = 0.5$.

4.1. Isothermal disc

Our disc only extends $7°$ above and below the discs midplane, so when simulating a planet with a higher inclination than that,
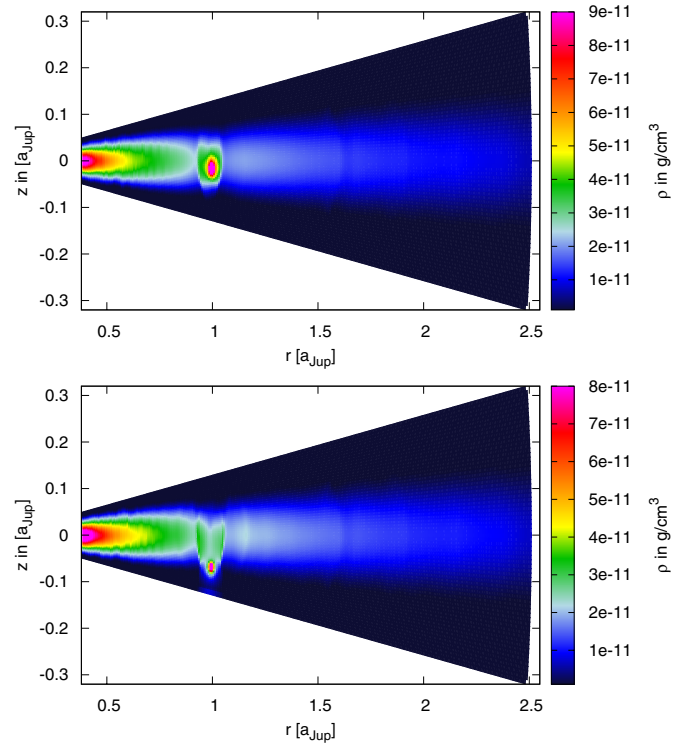
Fig. 10. Density (in g/cm³) of a $r - \theta$-slice through the fully radiative disc with embedded 20 M_{Earth} planets on fixed circular inclined orbits with $i = 1.0°$ (*top*) and $i = 4.0°$ (*bottom*). The planet is at its lowest point in orbit (lower culmination) at the time of the snapshot.

it is not fully embedded in the disc any more. As the disc's material is concentrated mainly in the middle of the disc, the material high above or below the disc's midplane will only have a small effect on the planet anyway. Test calculations with an extended θ region of the disc ($10°$ above and below the discs midplane) and an $i_0 = 8.0°$ 20 M_{Earth} planet have shown that we do not need such a high extension above and below the disc. The aspect ratio for the disc is $H/r = 0.037$ in the isothermal case, as this aspect ratio corresponds to the aspect ratio of the fully radiative disc.

In Fig. 11 the evolution of inclination of a 20 M_{Earth} planet in an isothermal $H/r = 0.037$ disc is displayed. After the planets have reached their final mass after 10 orbits, the inclination begins to drop immediately. Up to $i = 4.0°$ the planet's loss of inclination is increasing, while for even higher inclinations the damping of inclination is slowed down again (see Fig. 1). High inclined planets will first lose inclination at a quite slow rate, but as their inclination is damped the damping rate increases until the inclination reaches $\approx 4.0°$ and will slow down after that until the planets inclination is damped to zero. This results confirms our results for planets on fixed orbits.

When the planet remains in the main body of the disc for $i < H/r$ (i in radians), the damping of inclination is exponential: $\mathrm{d}i/\mathrm{d}t \propto -i$. By following Tanaka & Ward (2004) the linear damping rate for a small planet mass and a small inclination can be obtained:

$$\overline{\mathrm{d}i/\mathrm{d}t}{i} = -\frac{1}{\tau_{\mathrm{inc}}} = -\frac{0.544}{t_{\mathrm{wave}}} \tag{11}$$

with the characteristic time

$$t_{\mathrm{wave}} = q^{-1} \left(\frac{\Sigma_{\mathrm{P}} a^2}{M_*}\right)^{-1} \left(\frac{c_{\mathrm{s}}}{a\Omega_{\mathrm{P}}}\right)^4 \Omega_{\mathrm{P}}^{-1}. \tag{12}$$
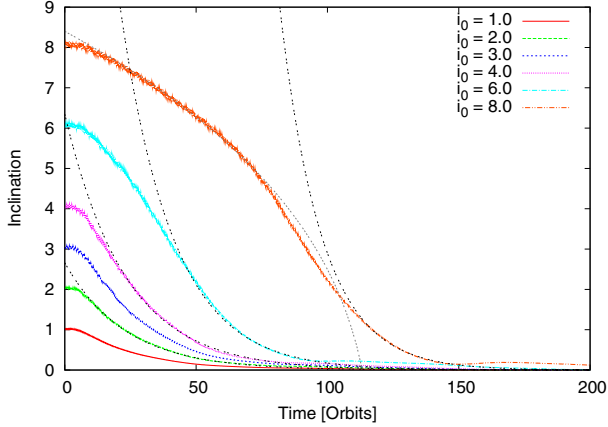
Fig. 11. Time evolution of inclination for 20 $M_{\rm Earth}$ planets with individual starting inclinations ranging from $i = 1.0°$ to $i = 8.0°$ in an isothermal $H/r = 0.037$ disc. The damping of inclination follows the trend of the calculated change of inclination for planets on fixed orbits, see Fig. 1. The black dotted lines indicate our manual fitting with $\tau_{\rm inc} = 23$ and in the $i_0 = 8.0°$ case an additional fit provides for a $di/dt \propto i^{-2}$ fit.

Fig. 12. Time evolution of semi-major axis for 20 $M_{\rm Earth}$ planets with individual starting inclinations ranging from $i = 1.0°$ to $i = 8.0°$ in an isothermal $H/r = 0.037$ disc. The dashed black line indicates a fit to the results with a slope of -3.45×10^{-4}/orbit. The change of semi-major axis follows the trend of the change determined for planets on fixed orbits, see Fig. 3.

Table 1. Exponential damping rate $\tau_{\rm inc}$ (in orbits), obtained from our isothermal and fully radiative simulations for three studied cases of planets in discs compared with the linear rate, as given by Tanaka & Ward (2004).

	Linear 3D	**Fixed orbit**	**Moving orbit**
iso $H/r = 0.037$	14.2	27	23
iso $H/r = 0.05$	47.25	–	53
fully radiative	27.7	20	26.5

Notes. Shown are results for planets on fixed orbits and for moving planets.

In Table 1 we display $\tau_{\rm inc}$ for the isothermal and fully radiative simulations. We compare the linear estimate according to Eqs. (11) and (12) with our full non-linear results from the fixed and moving planet simulations.

For our isothermal $H/r = 0.037$ simulations we estimate a linear damping time scale of $\tau_{\rm inc} = 14.2$ orbits, which is about a third smaller than our obtained result $\tau_{\rm inc} = 23$ for planets on moving orbits (see fits in Fig. 11). The difference between our actual fit and the linear value can be caused by the relatively small aspect ratio of the disc ($H/r = 0.037$), because the linear theory is formally valid only for embedded planets with $H \gg R_{\rm Hill}$. Below, we present additional result for an $H/r = 0.05$ disc and find indeed better agreement of linear and fully non-linear results. However, our obtained $\tau_{\rm inc} = 23$ for moving planets is very close to the predicted damping time scale of $\tau_{\rm inc} = 27$ for planets on fixed orbits, demonstrating the consistency of our results.

The exponential damping law should be only valid up to $i \approx H/r$, but Cresswell et al. (2007) stated that it is valid up to $i \approx 2H/r$, which in fact reflects our findings. The higher inclined planets do not lose inclination with an exponential rate at the beginning of the simulations, but with $di/dt \propto i^{-2}$. This is also indicated through the black dotted line in Fig. 11 for the $i_0 = 8.0°$ planet. As the planets lose their inclination, the damping becomes exponential again (at about $i \approx 3.0°$).

In Fig. 12 the evolution of the semi-major axis in an isothermal $H/r = 0.037$ disc is displayed. After a few orbits the semi-major axis decreases for all planets. During time the semi-major
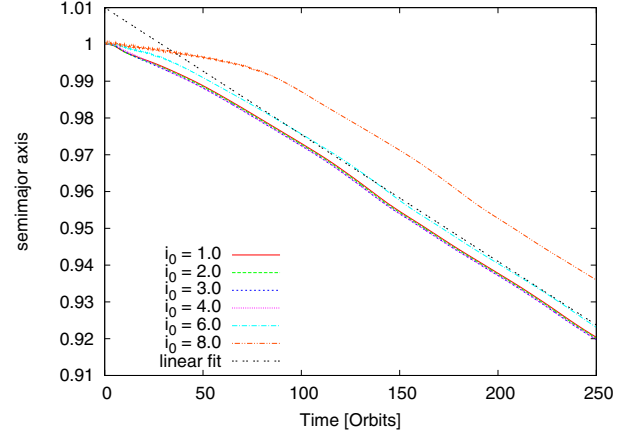
axis shrinks more and more, as you would expect from low mass planets in an isothermal disc. In the beginning the planets with $i_0 = 8.0°$ and $i_0 = 6.0°$ have a slower inward migration rate than the other planets, but as the inclination is damped in time, the inward migration settles for the same rate for all planets, although it takes about 80 orbits for the $i_0 = 8.0°$ planet. The initial higher inclination just delays the inward migration for a few planetary orbits, as could be expected from our results for planets on fixed orbits, see Fig. 3.

The observed migration rate for all planets is constant after the inclination has been damped. The black dashed line in Fig. 12 indicates a linear fit for the evolution of the semi-major axis with $\dot{a} = -3.45 \times 10^{-4}$/orbit. This decrease of semi-major axis from planets on moving orbits is within 15% of the result for planets on fixed orbits in Fig. 3. The slight difference may be just due to the different setup, stationary versus moving and cubic versus epsilon potential. Additionally, the fit in Fig. 12 is for a later evolutionary time, where the planet has already lost a few percent of its semi-major axis.

In our past simulations we found a dependence of the migration rate/torques due to the aspect ratio of the disc (Kley et al. 2009; Bitsch & Kley 2010). It is now logical to assume that the aspect ratio of a disc will change the damping of inclination for inclined planets as well. In Fig. 13 we display the evolution of the semi-major axis (top) and inclination (bottom) of planets embedded in an isothermal $H/r = 0.05$ disc.

The inward migration of the planets in the $H/r = 0.05$ disc is slower compared to planets embedded in a $H/r = 0.037$ disc, which is in agreement with Tanaka et al. (2002). The inclination damping is slower in the $H/r = 0.05$ disc by a factor of 2 to 3. Nevertheless, the final outcome is the same, an initially high inclination reduces the inward migration in the beginning, but as inclination is damped, the inward migration settles for the same rate for all the inclinations (but with different rates for different aspect ratios).

The theoretical, linear damping of inclination obtained by following Tanaka & Ward (2004) is $\tau_{\rm inc} = 47.25$ orbits (Eq. (12)), which is slightly smaller than our fitted value of $\tau_{\rm inc} = 53$ orbits (Fig. 13, bottom). The numerically obtained ratio of the migration rates ($53/23 \approx 2.3$) differs from the theoretical linear ratio of $(0.05/0.037)^4 \approx 3.3$. As the colder disc makes linear theory
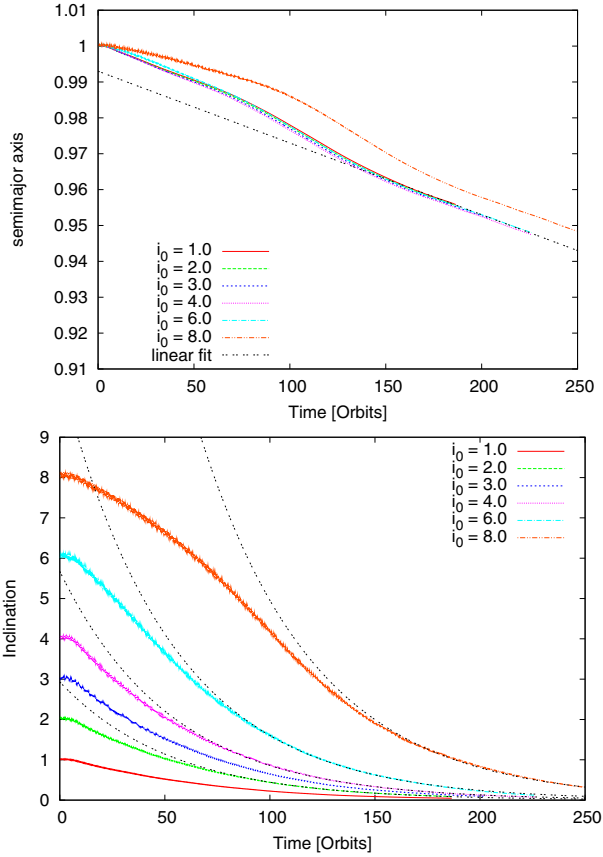
Fig. 14. Time evolution of inclination for 20 M_{Earth} planets with individual starting inclinations ranging from $i = 1.0°$ to $i = 4.0°$ in a fully radiative disc. The damping of inclination follows the trend of change of inclination for planets on fixed orbits, see Fig. 1. The black dotted lines indicate our manual fitting with $\tau_{\mathrm{inc}} = 26.5$ for planets with $i_0 = 2.0°$, $4.0°$, $6.0°$ and $i_0 = 8.0°$, which seems very good in the beginning/middle phase of the inclination damping. In the $i_0 = 8.0°$ case an additional fit provides for a $\mathrm{d}i/\mathrm{d}t \propto i^{-2}$ fit in the beginning of the evolution.

Fig. 13. Time evolution of the semi-major axis (*top*) and inclination (*bottom*) of a 20 M_{Earth} planet in an isothermal $H/r = 0.05$ disc. The planets initial inclinations reach from $i_0 = 1.0°$ to $i_0 = 8.0°$. The dashed black line in *the top panel* indicates a linear fit to the results with a slope of -2×10^{-4}/orbit. The black dotted lines in the evolution of inclination (*bottom*) indicate our manual fitting with $\tau_{\mathrm{inc}} = 53$.

less applicable in these circumstances, we can infer that the results obtained for the larger $H/r = 0.05$ disc are more accurate. The numerical exponential decay in the simulations with moving planets matches our estimated rate for planets on fixed orbits quite well. The higher pressure inside the disc seems to have a smoothing effect on the damping, resulting in more accurate results for discs with higher aspect ratio.

For the moving planets, the measured migration rate ($\mathrm{d}a/\mathrm{d}t$) for the $H/r = 0.037$ disc is approximately larger by a factor of $(0.05/0.037)^2$ compared to the $H/r = 0.05$ disc (see dashed black line fit in Fig. 13, top), which is to be expected in the linear case.

In an isothermal disc, inclined planets lose inclination and semi-major axis immediately after they are released in the disc, as predicted by our calculations of the change of inclination and semi-major axis for planets on fixed orbits. The migration rate is the same for all initial inclinations, a higher inclination just delays the inward migration for a few orbits.

4.2. Fully radiative disc

In the fully radiative regime we simulate planets to an inclination up to $i = 8.0°$. As always we use a 2D model in $r - \theta$ direction in the radiative equilibrium for the starting configuration of our 3D fully radiative disc. This procedure is described in more detail in (Kley et al. 2009). As in the isothermal case, the planet needs 10 planetary orbits to reach its full mass.
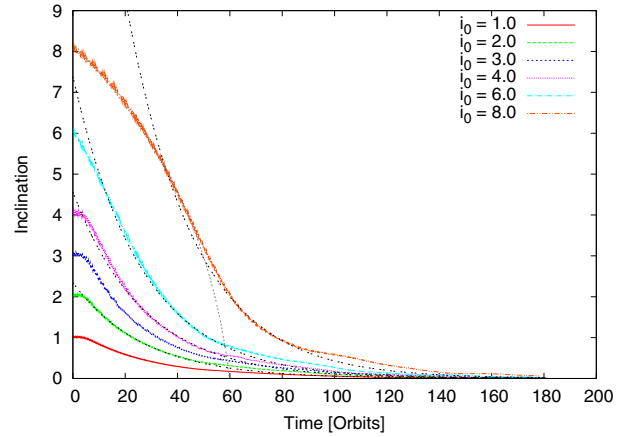
In Fig. 14 the change of inclination for moving planets in a fully radiative disc is displayed. The inclinations range from $i_0 = 1.0°$ to $i_0 = 8.0°$. The planets inclination reduces as soon as the planet is released in the disc according to the rate found in Fig. 1. After about 160 orbits the inclination of all planets has reached zero, so that the planet is now orbiting in the equatorial plane.

The estimated linear value for the damping of inclination in the radiative disc is $\tau_{\mathrm{inc}} = 27.76$ orbits (Eq. (12)), which lies within about a few percent of our fitted value of $\tau_{\mathrm{inc}} = 26.5$ orbits for moving planets. The difference with the calculated damping timescale $\tau_{\mathrm{inc}} = 20$ orbits for planets on fixed orbits is slightly larger in this case (see Table 1). But one should keep in mind as well that the exponential fit is valid for very low inclinations in the isothermal case as well, while it is only valid down to $\approx 0.5°$ in the fully radiative scheme.

On the other hand, the decay of inclination for initially high inclined planets fits even a little better than in the isothermal case, and the trend of an $\mathrm{d}i/\mathrm{d}t \propto i^{-2}$ decay is clearly visible.

In Fig. 15 the evolution of the semi-major axis of planets with initial inclination is displayed. After the planets have reached their final mass at 10 planetary orbits, the initially lower inclined (i up to $4.0°$) planets start to migrate outwards as expected from Fig. 3. The migration rates for planets on fixed orbits also matches nicely with the determined migration rate of 1.35×10^{-3}/orbit for planets on moving orbits. The two higher inclined planets first stay on their initial orbit before they start their outward migration. It seems that the planet has to lose a certain amount of inclination before it can start to migrate outwards. This result is in agreement with our observations for planets on fixed inclined orbits. A higher inclination weakens the torque responsible for outward migration and if the inclination is too high, the outward migration stops.

The planets seem to migrate outwards at nearly the same speed for all initial inclinations up to $4.0°$. But before the planets start to migrate outwards their initial inclination is damped by about 25% for all initial inclinations, which explains the similar migration speed for these planets, see Fig. 3.

Low inclinations seem to have only little effect on the migration of planets in the fully radiative scheme, but if the inclination
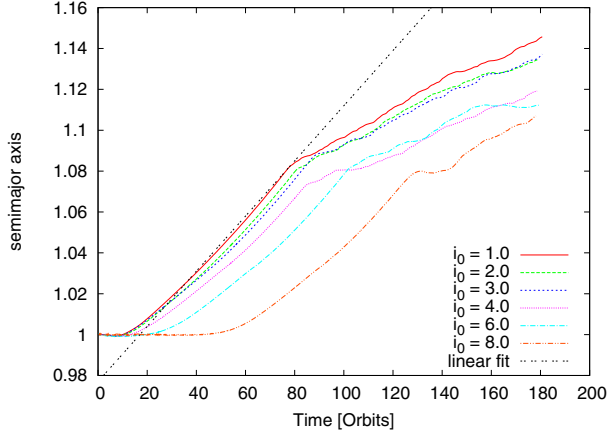
Fig. 15. Time evolution of semi-major axis for 20 $M_{\rm Earth}$ planets with individual starting inclinations ranging from $i = 1.0°$ to $i = 8.0°$ in a fully radiative disc. The change of semi-major axis follows the trend of change for planets on fixed orbits, see Fig. 3. The dashed black line in the top panel indicates a linear fit to the results with a slope of 1.35×10^{-3}/orbit.

of the planet is so high that its orbit is at some times high above the midplane of the disc, the disc becomes so thin that outward migration is not possible any more.

5. Planets with different masses

Small inclinations seem to have no big effect on migration for a 20 $M_{\rm Earth}$ planet on a circular orbit in the isothermal or fully radiative scheme. The planet's inclination is reduced in both thermodynamic systems and it migrates inwards in the isothermal and outwards in the fully radiative scheme. In our previous work we found that planets up to ≈ 33 $M_{\rm Earth}$ migrate outwards in a fully radiative disc (Kley et al. 2009). Planets with higher planetary masses migrate inwards, and considering our previous results it is unlikely that inclination changes this. Nevertheless we here present simulations of planets with masses ranging from 20 up to 100 $M_{\rm Earth}$ in an isothermal $H/r = 0.037$ disc and in a fully radiative disc. We only present results for moving planets with our usual tool for increasing the planetary mass to its designated mass during the first 10 orbits.

For all simulations we limit ourselves to the cases of $i_0 = 1.0°$ and $i_0 = 4.0°$ for all planetary masses, in the isothermal $H/r = 0.037$ disc as well as in the fully radiative disc. Additionally, we display Jovian mass planets with inclinations up to 15° in the isothermal case. For the isothermal case, we again use the ϵ-potential with a smoothing length of $r_{\rm sm} = 0.8$, as it turned out to be more stable in the isothermal case than the cubic potential, while we use the cubic $r_{\rm sm} = 0.5$ potential for the fully radiative simulations.

In all simulations displayed in this section the planet is inserted in the disc and starts to move immediately. This means that a massive planet will open a gap in time in the initially unperturbed disc. If the planet were allowed to open a gap before it starts to move in the disc, the evolution of the planet, especially the evolution of inclination, would be slower since an open gap slows down migration and inclination damping.

5.1. Isothermal disc

In Fig. 16 the evolution of inclination for planets with $i_0 = 1.0°$ (top) and $i_0 = 4.0°$ (bottom) for different planetary masses in an
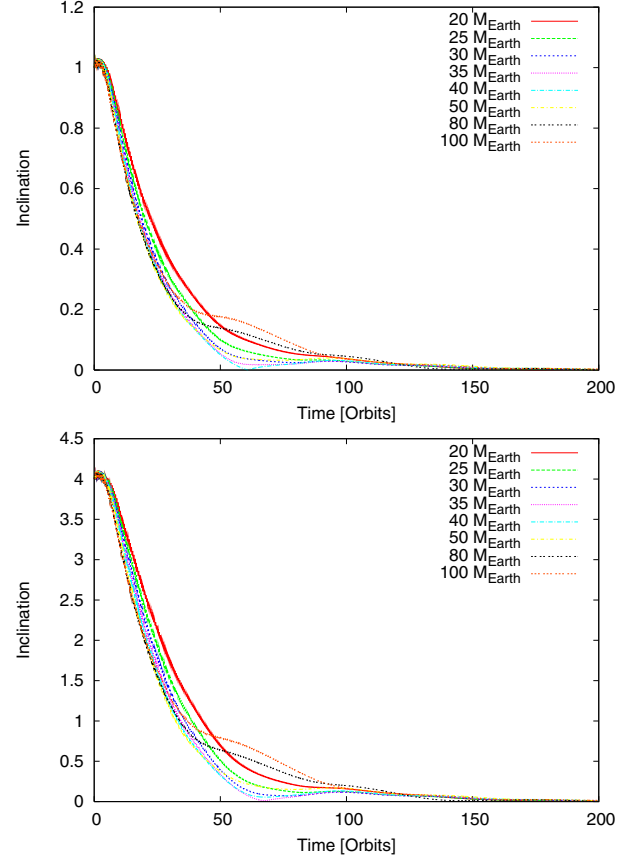

Fig. 16. Time evolution of the inclination for planets with $i_0 = 1.0°$ (*top*) and $i_0 = 4.0°$ (*bottom*) for different planetary masses in an isothermal $H/r = 0.037$ disc.

isothermal $H/r = 0.037$ disc is displayed. The inclination drops immediately after the planet reaches its destined mass at nearly the same rate for all planetary masses in both cases, for the $i_0 = 1.0°$ and $i_0 = 4.0°$ case. It seems that a higher planetary mass results in a slightly faster damping rate for the inclination. However, when the inclination reaches about 20% of the initial inclination, the 80 and 100 $M_{\rm Earth}$ planets stop their fast inclination damping for a few orbits. After about 150 orbits the inclination of all planets is damped to zero, even for the initially more highly inclined planets.

In Fig. 17 we display the surface densities for planets with different masses for the $i_0 = 1.0°$ (top) and $i_0 = 4.0°$ (bottom) cases after 60 planetary orbits. The two surface density profiles are very similar, although the planets have a different starting inclination i_0 and a different inclination at the time of the snapshot. As the inclination of the $i_0 = 4.0°$ and $i_0 = 1.0°$ planets evolves very similar (in the trend), it seems not surprising that the surface densities reflect this behaviour. On the other hand, the surface density profiles after 60 orbits do not give a clear hint to explain the slowed down inclination damping for the high mass planets when they reach $\approx 20\%$ of the initial inclination. As expected, higher mass planets clear deeper and wider gaps inside the disc.

The measured damping time scale $\tau_{\rm inc}$ for planets with different planetary masses is displayed in Fig. 18. Starting from the smallest planet in our calculations, the 20 $M_{\rm Earth}$, the damping time scale reduces until the planets mass is 40 $M_{\rm Earth}$. For higher mass planets the damping time scale increases again. The increase for the 80 and 100 $M_{\rm Earth}$ planets should be handled with
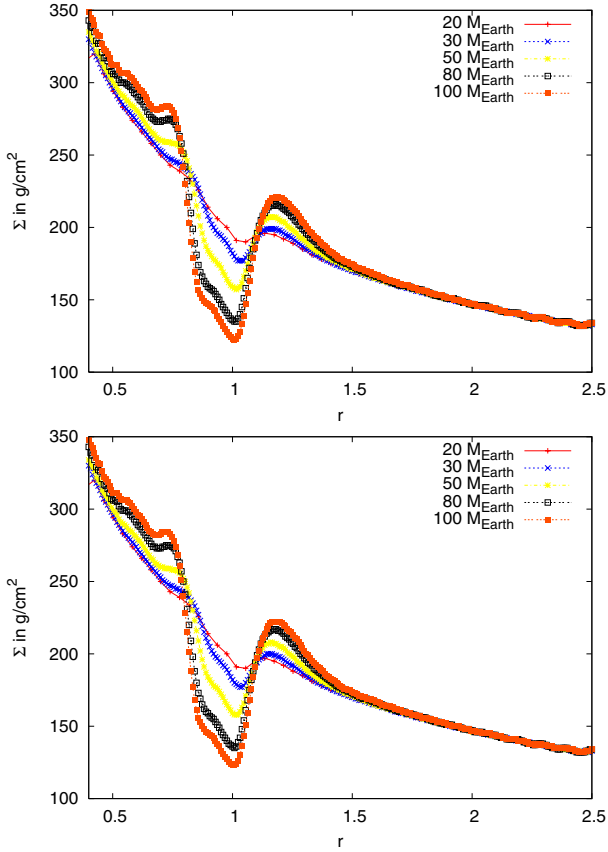
Fig. 17. Surface density for planets on initial inclined, circular orbits with $i_0 = 1.0°$ (*top*) and $i_0 = 4.0°$ (*bottom*) after 60 planetary orbits.
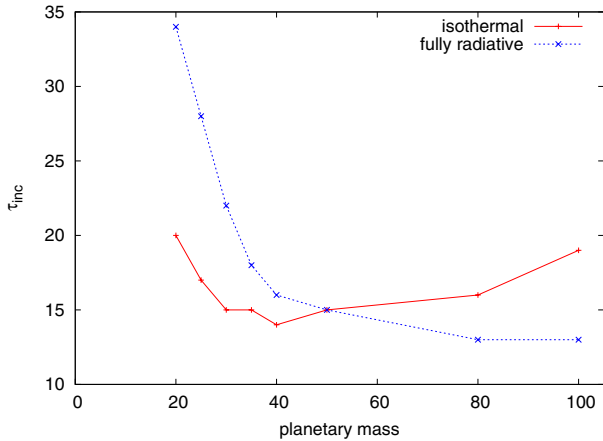

Fig. 18. Measured inclination damping time scale τ_{inc} for planets with different planetary masses in the isothermal and fully radiative regime.

care, as the measurement for these planets is quite difficult due to the bump in the evolution of inclination. If we do not include these two planets in our thoughts, we can safely conclude, that the inclination damping increases with the planetary mass. The inclination of a more massive planet will be damped faster than the inclination of a smaller planet, even more so for radiative discs.

In Fig. 19 the evolution of the semi-major axis for the above mentioned planets is displayed. Interestingly it seems that the evolution of the semi-major axis does not depend on the inclination for circular orbits. All planets with equal masses follow the same evolution independent of the initial inclination.
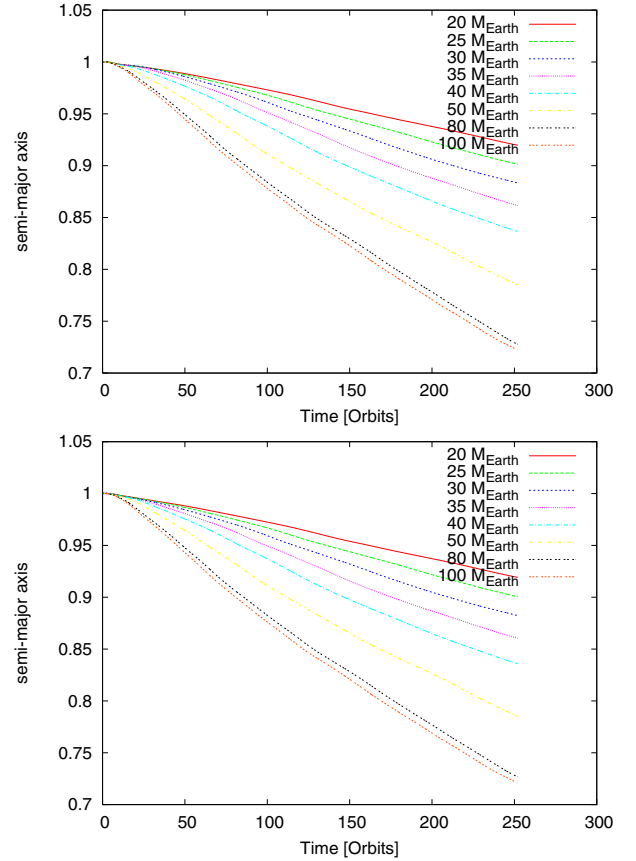
Fig. 19. Time evolution of the semi-major axis for planets with $i_0 = 1.0°$ (*top*) and $i_0 = 4.0°$ (*bottom*) for different planetary masses in an isothermal $H/r = 0.037$ disc.

For the 20 M_{Earth} planet we found that the migration rate in the isothermal case does not depend much on the inclination of the planet, see Fig. 3. For higher mass planets this feature seems to be true as well. Of course, the planets migrate inwards at a speed dependent on the planetary mass. A higher planetary mass results in a more rapid inward migration of the planet, as it is predicted by linear theory (Tanaka et al. 2002), although the theory formally applies only for an unperturbed disc. Our discs, however, show clear signs of perturbation in the surface density profile (Fig. 17).

In Fig. 20 the evolution the inclination for planets with a Jovian mass (and for an additional planet with 20 M_{Earth}) in isothermal discs with different aspect ratios is displayed. The damping of inclination follows the predicted trend that the inclination of planets embedded in discs with smaller aspect ratio ($H/r = 0.037$) is damped faster than the inclination of planets embedded in discs with higher aspect ratio ($H/r = 0.05$), which was the result for smaller mass planets in our previous isothermal simulations as well. Marzari & Nelson (2009) stated that inclination damping of higher mass planets (e.g. Jovian mass) is considerably faster than for low mass planets (e.g. 20 M_{Earth}). Figure 20 shows clearly the same result for high inclinations ($i_0 = 15.0$), as the 20 M_{Earth} planet loses inclination at a much slower rate.

However, for low inclinations ($i < 4.0°$) the damping of inclination for Jovian mass planets is considerably slower than for low mass planets. The damping time scales obtained by fitting our simulations are considerably higher for Jovian mass planets
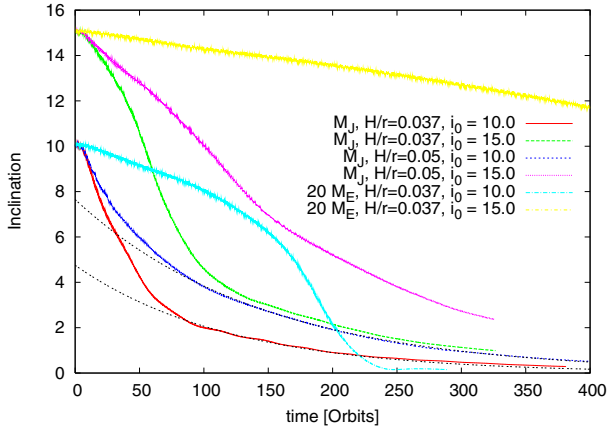
Fig. 20. Time evolution of inclination for Jovian mass planets in isothermal $H/r = 0.037$ and $H/r = 0.05$ discs. The evolution of a 20 M_{Earth} planet in an isothermal $H/r = 0.037$ disc is added for the inclination plot. The black dotted lines indicate a fit with $\tau_{\text{inc}} = 120$ for a Jovian mass planet in an $H/r = 0.037$ disc and a fit with $\tau_{\text{inc}} = 145$ for a Jovian mass planet in a $H/r = 0.05$ disc.

in isothermal discs, in the $H/r = 0.037$ disc $\tau_{\text{inc,Jup}} = 120 > 23 = \tau_{\text{inc},20M_{\text{E}}}$ as well as in the $H/r = 0.05$ disc $\tau_{\text{inc,Jup}} = 145 > 53 = \tau_{\text{inc},20M_{\text{E}}}$. The $i_0 = 10.0°$ planet with 20 M_{Earth} reflects this behaviour very well. First the damping of inclination is slower than for a Jovian mass planet, then the damping of inclination increases and the planet ends up in the midplane of the disc. The damping of inclination strongly depends on the interactions between disc and planet. As the Jovian mass planet opens a gap in the disc during the time of its evolution, the interactions between planet and disc are reduced, when the gap is opened. Therefore the damping of inclination of a Jovian mass planet is slowed down compared to a 20 M_{Earth} planet, when the inclination is already damped to about $i \approx 4.0°$ after the planet has evolved for about 120 orbits. After the gap has opened, only little mass remains adjacent to the planet to provide continuing damping. In the beginning of the simulations the gap has not opened yet and inclination damping is faster.

Overall, the damping of inclination starting from high inclinations ($i_0 = 15°$) is faster for planets with a Jovian mass compared to small mass planets (20 M_{Earth}) as the damping time of inclination at high inclinations is much slower for low mass planets, which overcompensates the faster damping at low inclinations. This is in agreement with the statement of Marzari & Nelson (2009).

Inclination seems to have no visible effect on the migration of planets inside an isothermal disc, as long as the planet's orbit is circular. Eccentric orbits, on the other hand, tend to change the migration rate of the planet. Later on, we also investigate planets on inclined and eccentric orbits at the same time.

5.2. Fully radiative disc

In Fig. 21 the evolution of inclination for planets with $i_0 = 1.0°$ (top) and $i_0 = 4.0°$ (bottom) for different planetary masses in a fully radiative disc is displayed. The inclination is damped for all planetary masses, but a higher planetary mass favours a faster damping of inclination for both starting inclinations. After about 150 orbits the inclination of all planets with both individual starting inclinations is damped to approximately zero. The damping rate of the inclination is about the same for the fully radiative and the isothermal $H/r = 0.037$ disc.
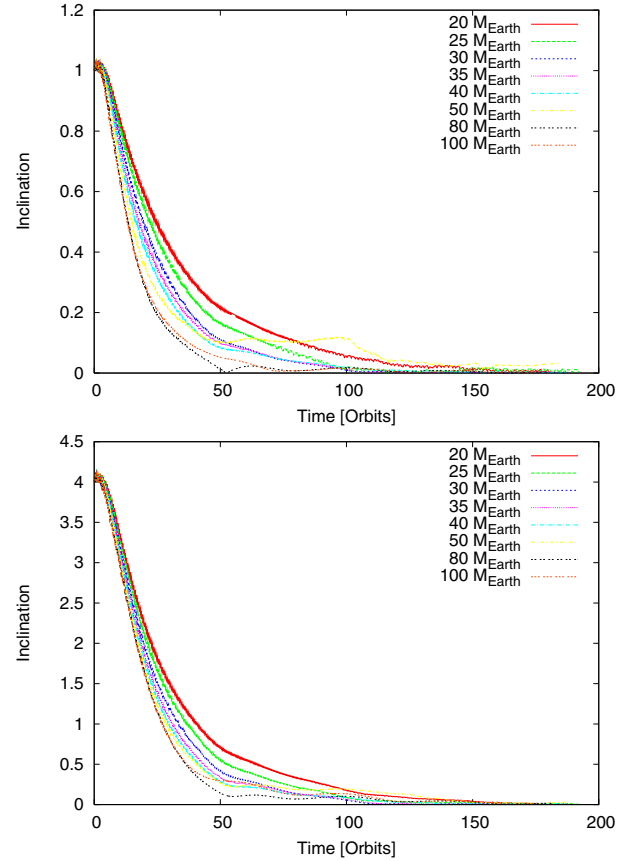

Fig. 21. Time evolution of the inclination for planets with $i_0 = 1.0°$ (*top*) and $i_0 = 4.0°$ (*bottom*) for different planetary masses in a fully radiative disc.

In Fig. 18 the measured damping time scale τ_{inc} is displayed for isothermal and fully radiative simulations. In the fully radiative case, the damping time scale is reduced for increasing planetary masses. If the planet reaches a certain mass (about 80 M_{Earth}), the damping time scale is not reduced any more. As the planets start to open gaps in the disc, the damping of inclination is not further accelerated. It seems that gap opening planets do not only migrate inwards at the same speed, independent of the planets mass, but also damp their inclination at the same speed.

In Fig. 22 the evolution of the semi-major axis for planets with $i_0 = 1.0°$ (top) and $i_0 = 4.0°$ (bottom) for different planetary masses in a fully radiative disc is displayed. As expected from our previous simulations (Kley et al. 2009) only planets with a planetary mass of $M_{\text{P}} \leq 33$ M_{Earth} migrate outwards, while heavier objects migrate inwards. The 35 and 40 M_{Earth} planets seem to migrate inwards just a little bit, before their migration is nearly stopped. The higher mass planets (50, 80 and 100 M_{Earth}) migrate inwards at nearly the same speed as the planets inside the isothermal $H/r = 0.037$ disc. These observations are independent of the planets inclination.

The outward migrating low mass planets travel outwards at a slightly faster speed in the $i_0 = 1.0°$ case compared to the $i = 4.0°$ simulations. This can be expected, as the calculated migration rate for 20 M_{Earth} planets on fixed orbits is about a factor of 5 to 8 higher in the low inclined case. The higher migration rate for the lower inclined planets results in a faster outward migration. Finding the observed difference in the semi-major axis being so small after about 150 orbits is a result of inclination
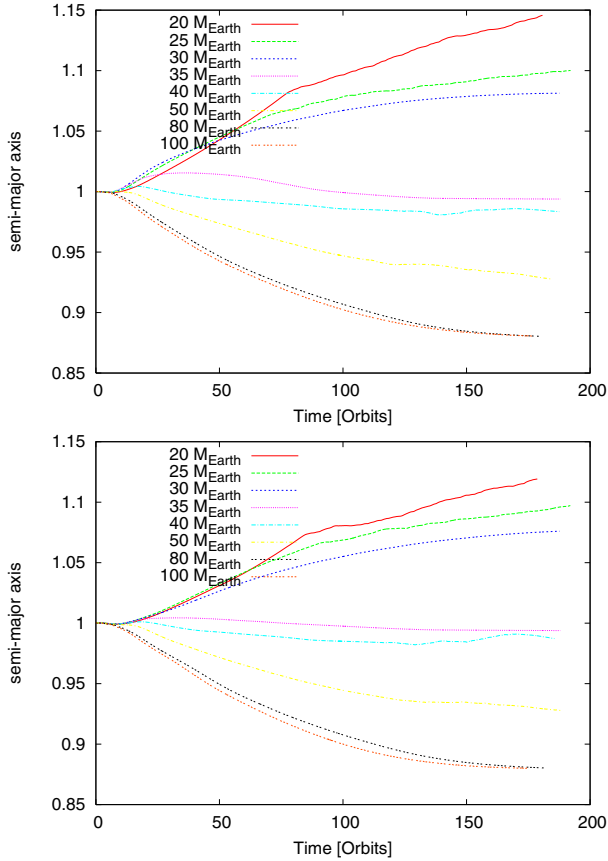
Fig. 22. Time evolution of the semi-major axis for planets with $i_0 = 1.0°$ (*top*) and $i_0 = 4.0°$ (*bottom*) for different planetary masses in a fully radiative disc.

damping. As the inclination is damped, the migration rate increases significantly until the inclination is $\approx 2.0°$, which takes only a few orbits starting from $i_0 = 4.0°$. In this little time frame, the planet is not able to migrate a large distance, so we only observe a small difference in the evolution of the semi major axis.

6. Inclined and eccentric planets

Inclination did not change the direction of migration for planets on circular orbits. Eccentricity on the other hand stopped the outward migration of low mass planets in fully radiative discs, as long as the eccentricity of the planet is higher than $e = 0.02$ (Bitsch & Kley 2010). However, planets with lower eccentricity migrate outwards in the fully radiative scheme. If an inclined planet surrounds a star on an eccentric orbit, in what way will these two properties of the orbit influence each other? To find an answer, simulations of a low mass planet (20 M_{Earth}) on an inclined and eccentric orbit in an isothermal $H/r = 0.037$ and in a fully radiative disc are computed.

6.1. Isothermal disc

Our recent work with planets on eccentric orbits has shown that for isothermal simulations with moving planets on eccentric orbits the cubic potential (for the planetary potential) should be replaced by the ϵ-potential. In the following, isothermal simulations of planets on eccentric and inclined orbits we use the ϵ-potential with a smoothing length of $r_{sm} = 0.8$.
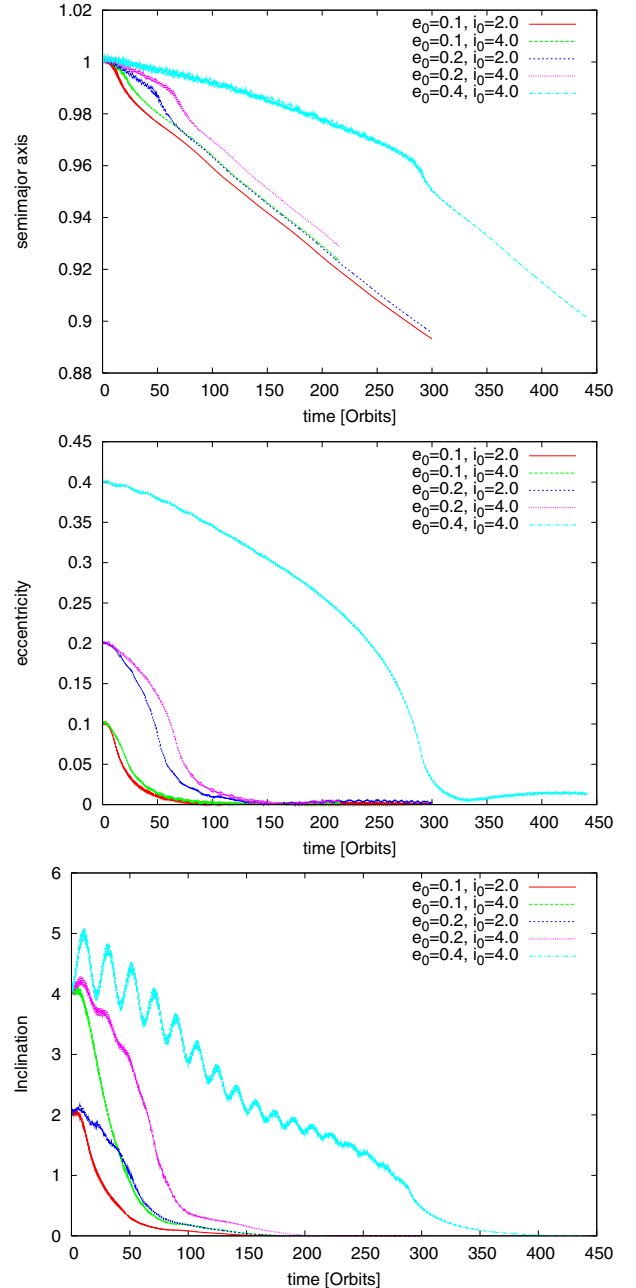
Fig. 23. Time evolution of semi-major axis (*top*), eccentricity (*middle*) and inclination (*bottom*) for planets (20 M_{Earth}) with different eccentricity and inclination in an isothermal $H/r = 0.037$ disc.

In this work we limit ourselves to planets with an initial eccentricity of $e_0 = 0.1$, $e_0 = 0.2$ and $e_0 = 0.4$ and with an initial inclination of $i_0 = 2.0°$ and $i_0 = 4.0°$. In Fig. 23 the evolution of the semi-major axis (top), the eccentricity (middle) and inclination (bottom) for planets in an isothermal $H/r = 0.037$ disc is displayed.

The planets migrate inwards (loss of semi-major axis) as expected for low-mass planets in an isothermal disc. For planets with an initial inclination of $i_0 = 4.0°$, the planets migrate inwards at a slower rate compared to the lower inclined cases. A lower initial eccentricity results in a faster inward migration in the beginning of the simulation for all inclinations. This faster inward migration seems to be in a direct correlation with the planet's eccentricity (Bitsch & Kley 2010). When the planets eccentricity reaches about $e \approx 0.1$, the planet undergoes a short

rapid inward migration and a more rapid loss of eccentricity, compared to the loss of eccentricity at different eccentricities. As soon as the $e_0 = 0.2$ planet's eccentricity is damped to about $e \approx 0.1$, the planet undergoes a rapid inward migration leading to nearly the same evolution of semi-major axis as the $e_0 = 0.1$ planet from this time on, again for both inclinations. Interestingly, a lower starting inclination results in a faster inward migration, when the planets have an initial eccentricity, compared to planets on circular orbits, where the inclination seems to have no effect on the migration. A higher initial inclination ($i = 4.0°$) seems to result in the opposite: a slower inward migration of the planet. We have observed a similar effect for eccentricities: planets with a lower initial eccentricity seem to migrate inwards at a slower rate compared to their highly eccentric counterparts (Bitsch & Kley 2010).

The initial eccentricity is damped for all these simulations with only two small differences. Planets with an initially higher eccentricity need a longer time to be damped to zero and planets with the same eccentricity but a higher inclination also need a longer time to damp their eccentricity. As the eccentricity is damped to lower values, at $e \approx 0.1$ we observe a more rapid loss of eccentricity compared to the loss of eccentricity at other times. At this point the planet loses about 50% of its (actual) eccentricity in the time of a few orbits. At this point in time we also observe a faster inward migration of the planet. This dependency of a rapid drop of eccentricity and a resulting decrease of semi-major axis in the isothermal regime is in agreement with the results found in Cresswell et al. (2007) and Bitsch & Kley (2010)

The evolution of the inclination for the low eccentric planet ($e_0 = 0.1$) follows nearly the evolution of a planet on circular orbit. The damping time is in fact marginally longer for the eccentric case, but besides this effect there is no difference. For the $e_0 = 0.2$ case the inclination starts to oscillate slightly in the beginning of the simulation until it is damped to about $i \approx 3.0°$ or $i \approx 1.5°$. Then the inclination follows approximately the damping rate of a planet on a circular orbit (see Fig. 11) until it is damped to about zero. The high eccentric case ($e_0 = 0.4$) shows even more and stronger oscillations in the inclination. In the beginning the planets inclination is pumped up to about $\approx 5.0°$, which is 25% more than the starting inclination. In time, the amplitude of the oscillations becomes smaller and the frequency higher while the overall inclination dissipates in time. These oscillations are observed in Cresswell et al. (2007) as well. The time until the inclination reaches zero is about 4 times as large as in the zero eccentricity case.

By comparing the migration rate of the inclined and eccentric planet with only an eccentric planet (migrating in midplane with a zero inclination), we observe nearly the same migration rate for both planets. Due to these results, it seems that inclination does not influence the migration in an isothermal disc at all.

6.2. Fully radiative disc

For the fully radiative simulations we rely on our cubic $r_{sm} = 0.5$ potential again. For comparison, the starting eccentricity and inclination for the fully radiative simulations match those of the isothermal simulations. In Fig. 24 the evolution of the semi-major axis (top), the eccentricity (middle) and inclination (bottom) for planets in a fully radiative disc are displayed.

In the beginning of the simulations all planets migrate inwards in the same way as in the isothermal simulations, but in contrast to the isothermal simulations the planets reverse their inward migration and migrate outwards after about ≈ 100 orbits
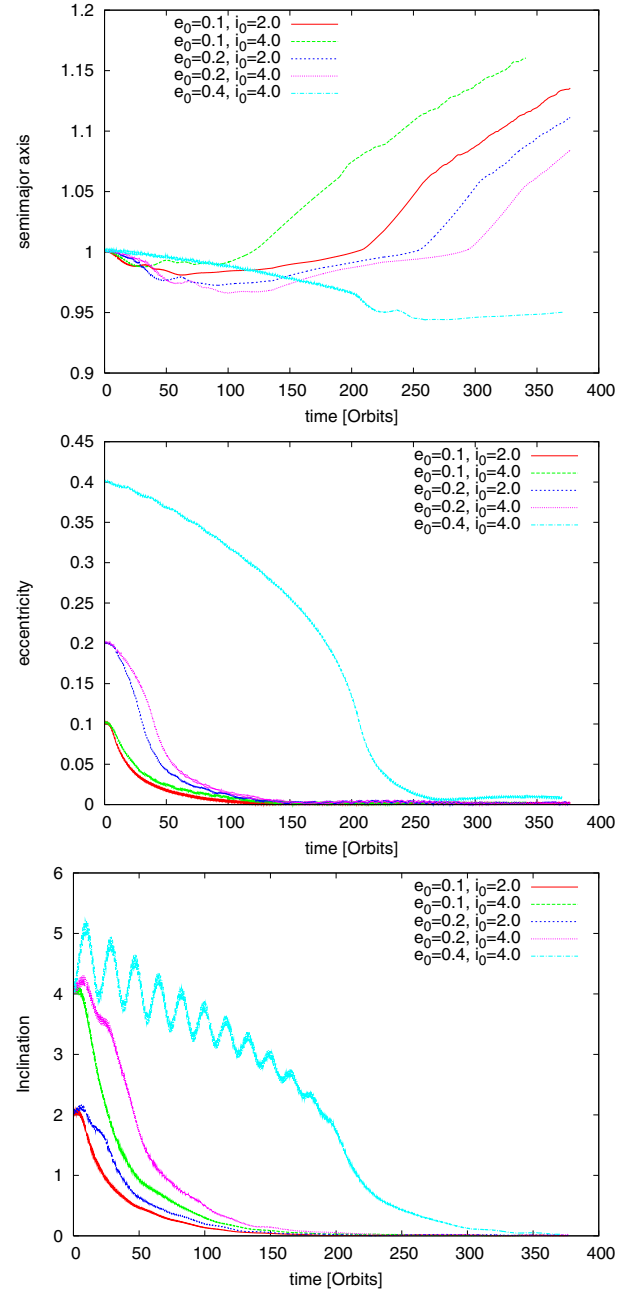

Fig. 24. Time evolution of semi-major axis (*top*), eccentricity (*middle*) and inclination (*bottom*) for planets (20 $M_{\rm Earth}$) with different eccentricity and inclination in a fully radiative disc.

in the low eccentric case ($e_0 \leq 0.2$). The high eccentric case ($e_0 = 0.4$) takes a much longer time to reverse its inward migration. A higher initial eccentricity results in a later outward migration of the planet. The evolution of the semi-major axis contains at some point a quite fast loss of semi-major axis for the initial low eccentric planets. This loss of semi-major axis correlates to the eccentricity. As soon as the eccentricity is damped to ≈ 0.1, the fast loss of the semi-major axis sets in. The inclination of the planet seems to play no significant role in the migration process of these simulations, as for the $e_0 = 0.1$ case the higher inclined planet ($i_0 = 4.0°$) migrates outward first, while for the $e_0 = 0.2$ case the lower inclined planet ($i_0 = 2.0°$) migrates outward first.

The initial eccentricity is damped for all planets, but for planets with the same starting eccentricity, the time needed to damp

the eccentricity is longer for the higher inclined planets, see the middle of Fig. 24. As the eccentricity is damped to ≈ 0.1, it is damped with an exponential decay, which seems to result in a faster loss of semi-major axis at the same time in the evolution of the planet. The damping for the initial low eccentric planets ($e \leq 0.2$) takes about 120 planetary orbits, while a higher initial eccentricity ($e_0 = 0.4$) takes about three times longer.

The inclination damping follows in principle the evolution of inclination of the isothermal simulations. As soon as the planet is released in the disc, the inclination is damped as long as the eccentricity is very low ($e_0 = 0.1$). Higher eccentricities seem to affect the inclination in such a way that the inclination begins to oscillate. This oscillation is already visible in the $e_0 = 0.2$ case, but becomes much stronger for even higher eccentricities. The oscillations begin to dissipate as soon as the planets eccentricity is damped to about $e \leq 0.1$. During time these oscillations lose amplitude and gain frequency (as we can see from the $e_0 = 0.4$ simulation). A higher eccentricity seems to cause a higher and more frequent oscillation of the inclination. These oscillations have been observed in Cresswell et al. (2007) as well.

7. Summary and conclusions

We performed full 3D radiation hydrodynamical simulations of accretion discs with embedded planets of different masses on inclined orbits. In a first sequence of simulations we have analysed in detail the dynamics of a planet with a given mass of 20 M_{Earth} for the isothermal as well as the fully radiative case. For planets on fixed orbits we calculate the expected change of inclination and semi-major axis of an inclined planet on a circular orbit embedded in the disc, which we confirm subsequently through simulations of moving planets. For the isothermal ($H/r = 0.037$ and $H/r = 0.05$) as well as for the fully radiative simulations the inclination is damped in time. The damping time scale in isothermal discs depends on the disc's thickness (H/r), as the inclination is damped faster for discs with lower aspect ratio than in discs with higher aspect ratio. A smaller H/r also results in a faster inward migration compared to a higher H/r. Our simulation results agree in this respect with Tanaka et al. (2002).

For planets on inclined orbits we confirm the outward migration. Our results for planets on fixed orbits agree very well with the simulations of planets moving inside the disc. We find that outward migration interestingly occurs over a relatively large range of inclination, up to about ($i = 4.5°$), with a faster outward migration for lower inclined planets. For higher inclined planets the migration seems to be stalled in general. In our simulations, the damping of inclination is slower in the fully radiative disc ($\tau_{\mathrm{inc}} = 26.5$) compared to the isothermal disc having the same scale height ($\tau_{\mathrm{inc}} = 23$), a difference that may be attributed to the different sound speeds, isothermal versus adiabatic.

As recent studies showed, planets in a fully radiative disc only migrate outwards if they do not exceed a certain critical mass (Kley et al. 2009), beyond which gap formation sets it. This outward migration does crucially depended on the shape of the orbit of the planet in the disc, as discussed in Bitsch & Kley (2010); Kley et al. (2009). Here, we extended those studies to inclined planets and found that planets on circular and inclined orbits migrate inwards in the isothermal case, and migrate outwards (if the planetary mass is low enough and the inclination of the planet is below the threshold of $i \approx 4.5°$) in the fully radiative case. For higher mass planets, our previous results have been confirmed in the expected way. Planets with a mass up to $\approx 33\,M_{\mathrm{Earth}}$ migrate outwards and planets with higher masses migrate inwards in the fully radiative scheme. In the isothermal

case, planets migrate inwards as predicted by linear theory (Tanaka et al. 2002). When evolving planets with higher planetary masses, the simulations started from unperturbed discs, which changes the damping rate of inclination compared to planets starting in perturbed discs (by the presence of the embedded planet). This was also stated for inclined high mass planets in isothermal discs by Marzari & Nelson (2009). After the inclination is damped in time, the direction of migration only depends on the thermodynamics of the disc and on the planetary mass.

For eccentric and inclined low mass planets we observe a quite different behaviour. Eccentricity seems to slow down the inward migration of planets in the isothermal regime and prevents outward migration in the fully radiative scheme (for low mass planets which would normally migrate outwards). Since eccentricity is damped with time, this leads to slightly faster inward migration in the isothermal regime and to a reverse of the migration direction in the fully radiative scheme. The origin of this outward migration is created by the delicate density structure near the planet, which is destroyed by even a very low amount of eccentricity (Bitsch & Kley 2010). A high initial eccentricity gives rise to oscillations in the inclination, which become weaker and more frequent in time, as the eccentricity is damped. These oscillations seem to be responsible for a slower damping of inclination compared to low eccentric planets.

The results by Marzari & Nelson (2009) for Jovian mass planets indicated that inclination and eccentricity is damped in a very short time compared to low mass planets. We can confirm their results for inclination damping in discs with two different aspect ratios, however this is only true for the damping of high inclinations. For low inclinations ($i \leq 10°$) the damping of inclination for low mass planets is faster than for high mass planets. However, when considering the total time needed to damp the inclination of a planet starting from $i_0 = 15.0°$, the damping is much faster for high mass planets, which confirms the results by Marzari & Nelson (2009). A Jovian mass planet with high inclination evolves more rapidly as its interactions with the disc is stronger if no gap has opened yet.

Our results indicate that the inclination as well as the eccentricity of single planets are damped by the disc. At the end of our simulations the planets end up in midplane, meaning they have no remaining inclination. While this is in agreement with the very flat solar system, it seems to be in contradiction to the observed highly inclined exoplanets (Triaud et al. 2010). However, it is known that higher eccentricities as well as inclinations can be produced via planet-planet interaction. For a pair of planets embedded in discs convergent migration processes can excite eccentricity to high values depending on the damping action of the disc (Crida et al. 2008). Stronger scattering events can be induced in case of a multiple planet system still embedded in the disc (Marzari et al. 2010). During the subsequent longterm evolution these initially excited system may then evolve into configurations with very high eccentricity as well as inclination (Chatterjee et al. 2008; Matsumura et al. 2010). Thus, the combination of initial planet-disc interaction with subsequent scattering processes and tidal interaction with the central star is one pathway towards the observed strongly tilted systems (Winn et al. 2010). On the other hand, systems such as Kepler-9 (Holman et al. 2010) seem to show clear evidence for continued migration towards the star.

References

Ayliffe, B. A., & Bate, M. R. 2010, MNRAS, 408, 876
Baruteau, C., & Masset, F. 2008, ApJ, 672, 1054
Bate, M. R., Lubow, S. H., Ogilvie, G. I., & Miller, K. A. 2003, MNRAS, 341, 213
Bitsch, B., & Kley, W. 2010, A&A, 523, A30
Bryden, G., Chen, X., Lin, D. N. C., Nelson, R. P., & Papaloizou, J. C. B. 1999, ApJ, 514, 344
Burns, J. A. 1976, Am. J. Phys., 44, 944
Chatterjee, S., Ford, E. B., Matsumura, S., & Rasio, F. A. 2008, ApJ, 686, 580
Cresswell, P., Dirksen, G., Kley, W., & Nelson, R. P. 2007, A&A, 473, 329
Crida, A., Sándor, Z., & Kley, W. 2008, A&A, 483, 325
Crida, A., Baruteau, C., Kley, W., & Masset, F. 2009, A&A, 502, 679
D'Angelo, G., Henning, T., & Kley, W. 2002, A&A, 385, 647
D'Angelo, G., Kley, W., & Henning, T. 2003, ApJ, 586, 540
Goldreich, P., & Tremaine, S. 1980, ApJ, 241, 425
Holman, M. J., Fabrycky, D. C., Ragozzine, D., et al. 2010, Science, 330, 51
Klahr, H., & Kley, W. 2006, A&A, 445, 747
Kley, W., & Crida, A. 2008, A&A, 487, L9
Kley, W., & Lin, D. N. C. 1999, ApJ, 518, 833
Kley, W., Bitsch, B., & Klahr, H. 2009, A&A, 506, 971
Levermore, C. D., & Pomraning, G. C. 1981, ApJ, 248, 321
Marzari, F., & Nelson, A. F. 2009, ApJ, 705, 1575
Marzari, F., Baruteau, C., & Scholl, H. 2010, A&A, 514, L4
Masset, F. 2000, A&AS, 141, 165
Matsumura, S., Thommes, E. W., Chatterjee, S., & Rasio, F. A. 2010, ApJ, 714, 194
Mihalas, D., & Weibel Mihalas, B. 1984, Foundations of radiation hydrodynamics (New York: Oxford University Press)
Paardekooper, S.-J., & Mellema, G. 2006, A&A, 459, L17
Paardekooper, S.-J., & Mellema, G. 2008, A&A, 478, 245
Paardekooper, S.-J., & Papaloizou, J. C. B. 2008, A&A, 485, 877
Papaloizou, J., & Lin, D. N. C. 1984, ApJ, 285, 818
Papaloizou, J. C. B., Nelson, R. P., Kley, W., Masset, F. S., & Artymowicz, P. 2007, in Protostars and Planets V, ed. B. Reipurth, D. Jewitt, & K. Keil, 655
Tanaka, H., & Ward, W. R. 2004, ApJ, 602, 388
Tanaka, H., Takeuchi, T., & Ward, W. R. 2002, ApJ, 565, 1257
Terquem, C., & Ajmia, A. 2010, MNRAS, 404, 409
Triaud, A. H. M. J., Collier Cameron, A., Queloz, D., et al. 2010, A&A, 524, A25
Ward, W. R. 1986, Icarus, 67, 164
Winn, J. N., Fabrycky, D., Albrecht, S., & Johnson, J. A. 2010, ApJ, 718, L145
Ziegler, U., & Yorke, H. 1997, Comput. Phys. Commun., 101, 54

Range of outward migration and influence of the disc's mass on the migration of giant planet cores

Bertram Bitsch[1] and Wilhelm Kley[1]

Institut für Astronomie & Astrophysik, Universität Tübingen, Auf der Morgenstelle 10, D-72076 Tübingen, Germany

Preprint online version: July 16, 2011

ABSTRACT

Context. The migration of planets plays an important role in the early planet-formation process. An important problem has been that standard migration theories predict very rapid inward migration, which poses problems for population synthesis models. However, it has been shown recently that low-masss planets (20-30 M_{Earth}) that are still embedded in the protoplanetary can migrate outwards under certain conditions. Simulations have been peformed mostly for planets at given radii for a particular disc model.

Aims. Here, we plan to extend previous work and consider different masses of the disc to quantify the influence of the physical disc conditions on planetary migration. The migration behaviour of the planets will be analysed for a variety of positions in the disc.

Methods. We perform three-dimensional (3D) radiation hydrodynamical simulations of embedded planets in protoplanteary discs. We use the explicit-implicit 3D hydrodynamical code `NIRVANA` that includes full tensor viscosity, and implicit radiation transport. For planets on circular orbits at various locations we measure the radial dependece of the torques for three different planetary masses.

Results. For all considered planet masses (20-30 M_{Earth}) in this study we find outward migration within a limited radial range of the disc, typically from about 0.5 up to 1.5-2.5 a_{Jup}. Inside and outside this intervall, migration is inward and given by the Lindblad value for large radii. Interestingly, the fastest outward migration occurs at a radius of about a_{Jup} for different disc and planet masses. Because outward migration stops at a certain location in the disc, there exists a zero-torque distance for planetary embryos, where they can contineu to grow without moving too fast. For higher disc masses ($M_{disc} > 0.02 M_{\odot}$) convection ensues, which changes the structure of the disc and therefore the torque on the planet as well.

Conclusions. Outward migration stops at different points in the disc for different planetary masses, resulting in a quite extended region where the formation of larger cores might be easier. In higher mass discs, convection changes the disc's structure resulting in fluctuations in the surface density, which influence the torque acting on the planet, and therefore its migration rate. Because convection is a 3D effect, 2D simulations of massive discs with embedded planets should be handled with care.

Key words. accretion discs – planet formation – hydrodynamics – radiative transport – planet disc interactions

1. Introduction

Planetary migration of embedded low-mass planets in isothermal discs indicates inward migration, so that the planet might be lost in the star before the accretion disc is gone (Tanaka et al. 2002). Recent studies (starting with the work of Paardekooper & Mellema (2006)) have shown that the inclusion of radiation transport in planet-disc interaction studies resulted in a slowed down or even reversed migration (Baruteau & Masset 2008a; Paardekooper & Papaloizou 2008; Paardekooper & Mellema 2008; Kley & Crida 2008; Kley et al. 2009; Ayliffe & Bate 2010, 2011).

All authors agree that the inclusion of radiation transport is an important effect that should be considered, however, not all authors find outward migration. The efficiency of outward migration depends on the magnitude of positive corotation torques. These are determined by the local entropy and vortensity gradients. For isothermal and adiabatic discs these gradients cannot be maintained and so-called torque saturation reduces the corotation effects. However, the inclusion of radiative transport and viscosity prevents saturation, and the negative Lindblad torques (caused by the spiral arms) can be overwhelmed by the positive contributions from the corotation region. The magnitude of the effect depends on the planetary mass (Kley & Crida 2008;

Kley et al. 2009) and the temperature gradient in the disc. For example, Ayliffe & Bate (2011) found for temperature slopes of $\beta > 1.0$ (with $T \propto r^{-\beta}$) that outward migration is possible even for planets with up to $50 M_{Earth}$ in 3D simulations. The migration rate increases with an increasing temperature slope. These results are also reflected by the theoretical analysis from Masset & Casoli (2010). Recently, improved theoretical torque formulae for low-mass planets embedded in an adiabatic disc have been presented by Masset & Casoli (2009) and Paardekooper et al. (2010). The most recent improvements consider the necessary inclusions of radiative diffusion and viscosity (Masset & Casoli 2010; Paardekooper et al. 2011). These have been developed for 2D discs where the diffusive effects can operate only in the discs's plane. Interestingly, radiative cooling alone can lead to similar, even stronger effects (Kley & Crida 2008).

A very important open question is how far the planet will move outwards in a fully radiative disc. When the protoplanets are stopped from migrating outwards at a certain point in the disc, a protoplanet moving inwards from farther out will stop at the same location in the disc. Therefore, a planetary trap inside the disc can be created, which can act as an area of planetary mergers, leading to larger cores. A planetary trap inside the disc created by surface density changes can function as a feeding zone to planetary cores (Morbidelli et al. 2008), but it is unclear how realistic these surface density changes are. The inclusion of radiation transport/cooling in a disc might provide such a trap in

a normal disc structure, at least for planets within a given mass range.

In Sándor et al. (2011) the authors show in N-body simulations that because of the inclusion of unsaturated type-I-migration (Paardekooper et al. 2010) large planetary cores (up to $10 M_{Earth}$) can form in protoplanetary discs well before the disc is accreted onto the star.

In population synthesis models that include the standard migration prescription for isothermal discs the migration is too fast, such that the outcome distribution does not match the observed one. Specifically, the type-I-migration rate should be 10 to 1000 times slower than expected from linear analysis (Alibert et al. 2004; Ida & Lin 2008; Mordasini et al. 2009). As pointed out above, this could be provided by the inclusion of radiation transport in hydrodynamical type-I-migration simulations. An updated version of the type-I-migration, by using the formula from Paardekooper et al. (2010), in population synthesis models shows very promising results (Mordasini et al. 2010), but additional simulations are needed to verify these assumptions.

In our previous simulations and studies (Kley et al. 2009; Bitsch & Kley 2010; Bitsch & Kley 2011) we have only considered one standard disc model with a given mass. In reality, of course, protoplanetary discs can have a variety of masses. A fully radiative disc will settle in an equilibrium state between viscous heating and radiative transport/cooling. Given that all other physical parameters are fixed, the resulting disc structure only depends on the disc's mass and viscosity, because a more massive or more viscous disc is able to heat the disc more effectively. A more massive disc therefore influences the migration rate of embedded planets. Here we focus on low-mass planets that can undergo outward migration in fully radiative discs.

In this paper we extend previous studies and investigate the possible radial range over which outward migration can occur and analyse the influence of the disc's mass on the migration in detail. An important effect is the onset of convection in the disc, whichs becomes stronger for more massive discs.

In Section 2 we give a short overview of our code and numerical methods, where more details can be found in (Kley et al. 2009). The influences of the distance of the embedded planet to the central star is discussed in Section 3. We then analyse the influence of the disc's mass on the disc's structure (density, temperature, aspect ratio) and then the influence on migration of embedded low-mass planets in Section 4. Convection in the disc is also briefly discussed in Section 4. We then summarize and conclude in Section 5.

2. Setup of the simulations

The protoplanetary disc is modelled as a three-dimensional (3D), non-self-gravitating gas whose motion is described by the Navier-Stokes equations. We treat the disc as a viscous medium, where the dissipative effects can then be described via the viscous stress-tensor approach. We also assume that the heating of the disc occurs solely through internal viscous dissipation and ignore the influence of additional energy sources (e.g. irradiation form the central star). This internally produced energy is then radiatively diffused through the disc and eventually emitted from its surface. For this process we use the flux-limited diffusion approximation, which allows us to treat the transition from optically thick to thin regions as an approximation. A more detailed description of the modeling and the numerical methodology is provided in our previous papers (Kley et al. 2009; Bitsch & Kley 2010; Bitsch & Kley 2011), and for that purpose we limit ourselves here to present only the most necessary information.

2.1. Physical setup

We solve the Navier-Stokes equations numerically using a spatially second order finite volume method based on the code NIRVANA (Ziegler & Yorke 1997), with implicit radiative transport in the flux-limited diffusion approximation and the FARGO (Masset 2000) extension as described in Kley et al. (2009). We use a spherical polar coordinate system (r, θ, ϕ), where the computational domain consists of a complete annulus ($0 \leq \phi \leq 2\pi$) of the protoplanetary disc centred on the star, extending from r_{min} to r_{max}, which are determined by the location of the planet. For symmetry reasons and because we only use non-inclined planets, we restrict ourselves in the standard setup to the upper half of the disc. Hence, in the vertical direction the annulus extends from the equator up to $7°$ above the disc's midplane, meaning $83° < \theta < 90°$. Here θ denotes the polar angle of our spherical polar coordinate system measured from the polar axis. For the study of convection we use in addition a two-sided disc, see below. The central star has one solar mass $M_* = M_\odot$, and the total disc mass inside $[r_{min}, r_{max}]$ is $M_{disc} = 0.01 M_\odot$, unless stated otherwise in Section 4. For our radiative models the temperature and subsequently H/r is calculated self-consistently from the equilibrium structure given by the viscous internal heating and radiative diffusion. We note that for given physics (equation of state, opacity, viscosity) the structure of the disc is solely dependent on its mass, and this is one aspect that we will investigate in this paper.

For the radiative transport we use a one-temperature approach and apply the flux-limited diffusion approximation using analytic Rosseland opacities, for details see Kley et al. (2009). To close the basic system of equations we use an ideal gas equation of state with constant mean molecular weight $\mu = 2.35$ for a standard solar mixture. The adiabatic index is $\gamma = 1.4$. For the present study, we use a constant kinematic viscosity coefficient with a value of $\nu = 10^{15}\,\mathrm{cm}^2/\mathrm{s}$, a value that relates to an equivalent $\alpha = 0.004$ at $5.2AU$ for a disc aspect ratio of $H/r = 0.05$, where $\nu = \alpha H^2 \Omega_K$. In standard dimensionless units with $r_0 = a_{Jup} = 5.2AU$ and $t_0 = \Omega_K(r_0)^{-1}$ we have $\nu = 10^{-5}$.

2.2. Calculation setup

Our coordinate system rotates at the initial orbital frequency of the planet (at $r = r_P$). We use an equidistant spherical grid in r, θ, ϕ with a resolution of $(N_r, N_\theta, N_\phi) = (266, 32, 768)$ active cells for our simulations. At r_{min} and r_{max} we use damping boundary conditions for all three velocity components to minimize disturbances (wave reflections) at these boundaries. The velocities are relaxed towards their initial state on a time scale of approximately the local orbital period. The angular velocity is relaxed towards the Keplerian values, while the radial velocities at the inner and outer boundaries vanish. Reflecting boundary conditions are applied for the density and temperature in the radial directions. We apply periodic boundary conditions for all variables in the azimuthal direction. In the vertical direction we set outflow boundary conditions for $\theta_{min} = 83°$ (the surface of the computational domain).

In our previous work, we have discussed the calculation of the torque acting on a planet in great detail. Outward migration seems only possible and is strongest when the planet is on nearly circular orbits in the midplane of the disc (Bitsch & Kley 2010; Bitsch & Kley 2011). Additionally, we stated in Bitsch & Kley (2011) that the measured migration rate from planets on fixed orbits is equivalent to the migration rate determined from moving planets in discs. Hence, we consider here primarily planets

on fixed circular orbits in the midplane of the disc, and calculate the torque acting on the planet, because the torque represents a direct measurement of migration in this case. For a one-sided disc we use symmetric boundaries at $\theta_{max} = 90°$ (the disc's midplane). To correctly see the influence of convection in the disc we use two-sided discs for some high-mass discs. For these simulations we used outflow boundaries for both θ_{min} and θ_{max}.

The models are initialized with constant temperatures on cylinders with a profile $T(s) \propto s^{-1}$ with $s = r \sin \theta$. The initial vertical density stratification is approximately given by a Gaussian where the radial surface density follows a $\Sigma(r) \propto r^{-1/2}$ profile. In the radial and θ-direction we set the initial velocities to zero, while for the azimuthal component the initial velocity u_ϕ is given by the equilibrium of gravity, centrifugal acceleration, and the radial pressure gradient. This corresponds to the equilibrium configuration for a purely isothermal disc. Before embedding the planet, we bring the disc into radiative equilibrium by performing first 2D axisymmetric simulations in the $r - \theta$ plane. This takes about 100 orbits. We then extend this model to a full 3D simulation by expanding the grid into the ϕ-direction, and the planet is embedded.

For the gravitational potential of the planet we utilize the cubic potential, where the potential is exact beyond a transition (smoothing) radius r_{sm} and smoothed by a cubic polynomial inside (Klahr & Kley 2006; Kley et al. 2009). Here we use $r_{sm} = 0.5 R_H$, where R_H is the Hill radius of the planet.

The torques acting on 20, 25, and $30 M_{Earth}$ planets are calculated to determine the direction of migration. The gravitational torques acting on the planet are calculated by integrating over the whole disc, where we apply a tapering function to exclude the inner parts of the Hill sphere of the planet (Crida et al. 2008). This torque-cutoff is necessary to avoid strong, probably noisy contributions from the inner parts of the Roche lobe and to disregard material that is gravitationally bound to the planet (Crida et al. 2009). Here we assume (as in our previous papers) a transition radius of 0.8 Hill radii.

3. Range of outward migration

Previous simulations by several authors (Baruteau & Masset 2008a; Paardekooper & Papaloizou 2008; Paardekooper & Mellema 2008; Kley & Crida 2008; Kley et al. 2009) indicated that outward migration of low-mass planets may be possible during an early evolutionary state of planet formation. However, because the simulations dealt mostly with planets at a given distance from the star, typically 5.2 AU, the radial range over which the migration may be directed outwards has not been addressed in great detail. In Bitsch & Kley (2010) we obtained some results for moving planets but the extent of the outward migration remained unclear.

In order to address this problem, we simulate 20, 25, and $30 M_{Earth}$ planets on fixed circular orbits embedded in fully radiative discs at various distances from the host star. The planet's semi-major axis r_p lies in a range of $0.6 \leq r_P \leq 5.0 r_0$, where $r_0 = r_{Jup} = 5.2 AU$. With increasing distance from the star, the density and temperature of the disc decrease and at some point in the disc the conditions for outward migration might not be fulfilled anymore.

For this set of simulations with different planet locations we use a disc setup with a density profile such that the total disc mass equals $M_{Disc} = 0.01 M_\odot$ for a planet at $r_p = 1$ and $r_{min} = 0.4$ and $r_{max} = 2.5$ in units of r_0. The planets are embedded in a way that the distance to the inner edge is always the planets location divided by 2.5, while the distance to the outer edge is the

planet's location to the star multiplied by 2.5. This setup ensures that the radial boundaries are always far enough away so they do not influence our results of embedded planets. Since the overall surface density profile ($\Sigma \propto r^{-0.5}$) of the different disc models refers to the same physical situation, the total disc mass in the computational domain changes in the same way as the computed domain changes its size. The surface density at a given distance to the central star is constant for all disc models. The rotation frequency of the grid matches the rotation speed of the planet, so that the planet remains at a fixed position inside the computational grid at all times.

In Fig. 1 the specific torque acting on the three planetary masses at different distance from the central star is displayed. For all planet masses the most extended positive torque (indicating outward migration) is around $r \approx 1.0 r_{Jup}$. At longer distances to the central star, the torque acting on the planets decreases continuously to negative torques, and this transition from positive to negative torques occurs at longer distances for lower planet masses. For the lowest mass planet with $20 M_{Earth}$ the transition is at $r \approx 2.4 r_{Jup}$ (zero-torque distance to the central star). With even longer distances the torques remain negative but with diminishing strength, indicating inward migration. For higher planetary masses (25 and $30 M_{Earth}$) the zero-torque distance is decreasing (1.9 and $1.4 r_{Jup}$). For shorter distances to the central star, inside the maximum, the torque acting on the planet is reduced again until it reaches about zero for $r_P = 0.5 r_{Jup}$ for all planetary masses.

In Fig. 2 the torque for the $20 M_{Earth}$ planet is again displayed together with semi-analytical results from Paardekooper et al. (2010, 2011). The blue crosses refer to the torque formula presented in Paardekooper et al. (2010), which applies for the usaturated torques in adiabatic discs. It is given by

$$\gamma \Gamma_{tot}/\Gamma_0 = -2.5 - 1.7\beta + 0.1\alpha + 1.1(1.5 - \alpha) + 7.9\xi/\gamma , \quad (1)$$

with α and β being the slope of the radial surface density and midplane temperature profile, respectively

$$\Sigma(r) \propto r^{-\alpha}, \quad T(r) \propto r^{-\beta}. \quad (2)$$

In the plot we use $\alpha = 0.5$ and $\beta = 1.7$, as given by our disc model (Kley et al. 2009). For this case the slope of the entropy profile is $\xi = \beta - (\gamma - 1)\alpha = 1.5$. The torque is normalized to

$$\Gamma_0 = \left(\frac{q}{h}\right)^2 \Sigma_P r_p^4 \Omega_P^2 ,$$

with q the planet/star mass ratio, h the relative disc height (H/r), Σ_P the surface density at the planet's location and Ω_P the rotation frequency of the planet in the disc.

At $r = 1.0 r_{Jup}$ the formula from Paardekooper et al. (2010) agrees well with our 3D simulations. However, as seen from Eq. (1), the theoretical torque can never become negative, because all contributions (α, β, ξ) are constant. Hence, at larger radii it remains positive and does not show a zero torque equilibrium radius. For $r < 1.0 r_{Jup}$, the torque formula gives much more extended torques acting on the planet than our simulations. It should be noted that Eq. (1) includes Lindblad and corotation torques where the latter include contributions from the vorticity as well as entropy gradient. One should also be aware that Eq. (1) is valid only at the beginning of the evolution when the torques acting on the planet are not saturated. However, at later times the flow settles to an equilibrium state where the torques saturate and Eq. (1) is not valid any more.
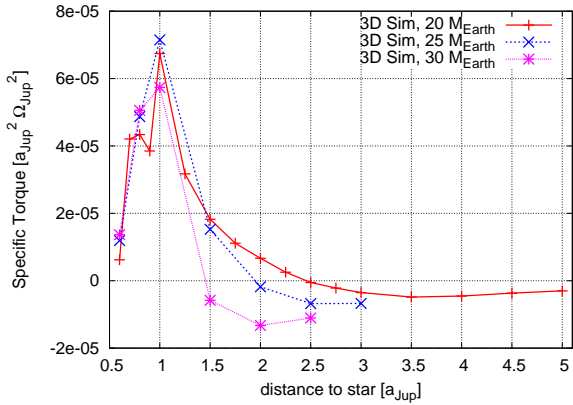
Fig. 1. Torque acting on planets with three different masses embedded in fully radiative discs located at various distances from the star (red for $20M_{Earth}$, blue for $25M_{Earth}$ and purple for $30M_{Earth}$). The torques are plotted when planet and disc have reached a quasi-stationary equilibrium where the torque acting on the planet is approximately constant in time.
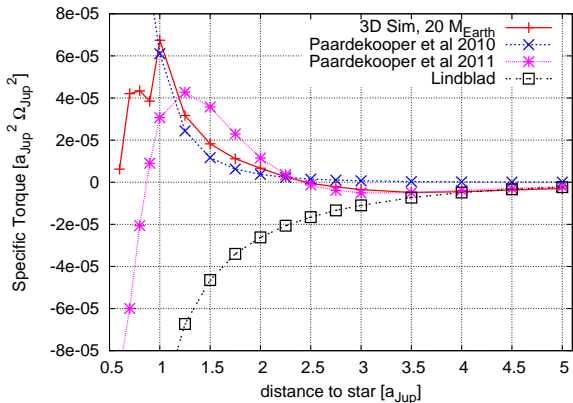

Fig. 2. Torque acting on a $20M_{Earth}$ planet in fully radiative discs as a function of distance from the star. Additional curves indicate the results from the torque formula published in Paardekooper et al. (2010) and Paardekooper et al. (2011). Additionally we also plot the linear Lindblad torque.

In Fig. 2 we additionally plot results from the improved formula in Paardekooper et al. (2011) (purple asterisk). Its derivation is quite complex and we give a brief summary in the appendix. The formula captures the behaviour of the torque caused by Lindblad resonances and horseshoe drag on low-mass planets embedded in gaseous discs in the presence of viscous and thermal diffusion (Paardekooper et al. 2011).

For $r > 2.0 r_{Jup}$ the formula matches our simulations almost perfectly. For $20M_{Earth}$ planets the torque equilibrium radius is also at $r \approx 2.4 r_{Jup}$ (and the torque becomes negative for longer distances to the central star), which is definitely a better approximation than that of Paardekooper et al. (2010). There seems to be only marginal differences between the Lindblad torque, our simulations, and the torque formula of Paardekooper et al. (2011). The torques converge towards the Lindblad torque as the effects of the corotation torque become less important. A longer distance to the central star increases the width of the horseshoe orbit ($x_s \propto a$), which in turn leads to a reduction of the corotation torque. The corotation torque staturates for long distances to the central star, so that its effect becomes small compared to the now dominating Lindblad torque. The total torque therefore
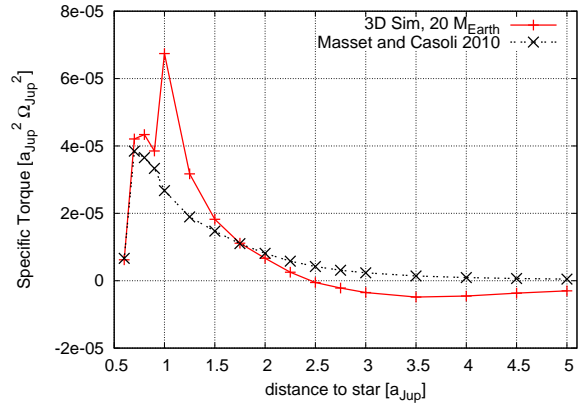

Fig. 3. Torque acting on a $20M_{Earth}$ planet in fully radiative discs as a function of distance from the star. The additional curve indicates the result from the theoretical formula by Masset & Casoli (2010).

converges towards the Lindblad torque in the formula and in the simulations.

For $r < 2.0 r_{Jup}$ the formula and our simulations show some differences. For $1.2 < r < 2.0 r_{Jup}$ the formula predicts more extended torques acting on the planet than the 3D simulations, while for $r < 1.2 r_{Jup}$ the formula predicts reduced torques acting on the planet. At the often used reference radius $r = 1.0 r_{Jup}$ the torque formula and our 3D simulations differ by a factor of about two. For even shorter distances to the central star, the formula shows a rapid drop-off that leads to extended negative torques, while the simulations only show a slower drop-off in the torque and remain in the positive regime.

There are many reasons for the differences between the simulations and the formulae. The formulae in Paardekooper et al. (2010) and Paardekooper et al. (2011) were derived for 2D discs only, but the horseshoe drag can be even stronger in three dimensions, as shown for isothermal discs in Masset et al. (2006). The radiative diffusion is also most effective in the vertical direction, meaning that the two-dimensional approximation is restricted to the orbital plane of the embedded planet. The formulae were derived for background gradients of temperature and surface density, but as the disc with an embedded planet evolves, the structure of the disc changes and the basic assumptions (gradients in temperature, density, and so on) used to derive the formulae might not be valid any more. This is in particular true for planets in the mass range studied here, because the theory has been developed for lower mass planets, which do not alter their surroundings significantly. A more detailed discussion about the smoothing of the planet in Paardekooper et al. (2011) can be found in Appendix A. Nevertheless, there seems to be a rough qualitative agreement between the improved torque formula of Paardekooper et al. (2011) and our numerical results.

In Fig. 3 we also plot the results from Masset & Casoli (2010), who provided an alternative recipe for planetary migration in viscous discs with thermal diffusion. We do not cite the full formula here, because it is very complicated and long. In paragraph 8 of Masset & Casoli (2010), a summary of the torque formula is given.

For short distances to the central star ($r < 0.9 r_{Jup}$) the formula agrees well with our simulations, but for an increasing distance to the central star, considerable differences arise. Moreover the formula seems not to become negative for our simulated regime, even for long distances to the central star, as in Paardekooper et al. (2010). The formula represents the torque
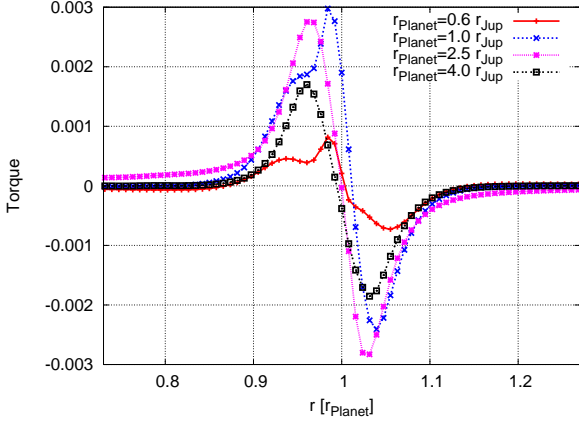
Fig. 4. Radial torque density $\Gamma(r)$ acting on $20 M_{Earth}$ planets at $r_P = 0.6$, $r_P = 1.0$, $r_P = 2.5$ and $r_P = 4.0 r_{Jup}$. The distances have been scaled in r-direction to the actual planet location r_P. The snapshots of the torque density have been taken in the equilibrium state at 80 Jupiter orbits.

drop off to shorter distances to the central star very well, which was also found in Paardekooper et al. (2011).

In Fig. 4 the radial torque density $\Gamma(r)$ is displayed for $20 M_{Earth}$ planets at $r_P = 0.6$, $r_P = 1.0$, $r_P = 2.5$ and $r_P = 4.0 r_{Jup}$, where the radius is normalized to the actual planetary distances to allow a direct comparison. In all curves the contributions by the Lindblad torques are clearly visible, positive for $r < 1$ and negative for $r > 1$. The contribution responsible for the torque reversal, the 'spike' just inside $r = 1$, is visible only for the $r_P = 0.6$ and $r_P = 1.0$ locations, which both show an overall positive total torque. Even though the torque acting on the $r_P = 0.6 r_{Jup}$ planet is much reduced, the spike in the torque distribution is clearly visible. In Kley et al. (2009) we discussed the origin of the spike for the $r_P = 1.0 r_{Jup}$ planet. It is an indicator for a density enhancement ahead of the planet just inside of r_P, and thus creating a positive torque.

For the $r_P = 2.5 r_{Jup}$ case the corotation spike in the fully radiative case in the torque density is not visible any more, only the Lindblad torques are visible. The resulting total torque is about zero, which indicates that the Lindblad torques are just counterbalanced by the corotation effects. For even longer distances to the central star, the torque is identical to the (negative) Lindblad torque, indicating inward migration (see also Fig. 1).

In Kley et al. (2009) we explained in great detail with the help of 2D surface density plots how the torque acting on the planet is created in fully radiative discs. The torque acting on a $20 M_{Earth}$ planet on a circular orbit at $r_P = r_{Jup}$ in a fully radiative disc is positive, indicating outward migration. In Fig. 5 the 2D surface density of the $20 M_{Earth}$ planets at $r = 0.6, 1.0, 2.5, 4.0 r_{Jup}$ (from top to bottom) is displayed. The origin of the structure of the standard $r_P = 1.0 r_{Jup}$ case (second from top) was described in Kley et al. (2009), and we display this case here again for better reference.

The planet located at $r_P = 0.6 r_{Jup}$ (top panel) is still prone to outward migration (see positive torque in Fig. 1), but at a slower rate. The surface density distribution shows some significant differences compared to the $r_P = 1.0 r_{Jup}$ planet. The density increase ahead and inside of the planet ($\phi > 180°$ and $r < 0.6$) is still visible in the $r_P = 0.6 r_{Jup}$ case, but the density decrease behind the planet ($\phi < 180°$ and $r > 0.6$) is not that clearly visible. Indeed it seems as if the density behind the planet increased in a way that the total torque acting on the planet is reduced dramatically, resulting in reduced positive torque acting on the planet.

For the planet at $r_P = 2.5 r_{Jup}$, where the total torque acting on the planet is about zero, the density increase ahead of the planet is no longer visible in the surface density plot, but the decrease behind the planet is clearly visible. It also seems that the planet is able to deplete a larger area around it, possibly owing to the onset of gap formation. For even longer distances to the central star (e.g. $r_P = 4.0 r_{Jup}$), the effect becomes ever stronger, and the gap is more pronounced. The density increase in front of the planet is no longer visible at all. The torque acting on this planet is clearly negative, indicating inward migration. With increasing distance from the host star, the opening angle δ of the spiral arms becomes smaller (see Fig. 5), as can be inferred from $\delta \approx c_s/v_{Kep}$ which scales $\propto r^{-0.35}$ for our temperature gradient of $T(r) \propto r^{-1.7}$.

To analyse the extent of outward migration from our disc properties in more detail, it seems useful to compare various time scales: the libration, the radiative and the viscous time scale in the disc. The necessary unsaturated torques needed for sustained outward migration require approximately equal libration and radiative diffusion times (see Baruteau & Masset (2008a); Paardekooper & Papaloizou (2008)). For the latter we use in our case the radiative diffusion time scale, τ_{rad}. We define (Bitsch & Kley 2010)

$$\tau_{rad} = \frac{s^2}{D_{rad}}, \tag{3}$$

with the diffusion coefficient

$$D_{rad} = \frac{4caT^3}{3c_v\rho^2\kappa}. \tag{4}$$

For the typical diffusion length s we substitute the vertical disc height, i.e. $s = H$, where we use $H = c_s/\Omega$ with the sound speed c_s. The libration time given by (Baruteau & Masset 2008a)

$$\tau_{lib} = 8\pi r_P/(3\Omega_K x_s), \tag{5}$$

where x_s denotes the half-width of the horseshoe-orbit, $x_s = 1.16 r_P \sqrt{q/(\sqrt{\gamma}H/r)}$. Similarly to the radiative diffusion time, the viscous time scale is given by $\tau_{visc} = s^2/\nu$, again with $s = H$, and a constant ν. To compute the time scales all required quantities are evaluated in the midplane of the unperturbed disc at the beginning of the simulations. This applies to the density, temperature, opacity $\kappa(\rho, T)$, and the sound speed and Ω.

The three time scales are displayed in Fig. 6. For accretion discs that are solely heated internally by viscous dissipation we expect in equilibrium $\tau_{rad} \approx \tau_{visc}$. Apparently, this relation is fulfilled well. We have plotted the libration time for two different planet masses, 20 and $30 M_{Earth}$. Time scale arguments suggest a most efficient outward migration for equal τ_{lib} and τ_{rad}, which is indeed roughly what we find in our 3D simulations. However, the overall range of outward migration is surprisingly broad. Specifically we find that $20 M_{Earth}$ planets are prone to outward migration up to about $r \approx 2.4$, where the two time scales differ by a factor of 3-4. For $30 M_{Earth}$ planets the range of outward migration is substantially smaller and centres directly around equal libration and radiative time scale.

We have checked the above estimates of the torques for a stationary planet with additional simulations of $20 M_{Earth}$ planets in discs, starting at $r = 2.0 r_{Jup}$ and $r = 3.0 r_{Jup}$ respectively, which were able to move freely inside the disc. The planets gather in this case indeed at the zero torque radius (results are not displayed here).
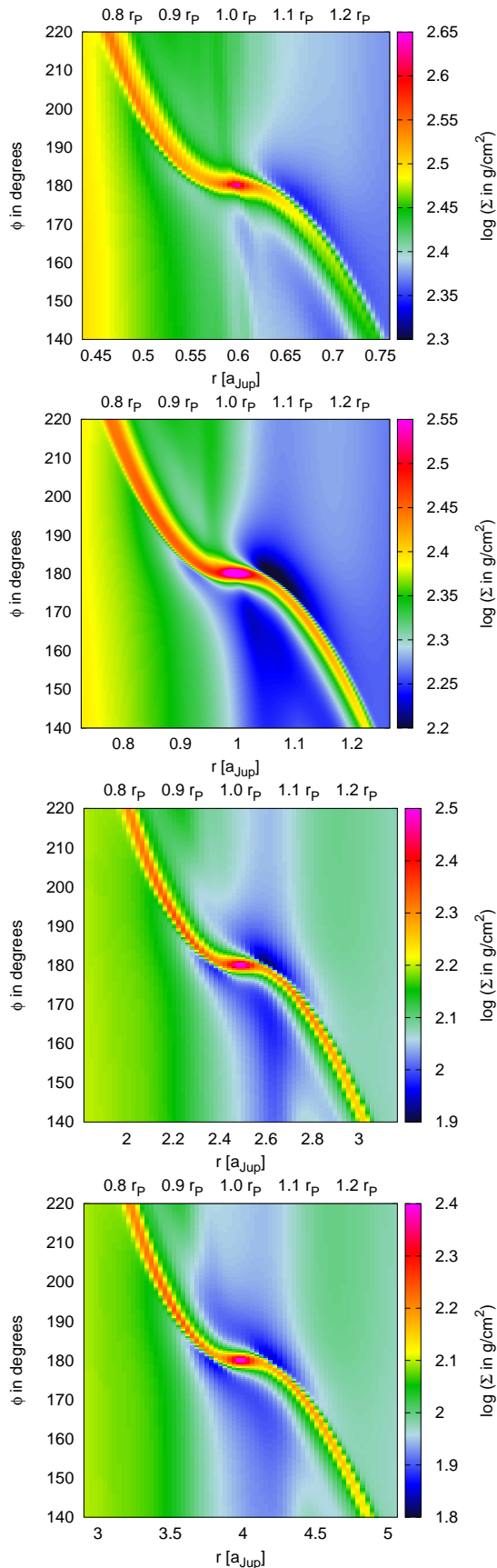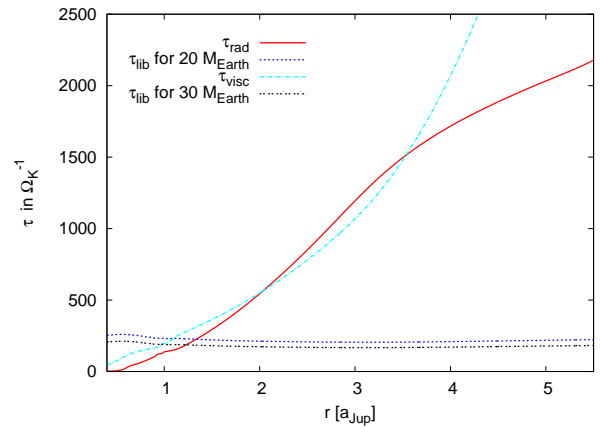
Fig. 6. Radiative and viscous diffusion time scales that depend on the distance from the central star for our standard disc model. To compute the time scales we used the density and temperature of the midplane at the beginning of the fully radiative simulations (when the disc is in the $r - \theta$ equilibrium between viscous heating and radiative transport/cooling). Libration time scales are stated for 20 and $30 M_{Earth}$ planets.

4. Influence of the disc's mass

In this section we examine the influence of the disc's mass on the migration of low-mass planets embedded in these discs. First we compare the relevant physical properties of the discs with different masses, and then we investigate the planetary migration in those discs. We then finally discuss convection inside fully radiative discs.

4.1. Properties of discs with different masses

In our previous work, the disc's mass was fixed to $0.01 M_\odot$. We now extend the range of disc masses from $0.005 M_\odot$ to $0.04 M_\odot$ (with respect to the standard radial distance, from $0.4 - 2.5$). All models started locally isothermal with $H/r = 0.05$ and during initial evolution on time this will change to the appropriate equilibrium configurations (between viscous heating and radiative transport/cooling).

In Fig. 7 we display the density, temperature, and the aspect ratio of the equilibrium discs for different disc masses at $r = 1.0$. Density and temperature, and H/r are evaluated in the disc's midplane. The results are as expected from our previous simulations. A higher mass of the disc results in a higher density, temperature, and aspect ratio of the disc in the equilibrium state. In the isothermal case, a higher aspect ratio of the disc would result in a slower inward migration of a low-mass planet, see Tanaka et al. (2002) for linear analysis and e.g. Bitsch & Kley (2010) for non-linear simulations. However, low-mass planets in fully radiative discs migrate outwards, so that the linear isothermal approach is not valid any more.

In Fig. 8 the radial distributions of surface density (top) and temperature (bottom) are displayed. The temperature has been measured in the disc's midplane. By construction, the surface density increases for higher disc masses, while it falls off with increasing distance to the star, on average according to $\Sigma(r) \propto r^{-1/2}$ as expected for a constant ν. The surface density profiles for the higher mass discs with $M_{Disc} \geq 0.015 M_\odot$ show some fluctuations. With increasing disc mass, these fluctuations become stronger and reach out to a longer distance from the star. While they are quite short for $M_{Disc} \leq 0.02 M_\odot$ and reach only to $r \approx 1.3$, they become very strong and reach out to $r \approx 2.3$ for

Fig. 5. Surface density maps for a $20 M_{Earth}$ planet on fixed circular orbit in fully radiative discs at four different locations. The distance from star to planet changes (from top to bottom): $r_P = 0.6$, $r_P = 1.0$, $r_P = 2.5$ and $r_P = 4.0$ (in Jupiter radii). Please note the slightly different colour scale for each plot.
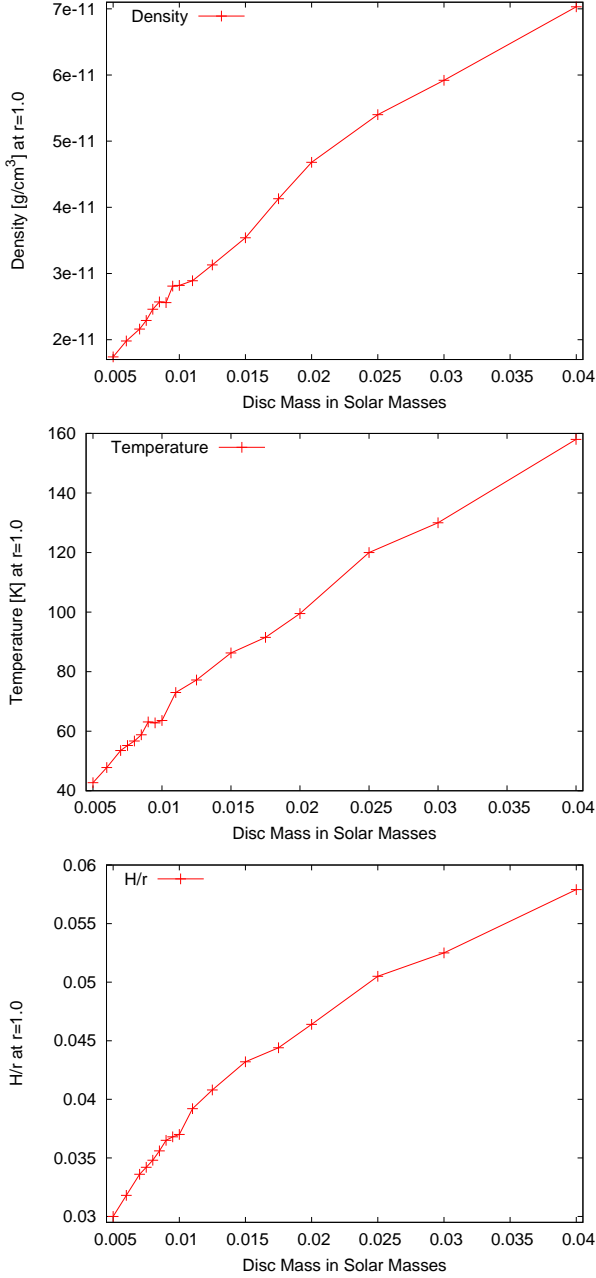
Fig. 7. Density (top), temperature (middle) and aspect ratio (bottom) of discs with different masses in the initial equilibrium state. All quantities are measured in the disc's midplane at the reference distance, $r = 1.0$.
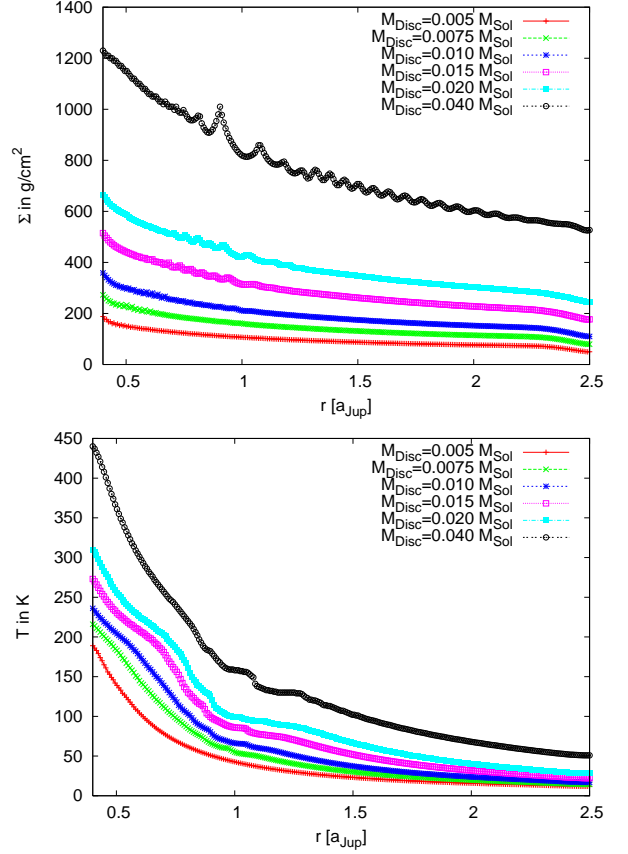

Fig. 8. Surface density (top) and temperature (bottom) of discs with different masses in the equilibrium state of the disc. The temperature is measured in the disc's midplane.

and temperature patterns at $\theta = 83°$ and $\theta = 97°$ for all disc masses (see also Kley et al. (2009)). However, a too low boundary substantially changes the distributions and might therefore influence convection in the disc as well.

The changes in the surface density profiles have a direct influence on the migration of an embedded planet. If a planet is embedded in a region in the disc where the fluctuations of the surface density are very strong (i.e. strong convection), the direction of migration might not be clearly determinable, because changes in the surface density profile directly influence the migration. Stationary gradients in surface density profiles can even be used as planetary traps to collect planetary embryos (Morbidelli et al. 2008).

4.2. Influences on the migration of low-mass planets

As mentioned above, a different aspect ratio of the disc will change the rate of planetary migration. In the isothermal case, a higher aspect ratio will result in slower inward migration in theory (Tanaka et al. 2002), which we supported in our previous simulations (Bitsch & Kley 2010; Bitsch & Kley 2011). A higher disc mass results in a higher aspect ratio and temperature of the disc, and we may expect changes in the migration rates. When the planet is farther away from the central star, the temperature and density of the disc are reduced. If the reduction in density and temperature is sufficient, the planets stop their outward migration (see Fig. 1). One might now expect that for discs with very low masses the torque acting on a $20 M_{Earth}$ planet at $r = 1.0 r_{Jup}$ might become negative. Very high temperatures and

$M_{Disc} = 0.04 M_\odot$. These fluctuations of the surface density vary in time and are related through convective motions in the disc, see below.

The described fluctuations in the surface density can also be seen in the temperature profiles of discs with different disc masses (bottom panel in Fig. 8). The variabilities of the temperature are not as strong as those for the surface density, nevertheless, they are clearly notable for $M_{Disc} \geq 0.015 M_\odot$ and increase with the disc's mass. They also, change in time, as does the surface density. A higher disc mass seems to support stronger fluctuations that reach farther out into the disc.

Because a higher disc mass results in a higher aspect ratio of the disc, the cut-off of the computed domain (at 7° above and below the midplane) might change the structure of the disc. Additional simulations with larger θ did not change the density

high densities inside the disc, on the other hand, might influence the outward migration as well. Following the formula of Paardekooper et al. (2010) in Equation (1), one might suspect stronger torques acting on planets in more massive discs for constant α, β and ξ (increase in surface density overcompensates the increase in aspect ratio).

In the top panel of Fig. 9 the total torque acting on $20M_{Earth}$ planets on circular orbits embedded in fully radiative discs with different masses and the theoretical results from Paardekooper et al. (2010) and Paardekooper et al. (2011) are displayed (blue and purple). The torque acting on the planet remains nearly constant within a small interval around our standard disc mass of $0.01M_\odot$. For lower disc masses, the torque drops off very rapidly to even negative values for $M_{Disc} = 0.005M_\odot$, as we expected. For higher disc masses, the torque drops off as well. First at a faster rate (to $\approx 0.020M_\odot$), then at a slightly slower rate, until it reaches an about zero torque state for $M_{Disc} = 0.040M_\odot$. This contradicts to our first expectation that planets in more massive discs should experience a higher torque, the reason may be a change in the temperature gradient and the influence of convection.

When looking at the surface density profile displayed in Fig. 8, it is clear that the changes in the surface density may disrupt the very sensitive density pattern near the planet. As the convection cells in the disc change with time, the torque acting on the planet will change as well, giving rise to high fluctuations/oscillations in the total torque acting on the planet. Hence, the torques acting on the planet have been averaged over 20 planetary orbits. After averaging, the torques acting on planets in convective discs show only very low fluctuations.

For disc masses around $\approx 0.01M_\odot$ the theoretical formula from Paardekooper et al. (2010) (see eq. 1) fits our 3D simulations quite well. For very low disc masses ($M_{disc} = 0.005M_\odot$), however, the fit is not as good. This may be because of the reduced disc mass and the consequently changed surface density distribution (which changes the torque acting on the planet), as explained in Section 3. For higher disc masses ($M_{disc} \approx 0.015M_\odot$), the two torque values differ more and more. As the torques of our simulations tend to go to zero, the theoretically predicted adiabatic torques from Paardekooper et al. (2010) become even more extended.

The formula from Paardekooper et al. (2011), which includes the important effects of viscosity and heat diffusion, differs by a factor of two near disc masses of $M_{disc} \approx 0.01M_\odot$ as one could have expected from the results presented in Fig. 2. For higher disc masses, the torques from Paardekooper et al. (2011) become even more reduced and even drift to the negative regime for $M_{disc} \approx 0.04M_\odot$. The torques from our simulations follow the trend of the reduction, but they do not reach negative values. Interestingly, the overall slopes of the simulations and torque formula generally agrees despite a constant shift. Besides the differences described in Section 3, more differences arise from convection in the disc, because convection results in fluctuations in the torque, which is not considered in the analytical formulae. However, convection seems to play a role only for discs with $M_{disc} > 0.02M_\odot$.

4.3. Torque analysis

In the bottom panel of Fig. 9 the radial torque density $\Gamma(r)$ is displayed for different disc masses. For the lowest disc mass in our simulations, $M_{Disc} = 0.005M_\odot$, the usual spike in the torque density cannot be seen. The spike in the torque density distribution is an indication for a positive torque in a fully radiative disc (Kley
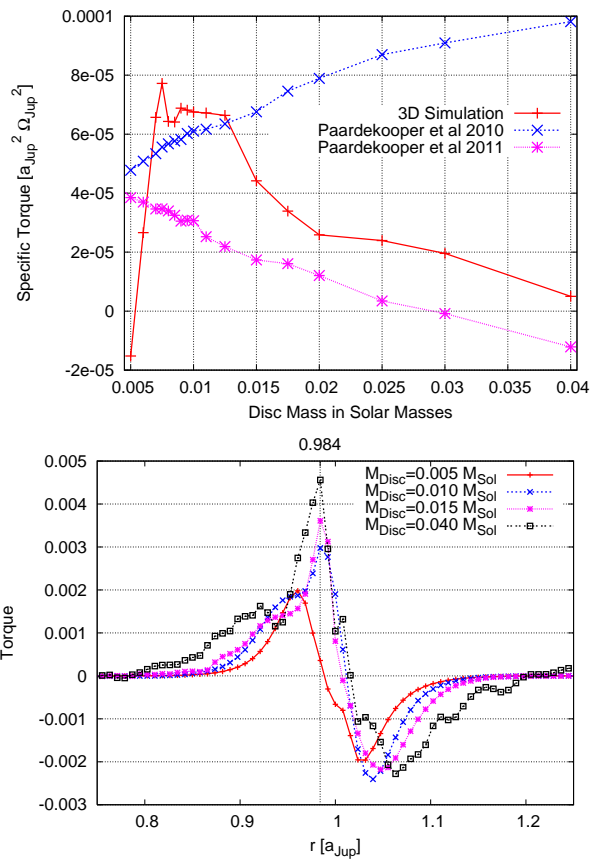

Fig. 9. Torque acting on a planet located at 5 AU for different disc masses. **Top:** Specific total torque acting on planets ($20M_{Earth}$) embedded in discs with different disc masses. The planets embedded in the higher mass discs $M_{Disc} > 0.02M_\odot$ are in the convective zone in the disc, so that the torque acting on the planet is very noisy and has been averaged over 20 planetary orbits. Additionally, we over-plotted results (blue and purple) from the theoretical torque formulae of Paardekooper et al. (2010, 2011) for $20M_{Earth}$ planets. **Bottom:** Radial torque density $\Gamma(r)$ acting on the planet for different disc masses. For comparison, the vertical line indicates the location of the maximum as found for our standard case.

et al. 2009). For higher disc masses (up to $M_{Disc} \approx 0.02M_\odot$), it is is clearly visible. For those disc masses, the total torque is indeed positive (see top panel of Fig. 9), indicating outward migration of the embedded protoplanet.

The torque density for the $M_{Disc} = 0.04M_\odot$ disc seems to indicate a total positive torque acting on the planet, and it is indeed positive at the moment of the snapshot, but as the fluctuations in the surface density change in time, so does the torque acting on an embedded planet. Therefore the torque density for the $M_{Disc} = 0.04M_\odot$ disc at one single moment during the evolution does not necessarily reflect the longterm outcome, if the fluctuations are to strong. This time variation of the total torque and torque density acting on the planet is displayed in Fig. 10. The top panel in Fig. 10 shows the time evolution of the total torque acting on embedded planets for discs with different disc masses. For $M_{disc} < 0.02M_\odot$ the torque acting on the planet is constant in time (after about 50 orbits), while it shows very high fluctuations for $M_{disc} = 0.04M_\odot$. In the bottom panel of Fig. 10 the torque density $\Gamma(r)$ for a $20M_{Earth}$ planet in a $M_{disc} = 0.04M_\odot$ disc is shown. The torque density is plotted at different times. Because the total torque was fluctuating very much, it is no surprise to find these fluctuations for the torque density as well. These fluc-
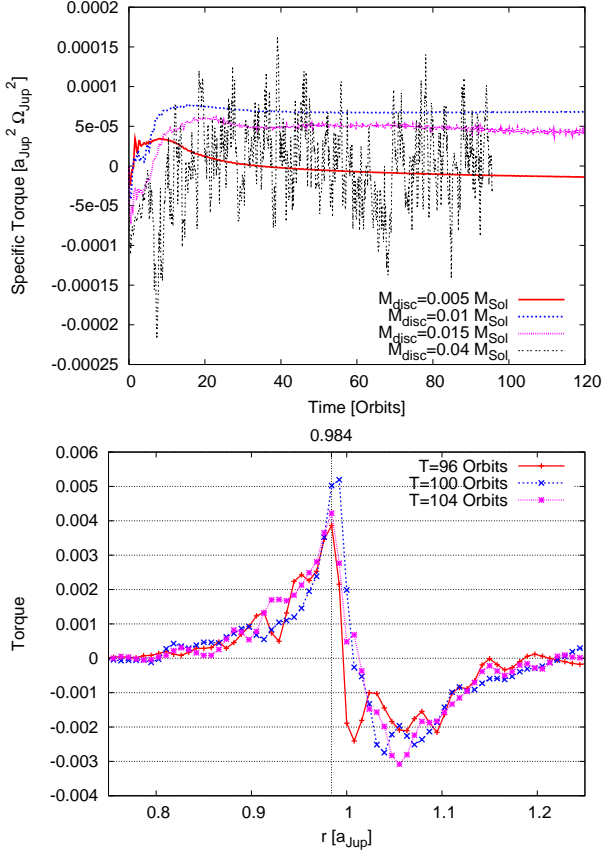
Fig. 10. Top: Specific total torque evolution acting on planets ($20 M_{Earth}$) embedded in discs with different disc masses. The planets embedded in the higher mass discs $M_{Disc} > 0.02 M_{\odot}$ are in the convective zone in the disc, so that the torque acting on the planet is very noisy compared to the low-mass discs. **Bottom:** Radial torque density $\Gamma(r)$ acting on the planet embedded in a disc with $M_{disc} = 0.04 M_{\odot}$ at different stages of the evolution.

tuations, induced by convection, clearly show that a higher disc mass disturbs the evolution of the torque.

In Fig. 11 the surface density profiles of fully radiative discs with disc masses of 0.005, 0.015 and $0.04 M_{\odot}$ with embedded $20 M_{Earth}$ planets are displayed. The planet in the $0.005 M_{\odot}$ disc generates a very similar surface density structure compared to our standard $0.01 M_{\odot}$ disc (second panel in Fig. 5). The overall density is, of course, reduced (because the disc mass is much lower), but the general pattern of the density increases in front of the planet $\phi > 180°$ and $r < 1.0$ and the decrease behind the planet $\phi < 180°$ and $r > 1.0$ remains intact. However, the density structure relevant for outward migration is not as pronounced as it should be to result in a positive torque acting on the planet.

For planets embedded in discs with higher masses, the picture is quite different. For a disc mass of $0.015 M_{\odot}$ (middle picture in Fig. 11) the density structure in the direction of the star ($r < 0.9 r_{Jup}$) is very distorted, but one can still see the density increase ahead and the density decrease behind the planet. The distortion seems to reduce the torque acting on the planet, but the overall torque is still positive, indicating outward migration. For an even higher disc mass (bottom picture in Fig. 11 with $M_{Disc} = 0.040 M_{\odot}$) the distortions in the disc increase more. The density structure, normally seen for low-mass planets in fully radiative discs, is no longer visible at all. The distortions are so strong that the torque acting on the planet becomes about zero, indicating only a low migration rate.
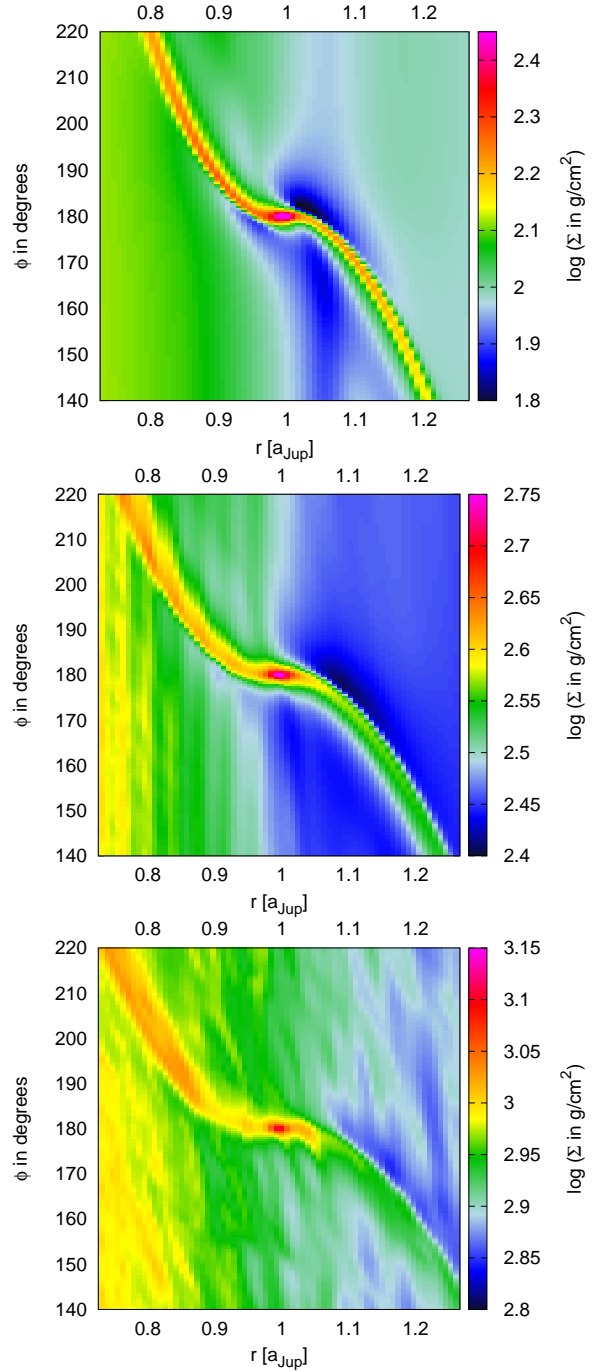
Fig. 11. Surface density maps for planets on fixed circular orbits in fully radiative discs with different disc masses (from top to bottom): $M_{Disc} = 0.005 M_{\odot}$, $M_{Disc} = 0.015 M_{\odot}$ and $M_{Disc} = 0.040 M_{\odot}$. The disruption in the surface density patterns for the higher mass discs are caused by convection inside the disc.

However, in this last case the torque is in a state of constant fluctuations, which complicates realistic predictions about the direction of migration in these massive discs. The fluctuations of the torque have their cause in fluctuations of the density patterns, which indicates that the convective zone inside the disc is enlarged compared to low-massive discs. We observed the phenomenon of convection briefly in our previous work (Kley et al. 2009) for discs with $M_{Disc} = 0.01 M_{\odot}$ as well, but the convective zone did not reach the planet, and thus did not disturb the density pattern around the planet.
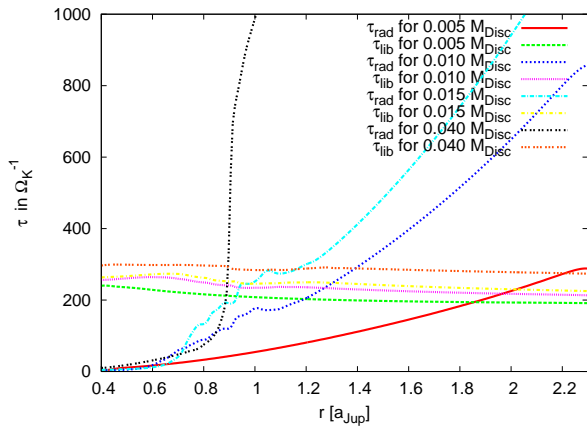
Fig. 12. Time scales depending on the distance from the central star for $0.005M_\odot$, $0.010M_\odot$, $0.015M_\odot$ and $0.040M_\odot$ discs. To compute the time scales we used the density and temperature of the midplane at the beginning of the fully radiative simulations (when the disc is in the $r-\theta$ equilibrium between viscous heating and radiative transport/cooling).

Fig. 13. Evolution of semi-major axis for $20M_{Earth}$ planets (starting at $r = 1.0r_{Jup}$) in isothermal and fully radiative discs with different disc masses.

In Fig. 12 we display the radiative diffusion time scale and the libration time scale for discs with different masses. In order to keep the torques acting on the planet unsaturated (to evoke outward migration), the libration and radiative diffusion time scale need to be approximately equal (Baruteau & Masset 2008a; Paardekooper & Papaloizou 2008). However, for convective discs the equilibrium state through cooling through convection is reached only when $\tau_{rad} > \tau_{visc}$ as observed in Fig. 12. The time scales for the $0.005M_\odot$ disc indicate outward migration in a region at $r \approx 2.0r_{Jup}$, but at $r = 1.0r_{Jup}$ the time scales differ by a factor of 4, indicating that the torques are not kept unsaturated in this region of the disc, which in turn indicates inward migration (as presented in in the top figure in Fig. 9).

For the $0.015M_\odot$ disc the time scales are nearly identical at $r = 1.0r_{Jup}$, which indicates outward migration (as can be seen in the top of Fig. 9). However, for longer distances to the central star, the time scales start to differ, which indicates inward migration. In the $0.040M_\odot$ disc, the time scales differ by a factor of 3 at $r = 1.0r_{Jup}$, which indicates inward migration. However, the measured torque acting on the planet is positive, indicating slow outward migration. But because the planet is embedded in a highly convective region in the disc, it is very difficult to predict the motion of the planet correctly by considering only the time scales.

4.4. Orbital evolution

In Fig. 13 the evolution of semi-major axis for $20M_{Earth}$ planets in isothermal and fully radiative discs with different disc masses is displayed. The isothermal reference simulations are started from a $H/r = 0.037$ disc, which represents the H/r value at the planets starting location in the fully radiative regime. In the isothermal disc, no convection is present and therefore the embedded planet migrates as expected. A higher disc mass results in a faster inward migration. However, it seems that for the $M_{disc} = 0.04M_\odot$ disc the type-III-migration regime is hit, because the planet moves inwards very fast.

For a planet on a fixed circular orbit in a fully radiative disc with $M_{disc} = 0.04M_\odot$ we determined a positive torque (see Fig. 9) by averaging in time. However, the total torque acting on the planet undergoes strong fluctuations in time (see Fig. 10). When embedding a $20M_{Earth}$ planet in such a highly convec-
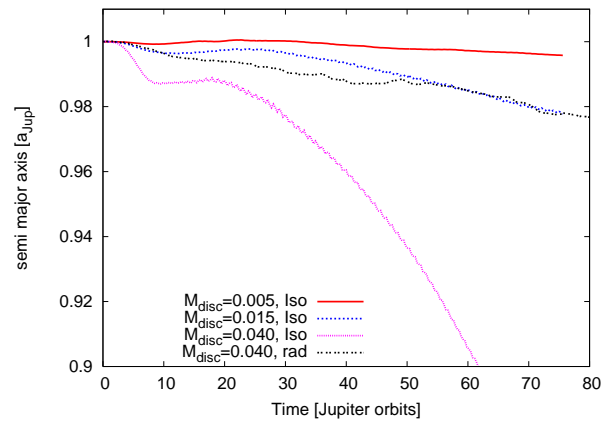
tive disc, the evolution pattern should to some extend reflect the strong fluctuations in the torque acting on a planet on a fixed orbit. Indeed, the planet experiences some small kicks in its evolution pattern (see Fig. 13). Interestingly, the planet migrates inwards despite the positive torque acting on a fixed planet. It seems that in the convective region of high-mass discs, the measurement of the torque for planets on fixed orbits is not as reliable as for planets in low-mass discs. Additionally, the time averaging may have to be performed over a longer time span.

4.5. Convective zone

In order to investigate whether convection is actually present in the disc, we display the velocities in z-direction (out of midplane of the disc) for different disc masses ($M_{Disc} = 0.005M_\odot$, $M_{Disc} = 0.015M_\odot$ and $M_{Disc} = 0.04M_\odot$) in the disc's midplane in Fig. 14. These plots represent simulations with a whole disc, meaning $83° \leq \theta \leq 97°$. As the surface density plots indicated, there are no disrupted areas in the velocity patters for the $M_{Disc} = 0.005M_\odot$ simulations. Therefore for this low disc mass we observe no convection near the planet.

However, for the $M_{Disc} = 0.015M_\odot$ case the surface density patterns already indicated that convection is possible in the disc inside of the planet's distance to the central star. The velocity distributions confirm this result, lines with positive velocities (indicating a flow towards the upper boundary of the disc) alternate with lines with negative velocities (indicating a flow towards the midplane of the disc). These flows are a clear indicator of motion caused by convection in the disc. In the $M_{Disc} = 0.040M_\odot$ case, the fluctuations in the surface density increased dramatically, as did the changes in the velocity pattern. Alternations between positive and negative velocities have increased and indicate a very strong convective region that disturbs the torque acting on the planet (and therefore it's migration). The flow pattern in the disc is very erratic, making it absolutely necessary to average the torque acting on an embedded planet for many orbits.

For simulations that cover only the upper half of the disc, the convection cells inside the disc end at the disc's midplane, but in reality these convective cells continue to the lower half of the disc. However, that convection inside the disc changes the behaviour of the planet disc interactions can also be seen for simulations containing only one half of the disc.
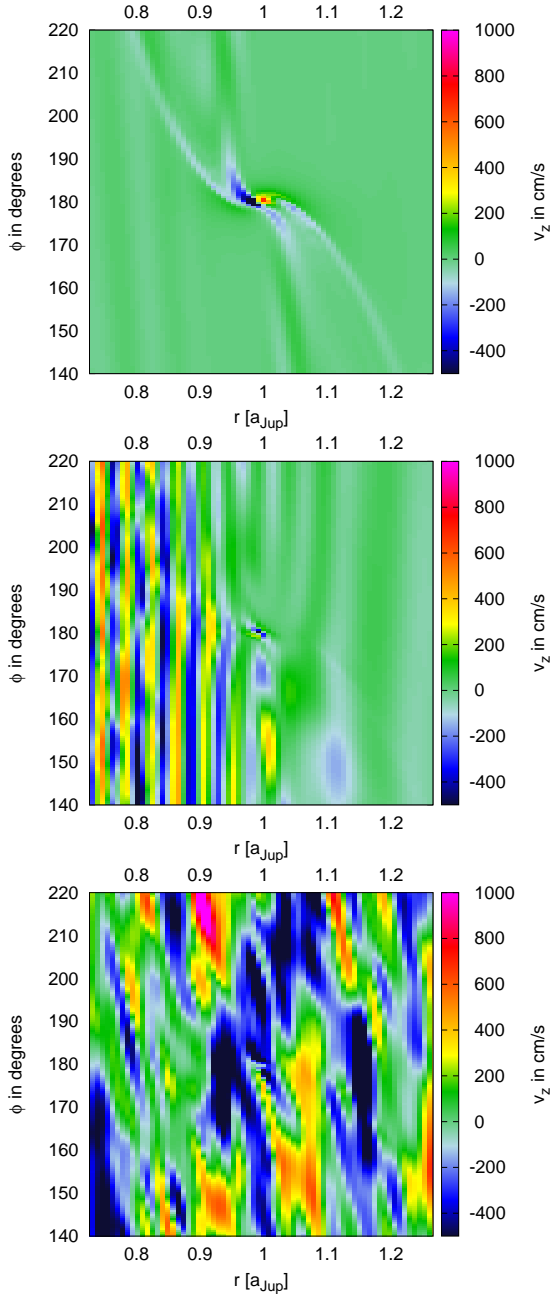
Fig. 15. Velocities in z-direction for $0.04M_\odot$ discs without planet. In the top panle only the upper half of the disc was simulated, while in the bottom panel both sides of the disc were simulated (with twice the number of grid cells in θ direction). The other simulation parameters are identical.

Fig. 14. Vertical velocities in z-direction for planets on fixed circular orbits in fully radiative discs with different disc masses (from top to bottom) in the disc's midplane: $M_{Disc} = 0.005M_\odot$, $M_{Disc} = 0.015M_\odot$ and $M_{Disc} = 0.04M_\odot$. The disruption in the velocity patterns for the higher mass discs are caused by convection inside the disc. A positive velocity simulates outward flows, while a negative velocity indicates a flow towards the disc's midplane.

In Fig. 15 the velocity in z direction is displayed for a half-size disc (only the upper half of the disc is computed, top figure) and for a full disc. These computations have been performed only for fully radiative axisymmetric 2D discs (in r-θ direction) with a disc mass of $M_{disc} = 0.04M_\odot$ without an embedded planet. The convection in the disc is clearly visible. In both simulations the convection cells in the disc become more symmetric for distances longer than $r > 1.25r_{Jup}$, meaning that the velocity changes from positive to negative only in radial direction and not in the vertical direction as well. For shorter distances to the central star the convection cells are very irregular in both cases.
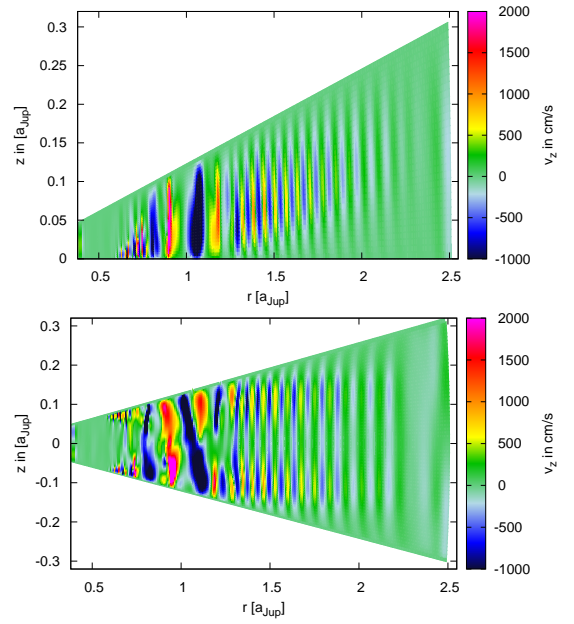
When putting a $20M_{Earth}$ planet in the $0.04M_\odot$ discs, the structure of the convective cells changes as the disc gets disturbed by the planet. Without the planet, the convective cells are very regular for distances to the central star exceeding $r > 1.25r_{Jup}$. With an embedded planet these regular structures break down and become very irregular, as can be seen in Fig. 16. This effect may caused by to the wake created by the planet inside the disc, which acts as an additional heat source. At shorter distances to the central star, the structure is irregular with or without an embedded planet.

The velocity patterns for the one sided and two sided discs show a little difference. It seems that the fluctuations in velocity are more centred in midplane for the one sided disc, while they seem to be located near the upper and lower boundaries for the two sided discs. This effect has several reasons. In the one sided disc, material is reflected at the midplane of the disc, which might lead to an increase of flucuations near the midplane. In the two sided disc, material can flow through the midplane, so that the fluctuations near the midplane are reduced. Furthermore, the one sided disc might be unrealistic if convection is present in the disc.

However, the general structure changes when both halves of the disc are computed, independent of an embedded planet. The convection cells are now moving through the midplane of the disc, which was not possible for simulations of only one half of the disc, see also Kley et al. (1993); Klahr et al. (1999). Therefore, the surface density structure in the two sided disc (with $M_{disc} = 0.04M_\odot$) is slightly different compared to the one sided disc. In the two sided case, the fluctuations in the surface density continue only to $\approx 1.5r_{Jup}$, while they covered the whole disc in the one sided case. The temperature profiles, on the other hand, show no difference at all. We therefore only expect little change in the torque acting on planets embedded in one or two sided discs at $r_P = 1.0r_{Jup}$.

Simulations of embedded $20M_{Earth}$ planets in fully radiative discs that cover both sides of the disc show only very small dif-
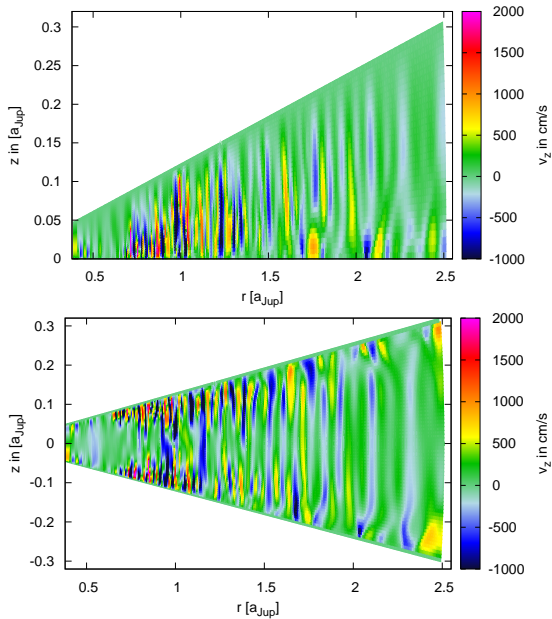
11

Fig. 16. Velocities in z-direction for $0.04M_\odot$ discs with embedded $20M_{Earth}$ planet. In the top panel only the upper half of the disc was simulated, while in the bottom panel both sides of the disc were simulated (with twice the number of grid cells in θ direction). The other simulation parameters are identical.

ferences in the velocity pattern in mid-plane of the disc. The fluctuations in time of the torque acting on the planet embedded in $M_{disc} = 0.04M_\odot$ and $M_{disc} = 0.03M_\odot$ discs are comparable (with only small differences in the amplitude of the fluctuations) for both simulations, confirming our previous assumptions. Simulations of planets embedded in lower mass discs show no difference at all (simulations not displayed here), because the convective region does not reach to the planet at all.

Considering that a longer distance from the central star resulted in a turn from outward to inward migration for a $20M_{Earth}$ planet (see Fig. 1) because of a reduction in temperature and density at the given location of the planet, one might argue that the zero-torque distance from the central star might be at longer distances for higher disc masses. Moreover, as the disrupting convective zone in massive discs reaches farther out from the star, outward migration might be possible at larger radii in more massive discs, because the disc's convective zone stops at longer distance to the central star and the density is still high enough to produce the surface density patter needed for outward migration.

Additional simulations with $20M_{Earth}$ planets in 0.02, 0.025, 0.03 and 0.04$M_\odot$ discs with $r_p = 2.0, 2.5, 3.0$ and $4.0r_{Jup}$, respectively, confirm our assumption (see Fig. 17). The torques acting on those planets are positive, indicating outward migration, and show no fluctuations in time. The surface density plots also show no sign of convection in the disc at the location of the planet (not displayed here). It seems that outward migration is therefore possible to farther distances from the central star in more massive discs.

The picture of convection in our disc would change when including stellar irradiation because it would heat the surfaces of the disc in contrast to the applied cooling right now. This would result in less convection in the disc. Because the convective region is a result of the higher surface density (increasing τ_{rad}) and viscosity in the disc, a reduction in viscosity could prevent convection in the disc. However, a reduction of viscosity also reduces the torque of an embedded planet, so that outward mi-
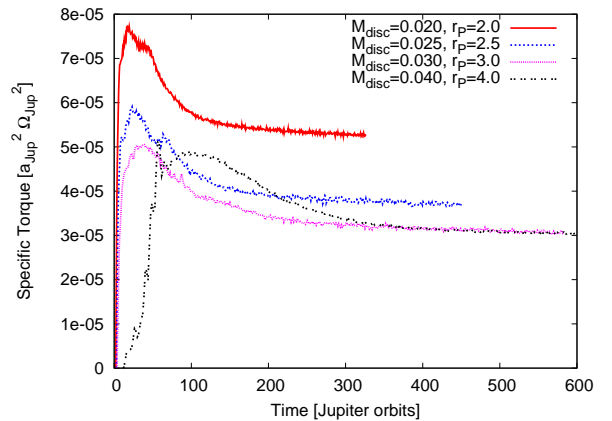

Fig. 17. Specific torque acting on $20M_{Earth}$ planets embedded in 0.02, 0.025, 0.03 and 0.04$M_\odot$ discs at the following distances $r_p = 2.0, 2.5, 3.0$ and $4.0r_{Jup}$, respectively.

gration might not be possible any more, even for low-mass discs. The influence of viscosity will also be adressed in a next paper in much more detail.

In self-gravitating discs, the torque acting on an embedded planet can differ by a factor of two compared to non self-gravitating discs, as shown by Baruteau & Masset (2008b). These authors also state that self-gravity has no effect on the corotation torque in the linear regime, but our 3D simulations are in the non-linear regime. Therefore the influence of self-gravity on planet migration in fully radiative discs should be investigated in the future.

The Toomre stability criterion can be used to estimate the stability of discs against self-gravity (Toomre 1964). The stability parameter reads

$$Q = \frac{c_s \kappa_{ep}}{\pi \Sigma G} , \qquad (6)$$

where c_s is the sound speed in the disc, κ_{ep} is the epicyclic frequency, which for Keplerian discs is approximately equal to the angular frequency Ω, Σ is the surface mass density and G is the gravitational constant. In order to achive stability in discs, the stability parameter must be $Q \gg 1$. For all disc masses used in this work, this criterion is fulfilled well, so that the discs are not gravitationally unstable.

Because convection is a 3D effect, 2D simulations (in r-ϕ direction in the midplane) of fully radiative discs with high discs masses ($M_{disc} > 0.02M_\odot$) cannot capture this effect. Therefore planets embedded in these 2D simulations will not be exposed to these fluctuations and might therefore be inaccurate near the central star because of convection in the disc.

5. Summary and conclusions

We performed full 3D radiation hydrodynamical simulations of low-mass planets embedded in accretion discs at different distances to the central star and for various disc masses.

In the first sequence of our simulations we changed the planetary distance to the central star of embedded planets on circular orbits. With increasing distance to the central star, the torque acting on $20M_{Earth}$ planets embedded in fully radiative discs becomes even more reduced and it reaches negative torques for longer distances. We find an equilibrium, zero-torque distance, to the central star for $20M_{Earth}$ planets at $r \approx 2.4r_{Jup}$. This equilibrium distance varies with the planetary mass (for $25M_{Earth}$

planets it is $r \approx 1.9 r_{Jup}$ and $r \approx 1.4 r_{Jup}$ for $30 M_{Earth}$ planets), indicating that a quite extended region in the disc might act as a feeding zone to create even larger planetary cores. The concept of equilibrium radius (zero torque radius) for planetary embryos in fully unsaturated discs has been stated in Lyra et al. (2010) as well and it could easily act as a feeding or collection zone for planetary embryos.

Planets embedded in fully radiative discs migrating outwards create a very sensitive pattern in the surface density distribution. Ahead and inside of the planet a density increase is visible (see second panel from the top in Fig. 5), which shrinks with increasing distance to the central star. This density enhancement is indeed accountable for the positive torque acting on the planet (also visible as a spike in the radial torque density distribution in Fig. 4), but as the distance to the central star increases, this effect becomes less, so that it cannot overcompensate the negative Lindblad torques any more, which results in inward migration.

We compared our results to the recently developed torque formulae by Paardekooper et al. (2010), Paardekooper et al. (2011) and Masset & Casoli (2010). Paardekooper et al. (2010) includes just the fully unsaturated torques in the inviscid and adiabatic case, shows no torque reversal option and is as such unphysical when comparing it with the long-term evolution of planets. This formula is only valid in the first orbits after the planet is embedded when the torques are still unsaturated, however, the torques do saturate in time. However, as expected, the improved version of Paardekooper et al. (2011) that includes viscous and heat diffusion describes our results more accurately. Even though an exact match has not been achieved, nevertheless the trend seems agree quite well. The Paardekooper et al. (2011) formula shows a difference of a factor of two at $r = 1.0 r_{Jup}$, which may have several causes.

The formulae are derived for 2D discs, while our simulations are 3D, which accounts for vertical diffusion that can change the structure of the disc. This might be a problem because the formulae were also derived for gradients in temperature and surface density, but in a real disc the temperature and surface density profiles are disturbed when a planet is embedded in a disc. Because the formulae were derived and checked for a $5 M_{Earth}$ planet (with about 20 per cent agreement), the disturbances of such a small planet in a disc are much weaker than for our embedded $20 M_{Earth}$ planet, which may give rise to more significant, non-linear disturbances in the temperature and density profiles. All of this may lead to differences between our simulations and the theoretical formulae in the torque acting on the planet.

For longer distances ($r > 2.0 r_{Jup}$) the formula of Paardekooper et al. (2011) fits our simulations quite well. As the distance to the central star increases, temperature and density decrease, so that the argument of disc disturbances due to the embedded planet might not be so strong any more, and the main contribution to the total torque comes from the Lindblad torques.

The formula of Masset & Casoli (2010) matches our simulations quite well in the inner parts of the disc, however, in the outer parts of the disc the differences become stronger and seem to be similar to Paardekooper et al. (2010), where the torques did not become smaller than zero. This behaviour may be triggered by the temperature gradient in the disc. In Ayliffe & Bate (2011) a steeper temperature gradient resulted in faster outward migration and triggered outward migration for planets with higher masses (even up to $50 M_{Earth}$). The same effect might be responsible for an positive migration rate even for long distances to the central star. However, it seems that the best match for the discs studied here is given by Paardekooper et al. (2011).

For increasing disc masses, the temperature, density (in midplane), and aspect ratio of the disc increases in the equilibrium state where viscous heating and radiative transport/cooling are in balance. The convective zone in the inner discs stretches farther out with increasing disc mass, resulting in high fluctuations of the surface density in our computed domain for discs with a mass higher than $M_{disc} \approx 0.02 M_\odot$.

Starting from a $M_{disc} = 0.01 M_\odot$ disc, the torque acting on embedded $20 M_{Earth}$ planets decreases for increasing disc masses. As the disc mass increases, the convective zone in the disc stretches farther out from the central star and influences planetary migration. The fluctuations in the disc's density disrupt the torque acting on the planet on a stationary orbit for high-mass discs in a way that the torque is very irregular and shows high fluctuations as well, making it difficult to determine the correct direction of migration. For lower disc masses, the torque reduces as well, assumably because of the same reasons as the torque reduced for longer distances to the central star in a discs with $M_{dics} = 0.01 M_\odot$.

The formula in Paardekooper et al. (2011) fits within a factor of two with our 3D simulations for planets in discs with $M_{dics} \approx 0.01 M_\odot$. For higher disc masses, the difference between the formula and our 3D simulations increases. Convection certainly plays a role in more massive discs, but it is unaccounted for in Paardekooper et al. (2011). In more massive discs the convective zone reaches longer distances from the central star, disrupting the density pattern near the embedded planet and thus creating fluctuations in the torque acting on the planet. These disruptions in the density pattern are caused by the convective cells evolving in the disc. These cells also change in time, giving rise to the stronger fluctuations of the torque.

Both the 3D simulations and the Paardekooper et al. (2011) formula show a decreasing torque for increasing disc mass. As the disc mass increases, viscous heating increases and cooling becomes inefficient, which results in a structure similar to an adiabatic disc. In adiabatic discs the corotation torques saturates, resulting in a lower torque acting on the planet, hence the drop of torque for increasing disc masses.

Interestingly, it seems that the analytical formulae match best when the distance to the central star is the standard value of $r \approx 1.0 r_{Jup}$ and $M_{dics} \approx 0.01 M_\odot$. In Appendix A we discuss the influence of the smoothing length on the formulae.

Convection is inefficient for transporting angular momentum (Kley et al. 1993; Lesur & Ogilvie 2010), but the influences of convection on planetary migration are very dramatic, because a planet close to the star in the convective zone of the disc is essentially disrupted. The direction of migration is not clearly determinable any more, but when the planet is farther out in the massive disc and the convection fades away, the direction of migration is easy to specify, indicating outward migration. Therefore the zero-torque radius for migration lies farther out in more massive discs.

Convection is also a 3D effect only and cannot be simulated in 2D discs (in r-ϕ direction in the midplane). Two-dimensional simulations of planets in massive discs ($M_{disc} > 0.02 M_\odot$) might therefore be inaccurate near the central star, because the effects of convection are not considered.

Appendix A: Comparison with Paardekooper et al. (2011)

In Section (3) we compared our numerical results to the analytical torque formula derived in Paardekooper et al. (2011). As the

derivation is rather cumbersome, we present here a brief summary of the relevant contributions to the total torque acting on a planet, so that the reader can follow our calculations. In our notation we closely follow Paardekooper et al. (2011).

The total torque acting on a low-mass planet consists of two main contributions the Lindblad torque, Γ_L, plus the corotation torque, Γ_c

$$\Gamma_{tot} = \Gamma_L + \Gamma_c \ . \tag{A.1}$$

The Lindblad torque is caused by the action of the induced spiral arms and is given as (Paardekooper & Papaloizou 2008)

$$\gamma\Gamma_L/\Gamma_0 = -2.5 - 1.7\beta + 0.1\alpha \ , \tag{A.2}$$

where α denotes the negative slope of the surface density profile $\Sigma \propto r^{-\alpha}$, β refers to the slope of the temperature profile $T \propto r^{-\beta}$, and γ is the adiabatic index of the gas.

It is important to notice that all torques listed here are normalized to

$$\Gamma_0 = \left(\frac{q}{h}\right)^2 \Sigma_P r_p^4 \Omega_P^2 \ ,$$

with q the planet/star mass ratio, h the relative disc's height, Σ_P the surface density at the planet's location and Ω_P the rotation frequency of the planet in the disc.

The corotation torque is now split into the barotropic part and an entropy-related part:

$$\Gamma_c = \Gamma_{c,baro} + \Gamma_{c,ent} \ ,$$

where the first part applies to barotropic flows where the pressure only depends on the density, and it depends on the gradient of the vorticity in the flow; the second part relates to the variations of entropy. Each of them is split again into a linear contribution and a so-called horseshoe drag contribution. This separation is necessary because the two parts are affected differently by the diffusion processes. The barotropic part of the (non-linear) horseshoe drag is given by

$$\gamma\Gamma_{hs,baro}/\Gamma_0 = 1.1(1.5 - \alpha) \tag{A.3}$$

and the entropy-related part of the horseshoe drag is given by

$$\gamma\Gamma_{hs,ent}/\Gamma_0 = 7.9\frac{\xi}{\gamma}, \tag{A.4}$$

where $\xi = \beta - (\gamma - 1.0)\alpha$ is the negative of the power-law index of the entropy. We note that the total torque formula given by Paardekooper et al. (2010), as summarized in Eq. (1), is exactly the sum $\Gamma_{tot} = \Gamma_L + \Gamma_{hs,baro} + \Gamma_{hs,ent}$.

The barotropic part of the linear corotation torque reads as

$$\gamma\Gamma_{c,lin,baro}/\Gamma_0 = 0.7(1.5 - \alpha), \tag{A.5}$$

and the entropy-related part of the linear corotation torque is given by

$$\gamma\Gamma_{c,lin,ent}/\Gamma_0 = \left(2.2 - \frac{1.4}{\gamma}\right)\xi. \tag{A.6}$$

Owing to the difference between the isothermal and adiabatic sound speed, differences in the torque arise. To compensate for this, the adiabatic index γ should be replaced by an *effective* γ:

$$\gamma_{eff} = \frac{2Q\gamma}{\gamma Q + \frac{1}{2}\sqrt{2\sqrt{(\gamma^2Q^2+1)^2 - 16Q^2(\gamma-1)} + 2\gamma^2Q^2 - 2}} \ ,$$

so that all γ's in the previous equations (A.2 to A.6) have to be replaced by γ_{eff}. The parameter Q is given by

$$Q = \frac{2\chi_P\Omega_P}{3hc_s^2} = \frac{2\chi_P}{3h^3r_P^2\Omega_P} \ ,$$

where $h = H/r$ and $\chi_P = 10^{-3}r_P^2\Omega_P$.

The final correction relates to the non-ideal effects of viscosity and heat transfer, which both have to be present to avoid the saturation of the corotation torque. The barotropic part of the horseshoe drag is not affected by thermal diffusion and is only determined by the viscosity. According to Paardekooper et al. (2011) it can be written as

$$\Gamma_{c,baro} = \Gamma_{hs,baro}F(p_\nu)G(p_\nu) + (1 - K(p_\nu))\Gamma_{c,lin,baro},$$

where $\Gamma_{hs,baro}$ and $\Gamma_{c,lin,baro}$ are given by equations (A.3 and A.5), but now with $\gamma \to \gamma_{eff}$. $F(p)$ (eq. A.7) governs saturation and $G(p)$ (eq. A.8) and $K(p)$ (eq. A.9) govern the cut-off at high viscosity.

For the non-barotropic, entropy-related corotation torque Paardekooper et al. (2011) find

$$\begin{aligned}\Gamma_{c,ent} &= \Gamma_{hs,ent}F(p_\nu)F(p_\chi)\sqrt{G(p_\nu)G(p_\chi)} \\ &+ \sqrt{(1 - K(p_\nu))(1 - K(p_\chi))}\Gamma_{c,lin,ent} \ ,\end{aligned}$$

where $\Gamma_{hs,ent}$ and $\Gamma_{c,lin,ent}$ are given by equations A.4 and A.6, again with $\gamma \to \gamma_{eff}$, and p_χ is the saturation parameter associated with thermal diffusion.

The function $F(p)$ is given by

$$F(p) = \frac{1}{1 + (p/1.3)^2} \ . \tag{A.7}$$

The function $G(p)$ is given by

$$G(p) = \begin{cases} \frac{16}{25}\left(\frac{45\pi}{8}\right)^{3/4}p^{3/2} & \text{for} \quad p < \sqrt{\frac{8}{45\pi}} \\ 1 - \frac{9}{25}\left(\frac{8}{45\pi}\right)^{4/3}p^{-8/3} & \text{for} \quad p \geq \sqrt{\frac{8}{45\pi}} \end{cases} \ . \tag{A.8}$$

The function $K(p)$ is given by

$$K(p) = \begin{cases} \frac{16}{25}\left(\frac{45\pi}{28}\right)^{3/4}p^{3/2} & \text{for} \quad p < \sqrt{\frac{28}{45\pi}} \\ 1 - \frac{9}{25}\left(\frac{28}{45\pi}\right)^{4/3}p^{-8/3} & \text{for} \quad p \geq \sqrt{\frac{28}{45\pi}} \end{cases} \ . \tag{A.9}$$

The parameters p_ν and p_χ, relate to the strength of viscosity and thermal diffusivity, and are given by

$$p_\nu = \frac{2}{3}\sqrt{\frac{r_P^2\Omega_P x_s^3}{2\pi\nu_p}} \ ,$$

$$p_\chi = \sqrt{\frac{r_P^2\Omega_P x_s^3}{2\pi\chi_p}} \ ,$$

where ν_p is the kinematic viscosity and χ_p the thermal conductivity at the planet location. x_s is the half width of the horseshoe, given by

$$x_s = \frac{1.1}{\gamma_{eff}^{1/4}}\left(\frac{0.4}{\epsilon/h}\right)^{1/4}\sqrt{\frac{q}{h}} \ ,$$

The scaling with ϵ/h breaks down for small softening ($\epsilon/h < 0.3$). All these contributions have to be substituted into equation (A.1) to calculate the total torque acting on the planet. In deriving these formulae one has to use a description for the smoothing of the gravitational potential. Here, a standard ϵ potential has
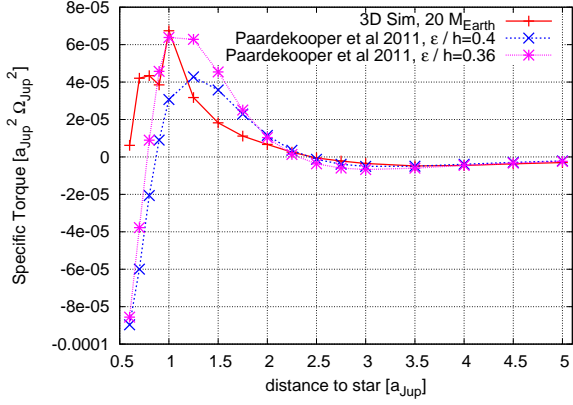
Fig. A.1. Specific torque acting on $20M_{Earth}$ planets embedded in a $0.01M_{\odot}$ disc. Overplotted are the results of Paardekooper et al. (2011) with $\epsilon/h = 0.4$ and $\epsilon/h = 0.36$.

been assumed, and a smoothing length of $\epsilon/H = 0.4$ has been made.

To compare with our simulations, we have used the following parameter in the formulae above $\alpha = 0.5, \beta = 1.7, \xi = 1.5$. To evaluate the viscosity parameter p_ν we use $\nu = 10^{-5}$. Please note that $\nu_p \approx \chi_p$ for discs in radiative equilibrium.

In Kley et al. (2009) we pointed out that a different planetary smoothing results in different torques. This phenomenon can be up to a factor of two for the ϵ potential with $r_{sm} = 0.5$ and the cubic potential with $r_{sm} = 0.5$. In Section (3) we compared our numerical simulations to the smoothing with $\epsilon/h = 0.4$.

Because our cubic potential with r_{sm} is deeper in the vicinity of the planet, we used $\epsilon/h = 0.36$ for the Paardekooper et al. (2011) formula as well. The results are shown in Fig. A.1. Compared to the $\epsilon/h = 0.4$, the $\epsilon/h = 0.36$ potential shows very good agreement at $r = 1.0r_{Jup}$, but for longer distances to the central star the differences between the formula and our simulations are much more pronounced than in the $\epsilon/h = 0.4$ case. The zero-torque radius is shifted to longer distances for the $\epsilon/h = 0.36$ case, indicating that a different smoothing of the planetary potential influences the zero-torque radius as well. For longer distances to the central star ($r > 3.0r_{Jup}$) both formula and the simulations agree very well because the Lindblad torques seem to dominate the torque regime.

References

Alibert, Y., Mordasini, C., & Benz, W. 2004, A&A, 417, L25
Ayliffe, B. A. & Bate, M. R. 2010, MNRAS, 408, 876
Ayliffe, B. A. & Bate, M. R. 2011, ArXiv e-prints
Baruteau, C. & Masset, F. 2008a, ApJ, 672, 1054
Baruteau, C. & Masset, F. 2008b, ApJ, 678, 483
Bitsch, B. & Kley, W. 2010, A&A, 523, A30
Bitsch, B. & Kley, W. 2011, A&A, 530, A41
Crida, A., Baruteau, C., Kley, W., & Masset, F. 2009, A&A, 502, 679
Crida, A., Sándor, Z., & Kley, W. 2008, A&A, 483, 325
Ida, S. & Lin, D. N. C. 2008, ApJ, 673, 487
Klahr, H. & Kley, W. 2006, A&A, 445, 747
Klahr, H. H., Henning, T., & Kley, W. 1999, ApJ, 514, 325
Kley, W., Bitsch, B., & Klahr, H. 2009, A&A, 506, 971
Kley, W. & Crida, A. 2008, A&A, 487, L9
Kley, W., Papaloizou, J. C. B., & Lin, D. N. C. 1993, ApJ, 416, 679
Lesur, G. & Ogilvie, G. I. 2010, MNRAS, 404, L64
Lyra, W., Paardekooper, S. J., & Mac Low, M. M. 2010, ApJ, 715, L68
Masset, F. 2000, A&AS, 141, 165
Masset, F. & Casoli, J. 2010, ApJ, 723, 1393
Masset, F. S. & Casoli, J. 2009, ApJ, 703, 857
Masset, F. S., D'Angelo, G., & Kley, W. 2006, ApJ, 652, 730
Morbidelli, A., Crida, A., Masset, F., & Nelson, R. 2008, A&A, 478, 929
Mordasini, C., Alibert, Y., & Benz, W. 2009, A&A, 1139
Mordasini, C., Dittkrist, K. M., Alibert, Y., et al. 2010, astro-ph.EP
Paardekooper, S., Baruteau, C., Crida, A., & Kley, W. 2010, MNRAS, 401, 1950+
Paardekooper, S. J., Baruteau, C., & Kley, W. 2011, MNRAS, 293
Paardekooper, S.-J. & Mellema, G. 2006, A&A, 459, L17
Paardekooper, S.-J. & Mellema, G. 2008, A&A, 478, 245
Paardekooper, S.-J. & Papaloizou, J. C. B. 2008, A&A, 485, 877
Sándor, Z., Lyra, W., & Dullemond, C. P. 2011, ApJ, L9
Tanaka, H., Takeuchi, T., & Ward, W. R. 2002, ApJ, 565, 1257
Toomre, A. 1964, ApJ, 139, 1217
Ziegler, U. & Yorke, H. 1997, Computer Physics Communications, 101, 54

Influence of viscosity and the adiabatic index on planetary migration

Bertram Bitsch[1], Aaron Boley[2] and Wilhelm Kley[1]

[1] Institut für Astronomie & Astrophysik, Universität Tübingen, Auf der Morgenstelle 10, D-72076 Tübingen, Germany
[2] University of Florida, Theoretical Astrophysics

ABSTRACT

Context. In our previous works we have shown that the outward migration of low mass planets in fully radiative discs can be possible. For these studies we only considered a constant viscosity and a constant adiabatic index in the disc, in which the planets were embedded. As the viscosity inside a real accretion disc is unknown, we want to investigate the influence of viscosity on planetary migration.
Aims. In this paper we focus on fully radiative discs with different viscosities (α and constant viscosity) and adiabatic indices. We compare profiles of accretion discs with different viscosities and adiabatic indices and want to determine the migration rate of embedded planets in these discs.
Methods. We use an explicit three-dimensional (3D) hydrodynamical code `NIRVANA` that includes full tensor viscosity. We have added implicit radiation transport in the flux-limited diffusion approximation.
Results. In low viscosity discs, planets migrate inwards even in fully radiative discs. The effect of outward migration can only be sustained if a large enough viscosity in the disc is present. The differences between the two different gas distributions seems to play only a role in discs with α viscosity. Simulations with a constant viscosity show no differences in the torque acting on an embedded planet for the two gas distributions.
Conclusions. A change in the adiabatic index and in the viscosity changes the zero-torque radius for outward migration. The difference between the two gas distributions seems to decrease with increasing viscosity (as the temperature in the midplane becomes higher and higher).

Key words. accretion discs – planet formation – hydrodynamics – radiative transport – planet disc interactions – adiabatic index

1. Introduction

Inward migration of a low-mass planet embedded in a fully radiative gaseous disc can be significantly different from migration in an isothermal or purely adiabatic disk (Paardekooper & Mellema 2006; Baruteau & Masset 2008; Paardekooper & Papaloizou 2008; Paardekooper & Mellema 2008; Kley & Crida 2008; Kley et al. 2009; Ayliffe & Bate 2010). While all authors agree that radiation transport can slow the rate of inward migration, there is still a lack of consensus whether the direction of migration can be outward. Part of this confusion may be due to the sensitivity of the direction and magnitude of migration on global disk parameters (Paardekooper et al. 2010; Masset & Casoli 2010; Paardekooper et al. 2011), including, e.g., the radial disk temperature gradient (Ayliffe & Bate 2011). Different authors also use different viscosities, usually either a constant viscosity or a Shakura & Sunyaev (1973) α-viscosity, with a typical value of α ranging between 10^{-4} and 10^{-2}.

An unperturbed, viscous, fully radiative disc will evolve toward an equilibrium state, where viscous heating is balanced by radiation transport and cooling (as described in, e.g., Kley et al. 2009). This equilibrium state is dependent on the disc mass, the viscosity, and the adiabatic index of the gas. Variations in the viscosity change the radial density, temperature, and entropy profiles. The entropy gradient, in turn, determines whether torques acting on an embedded, low-mass planet saturate (Baruteau &

Masset 2008). If the torques remain unsaturated, the net torque can be positive, leading to outward migration. This effect is also possible in isothermal discs (Paardekooper & Papaloizou 2008).

There is an additional complication to understanding the migration of low-mass planets in disks. The rotational states of molecular hydrogen are only fully accessible at temperatures $\gtrsim 300$ K (Decampli et al. 1978; Boley et al. 2007). As a result, the adiabatic index of the gas will transition from $\gamma = 7/5$ to $5/3$ as the temperature in a disk drops with radial distance. The region over which this variation occurs is precisely where we expect planetary cores and planets to form in the core accretion scenario and begin their initial stages of migration. So far, only a constant adiabatic index of $\gamma = 1.4$ has been explored in our previous simulations with radiative transport.

All of these effects on low-mass planet migration are relevant to understanding whether planet traps can exist, i.e., regions in the disk where a protoplanet would experience zero torque. Protoplanets migrating from a smaller radius outward or from an outer radius inward would collect at the zero-torque radius, creating areas conducive to planetary mergers, leading possibly to large cores. A planet trap could be formed by surface density changes, which would also create an enhanced feeding zone for these cores (Morbidelli et al. 2008); however, it is yet unclear how realistic surface density changes are in discs. In contrast, radiation transport might allow for traps to exist in smooth disc structure. As outward migration is dependent on the viscosity, disc mass, and adiabatic index, these parameters will influence the radius and breadth of the zero-torque region.

This paper is organized as follows: In Section 2 we give an overview of our numerical methods. We then describe the influence of the adiabatic index, viscosity, and the differences between the ortho-para and equilibrium gas configuration on the disc structure in Section 3. These changes in the disc structure influence the migration rate of an embedded $20 M_{Earth}$ planet, which is discussed in Section 4. In Section 5 the influence of viscosity and of the different gas mixtures on the zero-torque radius is investigated. We then summarise and conclude in Section 6.

2. Numerics and setup

2.1. Setup

The protoplanetary disc is modelled as a three-dimensional (3D), non-self-gravitating gas. Fluid motion is described by the Navier-Stokes equations, where the equations are solved numerically using a spatially second-order finite volume method that is based on the code NIRVANA (Ziegler & Yorke 1997). The disc is heated solely by internal viscous dissipation, and is allowed to cool by flux-limited diffusion (FLD, Levermore & Pomraning 1981). The FLD approximation allows internally produced energy to diffuse radiatively through the optically thick regions of the disc and into the optically thin regions, where the energy can be radiated away by free-streaming. The flux-limiter interpolates between the optically thick and thin regimes and ensures that energy loss never exceeds the free-streaming limit. Radiative transport is handled implicitly and uses the FARGO (Masset 2000) extension as described in Kley et al. (2009). A more detailed description of the modelling and the numerical methodology is provided in our previous papers (Kley et al. 2009; Bitsch & Kley 2010; Bitsch & Kley 2011).

The three-dimensional (r, θ, ϕ) computational domain (with $266 \times 32 \times 768$ active cells) consists of a complete annulus of the protoplanetary disc centred on the star, extending from $r_{min} = 0.4$ to $r_{max} = 2.5$ in units of $r_0 = a_{Jup} = 5.2 AU$. In the vertical direction the annulus extends $7°$ above the disc's midplane, meaning $83° < \theta < 90°$. Here θ denotes the polar angle of our spherical polar coordinate system measured from the polar axis. The central star has one solar mass $M_* = M_\odot$, and the total disc mass inside $[r_{min}, r_{max}]$ is $M_{disc} = 0.01 M_\odot$. The aspect ratio of the disc is calculated self-consistently from the equilibrium structure, given by the viscous internal heating and radiative diffusion. This also determines the surface density gradient in the equilibrium state of the disc. To calculate the equilibrium state, we first use 2D models in the r-θ directions.

The planet is located at $r_P = 1.0 a_{Jup}$. For the planet, we use the cubic potential (Klahr & Kley 2006; Kley et al. 2009) with $r_{sm} = 0.5$. The planetary potential and its influence on planetary migration is discussed in great detail in Kley et al. (2009).

2.2. 2D axisymmetric models

The initialisation through an axisymmetric 2D phase (in the $r - \theta$ plane) reduces the required computational effort substantially. The evolution from the initial isothermal state towards the equilibrium between viscous heating and radiative transport/cooling takes about 100 orbits, if the disc is started with an isothermal equilibrium having constant H/r. The surface density or temperature profiles of the initial (isothermal) state are unimportant as the equilibrium state of the disc solely depends on the disc mass, viscosity and adiabatic index of the disc.
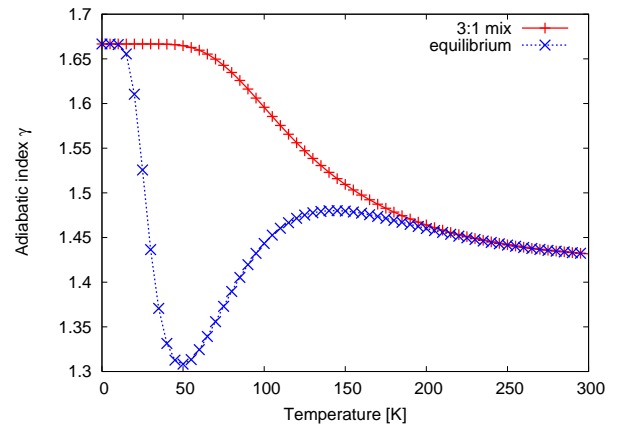

Fig. 1. Adiabatic index for the $3 : 1$ ortho to para mix and equilibrium gas configuration in dependence of the temperature.

After reaching the equilibrium between viscous heating and radiative transport/cooling, we extend this model to a full 3D simulation, by expanding the grid into the ϕ-direction and by embedding the planet. From this starting configuration it is also possible to investigate the vertical structure of an unperturbed disc in the equilibrium state.

2.3. Adiabatic index

The gas in an existing accretion disc is primary molecular hydrogen, which exists as para and ortho-hydrogen for proton spins that are antiparallel and parallel, respectively. If enough protonated ions (e.g., H_3+) are available to exchange proton spins on time scales that are shorter than the dynamical time, the para- and ortho-hydrogen should be treated as being in statistical equilibrium (Boley et al. 2007). If the dynamical timescale is shorter than the equilibrium timescale, a fixed ratio should be used, where a $3 : 1$ ortho-to-para mix is common for many astrophysical systems. A different mixture of gas changes the ratio of specific heats, which is the adiabatic index γ. The adiabatic index is dependent of the temperature of the underlying gas (Boley et al. 2007), and astrophysical disks should transition between $\gamma = 5/3$ to $\gamma = 7/5$ *near the frost line*. This is represented in Fig. 1, where the adiabatic index's dependence on temperature is plotted for the equilibrium (blue) and the $3 : 1$ ortho to para mix (red) gas. The adiabatic index can span quite a large region in γ for low temperatures. In our typical disc simulations (with $\gamma = 1.4$) the temperature at $r = 1.0 r_{Jup}$ is about $65 K$, which is in a region where the adiabatic index changes rapidly. Such variation could affect an embedded planet's migration rate, as the planet modifies the temperature structure of its surroundings.

2.4. Viscosity

One can assume the viscosity of an accretion disc to be either constant or an α viscosity, with $\nu = \alpha c_s H$ (Shakura & Sunyaev 1973), where H is the disc's thickness and c_s the sound speed. In a real accretion disc in equilibrium, the viscosity can be determined through the mass accretion rate onto the star:

$$\dot{M} \approx 3\pi\nu\Sigma = 3\pi\alpha c_s H\Sigma, \qquad (1)$$

where $\dot{M}$ is the mass accretion rate onto the star, typically $10^{-9} - 10^{-7} M_\odot/yr$ (Hartigan et al. 1995; Gullbring et al. 1998) and Σ the surface density. For numerical studies one has to assume the viscosity in the disc. The viscosity determines the structure of

the disc and thus influences the migration of embedded planets. For simulations of accretion discs typically $10^{-4} \leq \alpha \leq 10^{-2}$.

2.5. Torque calculations

In our previous work, we have discussed the calculation of the torque acting on the planet in great detail. Outward migration seems only possible and is strongest, when the planet is on circular orbits (Bitsch & Kley 2010) and in the midplane of the disc (Bitsch & Kley 2011). Therefore it seems sufficient to consider only planets on fixed circular orbits in the midplane of the disc, and calculate the torque acting on the planet, as the torque represents a direct measurement of migration in this case. Therefore only the upper half of the disc ($83° \leq \theta \leq 90°$) is needed for the calculation, as the lower half is directly symmetric to the upper half.

The torques acting on a $20 M_{Earth}$ planets are calculated to determine the direction of outward migration. As the planet is simulated as a point mass, the planetary potential needs to be smoothed. We use the cubic potential (Klahr & Kley 2006; Kley et al. 2009) for our calculations:

$$\Phi_p^{cub} = \begin{cases} -\frac{m_p G}{d} \left[\left(\frac{d}{r_{sm}}\right)^4 - 2\left(\frac{d}{r_{sm}}\right)^3 + 2\frac{d}{r_{sm}} \right] & \text{for} \quad d \leq r_{sm} \\ -\frac{m_p G}{d} & \text{for} \quad d > r_{sm} \end{cases} \quad (2)$$

Here m_P is the planetary mass, $d = |\mathbf{r} - \mathbf{r_P}|$ denotes the distance of the disc element to the planet and r_{sm} is the smoothing length of the potential in units of the Hill radii. The construction of the planetary potential is in such a way that for distances larger than r_{sm} the potential matches the correct $1/r$ potential and is smoothed inside that radius ($d < r_{sm}$) by a cubic polynomial. The parameter r_{sm} is equal to 0.5 in all our simulations.

The gravitational torques acting on the planet are calculated by integrating over the whole disc, where we apply a tapering function to exclude the inner parts of the Hill sphere of the planet (Crida et al. 2008). This torque-cutoff is necessary to avoid large, probably noisy contributions from the inner parts of the Roche lobe and to disregard material that is possibly gravitationally bound to the planet (Crida et al. 2009). Here we assume (as in our previous papers) a transition radius of 0.8 Hill radii.

3. Changes in the disc structure

As the adiabatic index is connected to the sound speed, which is directly linked to pressure and density, a change in the adiabatic index, changes the structure of the disc. Also a change of viscosity in the disc changes the equilibrium state between viscous heating and radiative cooling/transport. The influences of these parameters on the disc structure (without an embedded planet) are discussed in this Section.

3.1. Influences of the adiabatic index

A change of the adiabatic index will change the relation between pressure and density and therefore change the internal structure of the disc. For the following simulations we limit ourselves to constant values of γ in the range of $1.05 \leq \gamma \leq 1.8$, which is larger than the range of the adiabatic index in Fig. 1. In Fig. 2 the midplane density and temperature and the resulting aspect ratio at $r = 1.0$ for a 2D disc in $r - \theta$ direction are displayed (using a constant viscosity of $\nu = 10^{15}$ cm^2/s). A lower adiabatic index leads to a higher midplane density, a lower midplane temperature and a lower aspect ratio in the disc at $r = 1.0$. The density falls

off very rapidly for low γ values, and as γ increases, the drop in density becomes less and less. For the temperature and aspect ration, it is the other way round. These quantities increase very fast for low γ's and then the increase becomes less and less. It seems that there is no big difference in density, temperature and aspect ratio for high γ values. Here $H = c_s/\Omega \propto \sqrt{T}$.

Now the radial density and temperature gradients result in a gradient in entropy $S \propto \frac{p}{\rho^\gamma}$. This gradient of entropy across the horseshoe region is very crucial to planetary migration, as it keeps the corotation torque acting on the planet unsaturated and thus determines the direction of migration in a fully radiative disc. As the density decreases and the temperature increases with increasing γ, the strength of the gradient in entropy might change and therefore influence planetary migration.

In the isothermal situation, the result would be clear, as a higher aspect ratio results in a slower inward migration of low mass planets (Tanaka et al. 2002). In our fully radiative discs, the structure of the disc is calculated self-consistently, meaning that the equilibrium configuration of the disc between viscous heating and radiative transport/cooling determines the structure. This structure is influenced by the adiabatic index, thus for each adiabatic index a disc with different aspect ratio H/r and different density and temperature profiles is created.

The structure of the aspect ratio of a fully radiative disc with different adiabatic indices is shown in Fig. 3. The aspect ratio H/r is computed through $H = c_s/\Omega = \sqrt{\frac{\gamma P}{\rho}}/\Omega$ in the disc's midplane. For $\gamma = 1.1$ the aspect ratio shows nearly constant profile (with small fluctuations), with a large dip around $r \approx 1.0$. But keep in mind that such a small adiabatic index is not predicted for accretion discs, following the $\gamma(T)$ profile of Boley et al. (2007) in Fig. 1.

In contrast, the profiles for a higher adiabatic index show a drop in aspect ratio (after a small increase for very small distance to the central star) with increasing distance to the central star. The $\gamma = 1.4$ simulation also shows a small dip around $r \approx 1.0$, which is not visible for higher γ. The interesting feature of a disc structure like this is the opposite of what one would expect. The general assumption would be an increasing H/r for increasing distances to the star.

With increasing distance to the central star, the temperature is decreasing. With increasing temperature the opacity in the disc increases until $T \approx 155K$. For higher temperatures the opacity is decreasing again. So with increasing distance to the central star, the opacity first increases and when $T \approx 155K$, the opacity decreases. This is exactly the point in the disc, where the aspect ratio H/r of the disc starts to decrease. Please note that the height H of the disc is still increasing, but at a lower rate, when $T < 155K$ compared to $T > 155K$. The structure of the disc is a result of the used opacity law.

3.2. Influences of viscosity

A change in the viscosity changes the equilibrium state between viscous heating and radiative transport/cooling. Therefore the density and temperature profiles of the disc are changed, as can be seen in Fig. 4, where we display the density (top) and temperature (bottom) of fully radiative discs in the equilibrium state. We plot the density and temperature for α-viscosities $0.001 \leq \alpha \leq 0.008$ and for a constant viscosity of $\nu = 10^{15}$ cm^2/s, a value used in our previous simulations (Kley et al. 2009; Bitsch & Kley 2010; Bitsch & Kley 2011).
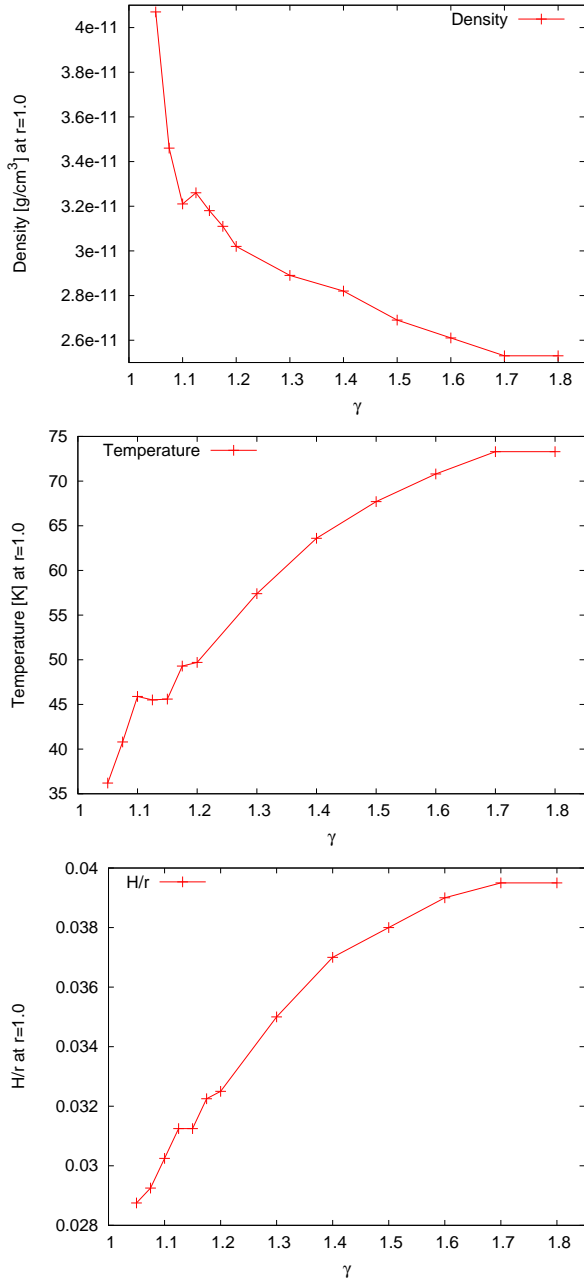
Fig. 2. Density (top), temperature (middle) and aspect ratio (bottom) of discs with different adiabatic indices in the equilibrium state of a 2D disc in r-θ direction. Density, temperature and aspect ratio are measured at $r = 1.0$ in the midplane of the disc.
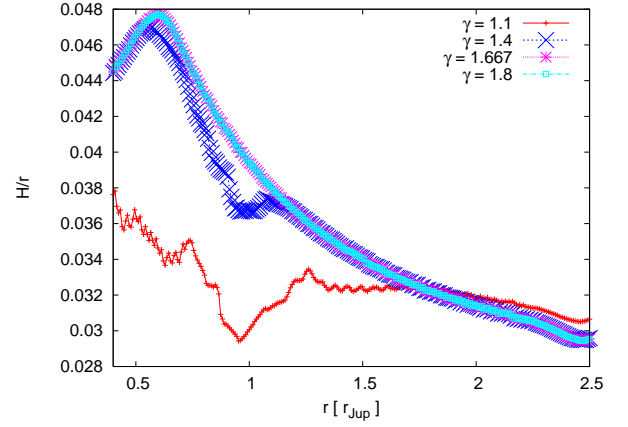

Fig. 3. Aspect ratio (H/r) of a fully radiative disc with different adiabatic indices without an embedded planet.
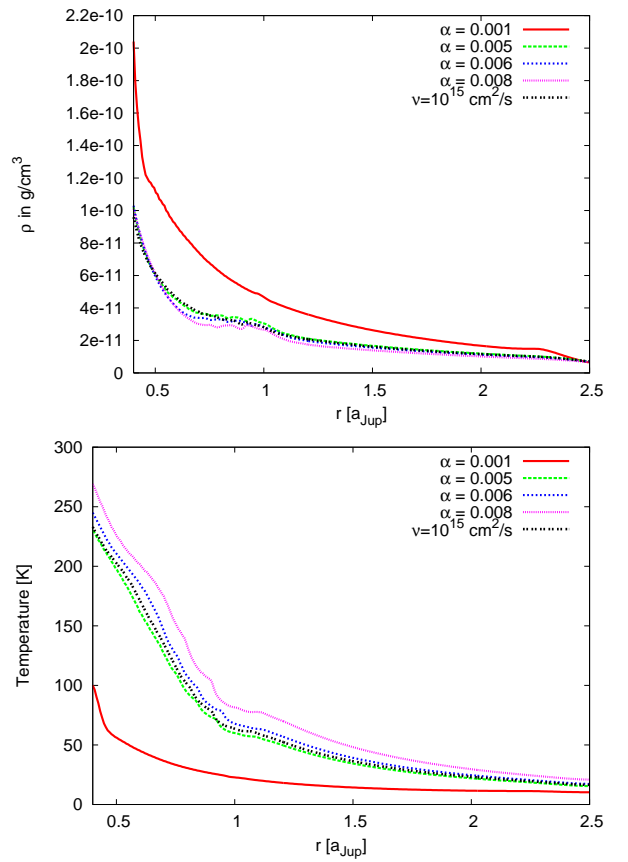

Fig. 4. Density (top) and temperature (bottom) of fully radiative discs with different viscosity in the equilibrium state. Density and temperature are measured in the disc's midplane.

For increasing α-viscosity the density in the midplane of the disc becomes smaller, but the differences in density become smaller for higher viscosities.

For the temperature profile, the trend is reversed: a higher viscosity results in a higher temperature in the midplane of the disc. As the viscosity increases, so does the viscous heating in the disc. The heating process mainly takes place in the midplane of the disc, as the density is highest there. Therefore the temperature in the midplane of the disc is higher for increasing viscosities. But not only is the temperature higher in the midplane, but also the temperature profiles change with viscosity ($T \propto r^{-\beta}$). For our constant viscosity of $\nu = 10^{15}$ cm²/s the slope of temperature was $\propto r^{-1.7}$ (Kley et al. 2009), while it is different for

the different α-viscosity models. The slope of temperature β is displayed in Table. 1.

The slope of the temperature has a direct influence on the migration of embedded planets, e.g. (Paardekooper et al. 2010, 2011). In Paardekooper et al. (2011) the slope of the temperature is needed to calculate the Lindblad torque, the entropy-related part of the horseshoe drag and the entropy-related part of the linear corotation torque. A change in β therefore influences the torque acting on an embedded planet quite severely (Ayliffe & Bate 2011). The formula of Paardekooper et al. (2011) also fits

quite nicely with our simulations to determine the zero-torque radius (Bitsch & Kley 2011b).

The aspect ratio H/r of the disc also increases for increasing viscosity (see Table. 1), indicating another factor that influences planetary migration in these discs. For isothermal discs, this has been know for a while (Tanaka et al. 2002).

It seems that the density and temperature profiles of our constant viscosity simulation are between $\alpha = 0.005$ and $\alpha = 0.006$ simulations (also H/r seems to match quite good), indicating that one could expect a very similar torque acting on a planet embedded in these discs. However, as the α-viscosity is not constant in r, one might also expect some differences in the spiral wave densities and temperatures in these discs. Also the area near the planet might be subject to some changes due to the different viscosity.

3.3. Influences of varying adiabatic index

In Fig. 5 the temperature (top) and density (bottom) profiles in the midplane of fully radiative discs are displayed. The discs feature different α viscosities and the two different mixtures of the gas (equilibrium and the ortho-para mix). As expected from simulations with a constant adiabatic index, an increasing α viscosity results in a smaller density and higher temperature in the midplane of the disc.

It seems that the gradients in density and temperature are comparable to the gradients for constant adiabatic indices. It also seems that the mixture of the gas does not have a huge influence on the temperature and density profiles for large viscosities. However, for $\alpha = 0.001$ there are differences between the two gas states in the density and temperature profiles. For $r < 1.0$ the temperature in the equilibrium state between viscous heating and radiative transport/cooling is smaller in the equilibrium gas configuration compared to the ortho-para mix. As a result the density is higher in the equilibrium gas configuration compared to the ortho-para mix. As γ is reduced largely for temperatures around $T \approx 50K$ in the equilibrium gas configuration compared to the ortho-para mix, the behaviour of density and temperature should be the same as for constant γ. This behaviour is expected from our simulations with constant γ, where a decrease in γ resulted in a drop in temperature and an increase in density.

In Fig. 6 the aspect ratio H/r for the same discs is shown. The profiles are very similar to those with alpha viscosity, but with a constant adiabatic index. In the $\alpha = 0.001$ case, the aspect ratio profile is nearly constant, with a dip for $r < 1.0$ in the equilibrium case, as discussed before for temperature and density. For the higher viscous discs, the aspect ratio increases for small r, but then decreases with increasing r continuously. Also a higher viscosity provides for a higher aspect ration in the disc.
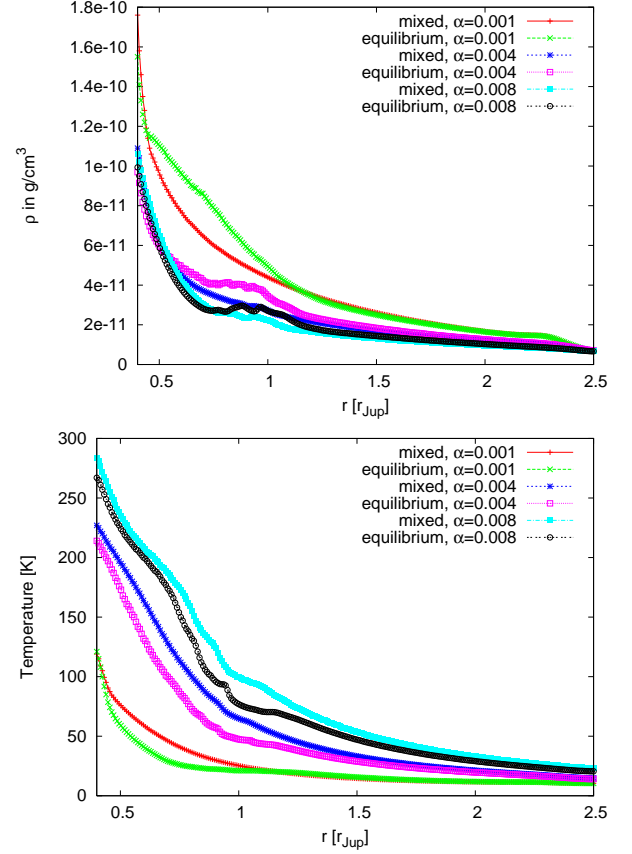

Fig. 5. Density (top) and temperature (bottom) in midplane for α viscosity discs with different transition assumptions of the gas for the adiabatic index.
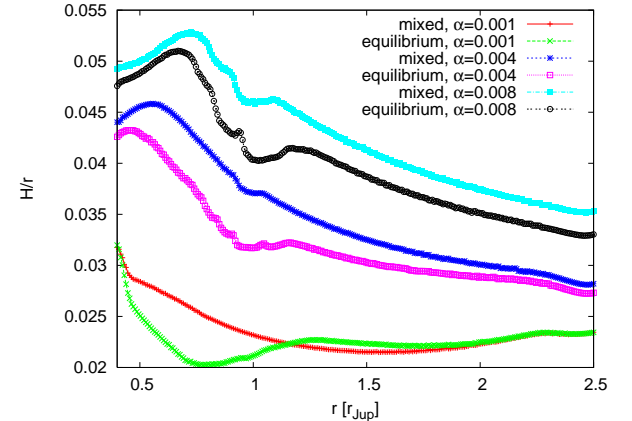

Fig. 6. Aspect ratio H/r of accretion discs with different α viscosities with different transition assumptions of the gas for the adiabatic index.

For $r > 1.0$ the equilibrium gas configuration shows a slightly smaller aspect ratio for viscosities $\alpha \geq 0.004$ compared to the ortho-para gas configuration.

The aspect ratio differs by about 10% for the high viscosity cases at $r = 1.0$. This difference in the aspect ratio can also influence the torque acting on embedded plants at this point in the disc, as it does in isothermal discs.

A higher viscosity inside the disc leads to larger temperature in midplane of the disc. Recently, Bitsch & Kley (2011b) have shown that in fully radiative discs with viscous heating a convective region arises near the central star dependent on the disc
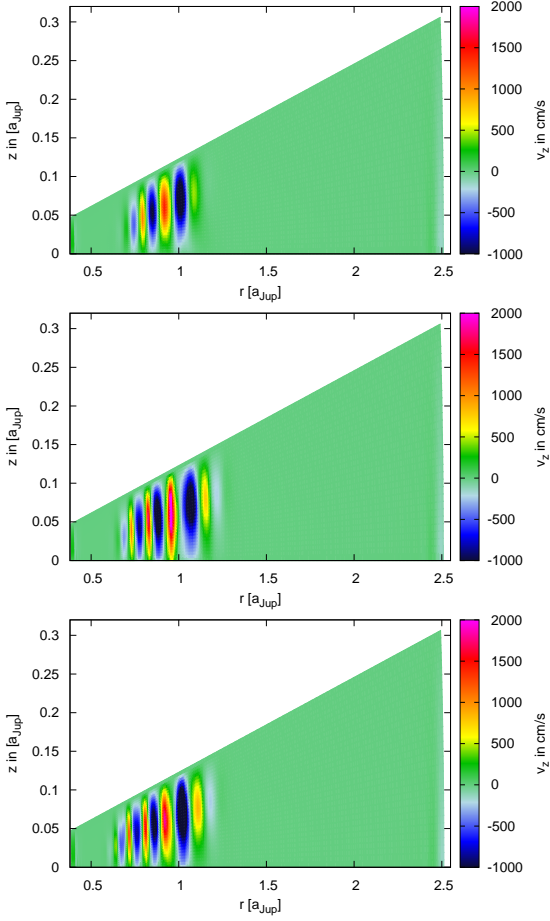
α	β	$H(r = 1.0)$
0.001	2.10	0.0220
0.002	2.10	0.0270
0.003	2.00	0.0301
0.004	1.85	0.0331
0.005	1.75	0.0357
0.006	1.70	0.0379
0.007	1.70	0.0415
0.008	1.60	0.0416
$\nu = const.$	1.70	0.0370

Table 1. Slope of the temperature profile β, where $T \propto r^{-\beta}$, and discs thickness H in dependence of viscosity.

Fig. 7. Velocities in *z*-direction for discs with $\alpha = 0.008$ with the ortho-para mix (top), the equilibrium gas configuration (middle) and with a constant adiabatic index of $\gamma = 1.4$ (bottom).
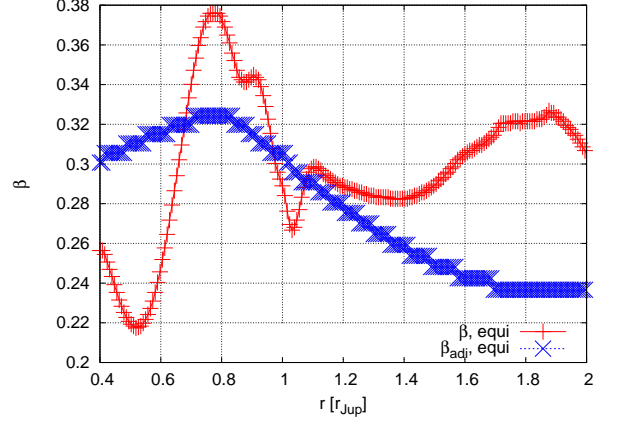

Fig. 8. Inverse of mass-weighted adiabatic gradient for an $\alpha = 0.008$ disc with the equilibrium gas configuration.

For $\beta > \beta_{adiabat}$, convection is present in the disc. $\beta_{adiabat}$ is defined as

$$\beta_{adiabat} = \frac{\gamma_{local} - 1}{\gamma_{local}} , \qquad (4)$$

where γ_{local} represents the local adiabatic index. For the constant γ and the ortho-para mixed gas configuration this is fulfilled in the region that features the fluctuations in the *z*-velocity. For the equilibrium gas configuration, this region covers also the outer parts of the disc, as can be seen in Fig. 8.

In the velocity pattern, no fluctuations can be seen for $r > 1.5$ in the equilibrium gas configuration, which indicates that no convection is present which is in contradiction with the evaluation of the mass-weighted adiabatic gradient. The reason that no convection in the outer parts of the disc can be seen might just be that the disc is too thin, the temperature too low and the optical depth too low to feature convection.

4. Influence on planetary migration

As a different adiabatic index and a change in viscosity changed the disc profiles, it is expected that it will also change the migration rate of an embedded planet. To determine the direction of migration of protoplanets embedded in discs, the torque acting on the planet is measured. A positive torque represents outward migration, while a negative torque indicates inward migration. The torque acting on planets on circular, non-inclined planets is directly proportional to the migration rate. We therefore only plot the torque acting on the embedded planets. The planetary mass is for all embedded planets $20 M_{Earth}$.

4.1. Constant adiabatic index

In Fig. 9 the total torque Γ_{tot} acting on planets on circular orbits embedded in discs with different adiabatic indices ($\nu = 10^{15}$ cm^2/s) are displayed. For adiabatic indices higher than 1.15 the torque acting on the planet is positive, while for $\gamma < 1.15$ it is negative, indicating inward migration. The maximum of the torque seems to be at $\gamma = 1.3$ and is decreasing for smaller and higher γ's. For lower γ's, the torque decreases very rapidly, even indicating inward migration, when γ comes closer to ≈ 1.0. The minimum in the curve of the torque acting on the planet seems to be at $\gamma = 1.1$, and the torque acting on the planet is increasing to smaller values of γ again. Please keep in mind, that the torque acting on a $20 M_{Earth}$ planet embedded in an isothermal
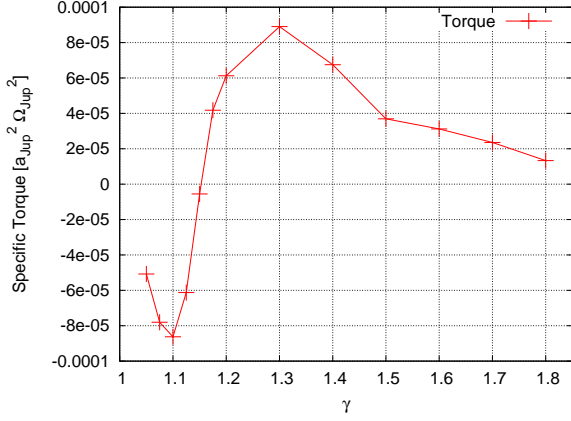
mass. A higher disc mass resulted in a larger convective zone in the disc. However, for our used disc mass of $M_{disc} = 0.01 M_{\odot}$ here, the convective region is minimal for our constant viscosity reference simulation. The density and temperature structures of the disc with constant viscosity seem to correspond to a disc with $\alpha \approx 0.0055$ (see Fig. 4). For lower viscosities we do not see any signs of convection in the velocity pattern (not displayed).

We display in Fig. 7 the velocity in *z*-direction for $\alpha = 0.008$ discs with a constant adiabatic index of $\gamma = 1.4$ and for the two gas mixtures. We note that convection is different when taking both sides of the disc into account, because the eddies cross the midplane. However, in Bitsch & Kley (2011b) we have shown that the first signs of convection can also be seen in simulations where only one half of the disc is simulated.

For all displayed gas configurations we see fluctuations (changes between positive and negative velocity) in the velocity pattern for $r < 1.2 r_{Jup}$, with the weakest and smallest pattern in the ortho-para gas configuration. For lower viscosities the convective region still exists, but it is not so pronounced in the velocity pattern. A higher viscosity might therefore leads to a larger convective region in the disc.

To investigate in more detail if really convection is present in the disc, we compute a mass-weighted adiabatic gradient as follows

$$\frac{1}{\beta} = \int_0^H \rho \frac{d \ln p}{dz} \frac{dz}{d \ln T} dz \Big/ \int_0^H \rho dz , \qquad (3)$$

Fig. 9. Total torque Γ_{tot} acting on planets ($20M_{Earth}$) embedded in discs ($\nu = 10^{15}$ cm^2/s) with different adiabatic indices. A $20M_{Earth}$ planet embedded in an isothermal disc, with matching H/r for the $\gamma = 1.4$ disc feels a negative torque of $\Gamma_{tot} = -2.1 \cdot 10^{-5}$.
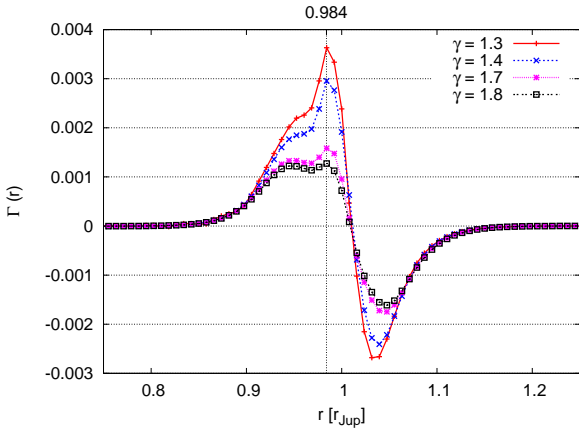

Fig. 10. Radial torque density $\Gamma(r)$ acting on $20M_{Earth}$ planets embedded in discs with different adiabatic indices (in the equilibrium state).

disc with the H/r corresponding to the disc with $\gamma = 1.4$ is about $\Gamma_{tot} = -2.1 \cdot 10^{-5}$, confirming the trend for $\gamma \leq 1.1$.

It seems that the change of the adiabatic index influences the overall results of planetary migration only by magnitude, not by direction. For higher adiabatic indices the torque acting on the embedded planet is decreased by a factor of 3 to 4 compared to the maximum torque at $\gamma = 1.3$. The tendency of outward migration, however, remains intact for $\gamma \geq 1.15$. For lower adiabatic indices, the direction of migration is reversed as γ approaches the value for isothermal discs. On the other hand, the torque has strong fluctuations in time, indicating that the planet has reached the convective zone of the disc.

In Fig. 10 the torque density ($\Gamma(r)$)

$$\Gamma_{tot} = \int_{r_{min}}^{r_{max}} \Gamma(r)\, dr \,, \tag{5}$$

for $20M_{Earth}$ planets embedded in fully radiative discs with a constant adiabatic index is displayed. All displayed torque densities $\Gamma(r)$ feature the spike in the torque density around $\approx 1.0 a_{Jup}$ with the underlying Lindblad torque curve. For increasing γ the Lindblad torque and the spike in the torque density is reduced. This reduction in the torque density is also represented by a reduction in the total torque, which is reduced for increasing adiabatic indices as well (see Fig. 9).

In Fig. 11 the surface density for a $20M_{Earth}$ planet embedded in fully radiative discs with $\gamma = 1.1$ (top), $\gamma = 1.4$ (middle) and $\gamma = 1.7$ (bottom) is displayed. Please keep in mind, that the $\gamma = 1.4$ case represents the case discussed in great detail in Kley et al. (2009). For the $\gamma = 1.1$ case, strong variations in the density surrounding the planet are visible. The variations are due to convection inside the disc. It seems, that a smaller adiabatic index, favours convection inside the disc. The convective zone reaches out much farther than for discs with a higher adiabatic index (e.g. for $\gamma = 1.4$, middle in Fig. 11). The torque acting on a planet in the convective zone is in constant fluctuations and therefore it is very difficult to determine the total torque (it has to be averaged).

When the planet is further out in the disc (outside of the convective zone), the temperature and density in the disc are very low (which prevents outward migration, see Bitsch & Kley (2011b)), so that outward migration seems unlikely.

The surface density pattern of the $\gamma = 1.7$ disc, on the other hand, shows no sign of convection. In fact it is very similar to the $\gamma = 1.4$ (middle in Fig. 11), the only difference being that the density increase in front of the planet and the density increase behind of the planet is not as well pronounced. It also seems that the spiral waves exerted by the planet are not as dense as for the $\gamma = 1.4$ case. Consequently this leads to a smaller positive torque acting on the planet compared to the $\gamma = 1.4$ disc, as can be seen clearly in Fig. 9.

4.2. Influence of viscosity

In Section 3, we discussed the changes of the structure of planetary discs with different viscosities. Changes in the temperature gradient lead to changes in the torque acting on embedded planets (Paardekooper et al. 2011). In Fig. 12 the torque acting on embedded $20M_{Earth}$ planets in discs with different viscosity is displayed. As expected, planets in discs with $\alpha \leq 0.002$ feel a negative torque, indicating inward migration. A decrease of the torque with decreasing viscosity can also be found in isothermal discs (see for example our simulations in Fig. 1 in Bitsch & Kley (2010)). The decrease in the total torque has is origin in the lower viscosity. If the viscosity is very low, the corotation torques saturate and outward migration can not be supported any more.

For increasing viscosities ($\alpha \geq 0.003$) the torque acting on the planet becomes positive. For even larger viscosities ($\alpha \geq 0.004$) the torque seems to settle. However, the torque acting on the planet with a constant viscosity of $\nu = 10^{15}$ cm^2/s is still about 50% larger, which is a little bit surprising as the unperturbed density and temperature profiles seemed to match quite well for $\alpha \approx 0.0055$.

In Fig. 13 we display the radial torque density $\Gamma(r)$ acting on a $20M_{Earth}$ planet in discs with different viscosity. In the $\alpha = 0.001$ case, the displayed torque density shows a typical Lindblad torque curve, without a trace of the typical pattern of a fully radiative disc with a higher viscosity (Kley et al. 2009). In fact the torque density is very similar to an isothermal disc.

The $\alpha = 0.005$ and $\alpha = 0.006$ torque density patters are very similar to the one of a constant viscosity of $\nu = 10^{15}$ cm^2/s. The 'spike' in the distribution at $r = 0.984$ is nearly identical for all three simulations. However, there are some differences. For smaller and larger distances to the central star ($r < 1.0 r_{Jup}$ and $r > 1.0 r_{Jup}$) the torque density is larger for the constant viscosity case, although all simulations follow the same trend. These differences might be due to small fluctuations in the density patterns in the vicinity of the embedded planet. Also the underlying
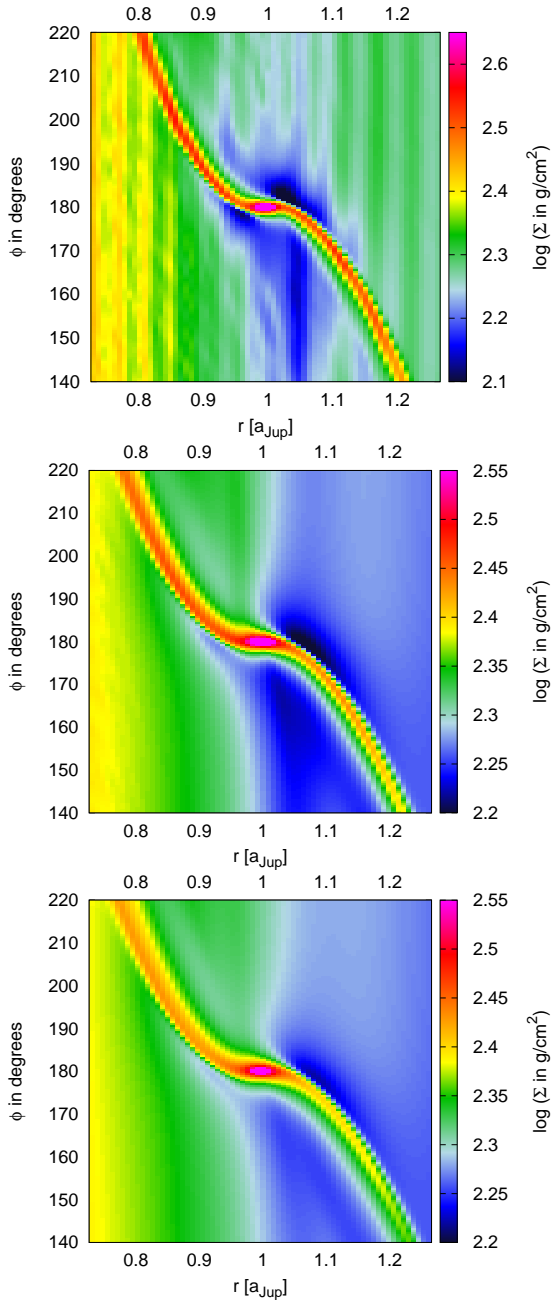
Fig. 11. Displayed are the surface density maps for planets on fixed circular orbits in fully radiative discs with different adiabatic indices (top: $\gamma = 1.1$, middle: $\gamma = 1.4$, bottom: $\gamma = 1.7$) and a constant viscosity of $\nu = 10^{15}$ cm^2/s. The disruption in the surface density pattern for the $\gamma = 1.1$ disc is due to convection inside the disc.

Fig. 12. Torque acting on $20M_{Earth}$ planets embedded in discs with different viscosity ($\gamma = 1.4$).

Fig. 13. Radial torque density $\Gamma(r)$ acting on $20M_{Earth}$ planets embedded in discs with different viscosity (in the equilibrium state) and a constant adiabatic index $\gamma = 1.4$.

Lindblad torque distribution is smaller for the $\alpha = 0.006$ disc compared to the $\alpha = 0.005$ disc. These small differences might be the reason why the total torque of the constant viscosity simulations is larger compared to the α viscosity discs.

In the $\alpha = 0.008$ disc, the Lindblad torque is much smaller compared to the other discs. However, the torque density shows the usual 'spike', indicating outward migration (Kley et al. 2009). One might suspect from the trend of the simulations that even higher viscosities might destroy this effect of outward migration and might also trigger convection.

In Fig. 14 we display the surface densities of $20M_{Earth}$ planets in disc with different viscosities in order to bring more insight to the torques acting on the embedded planets. For very low vis-
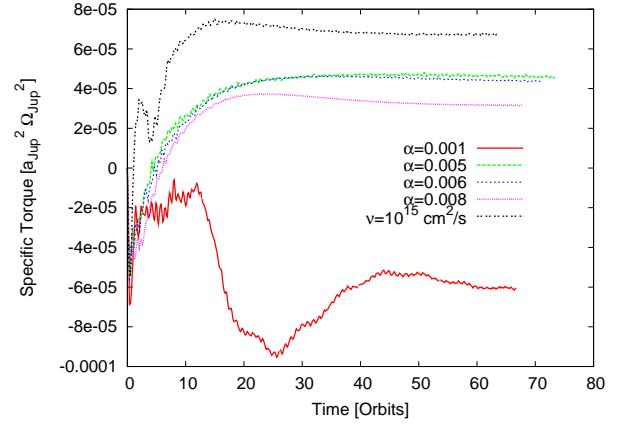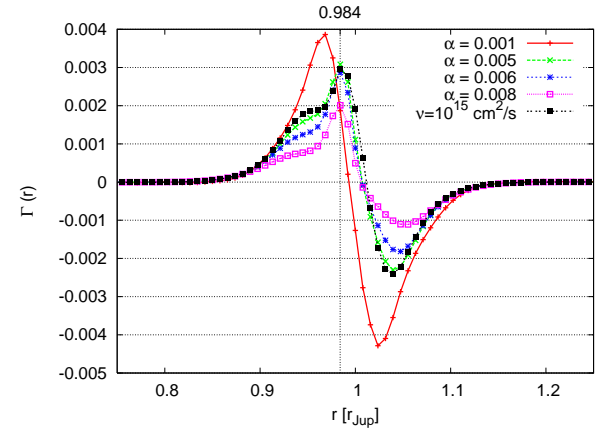
cosities ($\alpha = 0.001$), the planet seems to open a very small or partial gap inside the disc. Additionally the spiral waves of the planet are more dense compared to the constant viscosity simulation (middle picture in Fig. 11), which may be due to the higher density in the midplane of the disc. It seems that a low viscosity encourages the formation of gaps in the disc, thus explaining the torque density in Fig. 13.

The $\alpha = 0.005$ surface density profile seems very similar to the constant viscosity profile we discussed in great detail in Kley et al. (2009). The density increase ahead of the planet ($\phi > 180°$ and $r < 1.0$) is clearly visible in both cases, thus creating a nearly identical 'spike' in the torque density distribution (Fig. 13). However, the density decrease behind the planet ($\phi < 180°$ and $r > 1.0$) is not so clear in the $\alpha = 0.005$ simulation compared to the $\nu = 10^{15}$ cm^2/s simulation (middle picture in Fig. 11). This directly reflects on the torque density, as the torque density is higher for the constant viscosity simulation compared to the $\alpha = 0.005$ simulation at that distance to the central star, thus explaining the higher total torque.

For $\alpha = 0.008$ the surface density profile shows the same structure as for the constant viscosity simulation, but the surface density is generally reduced. The spiral waves and the vicinity near the planet show smaller surface densities. Also the structure ahead and behind the planet is not as distinctive as in the constant viscosity (or $\alpha = 0.005$) simulation. This all leads to a smaller
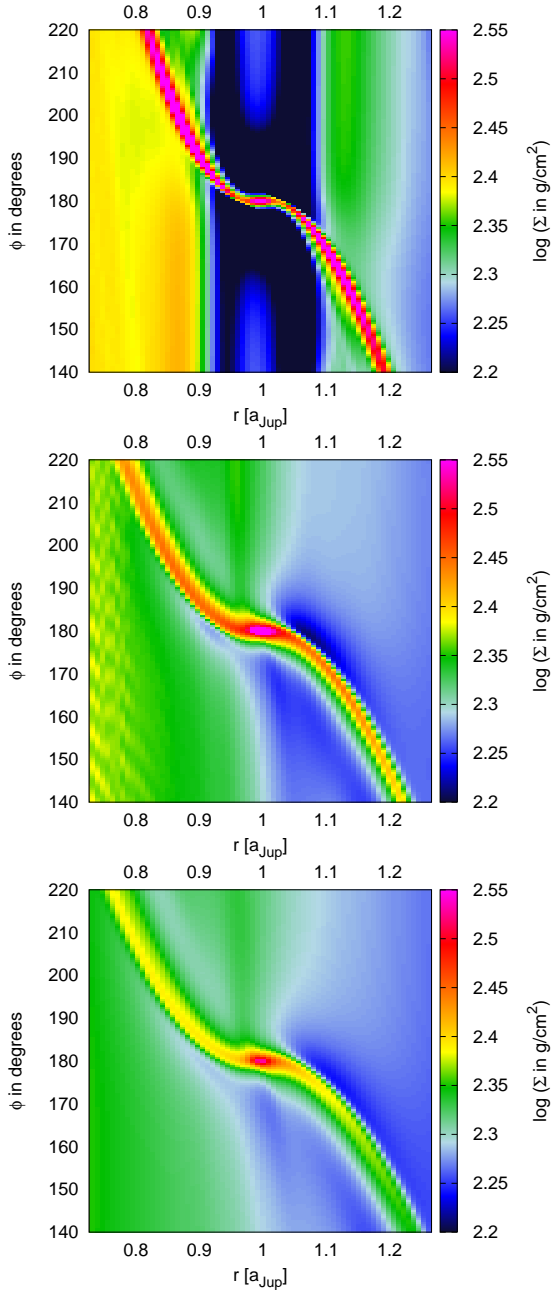
Fig. 14. Displayed are the surface density maps for $20 M_{Earth}$ planets on fixed circular orbits in fully radiative discs (with $\gamma = 1.4$). The viscosities in the discs are (from top to bottom): $\alpha = 0.001$, $\alpha = 0.005$ and $\alpha = 0.008$. The snapshots are taken in the equilibrium state of the disc.

curve in the torque density plot (Fig. 13) and to a smaller total torque (Fig. 12).

4.3. Varying adiabatic index

In Fig. 15 the torque acting on $20 M_{Earth}$ planets in discs with different viscosity and with the two different gas configurations is displayed. For low viscosities ($\alpha = 0.001$) the torque is negative (not displayed), indicating inward migration and for higher viscosities it is positive indicating outward migration, as expected from simulations with a constant adiabatic index.

For all shown viscosities, the torque acting on the planet is positive, indicating outward migration. In the equilibrium gas configuration disc the torque is higher than the torque for a
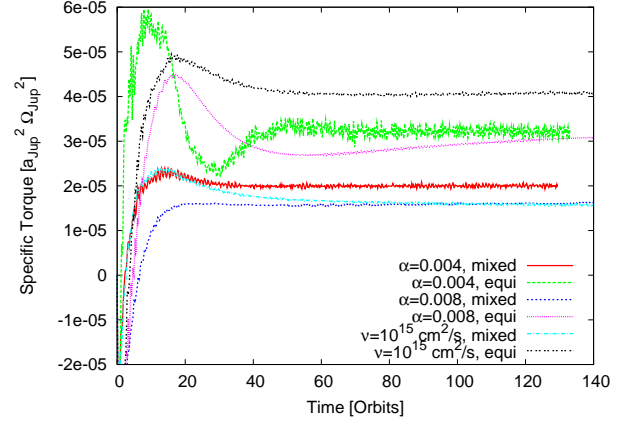

Fig. 15. Torque acting on $20 M_{Earth}$ planets embedded in discs with different viscosity. The picture features $\alpha = 0.004$, $\alpha = 0.008$ and constant viscosity for both gas configuration.

Fig. 16. Torque density of $20 M_{Earth}$ planets embedded in discs with different viscosity. The picture features $\alpha = 0.004$, $\alpha = 0.008$ and a constant viscosity for both gas configurations.
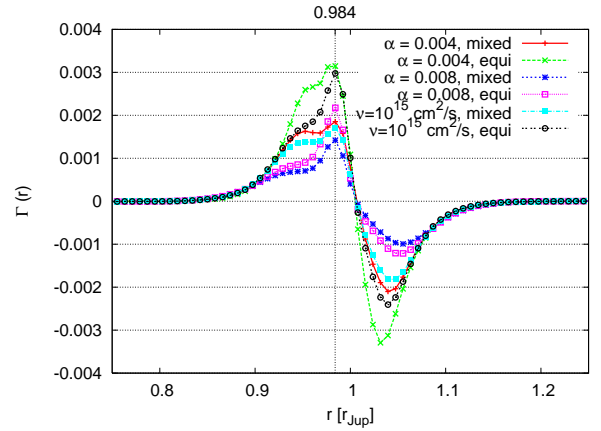
planet in the ortho-para mixed gas configuration (with the same viscosity). The largest differences between the two gas configurations is observed for the disc with constant viscosity. It also seems that the torque in the $\alpha = 0.004$ disc is showing some fluctuations in time, which might be due to convection in the disc.

The temperature near the planet is in the region of $80K \leq T_{Planet} \leq 130K$, which is where the separation of the adiabatic index between the equilibrium and ortho-para mixed gas starts to occur (see Fig. 1). This difference in temperature leads to a change in the total torque acting on the planet (see Fig. 9), which can be up to a factor of two in this temperature region. Therefore the total torque in the equilibrium gas configuration is higher than in the ortho-para gas configuration.

In Fig. 16 the torque density $\Gamma(r)$ is displayed. As all total torques are positive (Fig. 15), each simulation shows a spike on top of the Lindblad torque in the $\Gamma(r)$ distribution near $r \approx 0.99$. The spike on top of the Lindblad torque distribution is largest for the equilibrium gas configuration in the constant viscosity simulation, which is also the simulation featuring the highest total torque. Also the spikes in the $\Gamma(r)$ distributions are smaller for the ortho-para gas mixture compared to the equilibrium gas configuration, which was also reflected by the total torque (Fig. 15). However, the Lindblad torque seems strongest for the $\alpha = 0.004$ disc with the equilibrium gas configuration.

In Fig. 17 the surface density for the $\alpha = 0.004$ and $\alpha = 0.008$ simulations with the two gas configurations are displayed. The simulations with constant viscosity are not displayed, as the difference between the equilibrium and ortho-para gas distributions is minimal. The surface density is a little bit higher in front of the planet ($\phi > 180$ and $r < 1.0$) and a little low behind the planet ($\phi < 180$ and $r > 1.0$) in the equilibrium gas configuration compared to the ortho-para mix gas configuration, which results in the observed higher torque of the equilibrium gas disc.

For the lower viscosity ($\alpha = 0.004$), the density in the spiral waves exerted by the planet is higher compared to the high viscosity case ($\alpha = 0.008$), which could also be observed for discs with a constant γ (Fig. 14). Also, the surface density near the planet is higher for the lower viscosity discs. These two features are the origin in the higher torque of the $\alpha = 0.004$ compared to the $\alpha = 0.008$ discs (compared with the same gas configuration).

In the $\alpha = 0.004$ discs, the spiral waves in the equilibrium gas disc are much denser compared to the ortho-para mix gas disc. Also the density increase in front of the planet ($\phi > 180$ and $r < 1.0$) and the decrease behind the planet ($\phi < 180$ and $r > 1.0$) is more pronounced, which results in the larger Lindblad torque and a somewhat larger spike in the $\Gamma(r)$ distribution (Fig. 16). In the equilibrium gas configuration, the disc shows some fluctuations in the surface density for $r < 0.85$. These fluctuations might also be due to convection, also we did not see any big signs of that in simulations without a planet. However, the convective region seems sufficiently far enough away from the planet, so that the torque is not influenced much by this behaviour of the disc.

The surface density profiles of the $\alpha = 0.008$ discs show the expected trend from the total torque and $\Gamma(r)$ distributions. In the equilibrium gas configuration the density ahead of the planet ($\phi > 180$ and $r < 1.0$) is a little bit higher than in the ortho-para gas disc, which results in the higher spike in the $\Gamma(r)$ distribution.

All in total it seems that the differences between the two gas mixtures is larger in a constant viscosity disc compared to a disc with α-viscosity. The reason for that might be in the complicated relation that arises when an α viscosity is used. The viscosity is then dependent on the temperature, which in turn influences the adiabatic index, which changes the disc structure and therefore the temperature and with it the viscosity again.

5. Zero-torque radius

As density and temperature decrease with increasing distance to the central star, the torque acting on an embedded planet also decreases. At some point in the disc, the torque becomes zero (zero-torque radius) and the planet does not move any more due to planet-disc interactions. This point in the disc is dependent on the disc mass (Bitsch & Kley 2011b). In our simulations in Section 4, we stated that the strength of outward migration is dependent on viscosity and the gas configuration. It is only logical to assume an influence on the zero-torque radius as well.

In Fig. 18 the torque acting on $20 M_{Earth}$ planets in fully radiative discs with different viscosities is displayed. The Figure also features the two different gas configurations (ortho-para mix and equilibrium) and simulations with a constant adiabatic index $\gamma = 1.4$. The simulations with $\gamma = 1.4$ and a constant viscosity are taken from Bitsch & Kley (2011b).

As the details of the torque acting on planets in discs with different viscosity has been discussed for the different gas distributions in great detail in Section 4, we just want to discuss the influence of these configurations on the zero-torque radius.
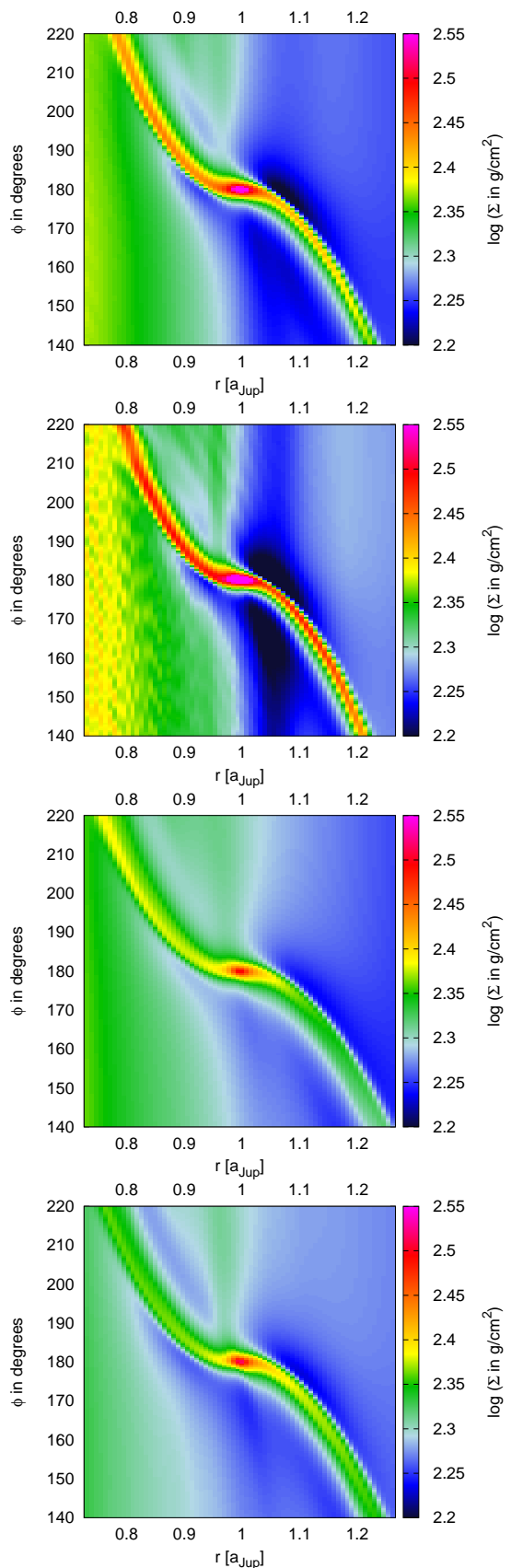

Fig. 17. Displayed are the surface density maps for $20 M_{Earth}$ planets on fixed circular orbits in fully radiative discs. The viscosities and gas configurations in the discs are (from top to bottom): $\alpha = 0.004$ with ortho-para mix, $\alpha = 0.004$ with equilibrium gas, $\alpha = 0.008$ with ortho-para mix and $\alpha = 0.008$ with equilibrium gas. The snapshots are taken in the equilibrium state of the disc.
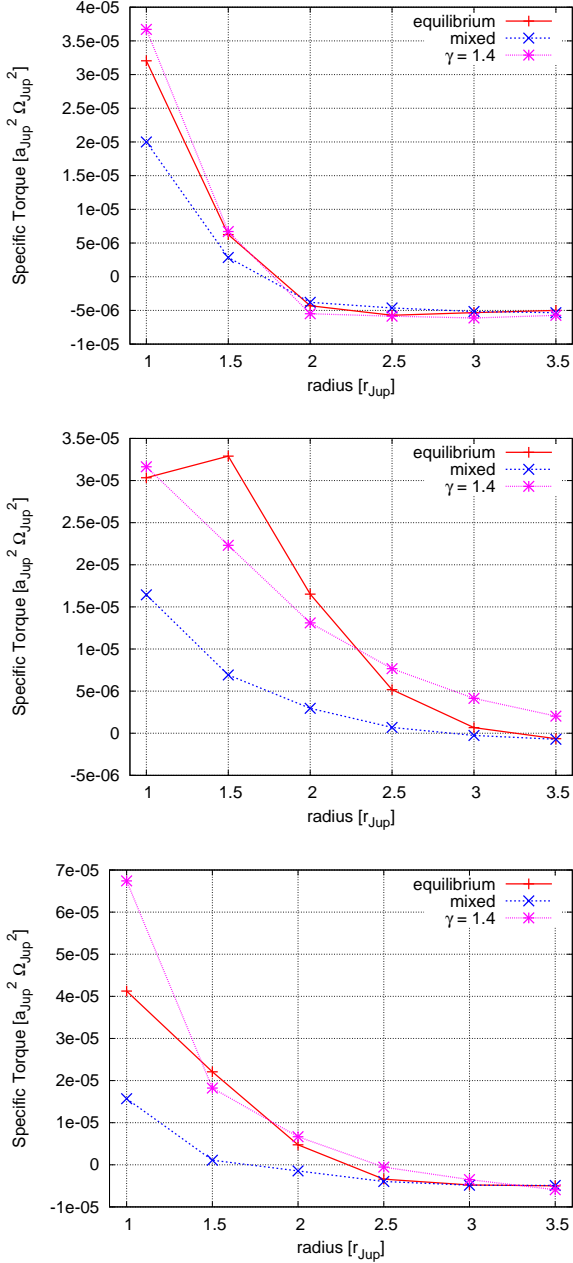
Fig. 18. Torque acting on $20M_{Earth}$ planets in discs with different viscosities. Each plot features the two gas configurations (ortho-para mix and equilibrium) and a constant $\gamma = 1.4$. From top to bottom the viscosity is: $\alpha = 0.004$, $\alpha = 0.008$ and $\nu = 10^{15}$ cm²/s. The simulations with $\gamma = 1.4$ and a constant viscosity are taken from Bitsch & Kley (2011b).

In Table 2 the zero-torque radius for the mentioned simulations is presented. In the $\alpha = 0.004$ the zero torque radius is closer to the star compared to the simulations with $\alpha = 0.008$ and $\nu = 10^{15}$ cm²/s. As viscosity is needed to keep the torques acting on the planet unsaturated, it is not surprising that the zero-torque radius is further out for discs with higher viscosity.

With an increasing adiabatic index γ the torque acting on an embedded $20M_{Earth}$ planet is decreasing (see Fig. 10). For lower temperatures the adiabatic index is constantly increasing in the ortho-para gas mixture (until $T < 50K$, when $\gamma = 1.67$), while it is first decreasing in the equilibrium configuration (to $\gamma = 1.3$) and then increasing until it reaches $\gamma = 1.67$ at $T \approx 20K$. As the

temperature decreases further out in the disc, one might suspect a larger zero-torque radius for the equilibrium gas configuration compared to the ortho-para configuration (as density is about the same for these configurations for large distances to the central star).

For all displayed viscosities the zero-torque radius is farther out in the disc in the equilibrium gas configuration compared to the ortho-para mixed gas. However, the constant γ simulations feature a zero-torque radius that is in most cases even farther out than in the equilibrium gas configuration.

6. Summary and Conclusions

The viscosity determines the structure of the disc. For increasing α-viscosity we find a decrease of density and an increase of temperature in midplane of the disc. The aspect ratio of the disc is also increasing for increasing viscosity. The slope of the temperature β is decreasing for increasing viscosity. It seemed that the simulation with a constant viscosity of $\nu = 10^{15}$ cm²/s is in between the $\alpha = 0.005$ and $\alpha = 0.006$ simulations.

The aspect ratio of the disc increases for increasing viscosity and increasing γ. The aspect ratio profile for very low viscosities is about constant with little fluctuations. However, for increasing viscosity the aspect ratio is no longer constant, but after a small increase for small distances to the central star, the aspect ratio decreases with increasing distance to the central star. A decreasing H/r profile with increasing distance to the star is not what one would expect, and is the result of the temperature dependence of the opacity.

A change in aspect ratio of the disc influences the migration of embedded planets. For the aspect ratio this has been shown for isothermal discs, where embedded planets migrate inwards faster for smaller aspect ratios of the disc (Tanaka et al. 2002). The slope of the temperature β also influences the torque acting on an embedded planet. In many theoretical formulae (Masset & Casoli 2010; Paardekooper et al. 2011) the parameter β is not only used to calculate the Lindblad torque, but also to calculate the entropy-related part of the horseshoe drag and the entropy-related part of the linear corotation torque. A change in these parameters therefore changes the torque acting on a planet embedded in these discs.

For very small viscosities ($\alpha < 0.0025$) we find a negative torque acting on a $20M_{Earth}$ planet in a fully radiative disc, indicating inward migration. Interestingly in the low viscosity case, a low mass planet seems to open up a partial gap in the disc. A lower viscosity also reduces the torque acting on planets embedded in isothermal discs (Bitsch & Kley 2010).

For increasing viscosities ($\alpha > 0.003$), the torque becomes positive and seems to stall for even higher viscosities ($\alpha \approx 0.005$). Even as the density, temperature and aspect ratio profiles of the $\alpha = 0.005$ simulation match quite well with the constant viscosity simulation of an unperturbed disc, a difference of about 50% in the total torque acting on an embedded $20M_{Earth}$ planet arises. As the α-viscosity is dependent of the temperature in the disc ($c_s \propto \sqrt{T}$) and the temperature undergoes substan-

	equilibrium	ortho-para	const. $\gamma = 1.4$
$\alpha = 0.004$	1.8	1.7	1.75
$\alpha = 0.008$	3.3	3.0	>3.5
const. ν	2.35	1.7	2.5

Table 2. Zero-torque radius (in a_{Jup}) for planets in fully radiative discs with different viscosity and different gas configurations.

tial changes near the planet, the torque is influenced as well as the major contributions of the torque arise from near the planet. This difference results in a smaller torque acting on the embedded planet.

Paardekooper & Papaloizou (2008) stated that viscosity can prevent the torques from saturation in isothermal discs. In fully radiative discs, the effects of viscous heating and radiative transport/cooling in the disc prevent the torques from being saturated (Kley et al. 2009), but as we showed here, only if the viscosity in the disc is high enough to do so.

As the accretion rate onto the star might be higher for more massive discs, the viscosity in those discs might also be higher, resulting in a more likely scenario for outward migration of embedded planets. The viscosity of the disc determines the torque acting on the planet, which therefore also changes the zero-torque distance to the central star. At the zero-torque distance to the central star, planetary embryos can pile up and form larger planetary cores (Sándor et al. 2011). When this distance changes dramatically due to a too small viscosity in the disc, the creation of larger bodies may be too close to the central star, so that these new formed cores might be lost in the central star anyway.

The torque acting on planets embedded in discs with the equilibrium gas configuration is higher than the torque in the ortho-para mixed disc for the same viscosity (constant and α). A larger viscosity in a disc, results in a higher temperature in the midplane of the disc. As the adiabatic index is dependent of the temperature in the disc, the viscosity directly influences the adiabatic index. A transition from $\gamma = 1.4$ to $\gamma = 1.67$ reduces the torque by a factor of ≈ 3 for discs with a constant adiabatic index.

In an $\alpha = 0.004$ disc the temperature in midplane is lower than in the $\alpha = 0.008$ disc. In the equilibrium gas configuration the adiabatic index first becomes smaller and increases towards $\gamma = 1.67$ when the temperature in the disc decreases. If the disc is then sufficiently cool enough, the total torque acting on an embedded planet in an equilibrium gas disc is higher than in an ortho-para gas disc as simulations with a constant γ have shown.

The consideration of a temperature dependent adiabatic index is crucial for discs with a sufficiently high α viscosity, as the adiabatic index influences the disc structure, which then influences the torque acting on an embedded planet.

As the equilibrium gas configuration features a smaller adiabatic index for low temperatures, which in return results in a higher torque acting on planets in discs with constant viscosity, the zero-torque radius for embedded planets is larger in the equilibrium gas configuration compared to the ortho-para mix configuration. It seems that due to the consideration of the temperature dependent adiabatic index, the zero-torque region in the disc can be much larger than for a constant adiabatic index. In general, a wider area of stopped inward and outward migration can function as a planetary trap, where larger planetary embryos can be created.

References

Ayliffe, B. A. & Bate, M. R. 2011, ArXiv e-prints
Ayliffe, B. A. & Bate, R. 2010, MNRAS, 408, 876
Baruteau, C. & Masset, F. 2008, ApJ, 672, 1054

Bitsch, B. & Kley, W. 2010, A&A, 523, A30
Bitsch, B. & Kley, W. 2011, A&A, 530, A41
Bitsch, B. & Kley, W. 2011b, A&A, in prep.
Boley, A. C., Hartquist, T. W., Durisen, R. H., & Michael, S. 2007, ApJ, 656, L89
Crida, A., Baruteau, C., Kley, W., & Masset, F. 2009, A&A, 502, 679
Crida, A., Sándor, Z., & Kley, W. 2008, A&A, 483, 325
Decampli, W. M., Cameron, A. G. W., Bodenheimer, P., & Black, D. C. 1978, ApJ, 223, 854
Gullbring, E., Hartmann, L., Briceno, C., & Calvet, N. 1998, ApJ, 492, 323
Hartigan, P., Edwards, S., & Ghandour, L. 1995, ApJ, 452, 736
Klahr, H. & Kley, W. 2006, A&A, 445, 747
Kley, W., Bitsch, B., & Klahr, H. 2009, A&A, 506, 971
Kley, W. & Crida, A. 2008, A&A, 487, L9
Levermore, C. D. & Pomraning, G. C. 1981, ApJ, 248, 321
Masset, F. 2000, A&AS, 141, 165
Masset, F. & Casoli, J. 2010, ApJ, 723
Morbidelli, A., Crida, A., Masset, F., & Nelson, R. 2008, A&A, 478, 929
Paardekooper, S., Baruteau, C., Crida, A., & Kley, W. 2010, MNRAS, 401, 1950+
Paardekooper, S. J., Baruteau, C., & Kley, W. 2011, MNRAS, 293
Paardekooper, S.-J. & Mellema, G. 2006, A&A, 459, L17
Paardekooper, S.-J. & Mellema, G. 2008, A&A, 478, 245
Paardekooper, S.-J. & Papaloizou, J. C. B. 2008, A&A, 485, 877
Sándor, Z., Lyra, W., & Dullemond, C. P. 2011, ApJ, L9
Shakura, N. I. & Sunyaev, R. A. 1973, A&A, 24, 337
Tanaka, H., Takeuchi, T., & Ward, W. R. 2002, ApJ, 565, 1257
Ziegler, U. & Yorke, H. 1997, Computer Physics Communications, 101, 54

5 Summary and conclusions

In the papers, I studied the influence of radiation transport in fully radiative discs on embedded planets. The motion of the planets in isothermal discs is inwards, at a rate proportional to the planets mass (Tanaka *et al.*, 2002). In 2D and 3D simulations of fully radiative discs, planets can migrate outwards, if they do not exceed a certain threshold in mass (Kley and Crida, 2008; Kley *et al.*, 2009). The outward migration of planet embryos with several earth masses certainly represents a solution to the too rapid inward migration found in the mass regime of classical (isothermal) type-I migration. Growing planets can spend more time in the outer disc regions and move then later via type-II migration towards the star.

In Kley *et al.* (2009), we investigated the origin of the torque acting on the embedded planet in great detail. In Baruteau and Masset (2008) it was stated that the maximum of the torque density $\Gamma(r)$ lies at corotation. However, in our simulations we find that the maximum of the torque density is slightly shifted from the planets location (Kley *et al.*, 2009). This result is confirmed by numerical simulations for increasing resolution and for changes in the planetary mass.

The maximum of the torque density in a fully radiative disc, is represented as a little 'spike' in Fig. 2.9. Without the 'spike' the torque density would follow the adiabatic torque density, which saturates, so that the planet can not sustain outward migration any more. As the maximum of the torque density is slightly shifted from the planets location, it might have a dramatic effect, if the planet would move from its location beyond the torque maximum. This could happen, for example, if the planet was on an eccentric orbit around the star.

The evolution of planets on eccentric orbits in fully radiative discs is investigated in Bitsch and Kley (2010). Outward migration of low-mass planets in fully radiative discs is possible for planets on circular orbits. However, if the planet moves on a small eccentric ($e \leq 0.02$) orbit, it can still migrate outwards. For larger eccentricities, the direction of migration is inwards. The maximum value of eccentricity by which a planet can still undergo outward migration seems to be determined by the 'spike' in the torque density configuration $\Gamma(r)$. This torque maximum has a slight offset to the planets location (Kley *et al.*, 2009), which then results in a limiting eccentricity for outward migration of about $0.015 - 0.025$. If the eccentricity of the planet is larger than this value, it will migrate inwards, while it will migrate outwards for smaller eccentricities. It seems that a too large eccentricity overcompensates the effects of a fully radiative disc, so that the planet would migrate inwards.

In isothermal discs, the eccentricity of an embedded planet is damped in time (Cresswell

et al., 2007). This result was confirmed by isothermal reference simulations in Bitsch and Kley (2010). In this work, we also monitored the evolution of eccentricity in fully radiative discs. As expected, eccentricity is damped in these discs as well. However, the damping rate for low-mass planets is slightly slower in fully radiative discs compared to isothermal discs with the same aspect ratio H/r. Small eccentricities (with $e \lesssim 2H/r$) are damped exponentially with a time scale given approximately by the linear results (Ward and Hahn, 1994). Larger eccentricities are damped initially according to $\dot{e} \propto e^{-2}$ in agreement with Papaloizou and Larwood (2000) and Cresswell *et al.* (2007).

For increasing masses of the planet, the damping of eccentricity becomes faster in both thermodynamic cases. But if the planet is so massive that it can open a gap in the disc, eccentricity is damped at a slower rate, as an open gap reduces the damping rate.

In Cresswell *et al.* (2007) also the evolution of planets on inclined orbits in isothermal discs is discussed. In these discs, inclination is damped for all planetary masses. The results for isothermal discs could be verified in Bitsch and Kley (2011). In the main body of the disc ($i < H/r$, i in radiants), inclination is damped at an exponential rate, $di/dt \propto -i$. For higher inclined planets, the loss of inclination is determined through $di/dt \propto i^{-2}$.

In fully radiative discs, the evolution of inclination also follows the trend of an isothermal disc, but the damping rates are a little bit higher (Bitsch and Kley, 2011). For low-mass planets on circular inclined orbits, outward migration is still possible, but only if the inclination is smaller than the threshold of $i \leq 4.5°$. For higher inclinations, the planet migrates inwards. It seems that inclination does not have such a huge effect on migration as eccentricity. In the evolution of planets on eccentric and inclined orbits, both quantities are damped in time by the disc, but outward migration only occurs, when both quantities are damped below their thresholds.

Inclination is also damped at a faster rate for more massive planets (Bitsch and Kley, 2011). However, if the planet is massive enough to open a gap in the disc, the damping rate is reduced, as a gap in the disc reduces the damping effects of the disc.

As eccentricity and inclination are damped at a fast rate compared to the lifetime of the disc (Bitsch and Kley, 2010; Bitsch and Kley, 2011), one could just monitor the torque acting on a planet on a fixed circular orbit to determine its possible direction of migration. Also the migration rates determined from calculations of planets on fixed orbits, match the observed migration rates when the planet is allowed to move freely in the disc (Bitsch and Kley, 2011).

In Bitsch and Kley (2011) the range of outward migration is discussed. As planets migrate outwards in fully radiative discs, it is important to determine the so called zero-torque radius in the disc. At this location, the planet does not feel a net torque from the disc and it does not move. For more massive planets, the zero-torque radius is located nearer to the central star. The zero-torque radius is of special interest for planet formation, as planetary embryos will accumulate in this area of the disc where they can merge into bigger cores (Lyra *et al.*, 2010).

Planets migrating outwards in fully radiative discs generate a very sensitive density pattern

near their location. The density is increased ahead of the planet ($r < 1.0$ and $\phi > 180°$) and decreased behind the planet ($r > 1.0$ and $\phi < 180°$), see Fig. 2.10. As the planet moves farther out in the disc, the density decreases and the disc is not able to sustain outward migration.

In Bitsch and Kley (2011) the torques of planets in 3D fully radiative discs are compared with theoretical formulae of Paardekooper *et al.* (2010, 2011); Masset and Casoli (2010). The formula of Paardekooper *et al.* (2010) is only valid directly after the insertion of the planet in the disc, as it does not account for saturation. In reality, however, the torques do saturate. This formula also has the disadvantage that it does not become negative for increasing distances to the central star. The same problem arises for the formula of Masset and Casoli (2010), but the trend of the torque is fitted a little bit better.

The best quantitative fit for the 3D simulations in Bitsch and Kley (2011) is achieved with the formula of Paardekooper *et al.* (2011). Not only is the zero-torque radius predicted correctly, but also the general development of the torque is captured. This is of particular interest to planet population synthesis models, where the planet moves under theoretical predicted torques. A more accurate formula, checked with simulations, will provide for better results in these models.

The influence of the disc mass is also discussed in Bitsch and Kley (2011). As the structure of the disc is determined by viscous heating and radiative transport/cooling, a change in the disc mass results in change of the disc structure. This is of special interest, when the mass of the disc is increasing. As an increasing disc mass leads to higher temperatures in the midplane, an influence on embedded planets is expected. However, with increasing disc mass, the convective region in the discs grows, which results in an randomisation of the torque of an embedded planet. The torque acting on a planet embedded in the convective region of the disc is not clearly determinable.

For higher disc masses, the density farther out in the disc is also higher. A higher density farther out in the disc, results in a still positive migration rate for low-mass planets, even if they are farther out from the zero-torque radius as it would be possible in discs with less mass. This results is of interest for population synthesis models, as the disc feeds the planet and higher mass discs are needed to create higher mass planets.

As convection is a 3D effect, these results will not be visible in 2D simulations. 2D Simulations of high-massive discs should therefore be handled with care. However, the effects of convection should be investigated with higher resolution and including MRI effects for studies with farther turbulence.

As viscosity is needed to keep the torques unsaturated, we investigated the influence of it on planets embedded in fully radiative discs (Bitsch *et al.*, 2011). As expected from isothermal simulations, where a too low viscosity resulted in torque saturation, we find the same effect for fully radiative discs. Very small viscosities disrupt the sensitive density pattern needed for outward migration and even the onset of gap formation can be found for low-mass planets. However, if the viscosity is high enough, outward migration is achieved, as expected.

There are different assumptions for the gas mixture in the disc. In accretion discs around young stars, mainly hydrogen is present. One can assume an equilibrium gas configuration where ortho and para hydrogen are equally distributed or a 3 : 1 mixed gas configuration with a 3 : 1 ortho-para configuration. The gas configuration has a direct influence on the adiabatic index. The adiabatic index is now dependent on the temperature in the disc. A change in the adiabatic index changes the pressure of the disc, which directly influences the disc structure (Bitsch *et al.*, 2011). A change in the disc structure changes the zero-torque radius of embedded low-mass planets. The inclusion of a temperature dependent adiabatic index, results in a more accurate model of accretion discs.

Outlook

Different parameters of the disc (viscosity, adiabatic index, mass, etc.) can sometimes have a quite dramatic effect on the migration rates of embedded planets. A change in the disc parameters changes the disc structure, which in turn influences the embedded planets. However, in these models so far, not all disc parameters have been considered. Another interesting point to consider is stellar irradiation. Stellar irradiation heats the upper layers of the disc, so that the heating of the disc is not only dependent on the viscosity in the disc any more.

Also, as it is very unlikely that only one planetary core forms in a disc, one should consider models with many planetary embryos that merge and grow in the disc. This process can be investigated with N-body simulations, but the task of coupling hydrodynamical simulations with N-body simulations is very challenging. In the hydrodynamical simulations only a few thousand years are covered by the computation time, but in N-body simulations this time is about a factor of 100-1000 larger.

Planetary embryos embedded in gaseous accretion discs can grow through the accretion of gas from the disc and from gas giant planets. The process of accretion and how the planet growth in the discs is not investigated in detail at all. Material in the Roche lobe can be bound to the planet, but to display the movement of gas inside the Roche lobe, a very high numerical resolution is needed. The usage of Nested Grids in these simulations would certainly provide more insight in this topic, but the combination of Nested Grids and FARGO (Masset, 2000) has never been done before.

As the new Kepler telescope provides scientists with more and more data on exoplanets, more details have to be taken into account when modeling the evolution of planetary systems. Also, the structure of accretion discs can now be observed in much more detail than a decade ago, so that models of accretion discs should be adjusted to the observations. Future observations of planets and discs will continue to give more detailed informations that have to be taken into account. The inclusion of these aspects in simulations will make them more realistic, which will be an interesting and challenging task in the future.

Danksagung

Danken möchte ich Herrn Prof. Willy Kley, der mich zuerst in meiner Diplomarbeit und dann in meiner anschließenden Dissertation betreut hat. Er hat mich während dieser Zeit nicht nur einem interessanten und vielseitigen Thema in der Astrophysik nähergebracht, sondern hat mir auch beratend bei der Auswahl einer weiteren Stelle in der Wissenschaft zur Seite gestanden. Für Fragen und Diskussionen über wissenschaftliche Probleme und Ideen hatte er immer ein offenes Ohr.

Ich danke meinen lieben Kollegen in der Computational Physics, die immer für kleine Diskussionen, Ablenkungen und computertechnische Fragen offen waren, so dass es während den Arbeitszeiten auch nie langweilig geworden ist.

Ich danke Dr. Werner Dilling für seine Unterstützung und meine Einstellung am ZDV der Universität Tübingen, was mir während meiner Dissertation auch einen Einblick in die Arbeitsweisen eines Universitätsrechenzentrums gab, sowie auch meine Erkenntnisse über Linux und die Wartung von großen Rechenclustern förderte.

Ich danke meinem Bruder Benjamin, der mir gezeigt hat, dass es auch noch anderen Themen außerhalb der Astrophysik gibt, denen man Aufmerksamkeit widmen kann und die einen begeistern können und auch sollten.

Ich danke meine Eltern, Dr. Brigitte Bitsch und Dr. Gerhard Bitsch, für ihre Unterstützung und ihre Ratschläge in allen Lebensbereichen in den zurückliegenden Jahren. Ich danke ihnen dafür, dass sie mich immer unterstützt haben in meinem Vorhaben Physik zu studieren, mir zwei Auslandssemester in den USA ermöglicht haben und bei Problemen immer für mich da waren.

Bibliography

Adams, F. C., and G. Laughlin 2003. Migration and dynamical relaxation in crowded systems of giant planets. *Icarus* **163**, 290–306. 35

Alibert, Y., C. Mordasini, and W. Benz 2004. Migration and giant planet formation. *A&A* **417**, L25–L28. 12, 37

Artymowicz, P. 1993. On the Wave Excitation and a Generalized Torque Formula for Lindblad Resonances Excited by External Potential. *ApJ* **419**, 155–+. 15

Baruteau, C., and F. Masset 2008. On the Corotation Torque in a Radiatively Inefficient Disk. *ApJ* **672**, 1054–1067. 27, 28, 30, 31, 33, 125

Bitsch, B., A. C. Boley, and W. Kley 2011. Influence of viscosity and the adiabatic index on planetary migration. *A&A* **in prep.** 37, 38, 39, 127, 128

Bitsch, B., and W. Kley 2010. Orbital evolution of eccentric planets in radiative discs. *A&A* **523**, A30. 35, 37, 39, 125, 126

Bitsch, B., and W. Kley 2011. Evolution of inclined planets in three-dimensional radiative discs. *A&A* **530**, A41. 36, 39, 126

Bitsch, B., and W. Kley 2011. Range of outward migration and influence of the disc's mass on planetary migration. *A&A* **accepted**. 32, 37, 39, 126, 127

Boley, A. C., T. W. Hartquist, R. H. Durisen, and S. Michael 2007. The internal energy for molecular hydrogen in gravitationally unstable protoplanetary disks. *ApJ* **656**, L89. 37

Boss, A. P. 1997. Giant planet formation by gravitational instability19. *Science* **276**, 1836–1839. 6

Boss, A. P. 2000. Possible rapid gas giant planet formation in the solar nebula and other protoplanetary disks. *ApJ* **536**, L101–L104. 6

Cresswell, P., G. Dirksen, W. Kley, and R. P. Nelson 2007. On the evolution of eccentric and inclined protoplanets embedded in protoplanetary disks. *A&A* **473**, 329–342. 35, 36, 125, 126

Cresswell, P., and R. P. Nelson 2006. On the evolution of multiple protoplanets embedded in a protostellar disc. *A&A* **450**, 833–853. 35

Crida, A., F. Masset, and A. Morbidelli 2009. Long range outward migration of giant planets, with application to fomalhaut b. *ApJ* **705**, L148–L152. 13

D'Angelo, G., S. H. Lubow, and M. R. Bate 2006. Evolution of Giant Planets in Eccentric Disks. *ApJ* **652**, 1698–1714. 35

Ford, E. B., and F. A. Rasio 2008. Origins of Eccentric Extrasolar Planets: Testing the Planet-Planet Scattering Model. *ApJ* **686**, 621–636. 35

Goldreich, P., and R. Sari 2003. Eccentricity Evolution for Planets in Gaseous Disks. *ApJ* **585**, 1024–1037. 34

Goldreich, P., and S. Tremaine 1979. The excitation of density waves at the Lindblad and corotation resonances by an external potential. *ApJ* **233**, 857–871. 15, 19

Goldreich, P., and S. Tremaine 1980. Disk-satellite interactions. *ApJ* **241**, 425–441. 34

Gomes, R., H. F. Levison, K. Tsiganis, and A. Morbidelli 2005. Origin of the cataclysmic late heavy bombardment period of the terrestrial planets. *Nature* **435**, 466–469. 13

Holman, M. J., D. C. Fabrycky, D. Ragozzine, E. B. Ford, J. H. Steffen, W. F. Welsh, J. J. Lissauer, D. W. Latham, G. W. Marcy, L. M. Walkowicz, N. M. Batalha, J. M. Jenkins, J. F. Rowe, W. D. Cochran, F. Fressin, G. Torres, L. A. Buchhave, D. D. Sasselov, W. J. Borucki, D. G. Koch, G. Basri, T. M. Brown, D. A. Caldwell, D. Charbonneau, E. W. Dunham, T. N. Gautier, J. C. Geary, R. L. Gilliland, M. R. Haas, S. B. Howell, D. R. Ciardi, M. Endl, D. Fischer, G. Fürész, J. D. Hartman, H. Isaacson, J. A. Johnson, P. J. MacQueen, A. V. Moorhead, R. C. Morehead, and J. A. Orosz 2010. Kepler-9: A System of Multiple Planets Transiting a Sun-Like Star, Confirmed by Timing Variations. *Science* **330**, 51–. 12, 13

Ida, S., and D. N. C. Lin 2008. Toward a Deterministic Model of Planetary Formation. IV. Effects of Type I Migration. *ApJ* **673**, 487–501. 12, 37

Jurić, M., and S. Tremaine 2008. Dynamical Origin of Extrasolar Planet Eccentricity Distribution. *ApJ* **686**, 603–620. 35

Klahr, H., and W. Kley 2006. 3D-radiation hydro simulations of disk-planet interactions. I. Numerical algorithm and test cases. *A&A* **445**, 747–758. 34

Kley, W. 1989. Radiation hydrodynamics of the boundary layer in accretion disks. I - Numerical methods. *A&A* **208**, 98–110. 26, 28

Kley, W., B. Bitsch, and H. Klahr 2009. Planet migration in three-dimensional radiative discs. *A&A* **506**, 971–987. 11, 29, 30, 31, 34, 35, 37, 39, 125

Kley, W., and A. Crida 2008. Migration of protoplanets in radiative discs. *A&A* **487**, L9–L12. 28, 29, 30, 32, 33, 34, 125

Kley, W., and G. Dirksen 2006. Disk eccentricity and embedded planets. *A&A* **447**, 369–377. 35

Levermore, C. D., and G. C. Pomraning 1981. A flux-limited diffusion theory. *ApJ* **248**, 321–334. 26

Levison, H. F., and A. Morbidelli 2003. The formation of the kuiper belt by the outward transport of bodies during neptune's migration. *Nature* **426**, 419–421. 13

Lubow, S. H., and S. Ida 2010. Planet migration. *ArXiv e-prints*. 18

Lyra, W., S. J. Paardekooper, and M. M. Mac Low 2010. Orbital migration of low-mass planets in evolutionary radiative modesl: avoiding catastrophic infall. *ApJ* **715**, L68–L73. 36, 126

Malmberg, D., and M. B. Davies 2009. On the origin of eccentricities among extrasolar planets. *MNRAS* **394**, L26–L30. 35

Marzari, F., and A. F. Nelson 2009. Interaction of a giant planet in an inclined orbit with a circumstellar disk. *ApJ* *705*(2), 1575–1583. 36

Masset, F. 2008a. Planetary migration in gaseous protoplanetary disks. In *Exoplanets: Detection, Formation and Dynamics, Proceedings of the International Astronomical Union*, Volume 249, pp. 331–346. 16

Masset, F., and J. Casoli 2010. Saturated torque formula for planetary migration in viscous disks with thermal diffusion: Recipe for protoplanet population synthesis. *ApJ* **723**, 1393–1417. 37, 127

Masset, F. S. 2000. FARGO: A Fast Eulerian Transport Algorithm for Differentially Rotating Disks. In G. Garzón, C. Eiroa, D. de Winter, and T. J. Mahoney (Eds.), *Disks, Planetesimals, and Planets*, Volume 219 of *Astronomical Society of the Pacific Conference Series*, pp. 75–+. 128

Masset, F. S. 2001. On the Co-orbital Corotation Torque in a Viscous Disk and Its Impact on Planetary Migration. *ApJ* **558**, 453–462. 22, 23, 33

Masset, F. S. 2008b. Planet Disk Interactions. In M.-J. Goupil and J.-P. Zahn (Eds.), *EAS Publications Series*, Volume 29 of *EAS Publications Series*, pp. 165–244. 20

Masset, F. S., G. D'Angelo, and W. Kley 2006. On the Migration of Protogiant Solid Cores. *ApJ* **652**, 730–745. 21

Mayor, M., and D. Queloz 1995. A jupiter-mass companion to a solar-type star. *Nature* **378**, 355–359. 7, 8

Meyer-Vernet, N., and B. Sicardy 1987. On the physics of resonant disk-satellite interaction. *Icarus* **69**, 157–175. 15

Moorhead, A. V., and F. C. Adams 2008. Eccentricity evolution of giant planet orbits due to circumstellar disk torques. *Icarus* **193**, 475–484. 34

Moorhead, A. V., and E. B. Ford 2009. Type II migration of planets on eccentric orbits. *ArXiv e-prints*. 35

Morbidelli, A., A. Crida, F. Masset, and R. Nelson 2008. Building giant-planet cores at a planet trap. *A&A* **478**, 929–937. 12, 36

Mordasini, C., Y. Alibert, and W. Benz 2009. Extrasolar planet population synthesis. i. method, formation tracks, and mass-distance distribution. *A&A* **501**, 1139–1160. 12, 37

Mordasini, C., K. M. Dittkrist, Y. Alibert, H. Klahr, W. Benz, and T. Henning 2010. Application of recent results on the orbital migration of low mass planets: convergence zones. *astro-ph.EP*. 37

Ogilvie, G. I., and S. H. Lubow 2003. Saturation of the Corotation Resonance in a Gaseous Disk. *ApJ* **587**, 398–406. 33

Paardekooper, S., C. Baruteau, A. Crida, and W. Kley 2010. A torque formula for non-isothermal type I planetary migration - I. Unsaturated horseshoe drag. *MNRAS* **401**, 1950+. 37, 127

Paardekooper, S. J., C. Baruteau, and W. Kley 2011. A torque formula for non-isothermal type i planetary migration - ii. effects of diffusion. *MNRAS* **410**, 293–303. 37, 127

Paardekooper, S.-J., and G. Mellema 2006. Halting type I planet migration in non-isothermal disks. *A&A* **459**, L17–L20. 12, 26, 27, 30, 31, 32, 33, 34, 36

Paardekooper, S.-J., and G. Mellema 2008. Growing and moving low-mass planets in non-isothermal disks. *A&A* **478**, 245–266. 33

Paardekooper, S.-J., and J. Papaloizou 2009a. On corotation torques, horseshoe drag and the possibility of sustained stalled or outward protoplanetary migration. *MNRAS* **394**, 2283–2296. 33

Paardekooper, S.-J., and J. C. B. Papaloizou 2008. On disc protoplanet interactions in a non-barotropic disc with thermal diffusion. *A&A* **485**, 877–895. 28, 29, 30, 31, 33, 34

Paardekooper, S. J., and J. C. B. Papaloizou 2009b. On the width and shape of the corotation region for low-mass planets. *MNRAS* **394**, 2297–2309. 24, 25, 26

Papaloizou, J. C. B., and J. D. Larwood 2000. On the orbital evolution and growth of protoplanets embedded in a gaseous disc. *MNRAS* **315**, 823–833. 35, 126

Papaloizou, J. C. B., R. P. Nelson, and F. Masset 2001. Orbital eccentricity growth through disc-companion tidal interaction. *A&A* **366**, 263–275. 35

Sándor, Z., W. Lyra, and C. P. Dullemond 2011. Formation of planetary cores at type i migration traps. *ApJ* **728**, L9. 37

Sari, R., and P. Goldreich 2004. Planet-Disk Symbiosis. *ApJ* **606**, L77–L80. 34

Tanaka, H., T. Takeuchi, and W. R. Ward 2002. Three-Dimensional Interaction between a Planet and an Isothermal Gaseous Disk. I. Corotation and Lindblad Torques and Planet Migration. *ApJ* **565**, 1257–1274. 17, 19, 21, 27, 31, 34, 37, 125

Tanaka, H., and W. R. Ward 2004. Three-dimensional Interaction between a Planet and an Isothermal Gaseous Disk. II. Eccentricity Waves and Bending Waves. *ApJ* **602**, 388–395. 35, 36

Terquem, C., and A. Ajmia 2010. Eccentricity pumping of a planet on an inclined orbit by a disc. *MNRAS* **404**, 409–414. 35

Triaud, A. H. M. J., A. Collier Cameron, D. Queloz, D. R. Anderson, M. Gillon, L. Hebb, C. Hellier, B. Loeillet, P. F. Maxted, M. Mayor, F. Pepe, D. Pollacco, D. Ségransan, B. Smalley, S. Udry, R. G. West, and P. J. Wheatley 2010. Spin-orbit angle measurements for six southern transiting planets; New insights into the dynamical origins of hot Jupiters. *ArXiv e-prints*. 35

Tsiganis, K., R. Gomes, A. Morbidelli, and H. F. Levison 2005. Origin of the orbital architecture of the giant planets of the solar system. *Nature* **435**, 459–461. 13

Udry, S., and N. C. Santos 2007. Statistical Properties of Exoplanets. *ARA&A* **45**, 397–439. 34

Ward, W. R. 1986. Density waves in the solar nebula - Differential Lindblad torque. *Icarus* **67**, 164–180. 16

Ward, W. R. 1991. Horsehoe Orbit Drag. In *Lunar and Planetary Institute Conference Abstracts*, pp. 1463–+. 20, 23, 24

Ward, W. R. 1997. Protoplanet Migration by Nebula Tides. *Icarus* **126**, 261–281. 11, 13, 16

Ward, W. R., and J. M. Hahn 1994. Damping of orbital inclinations by bending waves. *Icarus* **110**, 95–108. 126